

**ULTRAFAST EXCITED STATE DYNAMICS OF
INTRAMOLECULAR CHARGE TRANSFER MOLECULES IN
SOLUTION**

By

RAJIB GHOSH
(CHEM01200904008)

Bhabha Atomic Research Centre, Mumbai

*A thesis submitted to the
Board of Studies in Chemical Science Discipline*

*In partial fulfillment of requirements
For the degree of*

DOCTOR OF PHILOSOPHY
of
HOMI BHABHA NATIONAL INSTITUTE



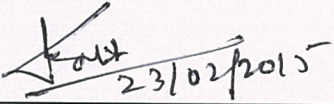
March, 2014

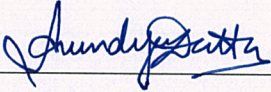
Homi Bhabha National Institute

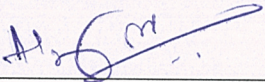
Recommendations of the Viva Voce Board


As members of the Viva Voce Board, we certify that we have read the dissertation prepared by **Rajib Ghosh** entitled “**Ultrafast Excited State Dynamics of Intramolecular Charge Transfer Molecules in Solution**” and recommend that it may be accepted as fulfilling the dissertation requirement for the Degree of Doctor of Philosophy.

 Date: 23.02.2015
Chairman: Prof. B. N. Jagatap

 Date: 23/02/2015
Guide/Convener: Prof. D. K. Palit

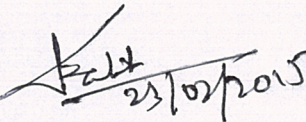
 Date: 23/02/2015
External Examiner: Prof. Anindya Datta

 Date: 23-02-2015
Member 1: Prof. A. C. Bhasikuttan

 Date: 23-2-15
Member 2: Prof. P. K. Pujari

Final approval and acceptance of this dissertation is contingent upon the candidate's submission of the final copies of the dissertation to HBNI.

I hereby certify that I have read this dissertation prepared under my direction and recommend that it may be accepted as fulfilling the dissertation requirement.

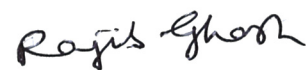
 Date: 23/02/2015
Dipak K. Palit

Date: 23/02/2015
Place: Mumbai

STATEMENT BY AUTHOR

This dissertation has been submitted in partial fulfillment of requirements for an advanced degree at Homi Bhabha National Institute (HBNI) and is deposited in the Library to be made available to borrowers under rules of the HBNI.

Brief quotations from this dissertation are allowable without special permission, provided that accurate acknowledgement of source is made. Requests for permission for extended quotation from or reproduction of this manuscript in whole or in part may be granted by the Competent Authority of HBNI when in his or her judgment the proposed use of the material is in the interests of scholarship. In all other instances, however, permission must be obtained from the author.



Rajib Ghosh

DECLARATION

I, hereby declare that the investigation presented in the thesis has been carried out by me.
The work is original and has not been submitted earlier as a whole or in part for a degree /
diploma at this or any other Institution / University.


Rajib Ghosh

List of publications arising from the thesis

1. Ultrafast Dynamics of the Excited States of the Uranyl Ion in Solutions;
Rajib Ghosh, J. A. Mondal, H. N. Ghosh, and D. K. Palit,
J. Phys. Chem. A **2010**, 114, 5263–5270.
2. Ultrafast Dynamics of the Excited States of Curcumin in Solution;
Rajib Ghosh, J. A. Mondal, and D. K. Palit.
J. Phys. Chem. B **2010**, 114, 12129–12143.
3. Ultrafast Dynamics of the Excited States of 1-(p-Nitrophenyl)-2-hydroxymethyl pyrrolidine;
Rajib Ghosh and D. K. Palit,
J. Phys. Chem. A **2012**, 116, 1993–2005.
4. Dynamics of solvent controlled excited state intramolecular proton transfer coupled charge transfer reactions;
Rajib Ghosh and D. K. Palit.
Photochem. Photobiol. Sci., **2013**, 12, 987–995.
5. Probing Excited State Charge Transfer Dynamics in a Heteroleptic Ruthenium Complex.
Rajib Ghosh and D. K. Palit;
Phys. Chem. Chem. Phys. 2014, 16, 219–226.
6. Role of Donor Acceptor Conjugation on Intramolecular Charge Transfer Dynamics;
Rajib Ghosh and D. K. Palit,
(To be submitted)

Dedicated to.....

*My Beloved
Family*

ACKNOWLEDGEMENTS

I take this opportunity to acknowledge some of the people who helped me to accomplish this journey successfully and made it memorable too.

I would like to express my deep and sincere gratitude to my guide, Prof. Dipak K. Palit for his invaluable guidance, constant encouragement, and good wishes. His wide knowledge and his logical way of thinking on critical scientific problems have been of great value for me. This thesis would not have been possible without his guidance, help, support and critical analysis. I am also grateful to him for being patient while critically reviewing this thesis.

I wish to express my sincere thanks to my senior colleague Dr. J. A. Mondal for his technical help, fruitful scientific discussions and moral support offered to me from time to time throughout the course of the work. I acknowledge the help rendered by all the lab members: Dr. H. N. Ghosh, Dr. S. Verma, Chandralekha, Snehal, Biswajit. I wish to express my sincere thanks to Dr. Raghunath Chowdhury for his help in synthesis of few organic compounds. I also thank Dr. Naresh Jena for his help in quantum chemical calculations. I gratefully acknowledge the help of Prof. Anindya Datta (IIT Bombay, India) and his students for TCSPC and fluorescence upconversion measurements.

I am highly grateful to the members of the doctoral committee Prof. T. Mukherjee (Chairman), Prof. A. C. Bhasikuttan (Member) and Prof. P. K. Pujari (Member) for their critical review and suggestions during the progress review and pre-synopsis viva-voce.

Life would have been extremely dull and monotonous without the pleasant and refreshing company of many of my friends like Prabhat Da, Raghu Da, Atindra Da, Simita Di, Naresh, Sidhhartha, Pradip, Ankur.

I am forever indebted to my parents and sister for their love and encouragement throughout my entire life. I owe special gratitude to my parents in law for their moral support.

Finally, I would like to thank my wife, Dipanwita, who has been my closest companion on this long journey. Words fail me to express my appreciation for her, whose love and care has taken the load off my shoulder. Without her persuasion, I would not have finished this thesis. I take this opportunity to express my deepest gratitude to her.

March, 2014

Rajib Ghosh
RPCD, BARC

CONTENTS

	Page No.
SYNOPSIS	xii
LIST OF FIGURES	xxiii
LIST OF TABLES	xxx
LIST OF ABBREVIATION	xxxiii
Chapter 1	
Introduction	
1.1. Characterization of the excited state of molecules	3
1.2. Relaxation processes following photoexcitation in solution	3
1.3. Vibrational relaxation	5
1.4. Internal conversion	6
1.5. Intersystem crossing	7
1.6. Excited state intramolecular proton transfer	8
1.7. Solute solvent interaction and solvation	10
1.8. Excited state structural relaxation: Twisted intramolecular charge transfer	12
1.9 Barrierless ultrafast structural dynamics	17
1.10 Photophysics and excited state dynamics of inorganic complexes	17
1.11 Scope of the present work	18
CHAPTER 2	
Experimental Techniques and Instrumentation	
2.1. Steady state absorption and fluorescence measurement	20
2.2. Fluorescence lifetime measurement	22
2.2.1. Basic Principle of TCSPC technique	23
2.2.2. Basic principle of fluorescence up-conversion	25
2.2.3 Brief description of fluorescence upconversion set up	27
2.3. Nanosecond laser flash photolysis	29
2.4. Femtosecond pump probe transient absorption spectroscopy	30
2.4.1. Femtosecond transient absorption spectrometer	33
2.4.2.1 Ultrashort pulse generation: Ti-sapphire oscillator	33

2.4.2.2 Chirped-Pulse Amplification (CPA) - Ti:Sapphire Amplifier	35
2.4.2.3 Pulse Stretcher and Compressor	36
2.4.2.4 Regenerative and Multipass Amplification	37
2.4.3. Measurement of ultrashort pulses	38
2.4.4 Generation of pump pulse: Second harmonic generation	40
2.4.5 Generation of probe light: White Light Generation	40
2.4.6 Setup of Pump probe spectrometer	41
2.5 Quantum chemical calculation	44
2.6 Materials	44

CHAPTER 3

Ultrafast Dynamics of the Excited States of Curcumin in Solution

3.1. Introduction	47
3.2. Results	51
3.2.1. Steady state absorption and fluorescence	51
3.2.2. Fluorescence upconversion study	53
3.2.3. Transient absorption spectroscopic studies	59
3.2.3.1. In aprotic solvents	59
3.2.3.1. In protic solvents	69
3.3. Discussion	71
3.3.1. Solvation dynamics in protic solvents	71
3.3.2. Solvation dynamics in aprotic solvents	75
3.3.3. Deactivation of the S ₁ state	77
3.3.4. Why did not we observe ESIHT process?	79
3.4. Conclusion	82

CHAPTER 4

Ultrafast Dynamics of Excited State Intramolecular Proton Coupled Charge transfer Reaction

4.1. Introduction	84
4.2. Results and Discussion	86
4.2.1. Ground state structure	86
4.2.2. Steady state photophysical studies	87
4.3.3. Transient absorption and fluorescence spectroscopic studies	89
4.3.3.1 Transient absorption studies in cyclohexane	89

4.3.3.2 Transient fluorescence studies in cyclohexane	91
4.3.3.3 Transient absorption studies in toluene	92
4.3.3.4 Transient absorption studies in acetonitrile	94
4.3.3.3 Transient fluorescence studies in acetonitrile	97
4.3.4. Excited state calculation	98
4.3.5. Potential energy surface diagram	101
4.4. Conclusion	104

CHAPTER 5

Effect of Donor-Acceptor Conjugation on the Intramolecular Charge Transfer Relaxation Dynamics

5.1. Introduction	105
5.2. Results and Discussion	107
5.2.1. Steady-state absorption and fluorescence studies	107
5.2.2. Time resolved fluorescence measurements	110
5.2.3. Transient absorption studies of DMAC-A in polar solvents	112
5.2.4. Effect of solvent viscosity on TICT dynamics of DMAC-A	113
5.2.5. Transient absorption studies of DMAC-B in polar solvents	115
5.2.6. Transient absorption studies in cyclohexane	117
5.2.7. Quantum chemical calculations	119
5.3. Discussion	120
5.4. Conclusion	122

CHAPTER 6

Ultrafast Dynamics of the Excited States of 1-(p-Nitrophenyl)-2-hydroxymethylpyrrolidine

6.1. Introduction	124
6.2. Results	129
6.2.1. Steady-state absorption and fluorescence studies	129
6.2.2. Transient absorption spectroscopic study	130
6.2.2.1 In nonpolar aprotic solvents	130
6.2.2.2. In polar aprotic solvent	134
6.2.2.3 In water	139
6.2.2.4 Dynamics in alcoholic solvents	141
6.3. Discussion	144

6.4. Conclusion	151
CHAPTER 7	
Charge Localization Dynamics in Heteroleptic Ruthenium Complex	
7.1. Introduction	152
7.2. Results and Discussion	154
7.2.1. Steady state absorption spectra	154
7.2.2. TDDFT calculation	156
7.2.3. Nanosecond flash photolysis studies	157
7.2.4 Femtosecond transient absorption studies	159
7.3. Conclusion	166
CHAPTER 8	
Ultrafast Dynamics of the Excited States of the Uranyl Ion in Solutions	
8.1. Introduction	167
8.2. Results and Discussion	172
8.2.1. Steady state absorption and fluorescence studies	172
8.2.2. Femtosecond transient absorption spectroscopic studies	176
8.2.2.1. In aqueous solution	176
8.2.2.2. In methanol solution	180
8.3. Conclusion	186
SUMMARY AND OUTLOOK	187
REFERENCES	191

SYNOPSIS

Chemistry deals with the transformation of molecular entity through several elementary steps occurring in different timescales. Therefore, understanding the overall mechanism of a chemical reaction involves the investigation of the elementary processes at a molecular level. Many such processes occur with great rapidity involving many short-lived intermediate species, called the transients. Hence, creating such short-lived transients involved in a chemical reaction and then monitoring the characteristics of these transients are essential to obtain a deep insight into the microscopic mechanism of the reaction. Creation of electronic excited state using short light pulse and monitoring of subsequent evolution of the excited states are the key to explore reaction dynamics in real time. In 1949, Norris and Porter developed microsecond flash photolysis technique to monitor short lived reaction intermediate, for the first time.¹ In following years, invention of pulsed lasers and pump probe technique revolutionized the field of time resolved spectroscopy. Advent of femtosecond laser pulses have offered direct observation of transition state of a chemical reaction.² Importance of femtochemistry in studies of reaction dynamics was recognized by awarding a Nobel Prize to Prof. Ahmed Zewail in 1999.

Subpicosecond and femtosecond experiments allow monitoring fundamental chemical processes in real time.^{3,4} An electronically excited molecule undergoes a number of relaxation pathways, such as vibrational relaxation, charge transfer, energy transfer, proton transfer, solvent relaxation, configurational relaxation, intersystem crossing, internal conversion, etc.⁵ These excited state deactivation pathways are relevant to many chemical and biochemical processes.^{6,7} Electron transfer, proton transfer and proton coupled electron transfer are the most important reactions in photosynthesis and solar energy conversion reactions.⁸⁻¹¹ Intramolecular charge transfer excited state serves to elucidate microscopic picture of solute solvent interaction and solvation dynamics.^{12,13} Large amplitude structural motion in donor-acceptor

molecules strongly influences extent of charge separation forming twisted intramolecular charge transfer (TICT) state. Time resolved measurements on TICT relaxation dynamics provide information about excited state potential energy surface.^{14,15} Development of materials for solar energy harvesting, artificial photosynthesis, molecular electronics, etc are relies on excited state relaxation and deactivation mechanism.^{16,17} Thus, fundamental understanding of excited state relaxation dynamics in real time holds crucial significance to unravel natural photoinduced processes as well as development of artificial photofunctional materials. Time resolved measurements on structurally simpler model molecules often provide in-depth understanding of the molecular level mechanism and timescale of these competing processes.

Employing femtosecond time resolved spectroscopy on several model molecular systems, the thesis aims at providing some important insights into the excited state dynamics of intramolecular charge transfer, proton transfer and structural relaxation and other electronic deactivation processes. For the convenience of presentation, the thesis is organized in the form of eight chapters. Chapter 1 and 2 describes the introduction of general photophysical aspects in electronic excited states and experimental techniques, respectively. Particular aspects of photoexcited state relaxation dynamics of model molecular systems are presented in self contained manner from chapter 3 to chapter 8. A concise description of the thesis is given below.

Chapter 1:

In this introductory chapter, some basic principles and concepts related to the present thesis have been discussed. The thesis deals with the photo-induced processes such as vibrational relaxation (VR), internal conversion (IC), intersystem crossing, charge transfer, proton transfer, TICT and solvation around the excited solute molecule. So a brief introduction to these interesting topics has been given in this chapter. The occurrence of a photo induced intramolecular process is strongly dependent on the geometry and electronic structure of the

molecule in the excited state as well as on the nature of interaction between chromophores and the surrounding solvent molecules. Role of solute-solvent interaction on the excited state dynamics has been discussed briefly in this chapter. Twisting induced charge transfer in donor-acceptor (D-A) molecules has been an interesting issue which has been discussed in the present thesis. Brief note on the objective and motivation of the present work has also been discussed in this introductory chapter.

Chapter 2:

This chapter provides the details of experimental methods used for the investigations of different processes presented in the thesis. Most of the work has been carried out using ultrafast transient absorption spectroscopic techniques. The basic principles of transient absorption spectroscopy and details of the femtosecond transient absorption instrument have been described in this chapter. Femtosecond fluorescence up conversion technique has been described which was used as a complementary technique to the transient absorption experiments. Basic principles of steady state absorption and fluorescence spectroscopic techniques have also been briefly described.

Chapter 3:

This chapter deals with the excited state relaxation dynamics of curcumin (figure 1), a natural pigment present in turmeric, in different protic and aprotic solvents. Structurally, Curcumin is a symmetrically substituted 1, 3-diketone which exist as keto-enol tautomer. The molecule possess strong charge transfer character in the S_1 state and shows strong solvent dependence of steady state photophysical properties. Because of structural diversity and flexibility, the molecule may undergo photoinduced proton transfer, keto-enol tautomerization or isomerization around C=C double bond. Because of large charge transfer character in the excited state, solvation can play important role in the excited state relaxation. To unravel the exact relaxation pathways, transient absorption and fluorescence studies were performed in different solvents. It was observed that in polar solvents, both aprotic and protic, solvation is

the major relaxation process following photoexcitation. Solvation dynamics in protic solvents is multimodal, and the linear correlation between the longest component of the solvation process and the longitudinal relaxation time of the solvent suggests the specific hydrogen-bonding interaction between the solute and the solvent. In nonpolar solvents, the lifetime of the S_1 state was observed to be very short because of efficient nonradiative deactivation, which is an important consequence of the ultrafast excited-state intramolecular hydrogen transfer (ESIHT) reaction in the six-membered hydrogen-bonded chelate ring of the *cis*-enol form. Although intramolecular proton transfer may be occurring in ultrafast timescale, it has not been possible to monitor due to the symmetrical structure of the molecule with respect to the hydrogen-bonded chelate ring which forms symmetrical double minima potential energy surface in the ground as well as in the excited states.

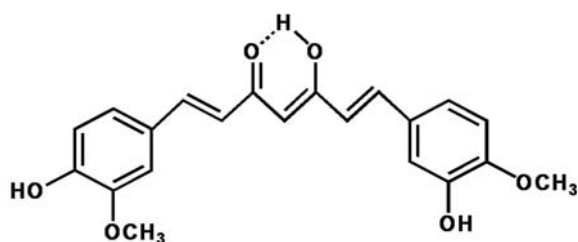


Figure 1: Structure of curcumin in keto-enol tautomeric form.

Chapter 4:

This chapter describes the steady state and ultrafast time resolved spectroscopic studies on an unsymmetrically substituted 1,3-diketone system, namely 4-dimethylamino dibenzoyl ketone (figure 2). Unsymmetrical substitution allowed us to decipher the ESIPT as well as intramolecular charge transfer dynamics and their consequence to the photophysical properties of the molecule. Steady state photophysical studies reveal strong solvent polarity dependent fluorescence behavior. In solvents of low polarity, fluorescence yield increases with polarity, becomes maximum in the medium polarity solvents but decreases in high polarity region. Because of the unsymmetrical substitution, the molecule may exist in two possible *cis*-enol tautomeric forms (Enol-A and Enol-B) which are interconvertible via intramolecular proton

transfer. The relative energetics of two tautomers and their structural consequences determine the excited state properties. Structure and relative energy of the two tautomeric states in the first excited state were determined in gas phase as well as in polar solvents, which revealed that planar ICT state of Enol-A govern the photophysics in nonpolar solvents whereas dimethylanilino twisted TICT state of enol-B controls the photophysics in polar solvents. Transient absorption and fluorescence studies reveal that in low and medium polarity solvents, the excited Enol-B molecule (Enol-B*) undergoes ultrafast excited state intramolecular proton transfer (ESIPT) leading to the population of Enol-A*, which undergoes the ICT process without any significant change in the geometrical structure of the molecule. In polar solvents, ESIPT dynamics in the S_1 state is reversed to populate Enol-B* and the relaxation process is mainly governed by solvation and twisting of the dimethylaniline group, leading to the population of the weakly emissive ‘twisted intramolecular charge transfer’ or the TICT state of Enol-B*.

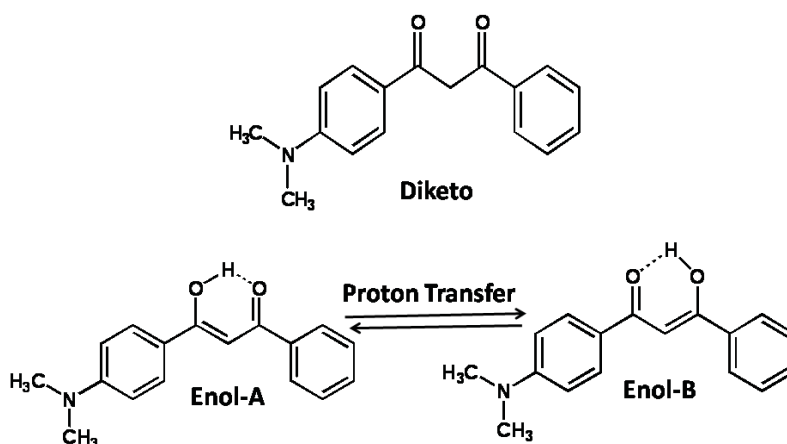


Figure 2: Structure of 4-dimethylamino dibenzoyl ketone (DMADK) in keto and keto-enol tautomeric forms.

Chapter 5:

Investigation of the role of donor acceptor conjugation on the ICT-TICT dynamics of charge transfer molecules is the subject matter of this chapter. Two isomeric charge transfer dimethylaminochalcone derivatives were synthesized (DMAC-A and DMAC-B, figure 3), which differ in relative positioning of the donor and acceptor groups. Steady state

photophysical measurements revealed that both the molecules have highly charge transfer character in their first excited singlet state but fluorescence behavior has been observed to be remarkably different. Fluorescence quantum yields of DMAC-A decreases with polarity of the solvents, whereas for DMAC-B, fluorescence yield increases in higher polarity solvents. In polar solvents, DMAC-A is more than two order of magnitude weaker fluorescent than the DMAC-B. Moreover, fluorescence band width of DMAC-A is significantly larger than that of DMAC-B in polar solvents. Remarkable difference in the fluorescence quantum yield and fluorescence lifetime is explained by invoking the formation of non-fluorescent TICT state for DMAC-A, whereas, for DMAC-B, planar ICT state is the relaxed S_1 state without occurrence of twisting process. Femtosecond transient absorption measurements in different solvents of varying polarity and viscosity revealed the twisting dynamics of DMAC-A. The difference has been attributed to the strong coupling between the donor and acceptor groups in DMAC-A due to shorter distance, whereas in DMAC-B, planar ICT structure is more stable and large barrier is involved along the TICT coordinate due to longer separation of the donor-acceptor group.

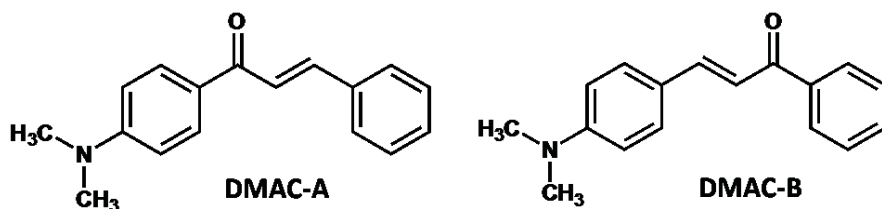


Figure 3: Structure of two isomeric dimethylaminochalcones, DMAC-A and DMAC-B.

Chapter 6:

Chapter six deals with the charge transfer dynamics of a nitro substituted D-A systems. Nitro group being a very strong acceptor moiety, can induce large charge transfer in the excited state and may undergo twisting of the nitro group to facilitate complete charge separation. Moreover, photophysics of the nitroaromatic compounds are dictated by the properties of low energy triplet state, which is populated with a large yield. Thus charge transfer, structural relaxation and intersystem crossing may give rise to complex solvent dependent dynamics in the excited state. This issue has been addressed by exploration of the excited state dynamics of

1-(p-nitrophenyl)-2-(hydroxymethyl)pyrrolidine (p-NPP, figure 4)) in different solvents. Following photoexcitation using 400 nm light, conformational relaxation via twisting of the nitro group, internal conversion (IC) and the intersystem crossing (ISC) processes have been established to be the three major relaxation pathways responsible for the ultrafast deactivation of the excited singlet (S_1) state. Although the nitro-twisting process has been observed in all kinds of solvents, the relative probability of the occurrence of IC and ISC has been found to be extremely sensitive to solvent polarity, because of alteration of the relative energies of the S_1 and the triplet (T_n) states. In the solvents of lower polarity, the ISC is predominant over the IC process, because of near isoenergeticity of the $S_1(\pi\pi^*)$ and $T_3(n\pi^*)$ states. On the other hand, in the solvents of very large polarity, the energy of the $S_1(\pi\pi^*)$ state becomes lower than those of both the $T_3(n\pi^*)$ and $T_2(n\pi^*/\pi\pi^*)$ states and the IC process to the ground electronic (S_0) state are predominant over the ISC, and hence the triplet yield is nearly negligible. However, in the solvents of medium polarity, the deactivation of the S_1 state is directed to both the IC and ISC channels. In the solvents of low and medium polarity, following the ISC process, the excited states undergo IC, vibrational relaxation, and solvation in the triplet manifold. On the other hand, in polar solvents, vibrational relaxation and reverse nitro-twisting process has been observed from the hot S_0 state following ultrafast IC.

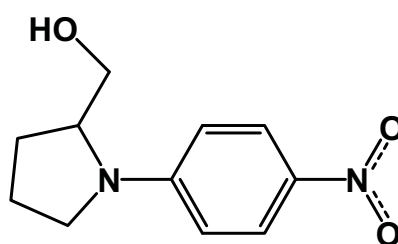


Figure 4: Structure of 1-(p-Nitrophenyl)-2-hydroxymethylpyrrolidine.

Chapter 7:

This chapter discusses metal to ligand charge transfer dynamics of a mixed ligand ruthenium complex. Charge transfer dynamics in ruthenium polypyridyl complexes are important for the development of artificial solar energy harvesting system. Mixed ligand complexes are

especially important for broader solar energy absorption. Thus understanding the charge transfer dynamics in mixed ligand complex is highly desirable for development of efficient solar energy harvesting materials. We have probed dynamics of ultrafast vibrational energy relaxation and inter-ligand charge transfer processes of a heteroleptic ruthenium complex, $[\text{Ru}(\text{bpy})_2(\text{pap})](\text{ClO}_4)_2$ (where *bpy* is 2, 2'-bipyridine and *pap* is 2-(phenylazo)pyridine, figure 5) using femtosecond to nanosecond time-resolved transient absorption spectroscopic techniques. A good agreement between the TA spectrum of the lowest excited $^3\text{MLCT}$ state of $[\text{Ru}(\text{bpy})_2(\text{pap})](\text{ClO}_4)_2$ complex and the anion radical spectrum of the *pap* ligand, which has been generated using pulse radiolysis technique, confirmed the charge localization at the *pap* ligand. While the lifetime of the inter-ligand charge transfer from the *bpy* to the *pap* ligand in the $^3\text{MLCT}$ state is about 2.5 ps, vibrational cooling of the *pap*-localized $^3\text{MLCT}$ state occurs in a much longer time scale with the lifetime of about 35 ps. Ultrafast charge localization dynamics observed here may have important consequences in artificial solar harvesting systems, which employ heteroleptic ruthenium complexes.

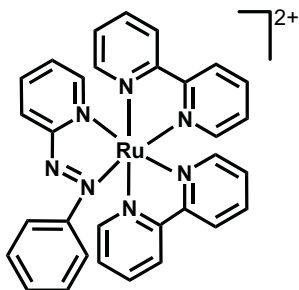


Figure 5: Structure of $[\text{Ru}(\text{bpy})_2(\text{pap})]^{2+}$

Chapter 8:

In this chapter, we describe the ultrafast electronic relaxation dynamics of uranyl ion in aqueous and methanolic solution following photoexcitation to the $S_1(^1\Phi_g)$ state using 400 nm light. The $S_1(^1\Phi_g)$ state undergoes ultrafast intersystem crossing (<100 fs) to the higher

vibrational levels of the $T_2(^3\Delta_g)$ state, followed by the intramolecular vibrational relaxation (IVR) process in the later electronic state ($\tau_{IVR} \sim 0.85$ and 1 ps in aqueous and methanolic solutions, respectively). Subsequently, the $T_2(^3\Delta_g)$ state undergoes an internal conversion (IC) process ($\tau_{IC} \sim 1.6$ and 4.5 ps in aqueous and methanol solutions, respectively) to the long-lived $T_1(^3\Phi_g)$ state, which is responsible for the luminescent properties of the uranyl ion. In methanol, because of stronger interaction between the excited triplet, $T_1(^3\Phi_g)$, state and the solvent via solvent to uranyl charge transfer, the U(VI) ion undergoes partial reduction to U(V) and the energy level of this state possibly lies lower than that of $(UO_2^{2+})^*$, which is the transient species existing in aqueous solution, and hence increasing the energy gap between the T_2 and T_1 states in methanol solution.

Summary:

The main aim of the thesis is to investigate the dynamics of intramolecular charge transfer, proton transfer, large amplitude structural relaxation and solvation dynamics in some model molecules. Competing relaxation pathways and their dependence on structure, functional group, solvent properties has been evaluated. Different aspects of the excited state relaxation processes were deciphered using specific model molecules. The main conclusions drawn from the different molecular systems studied in this thesis are as follows:

- Intramolecular charge transfer dynamics has been revealed to be associated with large amplitude structural relaxation of donor and acceptor moieties. Solvent polarity, viscosity and solvation dynamics were found to play significant role in ICT dynamics. Excited state properties have been revealed to be strongly dependent on the structure and functional group present in the molecular system. Solvent properties (i.g. polarity and proticity) have been found to significantly affect the excited state dynamics.
- In curcumin, six membered intramolecular hydrogen bonded system, excited state relaxation is mainly governed by solvation dynamics. The possible ESIPT dynamics

could not be resolved due to symmetrical structure of the molecule. Nonetheless, ESIPT was found to influence the excited state lifetime in nonpolar solvents.

- In a synthesized unsymmetrical diketone, namely DMADK, ESIPT process has been resolved which occurs in <200 fs timescale. Solvent polarity governs the direction of proton transfer and subsequent intramolecular charge transfer and structural relaxation.
- Effect of conjugation and coupling between donor and acceptor groups on twisted intramolecular charge transfer dynamics has been revealed from the comparative photophysics and excited state dynamics of the isomeric 4-dimethylaminochalcones.
- Studies on p-NPP revealed that twisting of nitro group governs the excited state charge transfer process followed by competing ultrafast internal conversion or Intersystem crossing depending on solvent polarity.
- Studies on two inorganic systems leads us to understand that excited state dynamics in inorganic molecules occurs on the triplet energy surface following ultrafast intersystem crossing. In uranyl nitrate, ultrafast ISC followed by vibrational relaxation and internal conversion to the lowest energy triplet state are the initial event upon photoexcitation. In a mixed ligand ruthenium complex, we observed the interligand electron transfer and vibrational relaxation to form lowest energy $^3\text{MLCT}$ state.

The studies of excited state dynamics in various model molecules with different structures and functionality have revealed that excited state processes are strongly dependent on the structure and functional moieties present in the molecule. Effect of surrounding solvent environment has also been observed to determine the fate of the photo excited state. The knowledge gained from the present study on the dynamics of photo-induced intra- and inter-molecular processes in condensed phase may be useful for their applications in different fields such as molecular based photonic devices, nonlinear optics, photovoltaics, etc.

References:

1. Norrish, R. G. W., Porter, G., *Nature*, **1949**, 164, 658.
2. Khundkar, L. R.; Zewail A. H.; *Annu. Rev. Phys. Chem.* **1990**, 41, 15.
3. Shank, C. V.; *Science* **1986**, 233, 1276.
4. Fleming G. R., *Annu. Rev. Phys. Chem.* **1986**, 37, 81.
5. Birks, J. B. "*Photophysics of Aromatic Molecules*", Wiley, New York, 1970.
6. Rohatgi-Mukherjee, K. K. "*Fundamentals of Photochemistry*", Wiley Eastern Ltd.India, 1986.
7. Sundstrom, V, *Annu. Rev. Phys. Chem.* **2008**, 59, 53-77
8. Balzani, V (Ed). *Electron transfer in chemistry*, Wiley-VCH Publishers Inc., New York, Volumes I to V, **2001**.
9. Elsaesser, T. Ultrafast excited-state hydrogen transfer in the condensed phase. In *Ultrafast hydrogen bonding dynamics and proton transfer processes in the condensed phase*; Elsaesser, T., Bakker, H. J., Eds.; Kluwer Academic Publishers: New York, 2002; pp 119.
10. Cukier, R. I.; Nocera, D. G.; *Annu. Rev. Phys. Chem* **1998**, 49, 337.
11. Hsieh C. C., Jiang C. M, Chou P-T. *Acc. Chem. Res.* **2010**, 43, 1364.
12. Barbara, P. F.; Jarzeba, W.; *Adv. Photochem.* **1990**, 15, 1.
13. Horng, M. L.; Gardecki; J. A.; Papazyan, A.; Maroncelli, M.; *J. Phys. Chem.* **1995**, 99, 17311.
14. Grabowski, Z. R.; Rotkiewicz, K. Rettig, W.; *Chem. Rev.* **2003**, 103, 3899-4031.
15. Glasbeek, G.; Zhang, H. *Chem. Rev.* **2004**, 104, 1929.
16. Gust, D.; Moore, T. A.; Moore, A.L.; *Acc. Chem. Res.* **2009**, 42, 1890.
17. Baranoff, E.; Barigelletti, F.; Bonnet, S.; Collin, J-P.; Flamigni, L.; *Struct. Bond.* **2007**, 123, 41.

LIST OF FIGURES

	Page No.
Figure 1.1	4
The Jablonsky diagram describing different photophysical processes undergone by an electronically excited molecule. Straight arrows and wavy arrows represent the radiative and non-radiative processes, respectively. Abbreviations are: Abs-Absorption; IC-Internal Conversion; ISC-Intersystem Crossing; RISC-Reverse ISC; VR-Vibrational Relaxation; FI-Fluorescence; Ph-Phosphoresence; S _i -ith singlet state and T _i -ith the triplet state.	
Figure 1.2	5
Different photoinduced excited state reactions and relaxation pathways.	
Figure 1.3	8
Schematic presentation of ESIPT reaction with an example of o-hydroxybenzoxazole.	
Figure 1.4	9
ESIPT reaction in keto-enol tautomers of 1, 3 diketones.	
Figure 1.5	11
Schematic diagram of solvent relaxation in photoexcited state.	
Figure 1.6	12
TICT model for dual emission of DMABN molecule.	
Figure 1.7	13
Schematic excited state potential energy surface of TICT relaxation.	
Figure 2.1	24
Schematic diagram of a Time Correlated Single Photon Counting Spectrometer.	
Figure 2.2	26
Schematic representation of sum frequency generation principle in a non-linear crystal which is the basis of fluorescence up-conversion.	
Figure 2.3	27
Schematic diagram of the femtosecond fluorescence up-conversion instrument.	
Figure 2.4	30
Basic layout of nanosecond flash photolysis set up.	
Figure 2.5	33
Scheme of the states involved in a pump probe experiment in a dye solution. (A) Excited state absorption (B) Stimulated emission. (C) Bleaching.	
Figure 2.6	34
Optical layout of femtosecond Ti-sapphire oscillator.	

Figure 2.7	36
Principle of chirp pulse amplification technique.	
Figure 2.8	37
Principle optical layout for pulse stretching (upper) and pulse compression (lower) .	
Figure 2.9	38
Schematic diagram of combined regenerative-two pass amplifier.	
Figure 2.10	39
Optical layout of intensity autocorrelator for femtosecond pulse measurement.	
Figure 2.11	40
A schematic diagram of second harmonic generation (SHG) principle.	
Figure 2.12	41
A schematic diagram showing the generation of white light continuum.	
Figure 2.13	42
Complete layout of pump probe transient absorption spectrometer.	
Figure 3.1	52
Steady-state absorption and fluorescence spectra of Curcumin in 1,4-dioxane, acetonitrile, DMSO and methanol.	
Figure 3.2	54
Fluorescence upconversion signals of curcumin in ethanol, recorded at different wavelengths, along with their biexponential or triexponential fit functions. Values of the lifetimes are given in Table 3.1. Inset of B: Signals recorded at 460 and 660 nm have been compared in sub-60 ps time domain to show the nearly equal rate of decay of the signal recorded at 460 nm and the rate of growth of the signal recorded at 660 nm.	
Figure 3.3	56
Time-resolved emission spectra constructed at different delay times (Delay times: 0.35, 0.5, 0.8, 1.2, 1.6, 2.0, 2.5, 3, 3.5, 4.0, 5, 6, 8, 10, 12, 14, 16, 18, 20, 24, 28, 32, 36, 40, 44, 48, 52, 56, 60, 65, 70, 75, 80 ps). Inset: Time-correlation function $C(t)$, constructed following equation 1, along with the tri-exponential fit function. The lifetimes associated with the fit function and the average lifetime calculated are also shown in the inset.	
Figure 3.4	58
Comparison of the fluorescence decay of curcumin in methanol and curcumin-d in methanol-d at 480, 520 and 640 nm.	

Figure 3.5

61

Time-resolved differential absorption spectra of the transient species formed following photoexcitation of curcumin in 1,4-dioxane using 400 nm laser. Olive colored curve represents the position and shape of the steady-state fluorescence spectrum.

Figure 3.6

62

Temporal profiles (circles) recorded at a few selective wavelengths following photoexcitation of curcumin in 1,4-dioxane using 400 nm light. The red lines represent the best fit multiexponential functions and the lifetimes associated with the best fit function are given in the insets.

Figure 3.7

64

Time-resolved absorption spectra of the transient species formed following photoexcitation of curcumin in acetonitrile using 400 nm laser pulses.

Figure 3.8

66

Temporal profiles (circles) recorded at a few selective wavelengths following photoexcitation of curcumin in acetonitrile. The red lines represent the best fit multi-exponential functions. The lifetimes associated with the fit functions are given in the insets. In each case, the fit function is associated with a slow decay component with a lifetime longer than 500 ps, which is not given in the insets.

Figure 3.9

67

Temporal profiles (circles) recorded at 470 and 870 nm following photoexcitation of curcumin in polar aprotic solvents. The red lines represent the best fit multi-exponential functions. The lifetimes (in ps) associated with the fit functions are as follows (in each case the fit function is associated with a slow decay component with a lifetime longer than 500 ps, which is not given here): (A) DMF: 470 nm - 0.3 (g), 2.3 (g), 162 (d); 870 nm – 3.5 (d), 150 (d).

(B) DMSO: 470 nm - 0.35 (g), 2.6 (g), 202 (d); 870 nm – 4 (d), 160 (d).

(C) PC: 470 nm - 1 (g), 6.3 (g), 300 (d); 870 nm – 1 (d), 7.7 (d), 270 (d).

(d) FA: 470 nm - 0.3 (g), 3.2 (g), 42 (d); 870 nm – 0.25 (d), 3.9 (d), 50 (d).

Figure 3.10

70

Time-resolved differential absorption spectra of the transient species formed following photoexcitation of curcumin in methanol. Olive coloured curve represents the steady-state fluorescence spectrum in this solvent.

Figure 3.11

70

Temporal profiles (circles) recorded at a few selective wavelengths following photoexcitation

of curcumin in methanol. The red lines represent the best fit multiexponential functions. The lifetimes associated with the fit functions are given in the insets.

Figure 3.12 72

Temporal profiles recorded at 480 nm following photoexcitation of curcumin in alcohols :EG (1), ethanol (2), 1-propanol (3), 1-butanol (4) and 1-pentanol (5). Lifetimes obtained from the best fit multiexponential function are given in Table 3.2.

Figure 3.13 77

A. Correlation between $\ln(\tau_2)$ with $\ln(\tau_L)$ of the solvents. The best-fit line, which represents the function: $\ln(\tau_2) = 0.81 + 0.76 \tau_L$ (Adj. R2 = 0.96, N=10), does not include the data point for ethylene glycol.

B. Correlation between $\ln(\tau_2)$ with $\ln(\langle\tau\rangle_{\text{avg}})$ of the solvents. The best fit line represents the function: $\ln\langle\tau\rangle_{\text{solv}} = 0.81 + 0.99 \langle\tau\rangle_{\text{coulm}}$ (Adj. R2 = 0.86, N =15), The solvents are: 1,4-dioxane (1), EA(2), TA(3), BN (4), acetonitrile (5), DMF(6), DMSO(7), PC(8), formamide(9), methanol (10), ethanol (11), 1-propanol (12), 1-butanol (13), 1-pentanol (14), and ethylene glycol (15).

Figure 4.1 85

Structure of DMADK in diketo- and two cis-enol (Enol-A and Enol-B) tautomeric forms.

Figure 4.2 86

DFT optimized structures of Enol A and Enol B, in the ground state using B3LYP/6-31G(d,p) basis set.

Figure 4.3 88

Normalized steady state absorption spectra (A), fluorescence spectra (B) and Lippert-Mataga Plot (C) in aprotic solvents. Insets shows the correlation of the absorption and fluorescence maxima and the Stokes shift (SS) with the solvent polarity parameter, $E_T(N)$.

Figure 4.4 88

Solvent Polarity, $E_T(N)$, dependence of Φ_F and k_{NR} of DMADK. Solid lines (red colored) simply provide a guide to the eye and not any functional fit.

Figure 4.5 90

Time-resolved absorption spectra of the transient species formed following photoexcitation of DMADK in cyclohexane using 400 nm laser pulses. Delay times are given in the insets.

Figure 4.6 91

Temporal profiles (circles) recorded at a few selective wavelengths following photoexcitation of DMADK in cyclohexane using 400 nm light along with the best-fit multiexponential

functions. Associated lifetimes are given in the insets. The temporal profiles recorded at 600 and 650 nm are also associated with a long-lived residual absorption, assigned to the T_1 state.

Figure 4.7 92

Fluorescence temporal profiles of DMADK in cyclohexane.

Figure 4.8 93

Time-resolved TA spectra recorded in toluene following 400 nm photoexcitation.

Figure 4.9 93

Temporal dynamics recorded at a few selective wavelengths in toluene.

Figure 4.10 95

Time-resolved TA spectra constructed following photo-excitation of DMADK in acetonitrile using 400 nm laser pulses. Inset shows the time-dependence of the dynamic red shift of stimulated emission maximum ($\bar{\nu}_p$) vs time.

Figure 4.11 96

Temporal evolution of transient absorption monitored at different wavelengths following photo-excitation of DMADK in acetonitrile using 400 nm laser pulses of 50 fs duration. Solid lines represent the best multi-exponential fit-functions. The lifetimes of the decay (d) and /or rising (r) components, thus determined, are given in the insets.

Figure 4.12 98

Fluorescence upconversion signals recorded at a few selective wavelengths along with the multi-exponential fit functions and the lifetimes associated with the different components given in the insets.

Figure 4.13 101

TDDFT optimized structures of Enol-A and Enol-B, in the S_1 states in the gas phase using B3LYP/6-31G(d,p) basis set.

Figure 4.14 102

Simplified schematic potential energy surface (PES) diagram depicting the polarity tuning of the excited state dynamics of the S_1 state of DMADK.

Figure 5.1 107

Structure of the two isomeric 4-dimethylaminochalcones.

Figure 5.2 108

Steady-state absorption (A) and fluorescence (B) spectra of DMAC-A in different solvents. Inset shows Lippert-Mataga plot to calculate the change in dipole moment in the excited state.

Figure 5.3	108
Steady-state absorption (A) and fluorescence (B) spectra of DMAC-B in different solvents. Inset shows Lippert-Mataga plot to determine the change in dipole moment in the excited state.	
Figure 5.4	110
Fluorescence decays of DMAC-A measured by fluorescence upconversion (A) and of DMAC-B measured by TCSPC technique (B).	
Figure 5.5	112
Femtosecond transient spectral evolution (A) and temporal decay behavior (B) at different probe wavelength of DMAC-A in acetonitrile. Lifetimes (in ps) from mutiexponential fitting are given in inset.	
Figure 5.6	114
Effect of solvent viscosity on the twisting dynamics of DMAC-A.	
Figure 5.7	115
Femtosecond transient spectral evolution of DMAC-B in acetonitrile (A) and the temporal decay behavior at different probe wavelength (B). Lifetimes (in ps) are given in inset.	
Figure 5.8	118
Femtosecond transient absorption spectra (left) and temporal decay kinetics (right) of DMAC-B in cyclohexane.	
Figure 5.9	119
Femtosecond transient absorption spectra (left) and temporal decay kinetics (right) of DMAC-A in cyclohexane.	
Figure 5.10.	120
Gas phase optimized structure of DMAC-A and DMAC-B in the ground electronic state (A) and the first excited singlet state (B).	
Figure 5.11:	122
Schematic potential energy surface (PES) diagrams illustrating the difference between the photophysical processes occurring in the excited states of DMAC-A and DMAC-B in polar solvents.	
Figure 6.1	128
Chemical structure of 1-(p-nitrophenyl)-2-hydroxymethyl-pyrrolidine (<i>p</i> -NPP).	
Figure 6.2	130
Steady state absorption and fluorescence spectra of <i>p</i> -NPP in 1,4-dioxane, ethanol, DMSO and water.	

Figure 6.3	131
Time-resolved TA spectra constructed for different delay times following photo-excitation of <i>p</i> -NPP in 1,4-dioxane using 400 nm laser pulses of 50 fs duration.	
Figure 6.4	133
Temporal evolution of TA monitored at a few selective wavelengths following photo-excitation of <i>p</i> -NPP in dioxane. Solid lines represent the best-fit multi-exponential functions along with an offset for a longer lived component of ESA. The lifetimes associated with the fit functions are given in the insets.	
Figure 6.5	135
Time-resolved TA spectra constructed for different delay times following photo-excitation of <i>p</i> -NPP in DMSO. Inset provides the normalized TA spectra recorded at 0.15 and 0.5 ps delay times.	
Figure 6.6	137
Temporal evolution of transient absorption of <i>p</i> -NPP in DMSO along with the best fit multi-exponential functions. Lifetimes of different components are given in the inset.	
Figure 6.7	140
Time-resolved TA spectra constructed at different delay times following photo-excitation of <i>p</i> -NPP in water.	
Figure 6.8	141
Temporal evolution of transient absorption monitored at different wavelengths following photo-excitation of <i>p</i> -NPP in water.	
Figure 6.9	142
Time-resolved TA spectra constructed at different delay times following photo-excitation of <i>p</i> -NPP in ethanol. Inset shows the blown up of the spectral region 460 – 600 nm.	
Figure 6.10	144
Temporal profiles recorded at a few selective wavelengths following photo-excitation of <i>p</i> -NPP in ethanol. Each of the temporal profiles is associated with a long-lived residual absorption.	
Figure 6.11	145
Gas phase optimized structure of <i>p</i> -NPP in the ground electronic state (A) and the first excited singlet state (B).	
Figure 6.12	146
Potential energy surfaces in the S_0 and S_1 states of <i>p</i> -NPP with respect to the twisting angle of the Nitro group (A) and the 2-hydroxymethyl-pyrrolidine group (B).	

Figure 6.13:	146
HOMO - LUMO pictures of the optimized ground and the first excited singlet states of <i>p</i> -NPP.	
Figure 6.14	150
Schematic potential energy surface (PES) diagrams illustrating the different photophysical processes occurring in the excited states of <i>p</i> -NPP in solvents of low polarity (A), medium polarity (B) and large polarity (C).	
Figure 7.1	154
Structure of $[\text{Ru}(\text{bpy})_2(\text{pap})]^{2+}$	
Figure 7.2	155
Steady state absorption spectra of $[\text{Ru}(\text{bpy})_2(\text{pap})]^{2+}$ in acetonitrile and water.	
Figure 7.3	156
Simplified energy level diagram to compare the MLCT transition of $[\text{Ru}(\text{bpy})_2(\text{pap})]^{2+}$ and $[\text{Ru}(\text{bpy})_3]^{2+}$.	
Figure 7.4	157
DFT calculated molecular orbitals associated with the different electronic transitions.	
Figure 7.5	159
(a) Steady state absorption spectrum in acetonitrile (inverted); (b) Differential TA spectrum recorded immediately after photoexcitation of $[\text{Ru}(\text{bpy})_2(\text{pap})]^{2+}$ complex using nanosecond laser pulses; (c) TA spectrum of the anion radical of <i>pap</i> ligand using pulse radiolysis technique; (d) True TA spectrum of the $^3\text{MLCT}$ state of the $[\text{Ru}(\text{bpy})_2(\text{pap})]^{2+}$ complex. Insets: Temporal profiles recorded at 570 nm and 500 nm with the single exponential fit function (solid line) deconvoluted with the laser pulse width (6 ns).	
Figure 7.6	160
Transient absorption spectral evolution of $[\text{Ru}(\text{bpy})_2(\text{pap})]^{2+}$ in acetonitrile following 400 nm excitation.	
Figure 7.7	162
Temporal dynamics of $[\text{Ru}(\text{bpy})_2(\text{pap})]^{2+}$ in acetonitrile at different wavelengths along with triexponential fit function.	
Figure 7.8	164
Temporal dynamics of $[\text{Ru}(\text{bpy})_2(\text{pap})]^{2+}$ in methanol and water at few selective wavelengths.	
Figure 7.9	165
Simplified Schematic potential energy diagram showing excited state processes of $[\text{Ru}(\text{bpy})_2(\text{pap})]^{2+}$ in acetonitrile.	

Figure 8.1	173
Normalized absorption (black line) and luminescence (red line) spectra of uranyl nitrate in aqueous solution of 1N nitric acid (A) and methanol (B).	
Figure 8.2	177
Time-resolved absorption spectra of the transient species created following photoexcitation of uranyl nitrate in aqueous solution of 1 N nitric acid using 400 nm light.	
Figure 8.3	178
Temporal profiles recorded at a few selective wavelengths following photoexcitation of uranyl nitrate in 1 M nitric acid solution. The red line represents the best fit multiexponential function associated with the temporal profile. The lifetimes of the ultrafast components are given in inset.	
Figure 8.4	179
Schematic potential energy surface diagram depicting the excited state relaxation processes taking place following photoexcitation of the uranyl nitrate ion in aqueous solution using 400 nm light.	
Figure 8.5	181
Time-resolved absorption spectra of the transients created following photoexcitation of uranyl nitrate in methanol using 400 nm light.	
Figure 8.6	183
Temporal profiles recorded at a few selective wavelengths along with the best-fit functions, depicting the temporal evolution of the transient species created following photoexcitation of uranyl nitrate in methanol. The lifetimes of the ultrafast components associated with the best-fit functions are also given in the insets.	

LIST OF TABLES

Page No.

Table 3.1	55
Decay parameters obtained by fitting the fluorescence upconversion signals presented in Figure 3.2, with multiexponential function.	
Table 3.2	68
Lifetimes of the processes associated with the relaxation dynamics of the excited states of curcumin in different kinds of solvents, determined using the transient absorption spectroscopic technique.	
Table 4.1	89
Solvent dependence of the photophysical parameters of DMADK.	

Table 4.2	95
Time constants for the relaxation dynamics of DMADK measured in different solvents using transient absorption spectroscopic technique.	
Table 4.3	106
Energies of the two enol tautomers in the ground (S_0) state and the first singlet excited (S_1) state in the gas phase and in polar solvent, DMSO. DFT/TDDFT calculations were performed using B3LYP functional and 6-31G (d,p) basis set. Calculations in DMSO were performed using polarizable continuum model (PCM).	
Table 5.1	111
Photophysical parameters of DMAC-A and DMAC-B in different aprotic solvents.	
Table 5.2	114
Average time constants of the relaxation dynamics of DMAC-A in different solvents of varying polarities and viscosities.	
Table 5.3	117
Average time constants of the relaxation dynamics of DMAC-B in different solvents.	
Table 6.1	137
Wavelength dependence of the lifetimes of the three processes in DMSO.	
Table 6.2	138
Lifetimes of the processes associated with the relaxation dynamics of the excited states of p-NPP in different kinds of solvents, determined using the transient absorption spectroscopic technique.	
Table 7.1	157
TDDFT (B3LYP/6-31++G, ECP (Ru)) calculated electronic excitation energies of $[\text{Ru}(\text{bpy})_2(\text{pap})]^{2+}$ complex.	

List of abbreviations:

Abs.: Absorption

Fl.: Fluorescence

ICT: Intramolecular charge transfer

TICT: Twisted intramolecular charge transfer

D-A: Donor-Acceptor

ISC: Intersystem crossing

VC: vibrational cooling

VR: Vibrational relaxation

ESIPT: Excited state intramolecular proton transfer

ESIHT: Excited state intramolecular hydrogen transfer

ESA: Excited state absorption

SE: Stimulated emission

DMAC: 4-Dimethylaminochalcone

DMADK: 4-Dimethylamino-1, 3-diketone

p-NPP: 1-(*p*-nitrophenyl)-2-hydroxymethyl-pyrrolidine

bpy: 2, 2'-bipyridine

pap: 2-(phenylazo)-pyridine

MLCT: Metal to ligand charge transfer

Chapter 1

Introduction

Chemistry deals with the study of structure, property and chemical transformation of materials. The macroscopic properties of any given system are essentially governed by the geometric and electronic details at molecular level. Devising new experiment, careful observation and logical interpretation have led us to the atomic and molecular level picture of the macroscopic world. Detail understanding of the molecular structure and reaction pathways involved in natural processes guide us to rational design of artificial materials for mankind. Development of sophisticated spectroscopic techniques and accurate theoretical formulations has given us opportunity to unfold the fundamental details of matter. Among the various spectroscopic techniques developed to date, electronic spectroscopy is one area where electronically excited states created by UV-Vis light absorption are followed. Electronic spectroscopy holds special importance due to the relevance to photosynthesis, solar energy harvesting and many other photoinduced chemical and biological processes. Energy transfer, electron transfer and proton transfer are the basic events associated with natural photosynthesis.¹⁻⁴ Photoinduced charge separation and charge migration are also important in various artificial solar energy harvesting processes. Hence, fundamental understanding of these processes are crucial towards understanding the natural photosynthesis as well as development of artificial solar energy harvesting systems.⁵⁻⁷ Detail characterization of molecular excited state and complete understanding of the relaxation dynamics of the excited state of various model molecular systems is important to manipulate the excited state energies for any desired application.⁸⁻¹⁰

Following excitation and prior to deactivation to the ground state, the molecules in the excited state undergo various intermediate relaxation processes.¹¹⁻¹³ Quantitative measurements of fluorescence quantum yield and emission lifetime provide the rate of radiative and nonradiative relaxation. For detail understanding of the fast elementary processes, it is necessary to monitor the short lived species formed after the light absorption. The development of flash photolysis technique in 1949 by Norrish and Porter to study the lifetime of transient molecular species in millisecond (10^{-3}) time scale was the first breakthrough in this regard.¹⁴ This discovery opened up a new direction to monitor very short time reactions. During the last few decades, the advent and continued development of pulsed lasers make possible to investigate the dynamical processes of the excited states in real time.¹⁵ Development of pico and femtosecond time resolved spectroscopic techniques has not only helped us to understand the basic aspects of electronic excited state relaxation, but also opened up new dimensions to the understanding of ultrafast reactions.¹⁶ Pump-probe techniques with ultrashort laser pulses nowadays allow tracking the chemical reactions on the time scale of molecular motions. This concept has led to the birth of the research area called femtochemistry for which the 1999 Nobel Prize in chemistry was awarded to Ahmed H. Zewail.¹⁷

Because of its fundamental importance, photoinduced charge transfer dynamics in donor-acceptor substituted molecular systems has been intensely studied during the last decades. Intensive studies on charge transfer systems consisting of semiconductor and organic dye molecules were performed due to the relevance in solar cells and led to the fascinating evidences that intermolecular charge transfer can occur in femtosecond timescale.¹⁸ Studies on the photoinduced charge transfer dynamics in the photoexcited states provide information about the various factors controlling this process as well as development of new molecular systems with high charge transfer rates.¹⁹⁻²³ Present thesis deals with the electronic and structural relaxation of various charge transfer systems in the excited state using transient

absorption and fluorescence techniques with sub-picosecond time resolution. An overview of some of the photochemical and photophysical aspects in relation to general photochemistry in condensed phase is briefly presented in the following sections.

1.1 Characterization of the excited states of molecules

To understand the photophysical and photochemical properties of a molecule, it is necessary to characterize the steady state absorption and fluorescence behavior in different solvent environments. Effect of solvent polarity on absorption and fluorescence maxima provides qualitative information regarding the nature of the electronic excited states. Position of the maximum of the emission spectrum is always shifted to longer wavelengths as compared to absorption spectrum. This shift in peak wavelength between absorption and emission spectra is called as "*Stokes shift*". Solvent polarity dependent Stokes shift measurement provides quantitative measurement of excited state dipole moment using *Lippert-Mataga* formula.¹¹ A large increase in excited state dipole moment suggests strong intramolecular charge transfer (ICT) excited state responsible for emissive excited state. Thus, distinction between a low dipole locally excited (LE) state and high dipole charge transfer (CT) state is possible from steady state absorption and fluorescence measurements. Measurements of fluorescence quantum yields and fluorescence lifetimes provide the rate of radiative and nonradiative deactivation processes which are important to understand the electronic relaxation channels associated in the excited state.

1.2 Relaxation processes following photoexcitation in solutions

Here an overview is given about the general relaxation channels following photoexcitation of molecules in order to provide the necessary background for the discussion of the results presented in the subsequent chapters of the thesis. UV & VIS light absorption results in the excitation of the molecules to the higher energy electronic states, which occur in a time scale of $\sim 10^{-15}$ sec. Following photoexcitation, excited molecules in solution experience various

competitive relaxation processes, which can be classified in the following major categories: vibrational relaxation, internal conversion (IC), intersystem crossing (ISC), radiative and nonradiative decay.¹¹⁻¹³ The schematic representation of the basic photophysics following photoexcitation of the molecule can be outlined with the aid of a diagram, commonly known as the Jablonsky diagram and has been depicted in Figure 1.1.

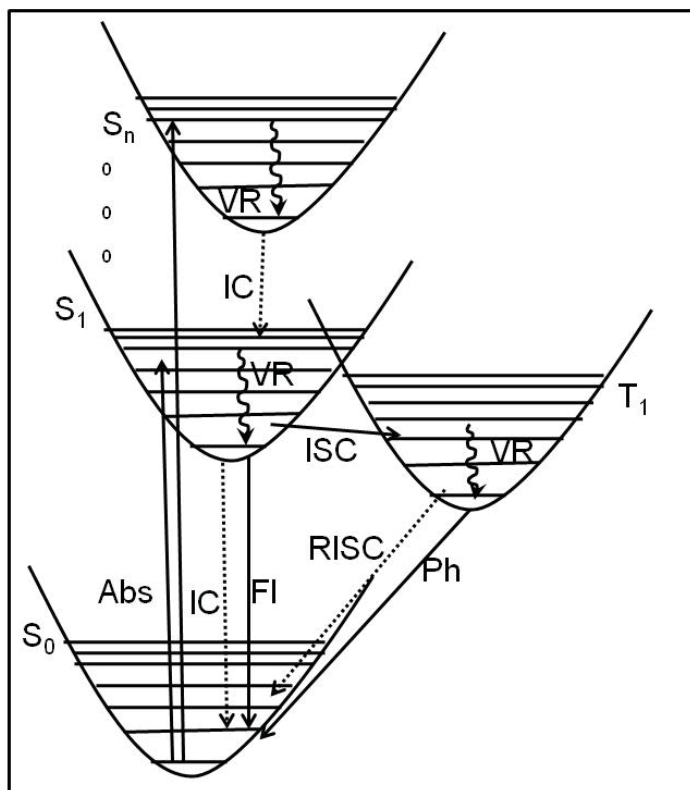


Figure1.1. The Jablonsky diagram, describing basic photophysical processes undergone by an excited state molecule. Straight and dotted downward arrows represent radiative and non-radiative relaxation processes respectively. Abbreviations: Abs-absorption, IC-internal conversion, ISC-intersystem crossing, RISC-reverse ISC, VR-vibrational relaxation, Fl-fluorescence, Ph-phosphorescence.

In addition to the general photophysical processes described in Jablonsky diagram, various important photoinduced chemical/physical processes occur namely, proton transfer, electron transfer, energy transfer, intramolecular structural relaxation, photoisomerization, etc (Figure 1.2).¹³ Occurrences of these processes depend on the chemical structure and functional group present in the molecular system. In solution phase, solvent reorganization plays an important role influencing the excited state relaxation. The above mentioned photophysical processes take place in a wide range of timescale, from a few femtoseconds to milliseconds.

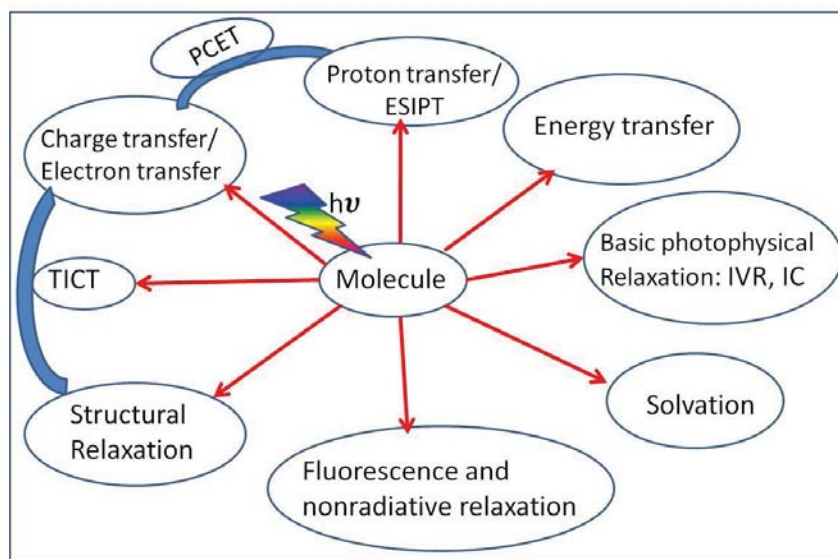


Figure 1.2. Different photoinduced excited state reactions and relaxation pathways.

1.3 Vibrational relaxation

Photoexcitation of any molecule to electronic excited states follows Franck-Condon principle.¹⁹ As a result, electronic excitation leads to excess vibrational energy localized in one or more Franck-Condon active vibrational modes which subsequently get redistributed and/or released to the entire molecule and the surrounding. In condensed phase, excess vibrational energy of a molecule is lost in two steps; (a) intramolecular vibrational redistribution (IVR), and (b) vibrational cooling (VC). Following photoexcitation, the FC localized energy is rapidly redistributed among the different vibrational modes of the molecule. This rapid redistribution is termed as ‘intramolecular vibrational redistribution’. During this process the total energy of the molecule does not change. This process can occur even in the isolated molecular system and does not need the surrounding solvent environment to be present. In medium to large organic molecules having large number of vibrational degrees of freedom, the timescale of IVR process is reported to be sub-100fs.²⁰ The second relaxation pathway is induced by interaction with the surrounding solvent molecules. In this process, the vibrationally hot molecules equilibrate thermally by vibrational energy transfer to the solvent and thus termed as vibrational cooling (VC). The timescale for this process is almost an order of magnitude slower

than IVR.²¹ The timescale of the vibrational cooling process is also dependent on the thermal conductivity of the surrounding solvent medium.^{22, 23} Because of the ultrafast nature of the vibration relaxation process, this may complicate the understanding of intramolecular structural relaxation dynamics which occur in similar time scale. Thus, the knowledge of the vibrational relaxation rate is important to distinguish from other ultrafast relaxation processes such as solvation and intramolecular structural relaxation.

1.4 Internal conversion (IC)

Internal conversion (IC) can be defined as the process through which electronic excitation energy is converted into vibrational excitation energy without changing the spin multiplicity of the electronic states. Usually IC is ultrafast from highly excited states to the lowest electronic excited state, i.e., S_n to S_1 . On the other hand, deactivation of the S_1 state tends to be dominated by fluorescence and intersystem crossing. This behavior has been observed to be almost general and known as Kasha's rule.²⁴ Rate of IC process from the S_1 state is generally smaller than radiative process and strongly depends on the energy gap between the S_1 and S_0 state. In case of rigid molecular systems, the decrease in IC efficiency with increasing energy gap between the S_0 and S_1 states can be correlated to an exponential drop of the Franck-Condon factor with increasing vibrational quantum number. This leads to a linear dependence of the logarithm of the internal conversion rate versus the (electronic excitation) energy gap which has been theoretically corroborated and is currently known as the well-established "energy gap law" for internal conversion.²⁵ In case of many structurally flexible molecular systems, rate of IC has been observed to be much faster than what is envisioned from the energy gap law. Low frequency vibrational modes of the flexible side groups is believed to promote the IC process and known as loose bolt and free rotor effect.²⁶ Recent experimental studies have revealed many examples with exceptionally ultrafast IC rate reaching down into the femtosecond time regime. The examples include DNA and RNA nucleobases, Green Fluorescent Protein (GFP)

chromophores outside the protein environments, etc.²⁷ Extremely rapid IC processes in these systems are explained by invoking the concept of conical intersections.²⁷

In solution, the solute-solvent interactions play an important role in governing the IC process. In case of charge transfer molecular systems, stabilization of highly polar excited state in polar solvent can significantly alter the energy gap between the S_1 and S_0 states leading to polarity dependence of the IC process. In addition, specific interaction between solute and solvent molecule, e.g., intermolecular hydrogen bonding plays an important role in promoting the IC process. It has indeed been a general observation that in protic solvents, the IC process is significantly faster as compared to that in aprotic solvent of similar polarities.²⁸ In case of many intramolecularly linked donor-acceptor (D-A; where D is electron donor group and A is electron acceptor group) molecules where the charge transfer excited state undergoes large amplitude structural relaxation, the energy gap between relaxed S_1 state and corresponding ground state becomes significantly small which results to exceedingly fast IC process. Solvent modulation of IC rate as compared to other relaxation channels can have strong implication on the excited state properties of charge transfer molecule in solution phase. In few of the molecular systems discussed in this thesis the solvent effects on IC process have been elaborated.

1.5 Intersystem Crossing (ISC)

Intersystem crossing is defined as the electronic relaxation between different spin multiplicity states.¹¹ In organic photophysics, the relaxation from the S_1 state to the closely lying triplet state is most commonly occurring ISC process. As the process is associated with the change in spin-multiplicity, which is a spin forbidden transition, significant spin-orbit coupling is necessary to promote the ISC process. Presence of heavy atom, thus, can induce excited state relaxation to the triplet state. Another important factor is the energetic closeness between two electronic states. In these situations, often a small coupling matrix element (i.e., without heavy

atom) suffices to induce an efficient transition between the states. Moreover, the ISC process may be facilitated if the symmetry of the participating electronic states is different. Aromatic carbonyl and nitro compounds with low energy triplet manifolds of $n\pi^*$ character imparts ultrafast intersystem crossing to the triplet state from the lowest energy singlet excited state. Indeed, the nitro aromatic compounds are known to undergo fastest intersystem crossing (<1 ps). The energy matching between the charge transfer S_1 state and $n\pi^*$ triplet state strongly depends on solvent polarity and thus can modulate the ISC rate. Knowledge of the ISC rate and the governing factors are important as ISC plays key role in photochemistry due to long lived triplet state formation which triggers many photochemical reactions.¹³

1.6 Excited state intramolecular proton transfer (ESIPT)

Due to fundamental importance in chemistry and biology, proton transfer reaction has been an important field of research for many decades.³⁰ A variety of molecular systems having five or six member intramolecular hydrogen bond undergo photoinduced intramolecular proton transfer reaction to produce tautomeric species in the excited state.

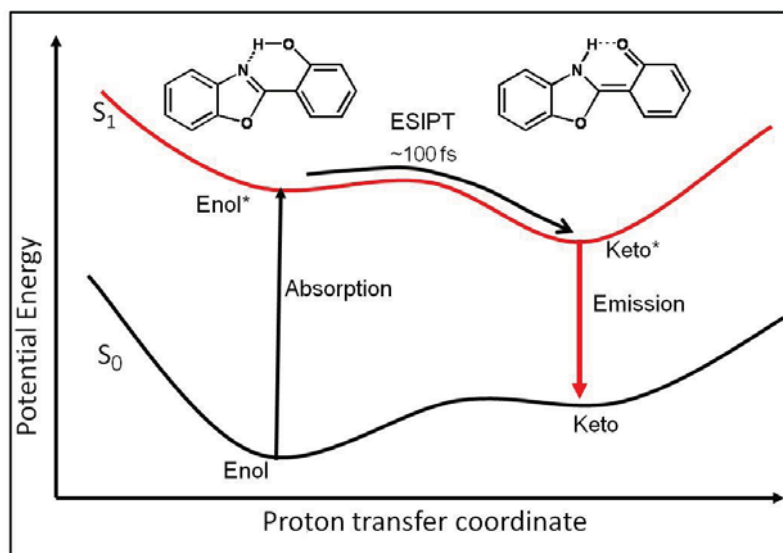


Figure 1.3. Schematic presentation of ESIPT reaction with an example of o-hydroxy benzoxazole.

In 1955, Weller reported the first example of ESIPT reaction from the unusually large Stokes shifted ($\sim 1 \times 10^4$ cm^{-1}) fluorescence of methyl salicylate molecule.³¹ Following this discovery,

studies on intramolecular proton transfer reactions gained extensive attention by many researchers and a large class of ESIPT molecules have been discovered. Schematic of keto-enol tautomerization via ESIPT reaction upon photoexcitation is shown in Figure 1.3. Large Stokes shifted ESIPT fluorescence leads to many interesting applications such as proton transfer laser, chemosensor, organo-luminescent laser diode, DNA complexing agent etc.^{32, 33} Recent development of ultrafast laser spectroscopic techniques has allowed the detail mechanistic understanding of the ESIPT reaction. Femtosecond transient absorption and fluorescence upconversion technique revealed that most of the ESIPT reactions occur in the timescale of 100-200 fs indicating barrierless motion along the proton transfer coordinate.^{34, 35} The main contribution to the proton transfer coordinates comes from the low frequency skeletal vibrational motion.^{36, 37} Large amplitude twisting motion has also been observed to be coupled to the proton transfer process in many ESIPT systems.³⁸ In case of highly charge transfer ESIPT system, proton transfer reaction is largely controlled by charge transfer as well as solvation dynamics. Proton coupled intramolecular charge transfer dynamics has extensively been explored in recent years.³⁹ Keto-enol tautomers of 1, 3 diketones also undergo ESIPT reactions.

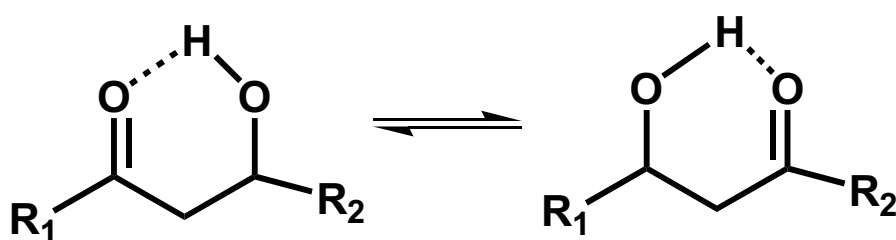


Figure 1.4. ESIPT reaction in keto-enol tautomers of 1, 3 diketones.

Unlike well explored ESIPT molecules, where a unidirectional proton transfer reaction occurs from enol to keto structure, photoinduced ESIPT in 1, 3-diketones may occur in either direction depending on the stability of two keto-enol tautomers in the ground and the excited electronic states (Figure 1.4). In the present thesis, ESIPT reactions and consequence to the excited state properties of symmetrical and unsymmetrical diketones have been discussed.

1.7 Solute- Solvent interaction and Solvation

Solvent plays subtle role in all condensed phase chemical reaction by changing the energetic of reactants, transition state and products via intermolecular solute solvent interaction.⁴⁰ Detailed understanding of the solute-solvent interactions is crucial in explaining the dynamics of chemical reactions. The motions of surrounding solvent molecules, which are coupled to the reaction coordinate, significantly affect these processes. All chemical reactions involve electronic and structural rearrangements during the course of the reaction and thus dynamic solvent interaction strongly influence the rate of a chemical reaction.⁴¹⁻⁴³ Response of solvent molecules to influence the energetic of reactants and intermediates is very rapid. The development of ultrashort laser pulses enabled time resolved fluorescence and absorption measurements that directly probe solvent polarization dynamics over molecular length scales. This research area, known as ‘*solvation dynamics*’, holds an important position in the ultrafast spectroscopy.⁴²⁻⁵³ Briefly, a chromophore whose permanent dipole moment undergoes a significant change upon instantaneous optical excitation, the solvent molecules surrounding the solute will no longer be in an equilibrium situation in the excited state. After the pulsed excitation, the solvent molecules will reorient in order to stabilize the newly created dipole and to reach the new equilibrium situation, as shown in Figure 1.5. As the solvent molecules reorganize to establish the equilibrium with the new charge distribution, the fluorescence spectrum shifts to lower energy as a function of time. This dynamic stokes shift, which shows the progress of the solvation energy relaxation can be used to quantify the solvent response by monitoring the solvation correlation function, $C(t)$, which is defined by

$$C(t) = \frac{\nu(t) - \nu(\infty)}{\nu(0) - \nu(\infty)}$$

Where, $\nu(0)$, $\nu(t)$ and $\nu(\infty)$ represent the frequency of the intensity maximum of the emission band immediately after photon excitation, at some time t after excitation and at a time sufficiently long to ensure the excited state solvent configuration is at equilibrium. The

experimental studies with sufficiently high time resolution have revealed biphasic nature for the solvent response which occurs in a few femtoseconds to several picoseconds time scale. The initial fast part of the solvent response, occurs in femtosecond timescale is assigned to small amplitude inertial rotational motions of solvent molecules in the first solvation shell.

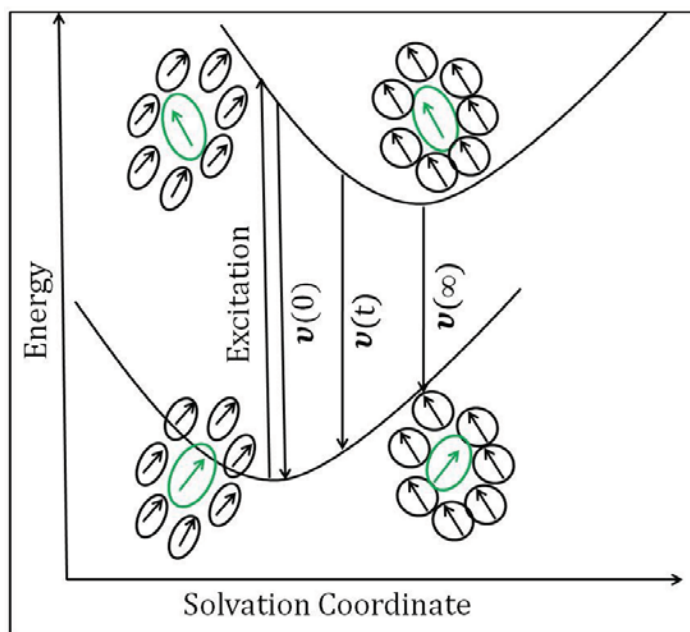


Figure 1.5. Schematic diagram of solvent relaxation in photoexcited state.

The slower component arises from diffusive restructuring of the solvent shell. Recent experimental results employed multi-exponential models to fit experimental data for various solvents.⁵³ Though ultrafast fluorescence experiments are generally used for solvation study, the same can be monitored by following the time evolution of stimulated emission or excited state absorption in transient absorption spectroscopy, subjected to the condition that the spectra are not complicated by the strong overlap with each other. The time scale of solvation and other intramolecular relaxation are often very close and disentangling the different relaxation processes indeed become a formidable task. Careful analysis of transient absorption spectral evolution in various solvents and aid of complementary fluorescence upconversion experiments is very useful to resolve intramolecular relaxation and solvation dynamics. Extensive research in past two decades deciphered the characteristic time constants of the

multimodal solvation process in varieties of solvents and solvent mixtures. As solvation is always associated with charge transfer dynamics, knowledge of solvent relaxation time helps to distinguish intramolecular dynamics from the solvent relaxation processes.

1.8 Excited state structural relaxation: Twisted intramolecular charge transfer

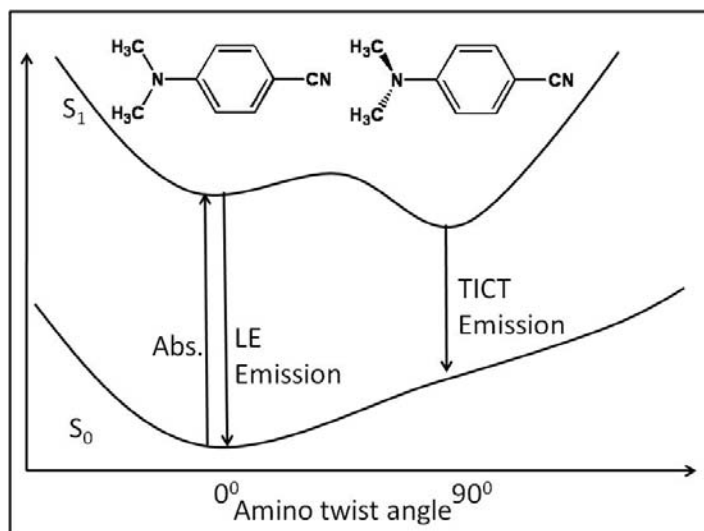


Figure 1.6. TICT model for dual emission of DMABN molecule.

Intramolecular donor-acceptor molecules or complexes undergo significant transfer of electronic charge from the donor group to the acceptor group in electronic excited state. Structural relaxation in the excited state can further facilitate the charge redistribution leading to complete separation of charge. Twisting of donor and acceptor groups to perpendicular orientation often leads to decoupling of donor and acceptor orbitals and a near quantitative charge separation may results. Large amplitude structural relaxation upon photoexcitation of charge transfer molecules has attracted great deal of attention for last few decades and a myriad of molecular systems have been studied to elucidate mechanistic insight of TICT relaxation.⁵⁴⁻⁶⁴ The concept of TICT relaxation via large amplitude structural change in the excited state of intramolecular charge transfer molecule was originated from the observation of dual fluorescence of 4-dimethylamino benzonitrile (DMABN). In 1973, Grabowski et. al. proposed twisted dimethylamino structure of DMABN in the excited state to account long wavelength ICT emission which is characterized by large dipole moment.⁵⁴ It was realized that

efficient charge separation is attained in the twisted configuration due to orbital decoupling between the donor and acceptor moieties.^{55, 56} Dual emission of DMABN was modeled by considering twisted structure of dimethylamino group relative to benzene ring which is responsible for low energy fluorescence band. Figure 1.6 pictorially represents the TICT concept proposed by Grabowski and coworkers. Studies on structurally constrained analogue of DMABN molecule apparently supported the twisting mechanism, which has been popular as *twisted intramolecular charge transfer* (TICT) mechanism. Rettig and coworkers generalized the TICT hypothesis by studying numerous donor acceptor molecular systems.^{57, 58} In many cases TICT states have been established to be nonfluorescent due to the diminished oscillator strength of the twisted conformer. In recent years, ultrafast time resolved experiments employing visible, infrared and Raman techniques have elucidated the timescale and mechanistic aspects of TICT reaction of DMABN and structurally related molecules.

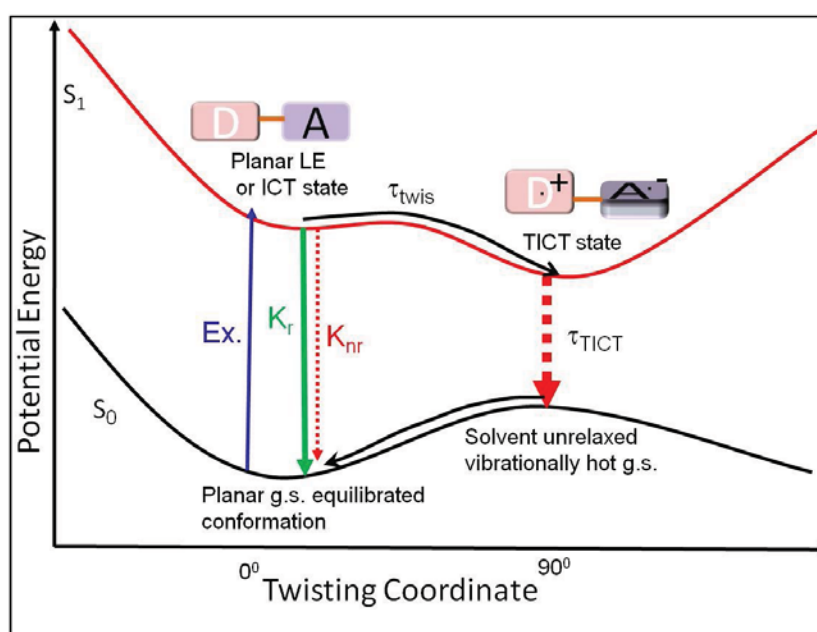


Figure 1.7. Schematic excited state potential energy surface of TICT relaxation.

Measurements on structurally constrained molecular systems have helped to identify the reaction coordinates and shape of the excited state potential energy surfaces along the twisting coordinate. A general scheme of excited state relaxation dynamics of the TICT molecules is

shown in Figure 1.7. The barrier along the twisting coordinate depends on the structure of the molecule and nature of donor acceptor group.

1.9 Barrierless ultrafast structural dynamics

The traditional picture of a chemical reaction is the passage of the reactant state over a high activation barrier to form the product. This picture of an elementary chemical reaction has played a key role in our understanding of many physical, chemical, and biological processes. However, a large number of important chemical and biological reactions in solution occur without the intervention of any potential barrier and the dynamics of a barrierless chemical reaction differs considerably from those having an activation barrier.⁶¹⁻⁷⁵ In the absence of a barrier between the reactants and the products, there is no separation of timescales between the motion in the reactive region and in the rest of the potential energy surface (PES). Therefore, these reactions are generally characterized by high reaction rates and often strongly coupled to solvent friction. Since barrierless chemical reactions are usually very fast (with time constants often in the picosecond range), detailed study of these processes required the development of ultrafast laser spectroscopy. Over the last few decades it has become clear that there exist a rather large number of organic dye molecules whose photophysics in solution follow barrierless dynamics. It was noticed that some diphenyl and triphenylmethane dyes (for example, auramine, crystal violet, malachite green, ethyl violet etc.) do not fluoresce in low viscosity solvents, but are strongly fluorescent in highly viscous solvents. Strong viscosity dependence of fluorescence yield in this class of molecules were explained by the occurrence of large amplitude structural motion in the excited state. Oster and Nishijima proposed a theoretical model for the barrierless reactions for the first time based on the viscosity dependence of fluorescence yield of Auramine in glycerol at various temperatures.⁶¹ They found that the reciprocal of the fluorescence intensity was proportional to T/η (where η is the macroscopic viscosity of the solvent). They assumed a flat excited state potential energy surface along the torsional

coordinate with two local sink functions, through which the population leaks away with the diffusion controlled rate. On the other hand, Förster and Hoffman reported a $\eta^{2/3}$ dependence of the fluorescence yield and proposed another theoretical model considering parabolically shaped potential energy surface with a sink at the minima, which was responsible for the torsional coordinate dependent radiationless decay to the ground state.⁶² This model could explain the dynamic Stokes shift of the emission band but failed to account broadening of the emission spectra. Moreover, the $\eta^{2/3}$ dependence of the fluorescence yield on the viscosity was not supported in many subsequent studies. Later, Bagchi, Fleming and Oxtoby (BFO) proposed a generalized model to describe the twisting motion of the phenyl groups in TPM dyes on the parabolically shaped excited state potential energy surface with a nonlocal sink function.^{63,64} BFO theory successfully explains both the dynamic Stokes shift and the emission band broadening observed during the excited state relaxation process. Time resolved transient absorption studies by Harris and coworkers with picosecond time resolution revealed detailed dynamics of TPM dyes and the effect of viscosity, pressure and temperature.^{65,66} Many of these observations could be well explained by the BFO model. In 1990, M.M Martin and his coworkers revealed the signature of structurally relaxed conformation in the excited states by employing TA spectroscopy with improved time resolution (~500 fs). Observation of conformationally relaxed dark excited state structure indicated that weak fluorescence, ultrafast fluorescence decay and their viscosity dependence are actually related to the dynamics within the excited state.⁶⁷⁻⁷¹ In 2000, Glasbeek and coworkers introduced the coordinate dependent radiative rate in theoretical model and explained their experimental observations on reaction dynamics of auramine and many other molecular systems.⁷² Barrierless reactions are not limited only to twisting in the electronic excited state of dye molecules. Many activationless processes are found in the photoinduced isomerization reaction such as isomerizations of stilbene or diphenylbutadiene is known to follow barrierless reaction pathways.⁶⁴ Barrierless

reactions are generally characterized by high reaction rates, exhibit a temperature dependence distinctly different from that of high barrier reactions, and are often strongly coupled to solvent viscosity. Indeed, viscosity dependence has been often used to characterize the reaction mechanism of these reactions because in the absence of a barrier, solvent friction is the only impediment to the reaction.⁶⁶ Another important feature is that these reactions may depend on the initial conditions so that the wavelength of the excitation light may also play an important role in controlling the relaxation dynamics.

In the last two decades, barrierless twisting relaxation dynamics of several charge transfer molecules such as 4-dimethylaminobenzophenone, Michler's ketone, push-pull stilbenes etc, have been extensively studied using femtosecond transient absorption spectroscopy.⁷³⁻⁷⁵ Because of large charge transfer character of the S_1 state, solvent polarity plays an important role to define the shape of the reactive PES and thus influence the rate of relaxation. The shape of the excited state potential energy surface along the reactive coordinates also depends on the strength of the donor and the acceptor groups. In presence of strong accepting groups, the relaxation dynamics of D-A charge transfer molecules can significantly vary due to modification of the shape of reactive PES. The capacity to accommodate high charge density at the acceptor unit can allow twisting of acceptor unit. Amino substituted nitro aromatic compounds are such kind of examples where twisting of nitro group has been proposed.^{76,77} Detailed studies of this kind of molecular system is necessary to attain a general description of relaxation behavior, their time scale and distinction of other competitive relaxation processes. In the present thesis we have emphasized to understand the effect of donor acceptor conjugation, strength of acceptor group and coupling of proton transfer on the TICT relaxation dynamics. Consequence of TICT relaxation to other deactivation channels such as internal conversion and intersystem crossing has also been revealed from systematic solvent dependent studies.

1.10 Photophysics and excited state dynamics of inorganic complexes

Photophysical studies of inorganic complexes gained a lot of attention due to importance in solar energy harvesting, and artificial photosynthesis.^{78, 79} Excited state properties of inorganic complexes mainly differ from organic molecules in two aspects. Firstly, effective charge transfer between metal and ligand orbitals generates low energy metal to ligand and/or ligand to metal charge transfer states (MLCT /LMCT), in addition to metal and ligand centered electronic states. Secondly, due to strong spin orbit coupling imparted by heavy central metal atom, intersystem crossing is extremely fast. Thus the excited state properties of metal complexes are generally characterized by long lived triplet MLCT state.⁸⁰ Ultrafast time resolved experiments have recently been extensively employed to understand the initial evolution of the excited electronic state, following optical excitation to the singlet MLCT excited states.⁸¹ Ultrafast spectroscopic investigations have disclosed that most inorganic complexes undergo intersystem crossing within 100 fs timescale and molecules reach triplet excited manifold (³MLCT) prior to even any vibrational relaxation or internal conversion. Consequently, the photophysical and photochemical properties of inorganic complexes is mainly characterized by the triplet excited state. Presence of the strong spin orbit coupling and high density of states facilitate ultrafast intersystem crossing leading to the formation of long-lived triplet states. The classic rules developed through the study of organic photophysics state that vibrational relaxation is the fastest relaxation process, followed by internal conversion, and intersystem crossing is the slowest relaxation process ($k_{VR} > k_{IC} > k_{ISC}$). The ultrafast spectroscopic investigation for transition metal systems show that the classic rules do not necessarily apply to inorganic systems and photodynamics of inorganic complexes are fundamentally different from organic photophysics.⁸⁰ Thus knowledge of ultrafast events in various inorganic molecular systems can provide a generalized description of excited state photodynamics. In the present thesis two inorganic systems have been probed by ultrafast transient spectroscopy.

1.11 Scope of the present thesis

Above discussion suggests that studies of the excited state properties of molecular systems in real time have immense importance for understanding the fundamentals of reaction dynamics. Photo initiated chemical reaction such as electron transfer, proton transfer and structural motion are relevant to solar energy conversion and photonic application. Time resolved measurements provide information about the factors which govern the excited state photo processes. Present thesis explored real time dynamics of different model molecular systems to understand the intricate relaxation processes in the excited state. Steady state absorption and fluorescence measurements have been used to obtain qualitative information on the relative radiative and nonradiative relaxation rates which helps to explain the ultrafast spectroscopic results. Ultrafast time resolved fluorescence and absorption techniques with subpicosecond time resolution have been extensively employed for the studies presented in the thesis. Quantum chemical calculations were used to obtain the structure of the molecule in electronic excited state. The remainder of the thesis is organized as follows. Chapter 2 describes the methodology and instrumental techniques employed in the present thesis work. Detail description of femtosecond amplified laser system and transient absorption spectroscopic technique has been provided. Chapter 3 to chapter 8 deal with the experimental results and discussion of excited state relaxation dynamics of different molecular systems. Solvent dependent intramolecular charge transfer excited state relaxation behavior such as solvation, charge transfer and proton transfer dynamics have been elaborately discussed. Effect of solvent polarity, viscosity and intermolecular hydrogen bonding has been systematically explored, which revealed how solute solvent interaction, specific hydrogen bonding and viscous hindrance from surrounding solvent molecules influence the excited state deactivation rates. At the end, summary of the results presented in the thesis are given followed by an outlook on

ultrafast structural dynamics which can be probed using advance spectroscopic techniques for better understanding of excited state reactions.

Chapter 2

Experimental Techniques and Instrumentation

Exploration of photophysical properties and excited state dynamics in model organic and inorganic molecules is the subject matter of the thesis. Various steady state and time resolved optical instruments have been employed as the experimental tool for the study of different chemical systems in solution phase. Steady state absorption and fluorescence spectroscopy were used to characterize the solvent dependence of spectral properties. Time correlated single photon counting (TCSPC) and fluorescence upconversion techniques were used to measure the excited state lifetimes of the emissive excited states. Femtosecond time resolved transient absorption spectroscopy was extensively employed as the main tool to monitor the excited state relaxation processes occurring in femtosecond and picosecond timescale. In addition, nanosecond laser flash photolysis was used to characterize the long lived excited state species. Principle of the detection techniques and the basic instrumental layouts are briefly described in this chapter.

2.1 Steady state absorption and fluorescence measurement

Optical absorption (ultraviolet-visible; UV-vis) spectroscopy provides information about the transition energies and transition probabilities to the different electronic excited states from the ground state.^{11, 12} UV-vis absorption is dependent on the electronic structure and the surrounding environment of the absorbing chromophore which allows the characterization of various chromophoric systems. Changes in the solvent polarity, polarizability and hydrogen bonding ability often induce significant change in the absorption spectral shape and position providing useful information regarding the nature of interactions between the ground-state of a

chromophoric molecule and its surrounding environment.^{12, 82} Measurements of the optical absorption spectra are always essential to adjust the concentration of the absorbing species in the solution for the purpose of their investigations using different other photochemical techniques.

Absorption of a sample is quantitatively measured as absorbance (A) defined by $\log(\frac{I_0}{I})$. The absorbance of a sample is given by Lambert-Beers law:

$$A = \log\left(\frac{I_0}{I}\right) = \epsilon_{\lambda} Cl$$

where I_0 and I are the intensities of the incident and transmitted light, respectively, and l is the path length in centimeter for the light beam passing through the sample, C is the molar concentration of the solute and ϵ is molar extinction coefficient expressed in $\text{lit.mol}^{-1}.\text{s}^{-1}$. For absorbance measurements, the sample is usually kept in a quartz cuvette of 1 cm path length. For very concentrated solutions, as used in femtosecond transient absorption studies, thinner quartz cells were used with typical path length of either 0.1 or 0.2 cm. Ground-state optical absorption spectra (in the 200-1100 nm range) of the chemical systems presented in this thesis were measured using 'Biomate' make absorption spectrometer available in our laboratory.

Photoexcited molecules eventually come back to the ground state by emitting a photon or nonradiative relaxation. Fluorescence spectroscopy directly measures the emission intensity distribution as a function of emission energies of photoexcited molecules. The fluorescence peak position (emission maximum), shape of the fluorescence spectrum and intensity of the fluorescence emission are in general very sensitive to the structure of the molecule as well as solvent properties. This provides the information regarding the characteristics of the emissive excited state.^{11,12,82} In the present study, steady-state fluorescence measurements were carried out using a Hitachi model F-4500 fluorescence spectrometer. The instrument uses a 150 watt continuous powered high pressure xenon lamp as the excitation source and the desired

excitation wavelength was selected using an excitation monochromator. Sample is excited in a 1 cm x 1 cm quartz cuvette and the fluorescence is collected and measured in a direction perpendicular to that of the excitation beam. The emission wavelength is selected using an emission monochromator and detected using R-928F (Hamamatsu) photomultiplier tube (PMT). The interference from the excitation and scattered radiation was eliminated using appropriate filters before the emission monochromator. The wavelength range covered by the instrument was 220 to 800 nm. Emission spectra were corrected for the detector and monochromator sensitivity by comparison with standard spectrum of quinine sulfate.

Quantitative evaluation of the emission probability relative to the total excited state deactivation is measured by fluorescence quantum yield (Φ_f). The emission quantum yield of a sample is measured relative to that of a standard sample having known quantum yield.⁸²

$$\phi_{sample} = \frac{A_{reference}}{F_{reference}} \times \frac{F_{sample}}{A_{sample}} \times \frac{\eta_{sample}^2}{\eta_{reference}^2} \times \phi_{reference}$$

where $A_{reference}$ and A_{sample} are the absorbances at the excitation wavelength, $F_{reference}$ and F_{sample} are the integrated fluorescence intensities and $\eta_{reference}$ and η_{sample} are the refractive indices for the reference and the sample solutions, respectively. The measurement of quantum yield in different solvents or a series of related molecular system provides important information regarding the excited state deactivation mechanism. Low quantum yield value reflects enhanced probability of nonradiative relaxation as compared to that of radiative relaxation.

2.2 Fluorescence lifetime measurement

Fluorescence lifetime measurement is essential to obtain the rate of the radiative and nonradiative process occurring from the excited singlet states. In general, time correlated single photon counting (TCSPC) technique is most widely used to determine the excited state lifetimes longer than 100 ps to ns.⁸³⁻⁸⁵ The shorter lived emissive excited states (lifetime less

than 100 ps to sub-ps) can be monitored using state of the art fluorescence upconversion technique which works on pump-probe configuration. It is a time gated emission detection technique and the experimental time resolution is limited only by the temporal width of the excitation pulse. Mode locked Ti-Sapphire laser systems provide ultrashort pulses of < 100 fs time duration. In the present thesis, TCSPC technique has been used to measure fluorescence lifetime of the emissive transients longer than 100 ps. Following is the brief overview of the TCSPC technique and instrumental set up:

2.2.1 Basic principle of TCSPC technique

The principle of TCSPC measurement relies on the fact that the time-dependent probability distribution of the single photon emission from an excited molecule following its excitation is equivalent to the time-dependent changes in the fluorescence intensity of the sample following its δ -pulse excitation.⁸³⁻⁸⁵ The schematic diagram of a typical TCSPC set up is shown in Figure 2.1. As shown in Figure 2.1, an excitation pulse (optical pulse) from a pulsed lamp or a laser is split into two parts. One part is used to excite the sample and the other part of the light pulse is directed to a start PMT. The start PMT generates an electrical signal called START signal, which after passing through a Constant Fraction Discriminator (CFD), fed to the START input of the Time to Amplitude Converter (TAC) unit to initiate its charging operation. On receiving the start signal, the TAC continues to undergo charging linearly with time. The part of the optical pulse, which excites the sample, effectively gives rise to the emission photon. This photon is then detected by the stop PMT (at the right angle to the direction of excitation) to generate electrical STOP pulses for each of the individual photons received. The STOP pulses thus generated in the stop PMT are also passed through a CFD and a variable delay line to the STOP input of the same TAC unit. On receiving the first STOP pulse, the TAC unit stops its charging operation and subsequently generates an electrical output pulse (TAC-output), having amplitude proportional to the time difference (Δt) between the START and the STOP pulses

reaching the TAC unit. The TAC output pulse is then fed to the input of a Multichannel Analyzer (MCA) through an Analog-to-Digital Converter (ADC). The ADC generates a numerical value proportional to the height of the TAC output pulse and thus selects the corresponding memory address (channel) in the MCA, where a single count is added up.

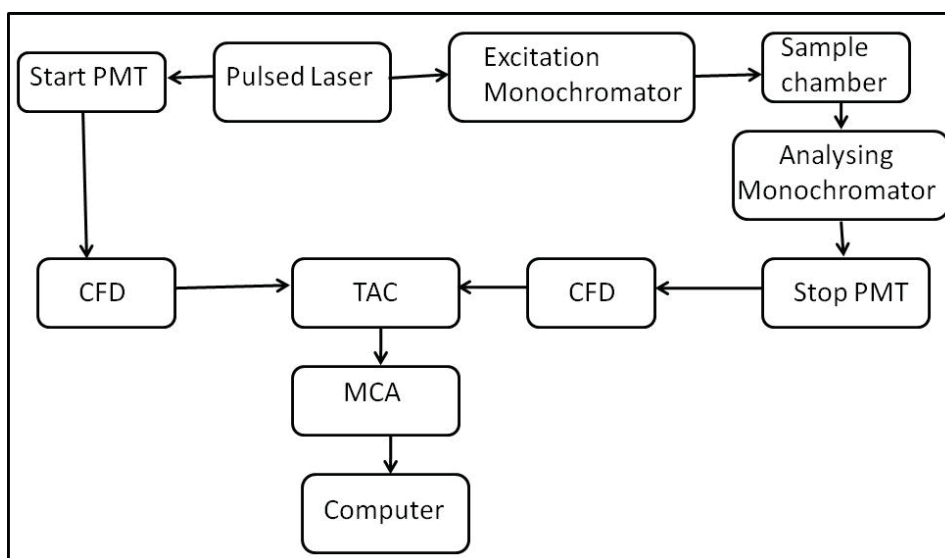


Figure 2.1. Schematic diagram of a Time Correlated Single Photon Counting Spectrometer.

The above cycle (from the triggering of the pulsed excitation light source to the data storage in the MCA) is repeated for a large number of times and thus a histogram of counts is collected in the MCA channels. The distribution of the counts against the channel number in the MCA then represents the fluorescence decay curve of the sample, provided the collection rate of the emission photons by the stop PMT is kept very low, only about 2% or less, compared to the repetition rate of the excitation pulses. This experimental condition effectively ensures that following an excitation pulse, in no circumstances more than one emission photon can be detected by the stop PMT. Thus, in the TCSPC measurement, for about 98% cases of the excitation pulses, though the sample is excited, there is effectively no emission photon that is directed to the stop PMT. Only about 2% cases of the sample excitations by the pulsed light source there is an effective emission of photon that is directed to the stop PMT and detected by the TCSPC setup. Such a low count rate is essential to maintain the time-dependent probability

distribution of the photon emission from a single excited molecule following its excitation process. From the measured fluorescence decay curves, the fluorescence lifetimes of the samples are estimated following a suitable analysis procedure and introducing a proper time calibration for the MCA channels.⁸⁶ In practice, experimentally measured fluorescence decay $F(t)$ is deconvoluted with the instrument response function $R(t)$ to extract the actual fluorescence decay $I(t)$. The least-squares method is used to extract the single or multiexponential decay parameters. The best fit is judged by the reduced χ^2 value, which should be close to 1 and a random distribution of weighted residuals.⁸⁷

The TCSPC instrument used in the present study was from Horiba Jobin Yvon IBH, UK, Model DataStation Hub. A 406 nm laser diode with vertical polarization of excitation pulse (~250 ps) was used as the excitation source. The repetition rate of the excitation pulses was kept at 1MHz. Emission was collected at magic angle (54.7°) polarization with respect to the excitation beam. Temporal resolution of the instrument was measured to be ~300 ps. The measured data were fitted with exponential decay function to extract the fluorescence lifetime of the sample.

2.2.2. Basic principle of fluorescence up-conversion

The basic principle of achieving ultra-short time resolution in the time-resolved fluorescence measurement is use of ultrashort light pulse to create the emissive excited state and monitoring of the fluorescence transient by time gating using the non linear frequency mixing technique (Figure 2.2). The emission light (frequency ω_f) collected from the sample following its excitation with an ultra-short laser pulse and a suitably delayed intense laser pulse, known as the gate pulse (frequency ω_g), are focused into a thin nonlinear crystal whose optic axis is oriented at an appropriate angle with respect to the ω_g and ω_f light beams. The sum-frequency photons (frequency $\omega_s = \omega_g + \omega_f$) are generated only during that time for which the ultra-short gate pulse is present at the crystal along with the comparatively long lived fluorescence light.

Thus, frequency mixing occurs only for a thin temporal slice of the fluorescence decay and accordingly acts as a light gate, providing time-resolution quite comparable to the width of the gate pulses used.⁸⁸⁻⁹²

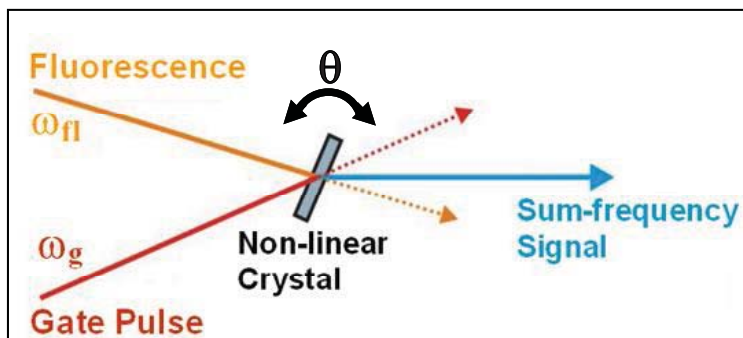


Figure 2.2. Schematic representation of sum frequency generation principle in a non-linear crystal which is the basis of fluorescence up-conversion.

One important criteria to be fulfilled is the “*phase matching condition*” among the interacting lights in the nonlinear crystal which is achieved by optical axis of the non-linear crystal is rotated with respect to the polarization direction and the direction of propagation of the gate and the fluorescence light pulses until the intensity of the sum-frequency light becomes the maximum for a selected ω_f value (i.e. the monitoring emission wavelength). The selection of ω_f or the monitoring emission wavelength is easily achieved by setting the wavelength of the monochromator in front of the photodetector corresponding to the sum-frequency light (ω_s) of the selected fluorescence light (ω_f) and the fixed gate pulse (ω_g). For a selected emission wavelength, optical axis of the non-linear crystal is tuned to maximize the intensity of sum-frequency light. Following this method, one can easily carry out the time-resolved fluorescence up-conversion measurements for a wide range of wavelengths covering the whole fluorescence spectrum of the sample. β -barium borate (BBO) is known to be the most useful nonlinear crystal in the fluorescence up-conversion measurements, because it has a high transmittance over a wide spectral range (covering most of the UV-visible spectral region) and a reasonably high non-linear efficiency for the sum-frequency generation process.⁸⁸⁻⁹²

2.2.3. Brief description of the fluorescence up-conversion setup

The block diagram of the femtosecond fluorescence up-conversion instrument (FOG, CDP, Russia) used for the measurements is shown in Figure 2.3. In this instrument a mode-locked Ti:sapphire oscillator (Tsunami, Spectra Physics) was used as the source of femtosecond laser pulses. The laser system provides 800 nm light having ~50 fs pulse duration which operates with a repetition rate of 82 MHz. The output laser beam from the Ti:Sapphire oscillator is passed through a second harmonic generator unit (a suitable BBO crystal with proper tuning of optical axis for phase matching) to generate 400 nm light. The 400 nm second harmonic light thus produced is separated from the residual fundamental light of the Ti:Sapphire laser by using a dichroic mirror and is used for the excitation of the samples of our interest. The residual fundamental light is used as the gate pulse for the fluorescence up conversion.

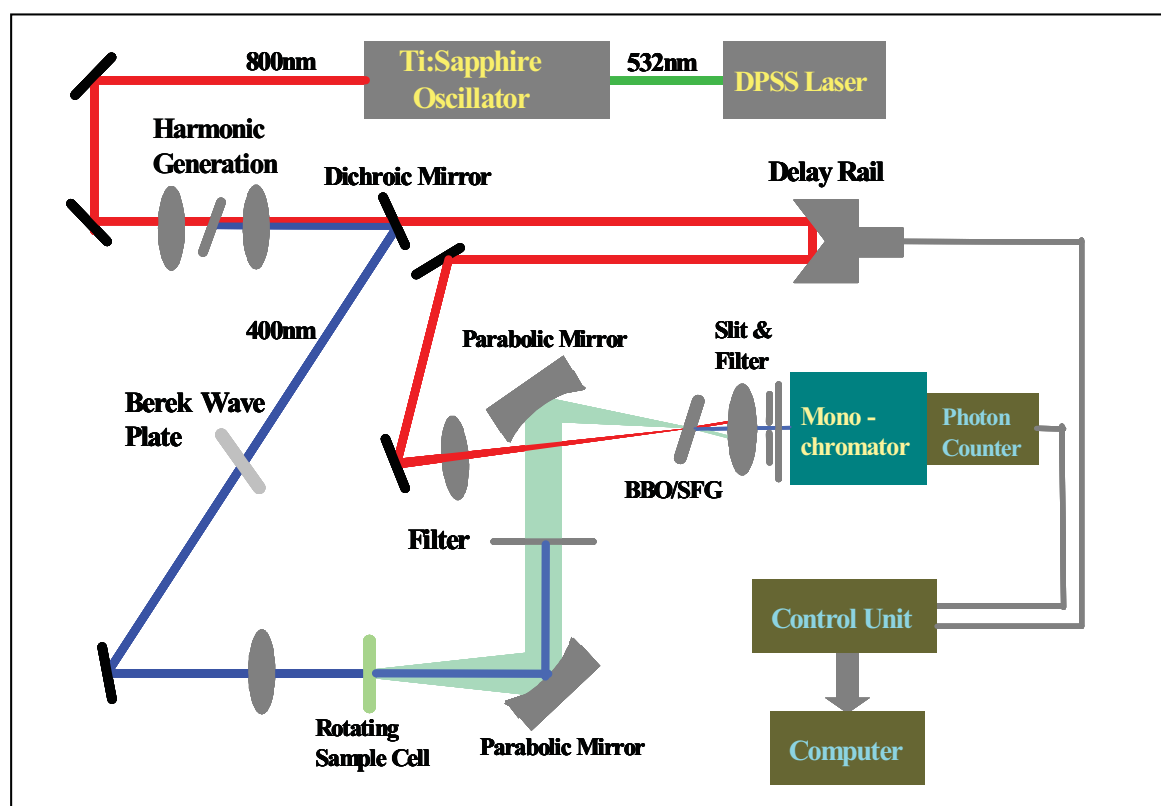


Figure 2.3. Schematic diagram of the femtosecond fluorescence up-conversion instrument.

In the actual experimental arrangement, the sample solution is kept in a rotating quartz cell of 1 mm thickness. The sample cell is rotated continuously during the measurement to prevent localized heating and photo-degradation of the sample. A cut-off filter is used immediately after the sample cell to prevent the residual 400 nm excitation light and/or Raman light to reach the detection system. The transient fluorescence emitted from the sample is then focused onto an up-conversion crystal (0.5 mm thick BBO crystal), using two elliptical mirrors. The residual fundamental beam used as the gate pulse is first directed to an Optical delay line and subsequently focused onto the up-conversion crystal. A translational stage, driven by a stepper motor with a step size of 0.1 μm , is used to change the delay of the gate pulse. Each step of the translational stage changes the optical path length of the gate pulse by 0.2 μm , thus delaying the pulse by 0.66 femtosecond per step. The gate pulse is focused onto the up-conversion crystal using a lens to mix with the fluorescence signal and thus to generate the sum-frequency or the up-converted signal. The upconverted light is focused onto a slit of a double monochromator after passing through a UV band pass filter (UG 11) that eliminates the gate and the unused fluorescence light but transmits the up-converted light. This up-converted light is finally detected by using a photomultiplier tube connected to a photon counting system (CDP Inc. Russia). A variable wave plate (Berek Compensator) in the path of the excitation beam is used to control the polarization direction of the excitation pulses relative to the horizontally polarized gate pulses. Fluorescence up-conversion measurements were carried out under magic angle condition to avoid the rotational depolarization effect of the probe molecules on the observed fluorescence decays. The fluorescence decay profiles measured for the samples at a given wavelength in the up-conversion method is a convolution of the sample response with that of the instrument response function (IRF). To extract the actual fluorescence decay parameters of the sample, the measured fluorescence decay is to be de-convoluted with respect to the instrument response function of the setup. The measurement of the IRF of the

up-conversion setup can be easily obtained by mixing the residual excitation light that passes through the sample with the gate pulse in the up-conversion crystal and measuring the concerned sum-frequency light, which is commonly referred as the cross-correlation light, by using the time-gated photon counter. The changes in the cross-correlation light intensity with the delay time of the gate pulse can be easily recorded similar to the measurements of the fluorescence decays and the temporal profile thus obtained for the cross-correlation light represents the IRF of the fluorescence up-conversion instrument. The FWHM of the IRF for the present instrument is found to be ~300 fs at the full width at half maximum.

2.3 Nanosecond laser flash photolysis

Photoinduced long lived excited state transients (e.g. triplet excited state, radical cation, anion etc.) can be monitored by laser flash photolysis experiment. The technique was introduced by Porter and Norris in 1949 and since then has become a basic tool in the study of the photochemical and photophysical properties of compounds under the effect of light irradiation. The sample is excited by the intense pulse of the pump source (normally a laser) to create the excited state population. The spectral and temporal properties of these excited state molecules are monitored by a probe light from a pulsed xenon lamp passed through the sample at right angles to the path of the exciting pulse. After passing through the sample the probe light is directed to a monochromator / spectrograph. The transmitted probe light is then measured either by a single detector (for kinetic analysis at a single wavelength) or by an array detector (for spectral analysis at a given time). The transmission intensity of the sample before, during, and after the exciting pulse are converted by the detector into electrical signals and measured by an oscilloscope (in the case of the single detector) or acquired by a CCD camera (in the case of an array detector). The changes in the transmission intensity are normally converted into changes of optical density. The basic layout of the set up is shown in Figure 2.4.

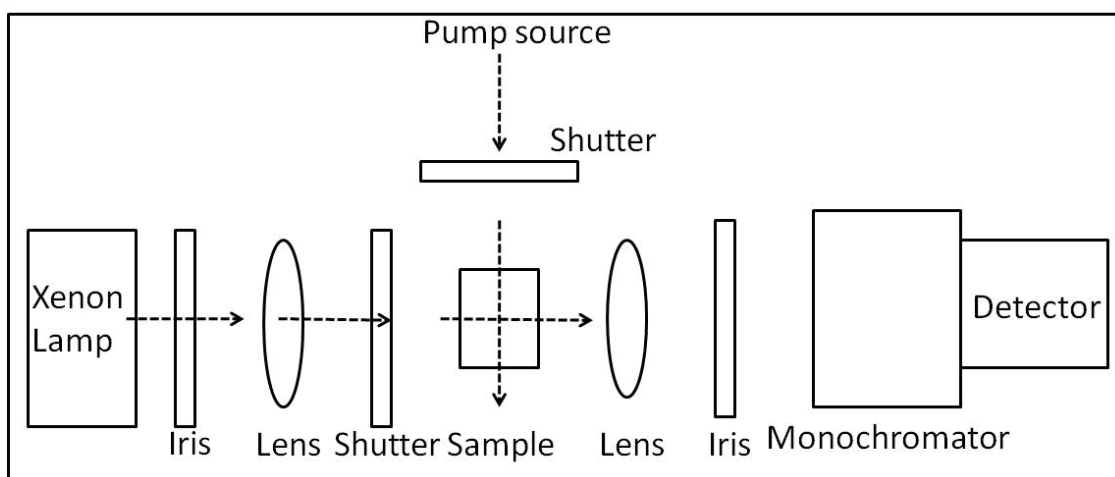


Figure 2.4. Basic layout of nanosecond flash photolysis set up.

In present thesis, transient absorption experiments with about 5 ns time resolution were performed using a Laser Kinetic Spectrometer (Edinburgh Instruments, UK, model LP920). The sample in a 10 mm × 10 mm quartz cuvette was excited using 532 nm laser pulses of 5 ns duration and 20 mJ/pulse energy generated using a frequency doubled Nd-YAG laser (Thales Laser SA, France, model: SAGA). Continuum light (250 – 1000 nm) from a pulsed 450 W xenon arc lamp was used as the optical probe. Time-resolved transient absorption spectra in the 300 - 950 nm region were recorded using an ICCD camera (Andor, UK, Model: iStar-320T) and the temporal absorption profiles at selected wavelengths were recorded using photomultiplier tube (Hamamatsu R920) connected to a 200 MHz digital oscilloscope.

2.4 Femtosecond pump probe transient absorption spectroscopy

2.4.1 Principle of transient absorption spectroscopy:

The central theme of the thesis is the investigation of the ultrafast relaxation dynamics of the photoexcited molecules which occur in sub-picosecond and picosecond timescale. Real time monitoring of the dynamics occurring in sub-picosecond timescale requires femtosecond time resolution. This is achieved either by fluorescence up-conversion or transient pump-probe

spectroscopy using femtosecond laser pulses. The principle of fluorescence up-conversion is described in section 2.2.2. In transient absorption spectroscopy, a strong pump pulse is used to create Franck Condon excited state population within a very short period of time defined by the temporal width of the pump pulse. This excited state population evolves with time due to relaxation in various pathways. This change in population of excited state molecules are followed by recording the changes in transmitted intensity of a weak monitoring pulse, as a function of the time delay between the pump and the monitoring probe pulse. In this technique, the optical delay is introduced to the probe pulse to travel more distance (ΔL) than that of the pump beam, so that a delay ($\Delta t = 2\Delta L/c$) between the pump and the probe can be generated. In the measurement, the probe pulse is divided into a sample and a reference pulse. The sample pulse is spatially overlapped with the pump pulse in the sample, while the reference pulse passes through an unexcited region (unaffected by pump pulse) of the sample. The experimental signal, i.e. the change in absorbance (ΔA), is obtained as the negative logarithm of the ratio of the intensity of the probe and reference pulses as given by:

$$\Delta A = \log \frac{I_0^S}{I^S} \times \frac{I^R}{I_0^R}.$$

Where, I_0^S and I^S are the transmitted intensity of the sample probe pulse in absence and presence of pump pulse and I_0^R and I^R are the same for the reference probe pulse respectively.

Solution phase absorption and emission spectra are usually very broad. Thus, differential absorption spectra generally covers the entire visible wavelengths, even extend to near infrared region. Hence, it is essential to examine the temporal behavior of the photoinduced reaction over a wide range of probe wavelengths. In the experiments described here, both the probe and the reference pulses are white light continuum (WLC). The WLC is generated by the non-linear phenomenon of self-phase modulation of an intense laser pulse

propagating through a dense but transparent medium. Under proper experimental conditions, a WLC can be made to extend from the visible to near infrared and it can be detected by either integrating photodiodes or a spectrograph together with a charge-coupled device. In these experiments, $\Delta A(\lambda, \Delta t)$ is obtained as a function of the probe wavelength λ and the delay time Δt between the pump and the probe pulses. In the experiments described above, there can be three different contributions to the transient absorption signal (see Figure 2.5). First the strong pump pulse excites the molecules from the ground state (S_0) to a higher excited state S_1 or S_n . Then, the molecules in the excited state absorb probe light, called as excited state absorption (process A in Figure 2.5). This is observed as decrease in the probe light and hence there is an increase in ΔA . If the probe wavelength falls in ground state absorption region, the probe pulse is attenuated more in absence of pump pulse as compared to presence of pump pulse. This results to negative absorbance signal which is called bleach signal (process C in Figure 2.5). A similar negative signal appears when probe light stimulates emission from the excited state molecules. This generally happens when probe wavelength overlaps with emission spectra of the sample. This signal is called stimulated emission (process B in Figure 2.5). The temporal evolution of stimulated emission provides the information regarding the population relaxation of the emissive excited state. This often provides complementary information to that of excited state absorption. The time resolution of such an experiment does not depend on the response of the detector, rather on the width of the pump and probe pulses.

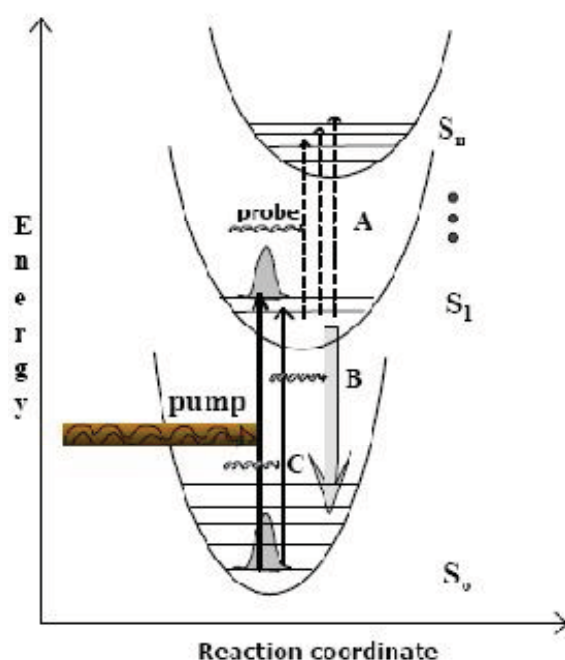


Figure 2.5. Scheme of the states involved in a pump probe experiment in a dye solution. (A) Excited state absorption (B) Stimulated emission. (C) Bleaching.

2.4.2 Femtosecond transient absorption spectrometer:

Femtosecond pump-probe spectroscopy needs to generate significant concentration of excited state to monitor absorption. This requires significantly large number of photons/pulse to generate adequate excited state population. This can be done with amplified laser system which uses a femtosecond Ti-sapphire oscillator and chirp pulse amplification technique to generate intense femtosecond laser pulses.⁹³⁻⁹⁴ The pump-probe spectrometer was built using an amplified laser system which was procured from Thales, France. The principle of femtosecond pulse generation and amplification is described below:

2.4.2.1 Ultrashort pulse generation: Ti-sapphire oscillator:

Femtosecond laser pulses are generated by Ti-sapphire oscillator. A continuous wave laser from a diode pumped solid state laser is used to excite the Ti^{3+} ions doped in sapphire. Ti^{3+} ions doped sapphire crystal show broad photoluminescence in 650-1000 nm. This provides large gain bandwidth which is an essential condition for ultrashort pulse generation. The basic principle of femtosecond pulse generation relies on Kerr lensing effect of the Ti-Sapphire gain

medium which leads to self focusing of the Gaussian laser beam passing through it. The Kerr lens forms a passive ‘intracavity’ aperture and introduces power dependent loss which makes resonator unstable in CW mode. On slight cavity disturbance, a pulsed transmission of the laser beam is energetically preferable over CW mode. Since the band width of the Ti-Sapphire gain medium is very large, it can produce optical pulses as short as 10 fs. To achieve the shortest pulse duration one need to compensate the dispersion introduced by the lens, crystal and other dispersive materials. This is done by intracavity pulse compression component such as ‘two prism compressor’ or by using ‘chirped mirror’ in the laser resonator cavity which provides requires negative group delay dispersion.

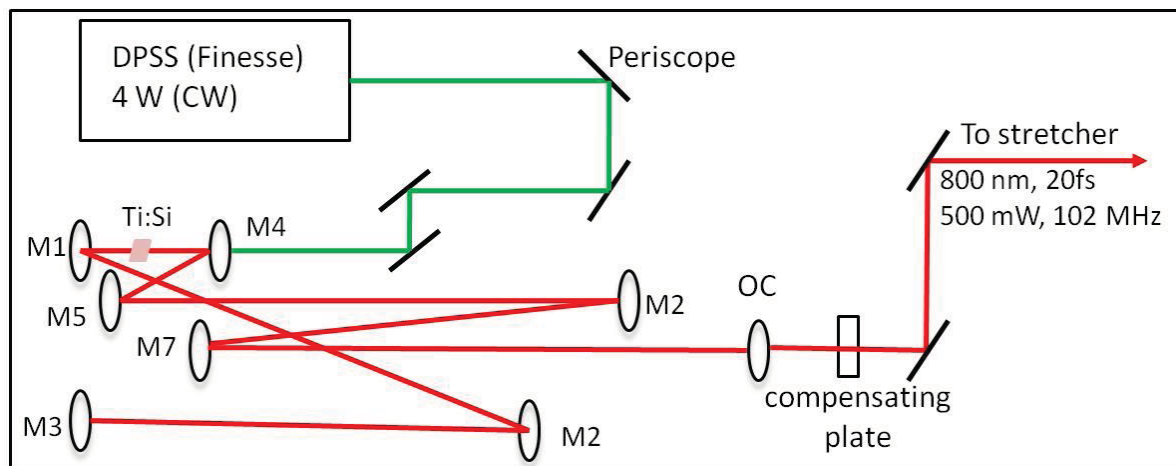


Figure 2.6. Optical layout of femtosecond Ti-sapphire oscillator.

In our setup Femtosource, Synergy (from FEMTO LASER, Vienna, Austria) has been used for generation of femtosecond pulses. The diode pump solid state (DPSS) laser (VERDI, 3.8W CW laser) with 532 nm wavelength has been used as pump laser. The optical layout of the oscillator cavity has been shown in Figure 2.6. The output beam of the pump laser is coupled through the lens which defines the resonator axis. Long cavity arm is aligned by using amplified spontaneous emission (ASE) from the Ti: Sapphire crystal or the transmitted green light from the pump laser. Output coupler is aligned by reflecting back the ASE beam collinearly into the gain medium. The output coupler is arranged with 10^0 to prevent reflections

from the rear side of the substrate. The quality of intra cavity dispersion is very crucial for the generation of high quality optical pulses in sub-femtosecond range. The chirped mirror used in mirror dispersion controlled Ti: Sapphire oscillator vary constant group delay dispersion over long range²⁴. For mode locking, small perturbation in the cavity lengths was made by moving mirror M4 towards output coupler and then released to its original position. After mode-locking starts, sometime optimization of the curved mirror M1 is necessary to get stable pulse train. The output of the oscillator was monitored by fast photodiodes and the stability of the optical pulses were observed in an oscilloscope. A spectrum analyzer is used to measure the spectral width of the mode locked pulse. The final output from the oscillator has 50 nm spectral width with nearly symmetric spectrum which corresponds to ~20fs pulse duration. The average output power of the oscillator is >500mW and output energy is ~5nJ/pulse at 102 MHz pulse repetition rate.

2.4.2.2 Chirped pulse amplification (CPA) - Ti:sapphire amplifier:

The amplification of femtosecond laser pulses takes place also in a Ti:sapphire crystal, which is called gain medium, pumped by an external laser source (pump laser). A femtosecond Ti:sapphire oscillator serves as seed laser for the amplification process. In order to avoid the damage of the gain medium by the high-intensities pulses, the peak power needs to be reduced. For example, a 1 mJ, 20 fs pulse focused to a 100 μ m spot size has a peak fluence of 5×10^{12} W/cm², which is ~ 1000 times higher than the damage threshold of most optical materials (GW/cm²).⁹⁵ The peak power reduction is done by temporal stretching of femtosecond pulses. The stretched pulses are then safely amplified, followed by recompression to the femtosecond duration. This is called as chirped pulse amplification (CPA) technique and the principle is shown in Figure 2.7.

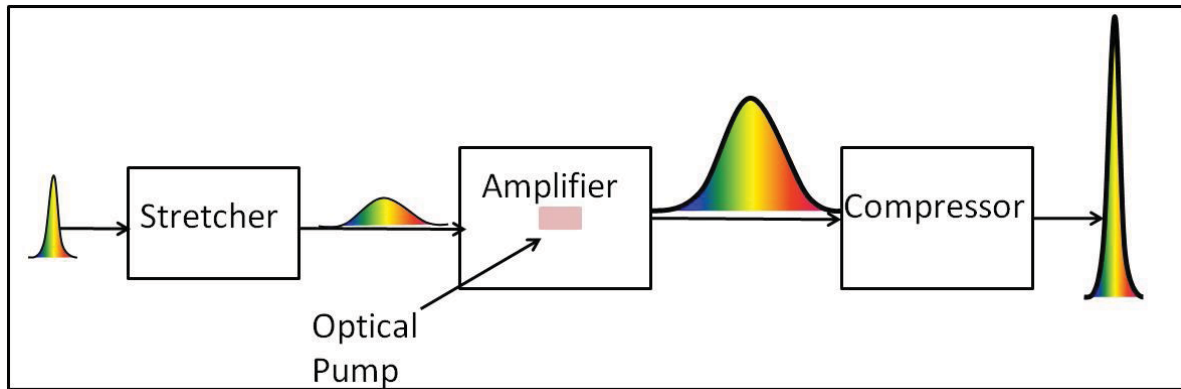


Figure 2.7. Principle of chirped pulse amplification technique.

2.4.2.3 Pulse stretcher and compressor:

An ultrashort laser pulse is characterized by the broad spectral distribution. By using a combination of gratings and/or lenses, the individual frequencies within an ultrashort pulse can be separated (stretched) from each other in time (see Figure 2.8). The longer component wavelength (red part) is diffracted at larger angle as compared to blue part. This wavelength dependent divergence creates a path difference between the red and blue part of pulse leading to temporal stretching of the incoming pulse. The duration of the incoming femtosecond pulse is usually stretched (chirped) up to 10^4 times from fs to a few hundred ps. The resulting chirped pulse is ready to be amplified, since peak power of a stretched pulse after amplification is lower than the damage threshold of the amplification crystal. After amplification the pulse is recompressed back to its original duration by a conjugate dispersion line in the compressor (Figure 2.8). The main challenge for a compressor is to recover not only the initial pulse duration and quality, but also to compensate the dispersion introduced in the amplification stage itself. To achieve this goal, the distance between gratings in the compressor is set longer than that in the stretcher. This will compensate overall second-order dispersion and help in producing relatively short pulses, but at the expense of introducing higher-order dispersion terms, which usually create extra temporal features in the compressed pulse such as prepulses and/or wings.

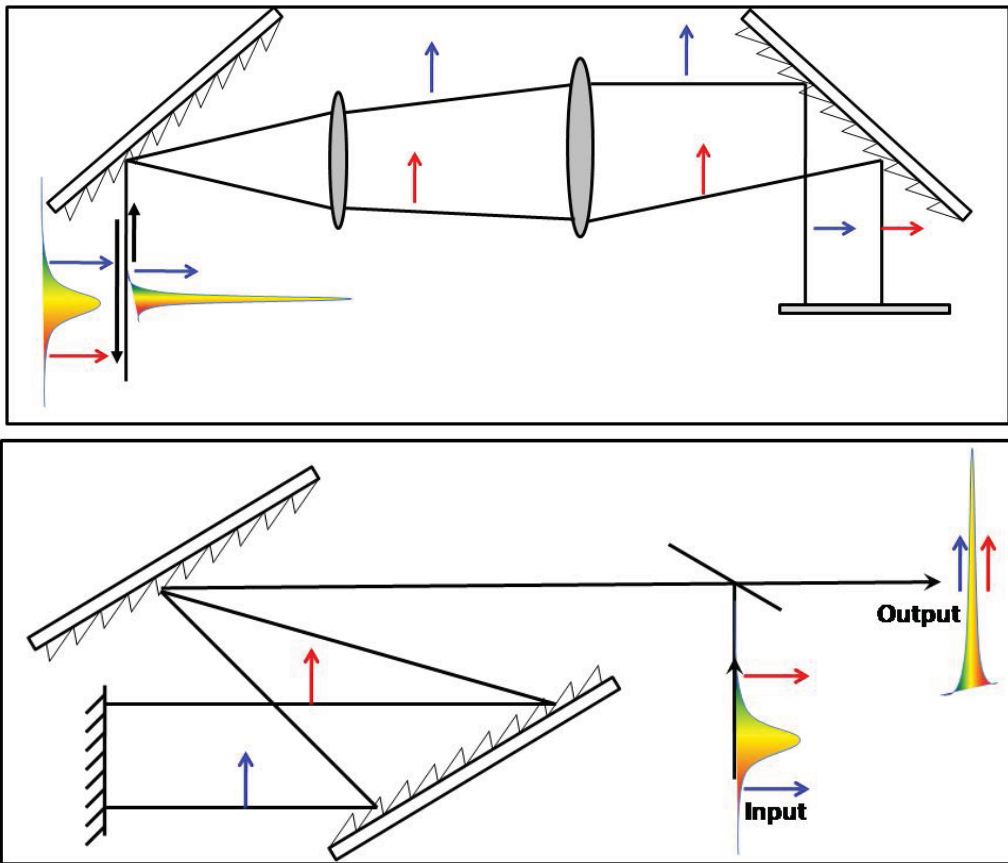


Figure 2.8: Principle of optical layout for pulse stretching (upper) and pulse compression (lower).

2.4.2.4 Regenerative and multipass amplification:

The most widely used approach of pulse amplification is the regenerative and the multipass techniques. The regenerative amplification traps the pulse to be amplified in a laser cavity until the gain is saturated. Trapping and dumping the pulse in and out of the resonator is performed by a fast-switching Pockel cell and a broad-band polarizer. The Pockel cell consists of a birefringent crystal, which can change the polarization of a traveling laser field by applying a voltage on it. In the multipass amplification, different passes are geometrically separated. A Pockel cell is used to inject a single pulse into the amplifier. The number of passes is usually limited by the difficulties on focusing all the passes on a single spot of the crystal.

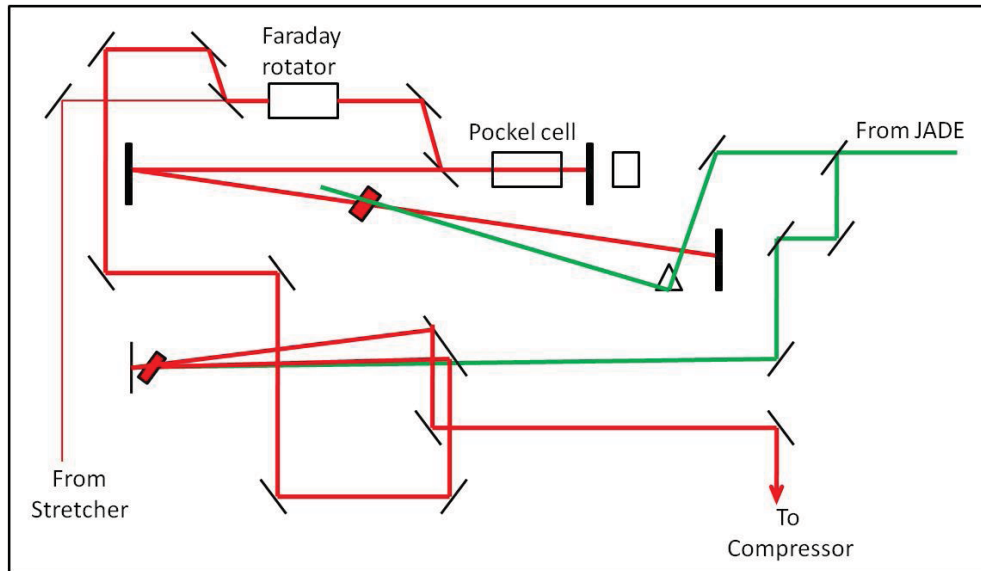


Figure 2.9. Schematic diagram of combined regenerative-two pass amplifier.

In present set up, we have two stage amplifications, consisting of both regenerative and two pass amplifier. The optical layout of combined regenerative-two pass amplifier is shown in Figure 2.9. The amplifier is pumped by second harmonic of a single 1 KHz Q switched (300 ns) Nd-YLF Laser (JADE) having 18 W power. Around 5.6 W power is used to pump the regenerative cavity while the remaining part (12.4 W) is used to pump the two pass amplification stage. Q switching and Pockel cell voltage are synchronized by master clock which is triggered by the oscillator signal through photodiode. The combined regenerative and two stage amplifier provides 3.5 W amplified laser output which is fed to compressor to generate highly intense femtosecond laser pulse.

2.4.3 Measurement of Ultrashort Pulses:

The most widely used technique for measuring an ultrafast femtosecond or picosecond optical pulse is an autocorrelator.⁹⁵ The basic optical configuration (Figure 2.10) is similar to that of a Michelson interferometer. An incoming pulse is split into two pulses of equal intensity by using a 50/50 beam splitter. One beam is headed to an adjustable optical delay, which delays the pulse by Δt . The two beams are then recombined within a nonlinear crystal for second

harmonic generation. The resulting second harmonic generation autocorrelation trace is detected by a photo-multiplier as a function of delay time between the two pulses.

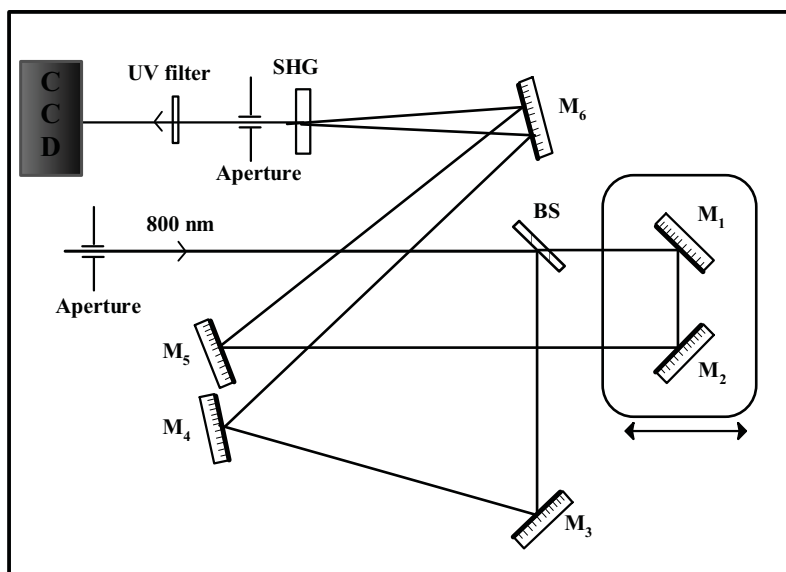


Figure 2.10. Optical layout of intensity autocorrelator for femtosecond pulse measurement.

The efficiency of the second harmonic generation resulting from the interaction of the two beams is proportional to the degree of pulse overlap within the crystal. Monitoring the intensity of second harmonic generation as a function of delay time between the two pulses produces the autocorrelation function directly related to pulse width. If the intensity of two pulses are $I(t)$ and $I(t-\tau)$, the autocorrelation (or convolution) of the two pulses is given by

$$A = \int_{-\infty}^{\infty} I(t)I(t - \tau)dt$$

By measuring the autocorrelation function, the pulse width of a given temporal shape can be determined. In order to determine the actual pulse width from the displayed autocorrelation function, it is necessary to make an assumption about the pulse shape (usually sech^2 shape for chirp-free pulse or Gaussian shape for linear chirped pulse). Intensity autocorrelation measurement provides 60 fs pulse (considering sech^2 shape) width of our amplified laser system which was used for setting up the transient absorption spectrometer.

2.4.4 Generation of pump pulse: Second harmonic generation

Fundamental wavelength of 800 nm light obtained from the femtosecond amplified laser source is not suitable for excitation, as most molecules absorb in UV and visible region. To obtain femtosecond pulses of 400 nm, which is suitable for photoexcitation of most organic and inorganic molecular systems, second harmonic generation (SHG) technique was employed.^{96, 97} Type I BBO crystal of 0.5 mm thickness is used for generating second harmonic of 800 nm to produce pulses at 400 nm. In present pump probe set up, 100 μ J/pulse energy of 800 nm pulses was used to focus with a lens on to the BBO crystal which generates \sim 10 μ J/pulse energy at 400 nm. This 400 nm light is separated from the fundamental by a dichroic mirror, and used for sample excitation (Figure 2.11). The second harmonic generated is polarized perpendicular to the fundamental (type I phase matching). This 400 nm wavelength light is used for sample excitation in all the transient absorption studies presented in the thesis.

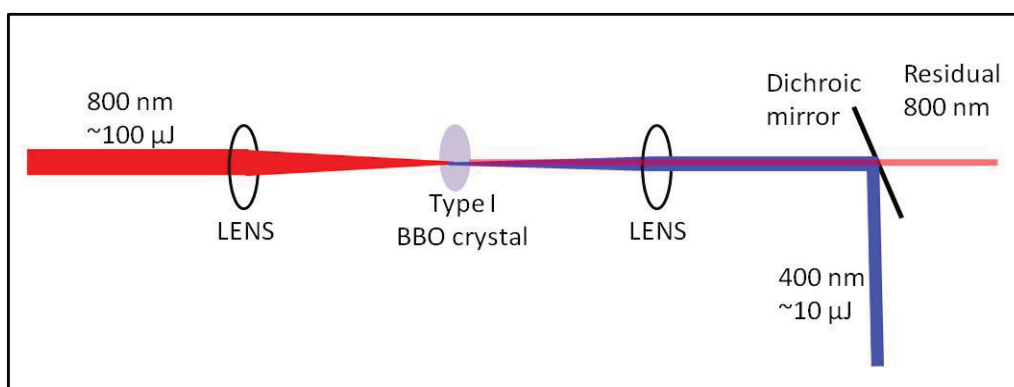


Figure 2.11. A schematic diagram of second harmonic generation (SHG) principle.

2.4.5 Generation of probe light: White light generation

In pump probe spectroscopy, it is necessary to have continuum of light to probe the photogenerated transient species. In the experimental setup presented here, white light is generated by focusing small part of 800 nm fundamental (\sim 2 μ J) with a lens on to a sapphire window of 1.5 mm thickness (Figure 2.12). Self phase modulation of the 800 nm laser pulse

leads to generation of higher and lower frequencies leading to spectral broadening covering visible and near-infrared region.^{98, 99} The spectrum of white light pulses is centered at 800 nm and bandwidth extends from 400-1000 nm. A non-divergent, low energy white light continuum is generated by keeping the energy of the fundamental pulses just above the threshold for continuum generation. This is accomplished with the help of neutral a density filter and suitable apertures.

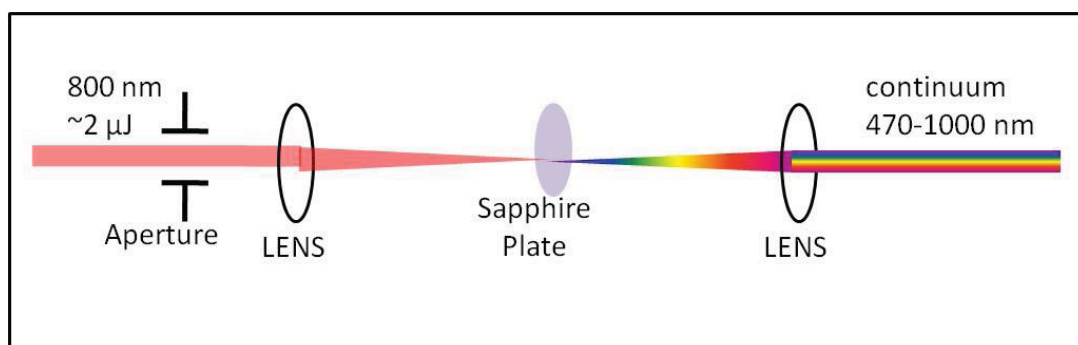


Figure 2.12. A schematic diagram of white light continuum generation principle.

2.4.6 Setup of pump-probe spectrometer

The block diagram of amplified laser system and the measurement setup is schematically shown in Figure 2.13. In present set up ~200 mW of laser power is used for pump probe experiments. The original 800 nm light is split by a 90:10 beam splitter. The major part of the beam is passed through a delay rail, followed by second harmonic generation to generate 400 nm pump pulse which is focused to the sample for excitation. The minor part is used to generate continuum probe light by focusing to a sapphire plate. The white light continuum beam is split with a neutral density filter into signal and reference beams. The signal beam is focused into the sample cell of 2 mm thickness which is spatially overlapped with the pump beam at the sample region. The sample solution is circulated through the cell during the measurements using a peristaltic pump. The polarization of pump light is set at the magic angle (54.7°) to eliminate sample reorientational dynamics. The pump and signal beams are focused in a near collinear ($\sim 10^\circ$) fashion on to 2 mm thick sample cell and the transmitted light is

filtered through 10 nm band pass interference filter. The focuses of the two beams are kept just after the sample cell. Integrating photodiodes are used to measure the intensity of signal, reference and pump pulses. To remove the noise arising from shot to shot laser fluctuations, a chopper is introduced in the path of the pump light. The chopper selects an alternate pulse with a repetition rate of 500 Hz. As the repetition rate of the probe is 1 KHz, the action of chopper makes the pump pulse to be divided into a pump condition and no-pump condition. As a consequence, the signal measured in the signal photodiode at no-pump

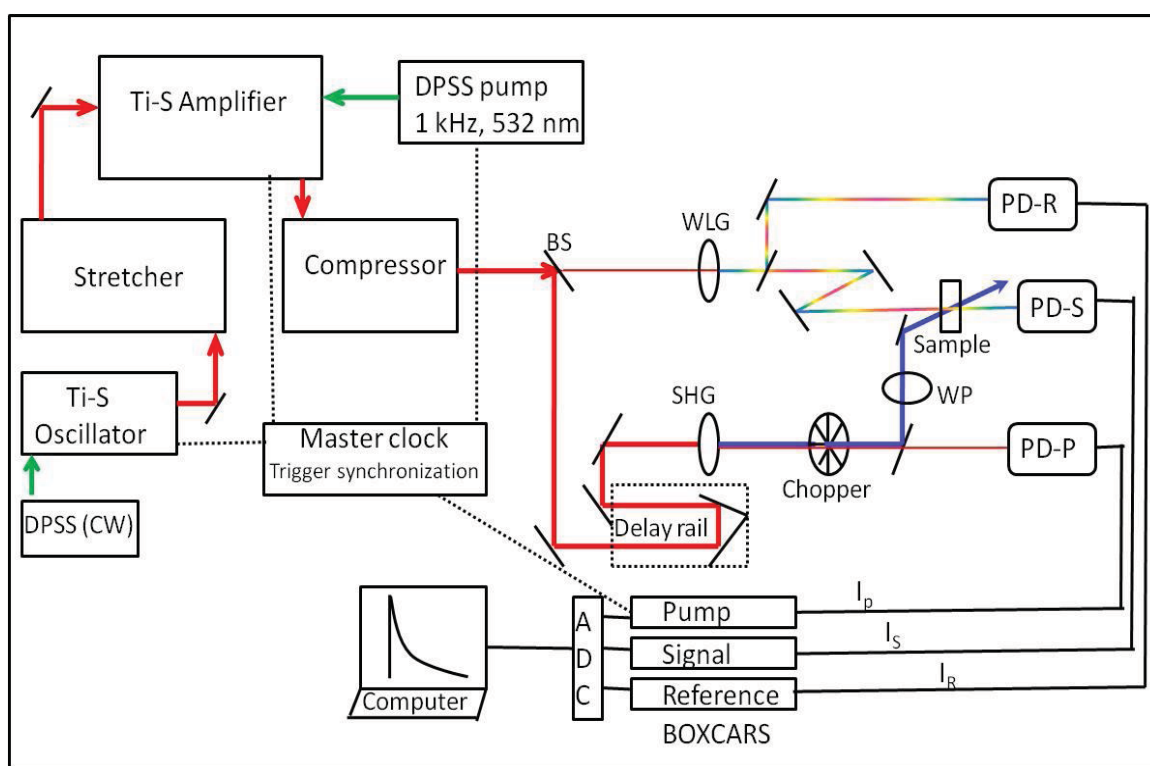


Figure 2.13. Complete layout of pump probe transient absorption spectrometer.

condition is taken to be I_0 and the one measured at pump condition to be I . The change in absorbance is calculated as negative logarithm of I/I_0 . The reference photodiode is used in the present setup to remove subtle fluctuations of the laser, which acts as a ratio to the signal. Signal to noise ratio is improved by averaging the signal over more than 1000 shots at each delay times and decay traces are taken twice in back and forth motion of the delay stage. Data averaging is done by BOXCAR average and the signal is fed to computer through Analogue to

digital converter and GPIB port. Signal calculation, signal averaging, delay stage movement, data recording are done by an automated data acquisition program run by LABVIEW interface. The optimum overlap of the pump and probe pulses (time zero) was achieved by measuring the maximum signal for the excited state absorption (ESA) of perylene (PE) in cyclohexane at 700 nm. Zero time delay (optimum temporal overlap of pump and probe) was set at the 50% of the maximum excited state absorption signal. After signal optimization, reference perylene cell was replaced by sample cell. A large volume of solution (~10 ml) was flown through the sample cell to minimize the effect of sample degradation under the strong laser excitation. Concentration of the sample was adjusted to get solution absorbance in 0.3-0.5 range at 400 nm excitation wavelength. The effect of concentration on dynamics was checked at two different concentrations for each of the samples studied. No significant concentration dependence was noted in any of the molecular systems presented in this thesis. All the experiments were performed at 296 K which is the temperature maintained in our laser laboratory.

The temporal profiles recorded using different probe wavelengths have been fitted with multi-exponential decaying or growing components by iterative deconvolution method using a sech^2 type instrument response function with fwhm of 120 fs. To provide the lifetime values associated with fit function, the notations “d” or “g” associated with the lifetimes, τ_1 , τ_2 , or τ_3 , have been used for the component having a positive or negative exponent, to indicate whether the transient absorption signal is decaying or growing, respectively. Similarly, the components representing the growth or decay of stimulated emission (SE) have been represented by the notation $\tau(d)$ or $\tau(g)$, respectively,. The lifetimes which are longer than 400 ps has not been shown, since lifetimes longer than 400 ps cannot be determined with reasonable accuracy by analyzing the temporal curve recorded up to maximum delay time of 1.2 ns in our instrument.

2.5 Quantum chemical calculation

Density functional theory (DFT) is a successful method to evaluate the ground state properties of molecular systems with an appreciable accuracy. The time dependent DFT approach (TD-DFT) has become a routine method for the evaluation of vertical electronic excitation spectra and excited state geometry. Though, TDDFT calculated energy parameters do not provide quantitative accuracy, qualitative information regarding the electronic and geometric structures and energetic are reasonably good. In particular, comparison of excited state parameters of a series of molecules provides important clues to substantiate the experimental observation.

All the quantum chemical calculations have been performed using GAMESS software package.¹⁰⁰ The ground state geometry of all the molecules were optimized using the density functional theory (DFT) without imposing any symmetry restriction. Becke's three parameter hybrid exchange function with the Lee-Yang-Parr gradient corrected correlated functional (B3LYP)^{101, 102} was used in conjunction with 6-311+G(d,p) basis set as implemented in GAMESS software package. Polarizable continuum model (PCM)¹⁰³ was used to incorporate the effect of the bulk solvent. The time dependent DFT (TDDFT) method using the B3LYP/6-31G (d,p) basis set were used for the optimization in the first singlet excited state to observe the change the geometrical change upon relaxation from the Franck-Condon state. Vertical excitation energies were also calculated using TDDFT method to calculate the potential energy in the ground and first singlet excited state at different twisted geometry. For every optimized structure, Hessian calculations were performed and it was found out that the vibrational frequencies were real and thus the optimized structures represent true minima in the potential energy surface.

2.6. MATERIALS

Curcumin (purity~80%) was purchased from Sigma-Aldrich and purified by repeated column chromatography to obtain 99% purity. Deuterated curcumin (curcumin-*d*3, in which only the

exchangeable hydrogen atoms of two phenolic groups and the enolic hydroxyl group were replaced by deuterium atoms) was prepared by the following method: curcumin was dissolved in deuterated methanol (CH_3OD) solvent and kept in a dry nitrogen atmosphere for 24 h and then the solvent was evaporated. To ensure complete deuteration of the exchangeable hydrogen atoms, the process was repeated three times. Curcumin- d_3 was dissolved in methanol- d in nitrogen atmosphere for studying the effect of deuteration on the excited-state dynamics. 1-(p-nitrophenyl)-2-hydroxymethyl pyrrolidine (p-NPP) (purity > 99%) was also obtained from Sigma-Aldrich and used as received. p-Dimethylamino-1, 3-diketone (DMADK) and two isomeric dimethylaminochalcones (DAMC-A and DMAC-B) were synthesized by following reported procedures.

Synthesis of DMADK: A tetrahydrofuran solution (10 mL) of 4-(N, N-dimethylamino)-acetophenone (9 mmol) and methylbenzoate (12 mmol) were added drop-wise to a boiling suspension of sodium hydride (12 mmol) in THF (10 mL) under argon atmosphere. After refluxing overnight, the reaction mixture was cooled and evaporated to dryness. The residue was dissolved in dichloromethane, and the solution was washed with dilute HCl. The dichloromethane solution was dried on sodium sulfate. The product was purified by a column chromatography and recrystallized from ethyl acetate (Yield: 30%). The product was identified by NMR spectroscopy. ^1H NMR (CDCl_3 , TMS): δ 3.12 (s, 6H), δ 6.73 (d, 2H), δ 6.79 (s, 1H), δ 6.9(d, 2H, 8Hz), δ 7.6 (m, 3H), δ 6.9(d, 2H), δ 7.95 (m, 4H). Proton NMR spectra indicates that the molecule mainly exists as keto-enol tautomeric forms.

Synthesis of DMAC-A: 4-(N, N-dimethylamino)-acetophenone (9 mmol) and benzaldehyde (9 mmol) was mixed thoroughly in 10 ml of aqueous ethanol. 20 mmol sodium hydroxide was added to the solution and was stirred for two hours which led to yellow precipitation. The precipitate was collected and washed several times with cold ethanol. The yellow product was recrystallized from ethanol which results to bright yellow needle (product yield= 80%). Purity

of the product was checked by thin layer chromatography and identified by proton NMR spectra. ¹H NMR (CDCl₃, TMS): δ 3.05 (s, 6H), δ 6.75 (d, 2H), δ 7.8 (s, 1H), δ 7.7(m, 4H), δ 7.4 (d, 2H), δ 7.82(s, 1H), δ 8.01 (d, 2H).

Synthesis of DMAC-B: A tetrahydrofuran solution (10 mL) of 4-(N, N-dimethylamino)-benzaldehyde (9 mmol) and acetophenone (9 mmol) were added drop-wise to a boiling suspension of sodium hydride (12 mmol) in THF (10 mL) under argon atmosphere and refluxed for 12 hours. After refluxing, the reaction mixture was cooled and evaporated to dryness. The residue was dissolved in chloroform and the solution was washed with dilute hydrochloric acid. The chloroform solution was dried on sodium sulfate and the product was purified by a column chromatography. A bright orange color product (yield: 65%) was obtained which was characterized by proton NMR spectroscopy. ¹H NMR (CDCl₃, TMS): δ 3.04 (s, 6H), δ 6.69 (d, 2H), δ 7.5(m, 5H), δ 7.4 (d, 1H), δ 7.82(s, 1H), δ 7.99 (d, 2H).

Nuclear grade crystals of uranyl nitrate (purity >99%) was obtained from Fuel Chemistry Division, Bhabha Atomic Research Centre and was dissolved in 1N nitric acid to avoid hydrolysis. Heteroleptic ruthenium polypyridyl complex, [Ru(bpy)₂(pap)](ClO₄)₂ (purity > 99%) was obtained from Dr. Dipanwita Das, IIT Bombay and used as received.

Each of the solvents, namely, Cyclohexane, Toluene, Ethyl acetate, Dioxane, Acetonitrile, Acetone, Dimethylsulfoxide (DMSO), Formamide, Propylene carbonate (PC), Dimethylformamide (DMF), as well as alcohols like methanol, Ethanol, Propanol, Butanol, Pentanol, ethylene glycol etc, were of spectroscopic grade (Spectrochem, India) and were used without further purification. Deuterated methanol (methanol-d) with 99 atom percent was purchased from Aldrich, USA.

Chapter 3

Ultrafast Dynamics of the Excited States of Curcumin in Solution

3.1. Introduction

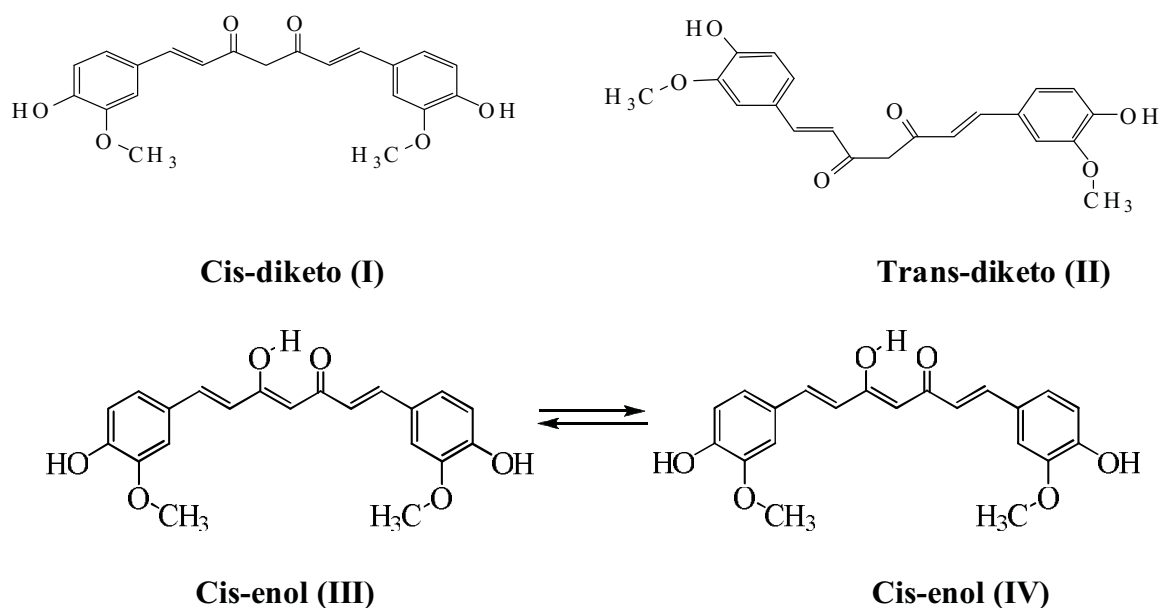
Curcumin has been the subject of intense investigations in the wide ranging fields of physics, chemistry, biology and medicine because of its potential applications as antioxidant, anti-inflammatory and anticancer agents.¹⁰⁴⁻¹⁰⁹ Curcumin has also been identified to have the ability to prevent protein aggregation in debilitating diseases such as Alzheimer's and Parkinson's.¹¹⁰⁻¹¹³

Structurally, curcumin is an α,β -unsaturated β -diketonic compound, in which two o-methoxy phenolic moieties are attached symmetrically through two π -conjugated ethylenic linkers (Scheme 3.1). NMR, absorption and fluorescence spectroscopic techniques have been widely employed to study the structural, photophysical, photobiological as well as biophysical properties of curcumin and its derivatives in solutions and in different kinds of heterogeneous media, such as micelles, vesicles and membranes.¹¹⁴⁻¹²⁸ Among several possible isomeric structures of curcumin, as proposed by Sun et. al.¹²⁹ only three of them, which can be considered as candidates for the ground state of curcumin, are shown in Scheme 3.1. The structure I, which is the cis-diketo form, is the most common representation of curcumin. However, full geometry optimization starting with the cis-diketo structure using high level ab initio computations performed by Balasubramanian did not produce a minimum but it rearranged to the trans-diketo form (Structure II).¹³⁰ In addition, the trans-diketo isomer was found to be a minimum with all real vibrational frequencies by computation, confirming this as

a potential isomer of curcumin. The reason for this isomerization was assigned to the negative charges on the C=O groups, that resulted in a strong electrostatic repulsion between the two C=O groups. Further, the ^1H and ^{13}C NMR and IR spectra of curcumin in chlorobenzene revealed that the cis-keto structure of curcumin undergoes a keto-enol rearrangement by transfer of a proton from the CH_2 group to form the enol form (Structure III) and it is essentially the major conformer of this molecule present in a variety of solvents.¹²³ NMR experiments performed by several other groups too established that the cis-enol form of curcumin is essentially the only form of this molecule present in a variety of solvents ranging from chloroform to mixtures of dimethylsulfoxide (DMSO) and water with varying pH in the range 3 to 9.¹²⁴⁻¹²⁸ Geometry optimization of the cis-enol structure at different levels of computational theories revealed that the enolic form with the dihedral angle of 180° was planar and was definitely the most stable form of the ground state both in the gas phase as well in aqueous solution.^{130, 131-135} Theoretical calculations have also established the fact that the cis-enol form is more stable than cis-diketo form, and the energy difference is about $7.75 \text{ kcal mol}^{-1}$.¹³¹ Further, Balasubramanian also showed that the diketo structure exists only in the trans form and it is 6.7 and $6.9 \text{ kcal mol}^{-1}$ above the enol form in the gas phase and solution, respectively. Formation of cis-enol structure becomes preferred because of its large dipole moment (7.7 and 10.8 D in the gas and solution phases, respectively), which leads to formation of strong intramolecular H-bond, as well as the extended conjugation of the molecular backbone compared with the diketone form.^{130,131} Moreover, the TDDFT calculated absorption spectra and oscillator strengths of both isomers provide further evidence to support the conclusion that the enol form of curcumin predominates in solution. The experimental value of the absorption maximum for the enol form of curcumin (417 nm in benzene or 419 nm in chloroform) is very close to the calculated absorption maximum (419 nm), suggesting the predominance of this form in solution.^{114-116, 131} On the contrary, the structure of the diketo form is twisted and the theoretically predicted absorption maximum shifts to the near-

ultraviolet region.^{130, 131} In fact, the cis-enol form may be considered as co-existing in two equivalent or symmetric keto-enol tautomers (Structures III and IV), which may interconvert between each other via intramolecular hydrogen atom transfer (IHT) process. NMR spectroscopic analysis in solution indicated only the presence of rapidly interconverting structures III and IV.¹²⁴

Several studies have focused on the photophysical properties of the excited states of curcumin in different kinds of solvents using time-resolved fluorescence spectroscopy in pico and sub-picosecond time scales and have predicted about the occurrence of two fundamental photophysical processes of the excited state, namely the excited state intramolecular hydrogen atom (or proton) transfer, ESIHT (or ESIPT) process, as well as dipolar solvation.¹¹⁵⁻¹²² Firstly, solvation is expected to play an important role in the excited-state relaxation dynamics of curcumin because of a significant change in the dipole moment ($\Delta \sim 6.1$ D) following photoexcitation of the molecule from the ground electronic (S_0) state to the first excited singlet (S_1) state.¹¹⁵ This value is comparable to that of Coumarin 153 ($\Delta \approx 8$ D), which has been extensively used as a standard probe for studying solvation dynamics.^{136,137} Secondly, the ESIHT process in the hydrogen bonded chelate ring of the cis-enol form has been predicted to play an important role in the efficient nonradiative deactivation process of the excited state.^{115, 117,119} Earlier studies on chemical systems having asymmetric intramolecular hydrogen bonded chelate centre and hence asymmetric potential energy surface (PES) for ESIPT reaction, have established the fact that the ESIHT process is ultrafast and the lifetimes of these processes are in the range of a few hundred femtosecond (vide infra).^{141- 147} Since curcumin is a symmetric molecule with respect to the hydrogen bonded chelate centre (structures III and IV), it is unlikely that ESIHT process leads to any change in the absorption and emission properties of the excited state to enable monitoring the process spectroscopically.



Scheme 3.1. Chemical structures of the cis- and trans-diketo forms of curcumin and the keto-enol tautomeric equilibrium.

Recently, Adhikary et. al. studied the excited-state photophysics of curcumin both in alcoholic solutions as well as in surfactant micelles using sub-picosecond fluorescence upconversion spectroscopy.^{119, 120} They reported about the presence of two decay components in the excited-state kinetics with the lifetimes of about 12 - 20 ps and 100 ps in methanol and ethylene glycol (EG). The lifetime of the shorter component was nearly insensitive to deuteration and this process was assigned to the process of solvation of the S_1 state. Whereas, the lifetime of the longer component (100 ps in methanol) was observed to become longer due to deuteration and they assigned this component to the ESIHT process. However, this inference was not in conformity with the general observation of ESIHT timescale (~ 100 -200 fs) in common six member hydrogen bonded system. In this chapter, the results of our investigations on the relaxation dynamics of the excited states of curcumin in wide varieties of solvents, which include apolar aprotic, polar aprotic and polar protic solvents have been described using both sub-picosecond time-resolved fluorescence upconversion and transient absorption spectroscopic techniques.

3.2. Results

3.2.1. Steady-state absorption and fluorescence: Absorption and fluorescence spectra of curcumin have already been well characterized by different groups in different kinds of solvents and media.^{115, 117, 118} However, for better understanding of the dynamics of the excited states in different kinds of solvents, the characteristics of the absorption and fluorescence spectra of curcumin have been compared in four different kinds of solvents, namely, 1,4-dioxane (an aprotic solvent of low polarity), acetonitrile (a polar aprotic solvent), methanol (a polar protic solvent and a strong hydrogen bond donor) and dimethylsulfoxide (DMSO) (a polar aprotic but a strong hydrogen bond acceptor) in Figure 3.1.⁴⁰ Curcumin has very low solubility in a non-polar solvent, like cyclohexane (static dielectric constant, $\epsilon_0 \sim 0$) and hence the sub-picosecond dynamics of fluorescence or transient absorption could not be studied in this solvent. Therefore, we choose 1,4-dioxane ($\epsilon_0 \sim 2.21$), which is a little more polar than cyclohexane, as the representative of the class of non-polar aprotic solvents. It is important to note that both the absorption and the fluorescence spectra exhibit significant solvent effect. Each of the absorption spectra presented in Figure 3.1 shows an intense absorption band in the 300–500 nm wavelength region. In 1,4-dioxane, acetonitrile and methanol, absorption maximum appears at the same wavelength (*ca* 420 nm) with a shoulder at *ca* 440 nm. However, in DMSO, the positions of both the absorption maximum and the shoulder are bathochromically shifted to 436 nm and 450 nm, respectively. It is also important to note that the intensity of the shoulder band increases significantly in methanol and DMSO, which are strong hydrogen bond donating and hydrogen bond accepting solvents, respectively. These facts suggest a significant perturbation of the intramolecular hydrogen bond existing in the cis-enol conformer and dictate the possibility of formation of intermolecular hydrogen-bonded complex in the ground state. However, formation of intermolecular hydrogen bond at the site of the phenolic OH groups too cannot be excluded.

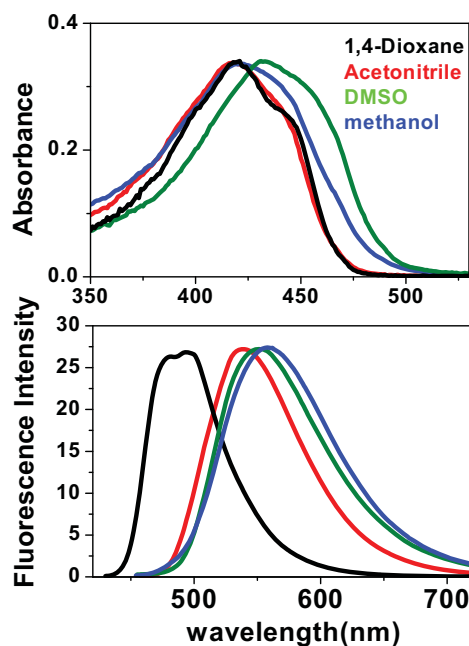


Figure 3.1. Steady-state absorption and fluorescence spectra of Curcumin in 1,4-dioxane, acetonitrile, DMSO and methanol.

Further, both the shapes and the wavelength maxima of the fluorescence spectra as well as the Stokes shifts are strongly dependent on the solvent characteristics. In 1,4-dioxane, the fluorescence spectrum shows a splitting of the maximum appearing at 480 and 494 nm. On the other hand, the same is broad with a maximum at 538 nm in acetonitrile, 550 nm in DMSO and 560 nm in methanol. The Stokes shifts are about 3400, 5220, 4754 and 5950 cm^{-1} in 1,4-dioxane, acetonitrile, DMSO and methanol, respectively. These values can be compared with that of about 1500 cm^{-1} in cyclohexane.¹¹⁵ Larger Stokes shifts in more polar solvents is obviously a consequence of solvation because of a large change in dipole moment, $\Delta\mu=6.1$ D) following photoexcitation of curcumin to the S_1 state.¹¹⁵ This implies that in the S_1 state, reasonable amount of charge is transferred from the aromatic 4-hydroxy-3-methoxyphenyl moiety to the dicarbonyl moiety through π -conjugation.¹³⁰ As a consequence of this, the properties of the S_1 state are expected to have strong solvent dependence and solvation dynamics is likely to play an important role in the relaxation dynamics of the S_1 state of curcumin. However, the larger solvatochromic red-shift observed in hydrogen bond donating solvent (methanol) can only be explained by the effect of both polarity and hydrogen bonding

ability of the solvent on the excited state of curcumin. In earlier work, better linear correlation of the Stokes shift with the solvent polarity parameter, $E_T(30)$ was observed as compared to that with the reaction field factor, ΔF .¹¹⁵ This fact supports the prediction about strong hydrogen-bonding interaction between the S_1 state of curcumin and the solvents.

3.2.2. Fluorescence Upconversion Study: Figure 3.2 shows the fluorescence upconversion signals of curcumin in ethanol recorded in the 460 – 660 nm region using laser pulses of 425 nm of 100 fs duration. They have been analyzed by deconvolution of the effects of the finite temporal resolution of the fluorescence upconversion apparatus (FWHM of the instrument response function ~ 300 fs) from the measured emission decays. The fluorescence dynamics is non-exponential and shows significant wavelength dependence. The upconversion signals recorded in the 460 – 500 nm region could be well fitted using a triexponential decay function, whereas those recorded in the 515 – 660 nm region could be fitted using an exponential function consisting of an ultrafast growth component and another two decay components. In the 600 - 650 nm region, the inclusion of the decay component with a lifetime longer than 500 ps, but of very small amplitude, was essential to obtain a good fit. The best-fit function corresponding to each of the temporal curves has been shown in Figure 3.2 and the values of the different decay parameters associated with each of them have been given in Table 3.1. While the decay component with the lifetime of 200 ± 15 ps is associated with each of the upconversion signals presented in Figure 3.2 region, the lifetimes of the other components, both the growth and the decay, are wavelength dependent. The presence of the long-lived component with the lifetime longer than 500 ps has already been reported in the fluorescence decay measured using single photon counting technique and has been attributed to the presence of a small amount of other conformers, namely, the trans-diketo form, in the ground state.^{115,117,118}

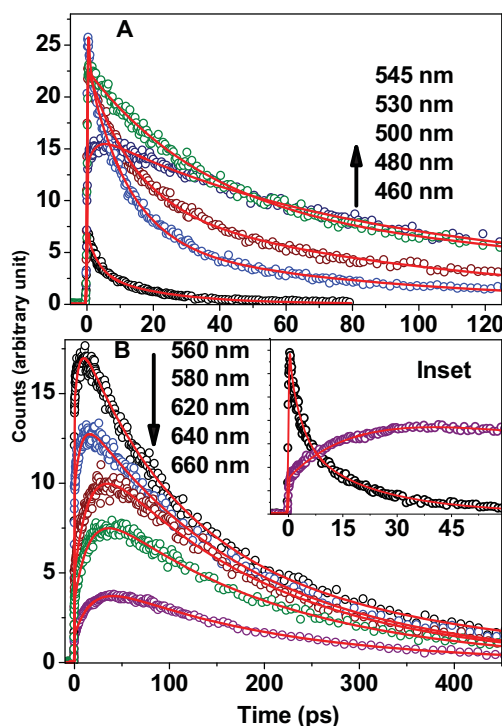


Figure 3.2. Fluorescence upconversion signals of curcumin in ethanol, recorded at different wavelengths, along with their biexponential or triexponential fit functions. Values of the lifetimes are given in Table 3.1. Inset of B: Signals recorded at 460 and 660 nm have been compared in sub-60 ps time domain to show the nearly equal rate of decay of the signal recorded at 460 nm and the rate of growth of the signal recorded at 660 nm.

This kind of fluorescence dynamics is the well-known characteristics associated with those chemical systems, such as coumarin 153, in which solvation plays a major role in the relaxation dynamics of the excited state of a molecule, which is created with a large molecular dipole moment following photoexcitation.^{136,148,149} This information, in combination with the fact that the fluorescence spectra of curcumin exhibit larger Stokes shift in more polar solvents, suggests that wavelength dependent dynamics observed in the fluorescence upconversion experiment is obviously a consequence of the solvation process. To delineate this aspect, we constructed the time-resolved emission spectra for the excited state of curcumin in ethanol at different delay times in the range of 0.35–80 ps using the fluorescence upconversion signals collected at different wavelengths (Figure 3.2) using the method of Maroncelli and co-workers.¹⁴⁸ In brief, the deconvoluted multiexponential decay function at each monitoring wavelength is normalized so that its time integrated value matches with the emission intensity at the corresponding wavelength in the steady-state emission spectrum in the same solvent.

This means that the emission spectrum of the ‘fully-solvated’ state recorded at infinite delay-time corresponds to the steady-state emission spectrum in the same solvent. In this way, the normalized fluorescence intensity is known at all delay times in the 0.35 to 80 ps time domain for the entire set of monitoring wavelengths in the 460 – 660 nm region and the time-resolved emission spectra at different delay-times are constructed by point-to-plot of the emission intensities at different wavelengths. They have been presented in Figure 3.3.

Table 3.1. Decay parameters obtained by fitting the fluorescence upconversion signals presented in Figure 3.2.

Wavelength (nm)	Decay parameters					
	τ_1 , ps	a_1	τ_2 , ps	a_2	τ_3 , ps	a_3
460	1.8	0.43	13.9	0.52	200	0.05
480	1.95	0.15	13.6	0.68	195	0.17
500	3.7	0.15	23.9	0.6	180	0.25
515	0.07	-0.01	27	0.6	201	0.4
530	0.4	-0.04	30.5	0.55	199	0.45
545	5.9	-0.17	51.8	0.46	215	0.54
560	6.0	-0.27	52	0.32	210	0.68
580	6.2	-0.34	70	0.12	212	0.88
600	12.3	-0.49	190	0.92	long	0.08
620	16.2	-0.62	190	0.93	long	0.07
640	17	-0.66	195	0.92	long	0.08
660	19	-0.69	185	0.92	long	0.08

The dynamic bathochromic shift of the emission maximum with increase in delay time is the clear signature of the process of solvation of the excited state. However, a significant decrease in intensity of emission with increase in delay time is an indication of concomitant decay of the excited state during the solvation process. This suggests that association of the excited state of curcumin with the solvent molecules via intermolecular hydrogen-bonding induces faster nonradiative decay of the former. The frequency, at which the maximum intensity appears in the time-resolved emission spectrum, shifts from 19509 cm^{-1} recorded at 0.35 ps to 18150 cm^{-1} recorded at 80 ps and hence the observed dynamic shift of the frequency maximum of the emission spectra due to solvation is about 1319 cm^{-1} . It is a normal practice to construct the

solvent correlation function, $C(t)$, as defined by equation 1, to determine the time constants associated with the solvation process.^{136,148}

$$C(t) = \frac{\nu(t) - \nu(\infty)}{\nu(0) - \nu(\infty)} \quad (1)$$

Here, $\nu(0)$, $\nu(t)$, $\nu(\infty)$, are the frequencies of the emission maxima at the delay times of zero (i.e. immediately after photoexcitation), intermediate time t , and infinity (i.e. after completion of the solvation process), respectively. To determine these emission maxima, we have used the peak frequency obtained directly from the log normal fits of the corresponding spectrum. If we compare the position of the emission maximum of the spectrum, which could be recorded at

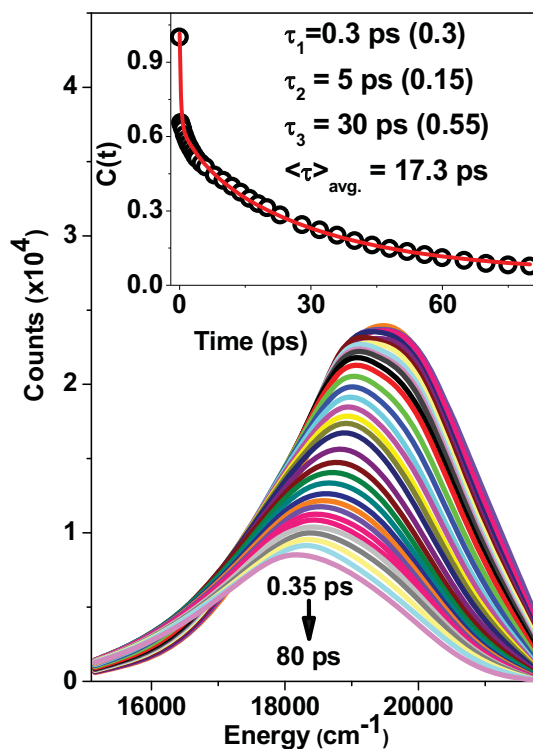


Figure 3.3. Time-resolved emission spectra constructed at different delay times (Delay times: 0.35, 0.5, 0.8, 1.2, 1.6, 2.0, 2.5, 3, 3.5, 4.0, 5, 6, 8, 10, 12, 14, 16, 18, 20, 24, 28, 32, 36, 40, 44, 48, 52, 56, 60, 65, 70, 75, 80 ps). Inset: Time-correlation function $C(t)$, constructed following equation 1, along with the tri-exponential fit function. The lifetimes associated with the fit function and the average lifetime calculated are also shown in the inset.

earliest delay-time, i.e. 19509 cm^{-1} at 0.35 ps, with that of the fluorescence spectrum recorded in a nonpolar solvent, i.e. at about 20000 cm^{-1} in cyclohexane,¹¹⁵ it becomes evident that we

have missed the early events of solvation phenomena, which have been completed prior to the delay time of 0.35 ps. So, because of limitation of the instrument response of about 300 fs, we have not been able to record the emission spectrum of the unsolvated species, which exists only at zero delay time. Hence, the value of $\nu(0)$ could not be determined in this experiment. However, accepting the value of 20000 cm^{-1} as that of $\nu(0)$ should be a good approximation. The maximum of the emission spectrum recorded at the delay time of 80 ps is seen to appear at 18150 cm^{-1} , This corresponds to that for the steady state fluorescence spectrum recorded in ethanol and this is the assumption made for construction of the time-resolved fluorescence spectra presented in Figure 3.3. This value is assigned to $\nu(\infty)$. Thus the correlation function, $C(t)$, constructed using equation (1) has been shown in the inset of Figure 3. This curve also includes the point, for which the value of $C(t)$ is equal to 1. The $C(t)$ curve could be fitted using a triple exponential function, which provides the lifetimes of the components with their relative amplitudes as 0.3 ps (0.3), 5 ps (0.15) and 30 ps (0.55). The average solvation time could be calculated as 17.3 ps and it agrees well with the value determined in ethanol using standard solvation probes ($\langle\tau\rangle_{\text{avg}} \sim 16\text{ ps}$).^{148, 149}

In Figure 3.4, we have compared the fluorescence upconversion signals for curcumin in methanol and curcumin-d in methanol-d recorded at a few selective wavelengths, namely 480, 520 and 640 nm. While in all the cases, the fluorescence upconversion signals are fitted with multiexponential functions consisting of decay and / or growth components, the lifetimes of each of the corresponding components is longer in the case of deuterated solute and solvent. However, the effect of deuteration is seen to be more prominent at the longer monitoring wavelengths and at longer delay time. This information, in combination with that obtained from the fluorescence upconversion experiment performed in ethanol (Figures 3.2 and 3.3), confirms the fact that association of the excited state of curcumin with the solvent molecules becomes stronger as the solvation process proceeds to completion and it involves the formation of intermolecular hydrogen (or deuterium, in the case of deuterated solute and solvent) bonds

between the solute and the solvent, via reorganization of the hydrogen (or deuterium) bonds of the solvent around the solute molecule (vide infra). Stretching vibrations in hydrogen (or deuterium) bonds induce fast nonradiative deactivation of the excited state and hence the longer lifetimes of the corresponding components in the case of curcumin-d in methanol-d as compared to those of curcumin in methanol is the result of deuterium isotope effect, imparted to strong intermolecular hydrogen bonding interaction between the S_1 state of curcumin and the solvent.

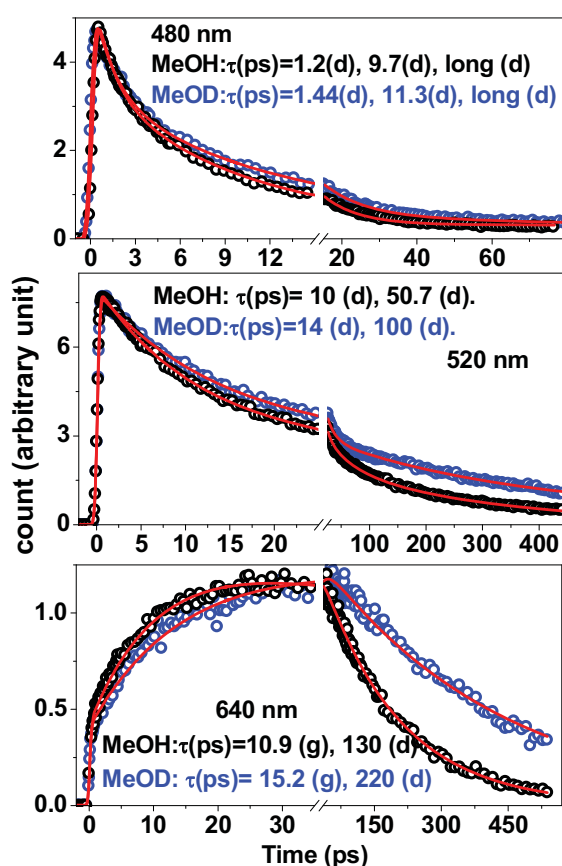


Figure 3.4. Comparison of the fluorescence decay of curcumin in methanol and curcumin-d in methanol-d at 480, 520 and 640 nm.

Earlier, Adhikary et. al reported the lifetimes of the S_1 state of curcumin as 70 and 120 ps in methanol and methanol- d_4 , respectively, on the basis of their measurement at 520 nm.¹¹⁹ However, our results described above show that the fluorescence decay monitored at this wavelength cannot provide the correct value of the lifetime of the fully relaxed or solvated S_1 state. Because of the dynamic shift of the fluorescence maximum representing the progress of

solvation phenomenon, the fluorescence decay monitored at different wavelengths through the entire region of the fluorescence spectrum is wavelength dependent and non exponential. Hence, the analyses of the upconversion signals recorded in the 460 – 600 nm region can provide any meaningful information neither about the solvation time nor the lifetime of the S_1 state. Since, at these wavelengths, we monitor a non-equilibrium mixture of differently solvated excited state species, the lifetimes obtained by multiexponential fitting of the fluorescence decay represents the average values of the lifetimes of a large number of differently solvated species. Meaningful information can be obtained by monitoring the fluorescence decay only at the red edge of the fluorescence spectrum, say, at 640 - 660 nm, at which the fully solvated S_1 state can be monitored. At 640 or 660 nm, the growth of the upconversion signal represents the formation of the fully solvated species and the decay lifetime of the signal can be assigned to that of the solvated species. Therefore, we find that the decay lifetimes of the S_1 state of curcumin in methanol and curcumin-d in methanol-d are 130 ± 7 ps and 220 ± 10 ps, respectively. These lifetimes are longer than those reported by Adhikary et. al. because of the reason explained above. Further, we have shown in the case of curcumin in ethanol that the solvation in alcoholic solvents are multimodal and hence the single exponential growth of the S_1 state monitored at 640 nm (or at any other wavelength) cannot provide the complete information regarding the solvation dynamics. However, the growth lifetimes, 10 ± 1 ps or 14 ± 1 ps, measured at this wavelength can be described as the longest component of the multimodal solvation process of curcumin in methanol or curcumin-d in methanol-d, respectively (details discussion is given in section 4.1.1).

3.2.3. Transient Absorption Spectroscopic Study

3.2.3.1. In aprotic solvents: Fluorescence upconversion experiments revealed that intermolecular hydrogen bonding interaction via hydrogen bond reorganization is possibly the major process contributing to the relaxation of the S_1 state of curcumin in alcoholic solvents.

However, this technique has not revealed the role of any other process, such as photoisomerization via twisting of the double bonds. In addition, the dynamics of the S_1 state of curcumin in aprotic solvents has not been studied earlier, and hence the aspect of solvation of curcumin in this class of solvents is yet unexplored. These are the reasons, which motivated us to investigate the relaxation dynamics of S_1 state of curcumin in different kinds of solvents using the transient absorption spectroscopic technique, which has a better time-resolution (~ 100 fs) as compared to that of the fluorescence upconversion method.

Figure 3.5 presents the time-resolved differential absorption spectra of the transient species created following photoexcitation of curcumin in 1,4-dioxane using 400 nm laser pulses of about 50 fs duration. The transient spectrum recorded at 0.2 ps delay-time consists of one negative absorption band in the 470 – 500 nm region (the entire band could not be recorded here because of limitation of the spectrometer) and a broad positive absorption band due to excited state absorption (ESA) in the 500 – 830 nm region. A comparison between the steady-state spectra (both absorption and fluorescence) of curcumin in 1,4-dioxane (Figure 3.1) and the negative absorption band observed here, the latter could obviously be assigned to stimulated emission (SE) and not to bleaching. In addition, comparison of the shapes and positions of the steady-state fluorescence spectrum and the ESA band, as shown in Figure 3.5, suggest significant overlapping between the SE and ESA bands in the 470 – 570 nm region. With increase in delay-time, both the SE and ESA bands decay. However, the pattern of evolution of the time-resolved spectra suggest that the decay of the ESA band in the lower energy (e.g. in the 650 – 700 nm) region is slower than that in the higher energy (e.g. in the 500 – 650 nm) region. Further, in the 700 – 770 nm region, an ultrafast decay of transient absorption is followed by a growth component (see Figure 3.6). All these characteristics lead to wavelength-dependent temporal dynamics, which suggest the involvement of more than one transient species or excited states in the relaxation dynamics of curcumin in this solvent.

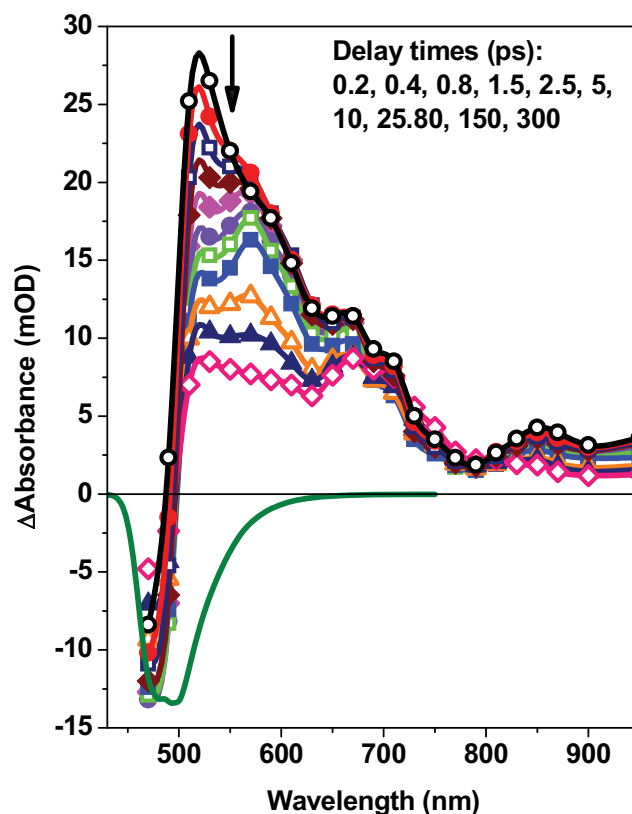


Figure 3.5. Time-resolved differential absorption spectra of the transient species formed following photoexcitation of curcumin in 1,4-dioxane using 400 nm laser. Olive colored curve represents the position and shape of the steady-state fluorescence spectrum.

In Figure 3.6, the temporal profiles recorded at a few selective wavelengths following photoexcitation of curcumin in 1,4-dioxane have been presented. The best-fit functions are also presented in this figure along with the lifetimes associated with the different components in the insets. Temporal profiles recorded in the 500 – 600 nm region show wavelength dependent dynamics because of overlapping of SE and ESA bands in this region. However, those recorded in the 470 – 500 nm region and in the 600 – 1000 nm region are expected to provide useful information regarding the dynamics of the S_1 state. The temporal profiles presented in Figure 3.6 could be best fitted by a four exponential (those recorded at 470, 590 and 870 nm) or three exponential (that at 790 nm) function consisting of both decay and/or growth components and the lifetimes of the components associated with these temporal profiles are seen to be very similar. Hence, four different kinds of excited states or processes are

responsible for the evolution of the transient spectra presented in Figure 3.5. Unfortunately, spectral characteristics of these four kinds of transient species could not be resolved in the transient spectra because of overlapping of the ESA and SE bands throughout the wavelength region. The average lifetimes of three of these processes could be determined as 1.6, 44 and 325 ps. Each of the temporal profiles recorded at different wavelengths is associated with a long-lived component, which has lifetime longer than 500 ps (not shown in the inset).

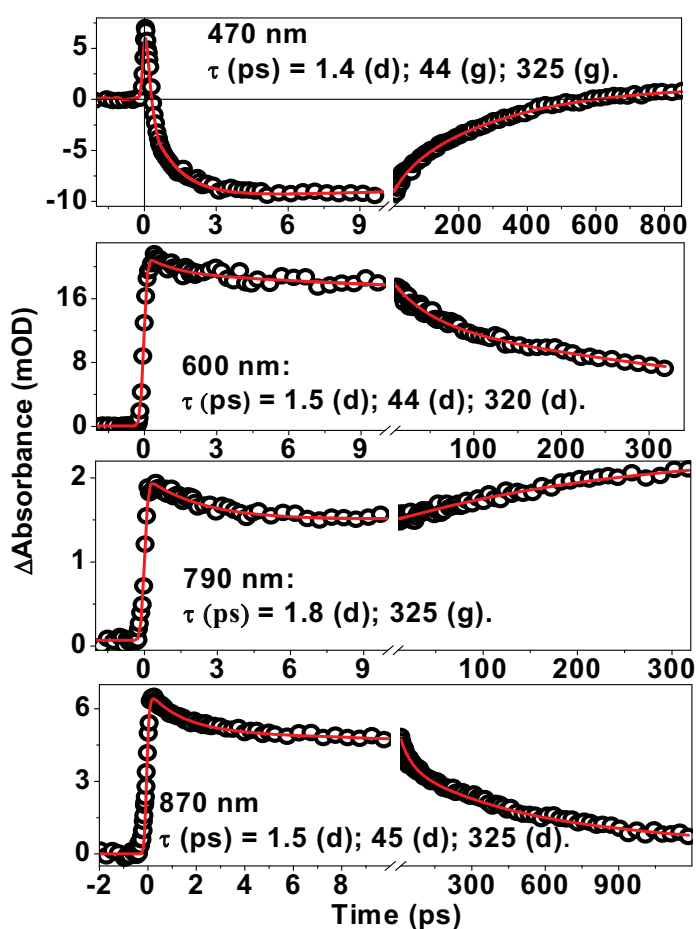


Figure 3.6. Temporal profiles (circles) recorded at a few selective wavelengths following photoexcitation of curcumin in 1,4-dioxane using 400 nm light. The red lines represent the best fit multiexponential functions and the lifetimes associated with the best fit function are given in the insets.

Nardo et. al. have found that in cyclohexane, a nonpolar aprotic solvent like 1,4-dioxane, the fluorescence decay of curcumin is tri-exponential (with the lifetimes of 57 ps, 256 ps and 1405 ps).¹¹⁷ It should be noted that the lifetimes of the two shorter lived components are comparable to the lifetimes determined in 1,4-dioxane. The presence of a long-

lived decay component with the lifetime of about 1100 ps, in addition to the shorter lived component with 52 ps lifetime, in the fluorescence decay in benzene has also been reported by Khopde et. al.¹¹⁵ We assign the lifetimes of 44 ps and 325 ps to the S₁ states of the cis-enol and trans-diketo conformers, respectively, which exist in the ground state of curcumin (see section 1). Since, the component with the lifetime of 1.6 ps is quite in agreement with the value of the average solvation time, $\langle\tau\rangle_{\text{coum}}$ (~1.7 ps), determined using coumarin 153 as a probe for solvation dynamics in the same solvent (Table 3.2), it possibly can be assigned to the solvation process.¹⁵⁰ However, we need to discuss the results in other solvents to confirm the assignment of this ultrafast component.

Figure 3.7 presents the time-resolved differential absorption spectra of the transient species generated following photoexcitation of curcumin in acetonitrile, which can be considered as a polar aprotic solvent. The transient absorption spectrum recorded at 0.2 ps delay-time shows the presence of two broad ESA bands with maxima at *ca* 590 and 900 nm. We do not observe an SE band in the 500 – 700 nm region, where the fluorescence emission band of curcumin in acetonitrile occurs (Figure 3.1), but a small negative absorption at 530 nm. The observed differential transient spectrum is the result of additive combination of SE and ESA bands in this wavelength region. With increase in delay-time in sub-5 ps time-domain, we observe the decay of the ESA band in the 550 – 800 nm region with the concomitant development of an ESA band in the 470 – 500 nm region. This evolution also leads to the development of a weak SE band with a maximum at *ca* 700 nm. It is also important to note that decay of the ESA band in the 530 – 800 nm region is faster than that in the 800 – 1000 nm region, which does not show any significant change in this time-domain. Evolution of the time-resolved spectra looks apparently different from that observed in 1,4-dioxane, because of the fact that the fluorescence spectrum is shifted significantly towards the lower energy region as compared to that in the case of 1,4-dioxane, leading to the overlap of ESA and SE bands in a spectral region, which is different from that in the case of 1,4-dioxane. However analyses of the

temporal profiles reveal the involvement of similar kinds of processes in the relaxation of the excited states of curcumin in these two solvents as well as in other solvents discussed earlier.

The pattern of evolution of the time-resolved transient absorption spectra in acetonitrile also supports these facts. Development of the ESA band in the 470 – 500 nm region and the SE band in the 650 - 750 nm region with increase in delay-time is the result of the dynamic bathoromic shift of the SE band but hypsochromic shift of the ESA band due to solvation of the excited state. That is why the shapes of the temporal profiles recorded in the 500 – 700 nm region and the corresponding lifetimes of the different components are wavelength dependent.

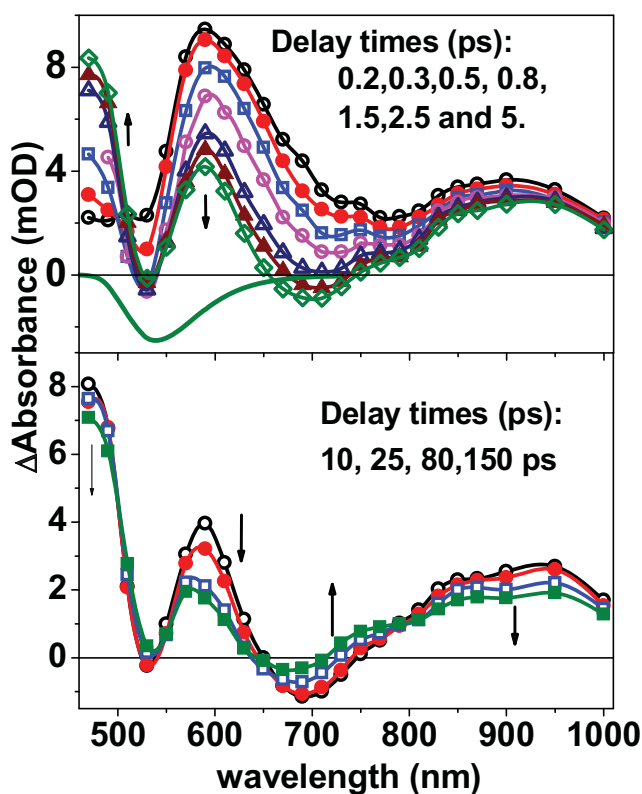


Figure 3.7. Time-resolved absorption spectra of the transient species formed following photoexcitation of curcumin in acetonitrile using 400 nm laser pulses.

Since, the steady-state fluorescence spectrum of curcumin in acetonitrile has very weak intensity in the 470 – 490 nm region (Figure 3.1), the ESA band is expected to be free from interference from the SE band in this region. Therefore, the temporal profiles recorded in this

region are expected to provide meaningful results regarding the lifetimes of the excited states or the processes associated with them. On the basis of similar arguments, temporal profiles recorded in the 700 – 1000 nm region are also expected to provide meaningful values of the lifetimes. At delay times longer than 5 ps, we observe the decay of all the ESA and SE bands occurring in the entire wavelength region, but a marginal increase of ESA in the 700 – 800 nm region.

In Figure 3.8, we have presented the temporal profiles recorded at a few selective wavelengths following photoexcitation of curcumin in acetonitrile. The temporal profiles recorded in the 470 – 490 nm region could be-fitted with a four exponential function consisting of two ultrafast growth components of ESA with the lifetimes of 0.3 and 0.65 ps, followed by its two exponential decay with the lifetimes of 310 ps and a long lived component having lifetime longer than 500 ps, which is not shown in the insets of the figure. However, those at other wavelengths could be fitted well with three exponential functions consisting of both decay and / or growth components. Although the ultrafast component with the lifetime of 0.3 ps is not evident in the temporal profiles recorded at wavelengths other than 470 nm, the values of the other two lifetimes determined at 690 nm and 870 nm are very similar to those determined at 470 nm. The values of two of the three lifetimes, determined at 610 nm, do not agree well with those determined at other wavelengths possibly because of overlapping of SE and ESA bands at this wavelength. Average values of the lifetimes of the three components determined at 490, 690 and 870 nm in acetonitrile are shown in Table 3.2.

Temporal profiles have been recorded at 470 and 870 nm in other polar aprotic solvents, namely, dimethylformamide (DMF), DMSO, Propylene carbonate (PC) and formamide, are shown in Figure 3.9. Temporal profiles recorded at 470 nm in each of the four solvents have been well-fitted with an exponential function consisting of two growth components and decay components. That recorded at 870 nm could be fitted well with a four exponential decay function. The lifetimes of three shorter lived components (but not the one

with lifetime longer than 500 ps) associated with the multiexponential best-fit function are given in the caption of the Figure3.9.

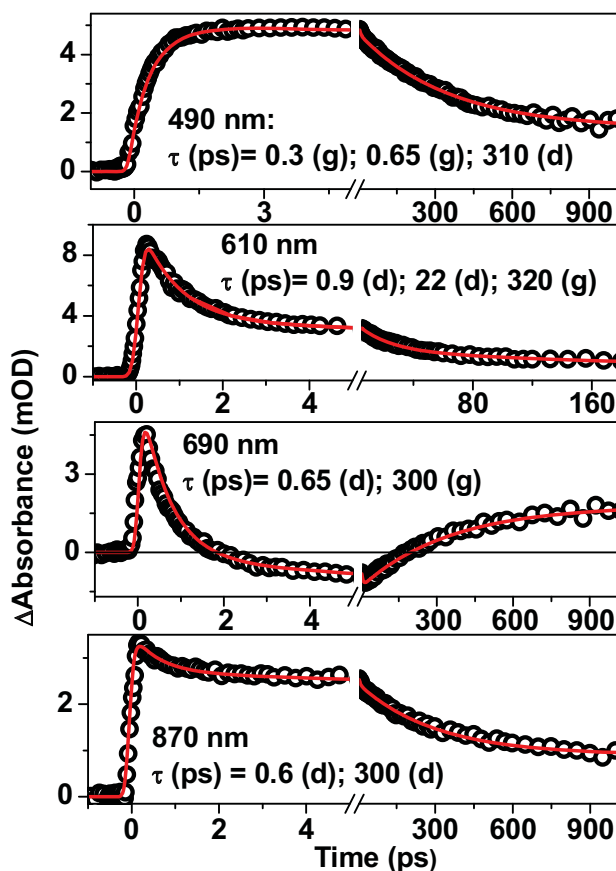


Figure 3.8. Temporal profiles (circles) recorded at a few selective wavelengths following photoexcitation of curcumin in acetonitrile. The red lines represent the best fit multi-exponential functions. The lifetimes associated with the fit functions are given in the insets.

The lifetimes of the corresponding components are very similar at these two wavelengths in each of these solvents and the average values of these lifetimes determined from these two measurements are given in Table 3.2. It is important to note that viscosities of DMSO and PC are six and forty times, respectively, larger than that of acetonitrile. Further, the polarity of formamide is more than about three times larger than that of acetonitrile. So it has been interesting to examine the effect of these factors on the lifetimes of different components which has been discussed in section 3.3 (vide infra). We have also studied the effect of hydrogen bonding solvents on the excited state dynamics and lifetime of curcumin in different alcoholic solvents. The experimental results are given in the next section.

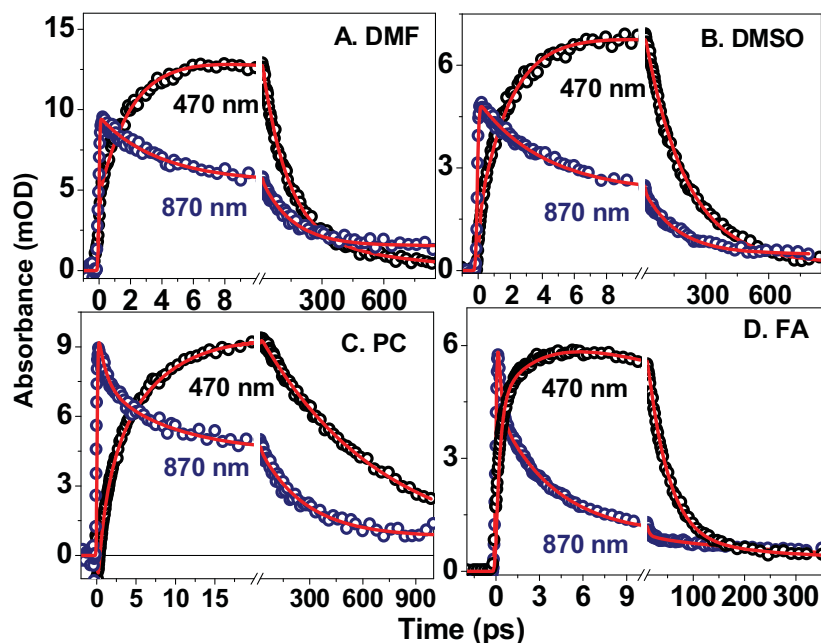


Figure 3.9. Temporal profiles (circles) recorded at 470 and 870 nm following photoexcitation of curcumin in polar aprotic solvents. The red lines represent the best fit multi-exponential functions. The lifetimes (in ps) associated with the fit functions are as follows (in each case the fit function is associated with a slow decay component with a lifetime longer than 500 ps, which is not given here):

- (A) DMF: 470 nm - 0.3 (g), 2.3 (g), 162 (d); 870 nm - 3.5 (d), 150 (d).
 (B) DMSO: 470 nm - 0.35 (g), 2.6 (g), 202 (d); 870 nm - 4 (d), 160 (d).
 (C) PC: 470 nm - 1 (g), 6.3 (g), 300 (d); 870 nm - 1 (d), 7.7 (d), 270 (d).
 (d) FA: 470 nm - 0.3 (g), 3.2 (g), 42 (d); 870 nm - 0.25 (d), 3.9 (d), 50 (d).

Table 3.2. Lifetimes of the processes associated with the relaxation dynamics of the excited states of curcumin in different kinds of solvents.

Solvent	ϵ_0 , ^a η (cP) ^b ; β , ^b E_T^{Nb}	τ_I , τ_{II} , τ_{III} , ps ^c	τ_L , ps ^d ; $\langle \tau \rangle_{\text{coulm}}$, ps ^e	τ_v , ps ^f	Solvation components		
					τ_1 , ps (a_1)	τ_2 , ps (a_2)	$\langle \tau \rangle_{\text{solv}}$ ps
1,4-dioxane	2.2; 1.42; 0.37; 0.164	2.2, 18.3, -	-; 1.7	-	-	1.6 ± 0.2	1.6 ± 0.2
EA	6.0; 0.43; 0.45; 0.228	0.21, 1.7, -	1.6; 2	0.5 ± 0.1	-	6 ± 0.5	6 ± 0.5
TA	7.3; 20; -; 0.34	-, -, -	-; 49.5	1.4 ± 0.2	-	50 ± 5	50 ± 5
BN	25.2; 1.24; -; 0.833	0.36, 5.3, 25	12.5; 5.1	0.3 ± 0.1	6.7 ± 0.5 (0.37 ± 0.05)	21 ± 3 (0.63 ± 0.05)	15.7 ± 1
Acetonitrile	35.8; 0.34; 0; 0.46	0.09, 0.63, -	0.2; 0.5	-	0.3 ± 0.05 (0.61 ± 0.05)	0.65 ± 0.1 (0.39 ± 0.04)	0.44 ± 0.02
DMF	36.7; 0.8; 0.69; 0.722	0.22, 1.7, 29.1	2.1; 0.92	-	0.3 ± 0.05 (0.36 ± 0.03)	2.9 ± 0.5 (0.64 ± 0.05)	1.6 ± 0.3
DMSO	46.5; 1.99; 0.76; 0.444	0.21, 2.3, 10.7	2.1; 1.8		0.4 ± 0.05 (0.43 ± 0.04)	3.3 ± 0.5 (0.57 ± 0.05)	1.8 ± 0.3
PC	64.9; 13; 0.4; 0.491	0.18, 2.03, 6.57	8; 2.6	-	1 ± 0.2 (0.39 ± 0.03)	6.3 ± 0.5 (0.63 ± 0.05)	4.4 ± 0.8
Formamide	111; 3.3; 0.55; 0.799	0.16, 2.9, 57.9	-; 5.0	-	0.34 ± 0.1 (0.5 ± 0.03)	3.5 ± 0.3 (0.5 ± 0.03)	1.1 ± 0.3
Methanol	32.7; 0.55; 0.62; 0.762	0.28, 3.2, 15.3	9.2; 5	0.2 ± 0.1	1.5 ± 0.2 (0.37 ± 0.03)	10 ± 1 (0.63 ± 0.05)	6.9 ± 0.8
Ethanol	24.6; 1.08; 0.77; 0.654	0.39, 5.0, 29.6	28.1; 16	-	3 ± 0.5 (0.25 ± 0.02)	27 ± 2 (0.75 ± 0.05)	21 ± 2
1-Propanol	20.5; 1.94; -; 0.617	0.34, 6.6, 47.8	58.7; 26	-	4 ± 1 (0.11 ± 0.01)	40 ± 3 (0.89 ± 0.06)	36 ± 3
1-Butanol	17.5; 2.57; -; 0.602	5.03, 42.6, 133	100; 63	-	17 ± 2 (0.17 ± 0.01)	77 ± 5 (0.83 ± 0.06)	67 ± 5
1-Pentanol	13.9; 3.51; -; 0.568	0.67, 21.7, 151	152; 103	-	30 ± 3 (0.2 ± 0.01)	155 ± 10 (0.8 ± 0.6)	130 ± 6
EG	37.7; 13.8; -; 0.790	5, 32	86; 15	-	2 ± 0.5 (0.47 ± 0.04)	18 ± 3 (0.53 ± 0.05)	10.5 ± 2

^a ϵ_0 is the static dielectric constant. ^b η is the viscosity, β is Kamlet-Taft hydrogen bond accepting strength and E_T^N is normalized solvent polarity parameter. ^c τ_I , τ_{II} , τ_{III} are the lifetimes associated with the multimodal solvation determined using C153 probe. ^dLongitudinal relaxation times. ^eThe average solvation time, $\langle \tau \rangle_{\text{coulm}}$, determined using Coumarin153 probe. ^fLifetime of the trans-diketo conformer.

3.2.3.2. In Protic Solvents: To delineate the aspect that solvation is the major process involved in the relaxation of the excited state of curcumin in alcohols, as revealed by the transient fluorescence spectroscopic study, we investigated the properties of the excited states in the series of normal alcoholic solvents. Evolution of the transient absorption spectra of the transient species generated following photoexcitation of curcumin in methanol has been shown in Figure 3.10. Spectral characteristics of the transient species formed in this solvent are very similar to those observed in acetonitrile. As discussed in the case of acetonitrile, dynamic hypsochromic and bathochromic shifts of strongly overlapping ESA and SE bands, respectively, occurring in the 500 – 750 nm region are responsible for the evolution of the time-resolved spectra presented in this figure. However, in this case, we observe the reverse dynamic shift of the SE band which is the net result of combination of the two opposite kinds of spectral shifts undergone by the ESA and SE bands. As a consequence of this, occurrence of wavelength dependent dynamics in the 500 – 700 nm region is obvious in this case too. Following the same arguments as presented earlier, the lifetimes of the components, which have lifetimes shorter than 500 ps, could be determined accurately by analyzing the temporal profiles recorded in the 470 – 490 nm region and 700 – 1000 nm regions. In Figure 3.11, we have presented the temporal profiles recorded at a few selective wavelengths. Analysis of the temporal profiles recorded in the 470 – 490 nm region reveals four exponential dynamics, which includes the contribution of a component with a lifetime of 400 ps (also shown in Table 3.2). In other solvents, this component is longer than 500 ps. However, in the case of the temporal profiles recorded in the 800 – 1000 nm region, inclusion of an ultrafast decay component with lifetime of 0.25 ps has been found necessary to fit the ultrafast decay part, in addition to the four other decay components. The average values of the lifetimes determined from the measurements at these three wavelengths are given in Table 3.2.

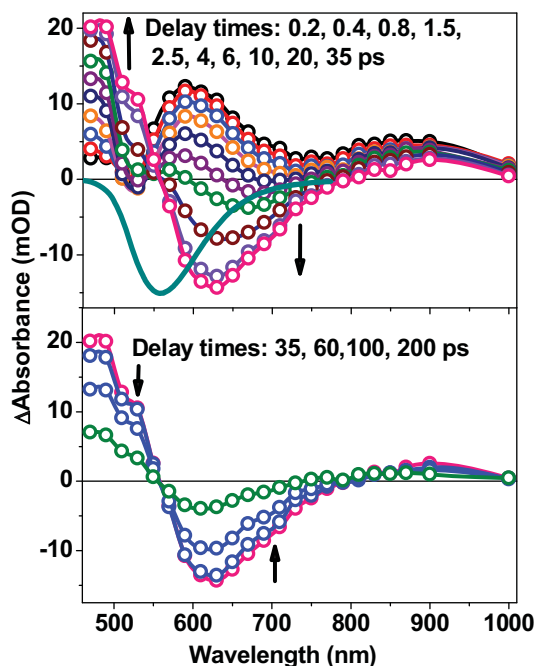


Figure 3.10. Time-resolved differential absorption spectra of the transient species formed following photoexcitation of curcumin in methanol. Olive coloured curve represents the steady-state fluorescence spectrum in this solvent.

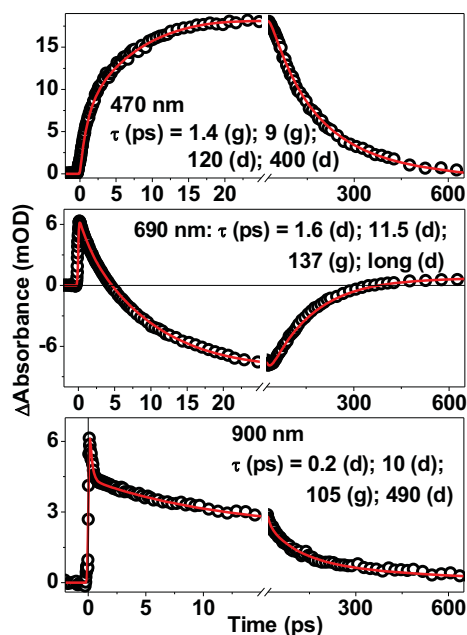


Figure 3.11. Temporal profiles (circles) recorded at a few selective wavelengths following photoexcitation of curcumin in methanol. The red lines represent the best fit multiexponential functions. The lifetimes associated with the fit functions are given in the insets.

Considering better strength of the transient absorption signal at 480 nm and also the fact that accurate information about the lifetimes are available at this wavelength because of negligible overlap between the ESA and SE bands, temporal profiles have been recorded at this

wavelength in other normal alcoholic solvents (i.e. ethanol to 1-pentanol) as well as in ethylene glycol (EG) (Figure 3.12). Each of the temporal profiles presented in this figure could be best fitted with a four exponential function consisting of two ultrafast growth components (τ_2 and τ_3) and two decay components (τ_4 and τ_5). While in methanol, τ_4 is about 425 ps, in other alcoholic solvents, it is longer than 500 ps and the same is not given in Table 3.2. It is important to note that the alcoholic solvents used here, viscosity varies from 0.55 in methanol to 3.51 in pentanol and 13.8 in EG and the average solvation time, $\langle\tau\rangle_{\text{coum}}$ varies from 5 ps in methanol to 103 in pentanol (Table 3.2). However, $\langle\tau\rangle_{\text{coum}}$ of EG (15.3 ps) is nearly equal to that of ethanol (~ 16 ps), viscosity of which ($\eta \sim 1.08$ cP) is much smaller than that of EG ($\eta \sim 13.8$ cP). The lifetimes of different components, which are presented in Table 3.2, show a large variation with the change in solvent characteristics. However, a preliminary observation reveals that while the τ_1 and τ_2 seem to have a better correlation with the solvation time rather than the viscosity, τ_3 may be better correlated with the hydrogen-bonding ability (measured by E_T^N values) in alcoholic solvents.

3.3. Discussion

3.3.1. Solvation dynamics in protic solvents: In the present study, we have combined two complementary ultrafast techniques, namely, subpicosecond fluorescence upconversion and transient absorption spectroscopy to investigate the dynamics of the excited states of curcumin in different kinds of solvents. Our fluorescence upconversion study in ethanol (section 3.2) has established beyond doubt that solvation process has a major contribution in the relaxation of the S_1 state of curcumin in alcohols. It has also been established that the solvation process is multimodal with three components having lifetimes of 0.3 ps, 5 ps and 30 ps in ethanol and the average solvation time, $\langle\tau\rangle_{\text{solv}}$ could be determined as 17.3 ps (Figure 3.3).

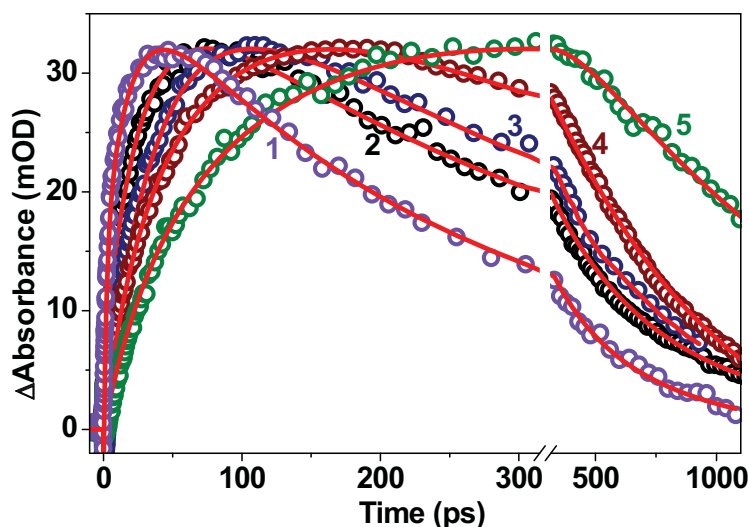


Figure 3.12. Temporal profiles recorded at 480 nm following photoexcitation of curcumin in alcohols :EG (1), ethanol (2), 1-propanol (3), 1-butanol (4) and 1-pentanol (5). Lifetimes obtained from the best fit multiexponential function are given in Table 3.2.

To compare them with the values of τ_1 ($= 3$ ps) and τ_2 ($= 27$ ps) (Table 3.2) determined by us in ethanol using transient absorption technique, we find that this technique provides an average value of 2 ps for two ultrafast components (0.3 ps and 5 ps), and the value of τ_2 (27 ps) agrees well with that (30 ps) of the longest component associated with the $C(t)$ function (equation 1), determined using the fluorescence upconversion technique. They also correspond well to the longitudinal relaxation time, ($\tau_L \sim 28.1$), of the solvent (Table 3.2). It is also important to note that the lifetimes of the three components associated with the $C(t)$ function are in good agreement with the lifetimes, τ_I , τ_{II} and τ_{III} (Table 3.2) associated with the multiexponential fit of the spectral response function determined by Maroncelli and his coworkers using the standard solvation probe, coumarin 153.¹³⁶ The average solvation time, $\langle \tau \rangle_{\text{solv}} = 17.3$ ps) determined by us also agrees well with that (16 ps) reported by these authors. In addition, the value of τ_2 in methanol is in perfect agreement with the lifetime of the component of 10 ps lifetime determined by Adhikary et. al., who also assigned this component to solvation process.¹¹⁹ Therefore, these arguments establish that the two ultrafast components (namely, τ_1 and τ_2) associated with the relaxation dynamics of the S_1 state of curcumin in normal alcohols

are associated with the solvent reorganization process and further confirms that in alcoholic solvents, solvation plays a major role in it.

We discussed earlier that curcumin adopts mainly the intramolecular hydrogen-bonded cis-enol form (Scheme 3.1), with minor amounts of the trans-diketo conformer, which has much smaller dipole moment (1.41 D) than that of the former (~ 10.8 D).¹²⁴ However, in polar hydrogen bonding solvents, the intramolecular hydrogen bond is perturbed significantly because of formation of intermolecular hydrogen bond. Increased absorption in the lower energy region of the absorption spectrum as well as large Stokes shifts in both polar and hydrogen bonding solvents suggest that both polarity and intermolecular hydrogen bonding perturb the intramolecular hydrogen bond existing in the cis-enol conformer.^{115,117} Therefore, the results presented in this work regarding the dynamics of the excited states of curcumin in alcoholic solvents describe the dynamics of specific interaction between the solute's electronic state and the solvent via intermolecular hydrogen bonding, which is accompanied by the reorganization of the hydrogen-bonding network structure of the alcoholic solvent. Berg and coworkers established the fact the solvent dynamics affecting the hydrogen bond reorganization time of the solvent is well correlated with the dielectric relaxation time or the longitudinal dielectric relaxation time, τ_L .^{155,156} Several groups of workers reported non-exponential solvation dynamics in n-alcohols.^{148,149, 153, 157-159} The short component observed in n-alcohols is shorter than τ_L , and is assigned to solvent restructuring in the proximity of the excited solute molecule.¹⁵⁹ Solvent restructuring is associated with the internal, like hydroxyl rotations, of solvent molecules rather than reorientation and can be described as formation of intermolecular hydrogen bond between the excited molecule and the solvent. The long component of the correlation function has its origin in the reorganization of the solvent hydrogen bond network structure to reach equilibrium. Matsumoto and Gubbins simulated the average lifetime for the first breaking or formation of the hydrogen bond in methanol is 0.9 ps,

whereas the autocorrelation time of hydrogen bond, which measures the time for reorganization of the solvent hydrogen bond network structure is 11.8 ps.¹⁶⁰ This value is comparable to the value of τ_L of methanol (9.2 ps).^{153,167} Based on these arguments, the ultrafast component (τ_1) determined in alcoholic solvents (e.g. the lifetimes of 1.5 ps and 3 ps in the case of methanol and ethanol, respectively) using transient absorption technique can be assigned to the inertial motion of the solvent molecule involving rotation of the hydroxyl group, which is directly involved in interaction with the ketonic group of curcumin leading to formation of intermolecular hydrogen bond. Further, the longest component of the solvent relaxation time (in the present case, this time is given by τ_2 in Table 3.2) can be assigned to the reorganization of the solvent hydrogen bond network structure. This has been correlated with the longitudinal relaxation time (τ_L) of the solvent by equations 2 and 3,^{155,156}

$$\tau_2 = A (\tau_L) \exp(\Delta H / RT) \quad (2)$$

$$\ln(\tau_2) = \ln(\tau_L) + \ln(A) + \Delta H / RT \quad (3)$$

If we assume that the enthalpy of the transition state, ΔH , does not vary significantly due to change of solvents belonging to the same class, e.g. primary alcohols, we expect a linear correlation between $\ln(\tau_2)$ and $\ln(\tau_L)$ (equation 3). As shown in Figure 3.13A we find a reasonably good linear correlation between these two parameters in n-alcohols and reconfirm the postulation that the hydrogen bond reorganization around the excited solute molecule is responsible for the dynamics of the relaxation process of the S_1 state in the alcoholic solvents observed here. This correlation also confirms that this lifetime associated with the relaxation of the S_1 state of curcumin is the property of the pure solvent and not of the excited state of the solute. Additionally, this also justifies the assignment of τ_1 and τ_2 determined from the measurement at a single wavelength, i.e. at 480 nm to the solvation process.^{60,61} Determination of $C(t)$ from the results of transient absorption measurements has been impossible because of

overlapping of the transient ESA and SE bands. However, close agreement between the results obtained from the measurements in methanol, ethanol and EG using both the fluorescence and absorption techniques support our arguments. We observe that in the case of EG, the data point shows significant deviation from the best fit line. Considering the fact that EG is a dihydric alcohol, the structure of the hydrogen-bonded complex formed between curcumin and EG, is expected to be different from that formed with a normal alcohol.

3.3.2. Solvation dynamics in aprotic solvents: Figure 3.13A also includes the data for a few aprotic solvents for which the τ_L values are available and we find quite a good agreement between τ_2 and τ_L values of the solvents, as observed in the case of alcohols. This suggests that not only the specific hydrogen bonding interaction as discussed above in the case of protic solvents, but also the dielectric relaxation of the pure solvent play an important role in all kinds of solvents. Barbara and his coworkers made some novel measurements on the microscopic solvation dynamics of a couple of coumarin dyes or other probes, such as bianthryl, in several aprotic solvents as well as in methanol and 1-propanol.^{148,162,163} Experimentally, $C(t)$ (equation 1), was well represented by a single exponential in relatively less polar solvents, such as acetone but by a double exponential function in polar solvents.⁴⁸ Therefore, in polar solvents, $C(t)$ was fitted biexponentially to obtain two time constants (τ_a and τ_b) and the average solvation time, $\langle\tau\rangle_{\text{solv}} = a_1\tau_a + a_2\tau_b$ (where a_1 and a_2 are the corresponding amplitudes), was found to be very similar to that predicted by dielectric continuum theory.¹⁶⁵⁻¹⁶⁷ Horng et. al also explored the intramolecular charge transfer (ICT) dynamics in a donor substituted acridinium dye in a variety of solvents and the lifetime of the charge transfer process was correlated to the average solvation time, $\langle\tau\rangle_{\text{coum}}$, which was measured with the solvation probe coumarin 153.^{154,168} Solvation times of C153 were employed because they represented the best measures of the time scales of polar solvation available these days.

We have calculated $\langle\tau\rangle_{\text{solv}}$ in the polar solvents studied here using the relative amplitudes, a_1 and a_2 , associated with τ_1 and τ_2 , respectively, which represent the double exponential growth of transient absorption measured at 480 nm (Table 3.2). Our discussion on the dynamics of the S_1 state of curcumin in the alcoholic solvents clearly reveals that τ_1 and τ_2 are correlated with the bimodal solvation process. We also consider the fact that in less polar solvents, the solvation process can be well represented by a single exponential response of the solvent.¹⁴⁹ Therefore, the ultrafast component, τ_1 , determined in nonpolar aprotic solvents, has been assigned to the lifetime of IVR process, τ_v (Table 3.2), and τ_2 is approximated to the average solvation time, $\langle\tau\rangle_{\text{solv}}$. In polar solvents, τ_1 has been assigned to the inertial component of the solvent response because of close similarity of its value with that determined earlier in the corresponding solvent.^{139,143} In Figure 3.13B, we have plotted $\ln(\langle\tau\rangle_{\text{solv}})$ vs $\ln(\langle\tau\rangle_{\text{coulm}})$ and the solid line in this plot is the fit of the data collected in all kinds of solvents to follow the relation: $\ln(\langle\tau\rangle_{\text{solv}}) = 0.13 + 0.99 \ln(\langle\tau\rangle_{\text{coulm}})$. The near unity slope of the best fit line suggests the close similarities in the values of the average solvation time determined by us and those determined earlier to establish its correlation with the dielectric relaxation behavior of the pure solvent predicted by the dielectric continuum model.^{163–168} Near unity slope of the line also suggests that the ICT process, which is responsible for the increase in dipole moment of the excited state ($\Delta\mu \sim 6.1$ D), is nearly barrierless in all kinds of solvents because of strong coupling between the local excited (LE) state and the ICT kind of S_1 state of curcumin.^{155,163,164} As a consequence of this, separation of emission into the spectra of LE and ICT states has not been possible.

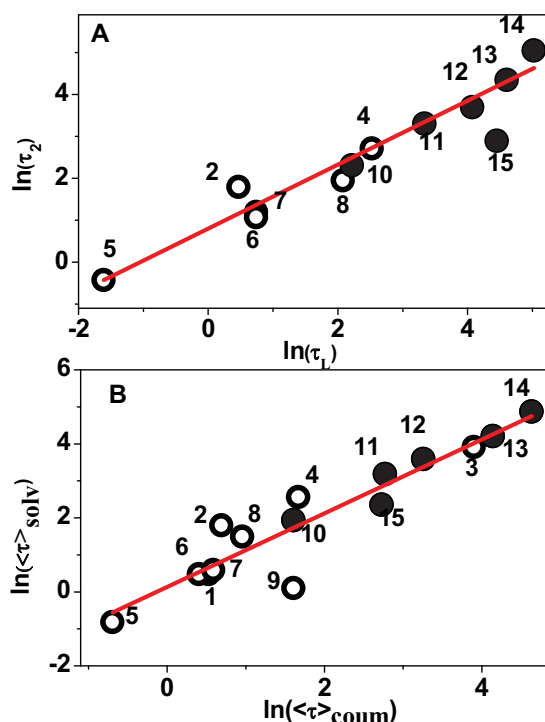


Figure 3.13. **A.** Correlation between $\ln(\tau_2)$ with $\ln(\tau_L)$ of the solvents. The best-fit line, which represents the function: $\ln(\tau_2) = 0.81 + 0.76 \tau_L$ (Adj. R2 = 0.96, N=10), does not include the data point for ethylene glycol. **B.** Correlation between $\ln(\tau_2)$ with $\ln(\langle\tau\rangle_{\text{avg}})$ of the solvents. The best fit line represents the function: $\ln\langle\tau\rangle_{\text{solv}} = 0.81 + 0.99 \langle\tau\rangle_{\text{coum}}$ (Adj. R2 = 0.86, N =15), The solvents are: 1,4-dioxane (1), EA(2), TA(3), BN (4), acetonitrile (5), DMF(6), DMSO(7), PC(8), formamide(9), methanol (10), ethanol (11), 1-propanol (12), 1-butanol (13), 1-pentanol (14), and ethylene glycol (15).

3.3.3. Deactivation of the S_1 State: Following the completion of the solvent reorganization process, the relaxed and solvated S_1 state decay to the ground electronic state by both radiative and nonradiative processes. Earlier single photon counting technique, having time resolution of about 40 ps, has been successfully used to determine the lifetime of the S_1 state in varieties of solvents.^{115,117} Fluorescence decay has been fitted with either monoexponential or biexponential functions. The lifetime obtained by monoexponential fitting or the shorter and major component in the case of multiexponential fitting has been assigned to the cis-enol form and the longer components with much smaller (a few percent) amplitude has been assigned to the other conformers.

The lifetime, τ_3 , given in Table 3.2, is assigned to the decay lifetime of the S_1 state of the cis-enol form in fifteen solvents. Since we have not been able to measure the lifetime

longer than 500 ps and the longer decay components of transient absorption may have the contribution from the triplet state too, we will not comment on those, which are assigned to the other conformers. However, the lifetime of the trans-diketo conformer has been seen to be less than 500 ps in a few solvents, say 1,4-dioxane and methanol and given in Table 3.2.

The values of τ_3 measured in 1,4-dioxane is very short (44 ps) and this value agrees well with that (~ 55 ps) reported in another nonpolar solvent cyclohexane.^{115,117} The shortest lifetime and the largest nonradiative rate ($\sim 15 \times 10^9 \text{ s}^{-1}$) in nonpolar solvent, in which the intramolecular hydrogen bond remains undisturbed by the solvent effect, was assigned to the ESIHT process.^{115,117} However, in more polar solvents, say EA, TA, BN, acetonitrile and PC, this lifetime becomes longer (230 – 300 ps), because of the fact that the intramolecular hydrogen bond is perturbed by the dipole-dipole interaction.^{37, 169} This hypothesis can be complemented by the reduced rate of the nonradiative process ($\sim 2.5 \times 10^9 \text{ s}^{-1}$).^{115, 117} Similar values of lifetimes in TA, PC and acetonitrile clearly reveal the lack of viscosity dependence on the lifetime of the S_1 state of the cis-enol form. This excludes the possibility of occurrence of any kind of configurational relaxation in the excited state. However, the lifetimes are shorter in DMSO (175 ps) and DMF (155 ps) and the shortest (45 ps) in formamide. These three can be considered as strong hydrogen bond accepting solvents (having large β -values, Table 3.2),¹⁴⁸ which possibly disrupt the intramolecular hydrogen bond and form intermolecular hydrogen bond not only with the enolic hydrogen, but also with the phenolic hydrogens. These multiple number of intermolecular hydrogen bonds induce efficient nonradiative deactivation pathways via hydrogen stretching vibrations.^{170, 171} One should note that in spite of the β -value of formamide being lower than those of DMSO and DMF, the decay lifetime of curcumin in formamide is shorter than those measured in the other two solvents. However, it should also be considered that both the E_T^N value (which is a measure of both polarity and hydrogen bonding ability of the solvent) as well as the α -value (~ 0.71 , which is a measure of hydrogen bond

donating ability of the solvent) of formamide are very large and these values ensure stronger hydrogen bonding interaction between the S_1 state and formamide.¹⁴⁸ This explains the shortest lifetime of the S_1 state of curcumin in this solvent.

In the case of normal alcohols, τ_3 increases steadily from methanol to 1-pentanol. Because of both the hydrogen bond accepting and the donating properties of the alcohols, the solvent molecules are expected to be involved in formation of hydrogen bonds not only at the phenolic and the enolic hydrogen atoms, but also with the ketonic oxygen atom, which acquire large negative charge due to intramolecular charge transfer in the excited state. Strength of the hydrogen bond between the ketonic oxygen and the alcohol molecule has been shown to become stronger with increase in negative charge on the oxygen atom.¹⁷² We have seen in the case of aprotic solvents that viscosity has no effect on the lifetime of the S_1 state of the cis-enol form. Therefore, although we find the monotonous increase of τ_3 with increase in viscosity of the normal alcohols, this viscosity dependence cannot be explained by occurrence of configurational relaxation of the excited state. However, the hydrogen bonding ability of the normal alcohols, given by the E_T^N value (Table 3.2), too varies monotonically. The E_T^N value decreases from methanol to 1-pentanol and the value of τ_3 increases with the decrease in the E_T^N value of the alcohol. This trend can only be explained by the fact that weaker hydrogen bonding interaction between the solvent and curcumin reduces the efficiency of the norradiative deactivation mechanism. This argument is also supported by the fact that τ_3 in EG has the value similar to that determined in methanol, in spite of its much higher viscosity than that of methanol and even that of 1-pentanol (Table 3.2). The E_T^N value of EG is very close to that of methanol.

3.3.4. Why Did Not We Observe the ESIHT Process?: The role of the ESIHT process in the deactivation mechanism of the S_1 state of curcumin has repeatedly been emphasized.^{115,}

¹¹⁷ Photoinduced ESIHT has been the subject of detailed investigations in several kinds of

molecules, which have an hydrogen bonded chelate ring as the reaction center but an asymmetric potential energy surface (PES), using different kinds of ultrafast spectroscopic techniques.¹³⁸⁻¹⁴⁵ For all these kinds of molecules, a time scale of a few hundred femtosecond has been assigned to the ESIHT process, and so far, no deuterium effect has been observed in dedicated investigations.^{138,141}

Harris and co-workers reported the first investigation of the fast ESIPT reaction in 3-hydroxy flavone (3HF) using sub-picosecond time-resolved stimulated emission and transient absorption spectroscopic technique and determined the ESIPT time to be 240 fs in a nonpolar solvent, methylcyclohexane (MCH).¹⁴¹ In hydrogen-bonding environments, the ESPT (not ESIPT) rate changed drastically and two distinct ESPT channels were observed in methanol solution. The fast ESPT for 3HF in MeOH took place in ≤ 125 fs and another slow component had a lifetime of about 10 ps, which agreed well with the longitudinal relaxation time of this solvent (Table 3.2) and hence could be related to solvent reorganization process. The faster ESPT time in MeOH solution has been explained by consideration of a 3HF-MeOH cyclically H-bonded 1:1 complex. The ESPT reaction coordinate in this aggregate comprises new modes resulting from hydrogen motion between the 3HF and the solvent molecules. The fast ESPT mechanism for the monosolvated 3HF could involve dual proton transfer. Lifetime of the double proton transfer reaction in 7-azaindole dimer in solution has been determined to be about 1.1 ps.^{146,147}

Lochbrunner and coworkers used the ultrafast UV pump – visible probe and Elsaesser and coworkers used the ultrafast UV pump – IR probe transient absorption spectroscopic techniques to study the ESIPT of 2-(2'-hydroxyphenyl)-benzothiazole (HBT) dissolved in nonpolar solvents to demonstrate that the intrinsic ESIHT is complete within 170 fs.^{138,139} In 2-(2'-hydroxyphenyl)benzoxazole (HBO) too, the ESIPT reaction occurs in 170 fs and is independent of solvent or isotope.¹⁴¹

From the results of fluorescence upconversion experiments on curcumin, the component with the lifetime of about 130 ps in chloroform and 100 ps determined in methanol and EG were assigned by Adhikary et. al. to the ESIHT reaction.¹¹⁹ This component corresponds to that assigned to τ_3 in this work. However, we discussed earlier in section 1 of this article that the cis-enol conformer is a symmetric molecule with respect to the intramolecular hydrogen bonded chelate centre. In this case, the ESIHT process should be characterized by a symmetrical double-minimum potential energy surface.^{37,169} Since the product of the ESIHT reaction is not different from the reactant molecule, the ultrafast spectroscopic techniques adopted here can obviously not monitor the progress of the ESIPT process in real time. In addition, the ESIHT process should be reversible in curcumin because of low barrier between two symmetrical double minimum potential wells for hydrogen atom transfer reaction, which have been calculated earlier for molecules containing similar kind of hydrogen-bonded chelate centres.^{37,169} Considering these arguments, our interpretation is at odds with the conclusions drawn by Adhikary et. al. and the component, τ_3 , which has values varying in the range of about 40 ps to a few hundred picoseconds in different kinds of solvents, cannot be assigned to the ESIHT process. However, the presence of the six-membered hydrogen bonded chelate ring, which is very similar to the that present in the ESIPT molecules described above, the occurrence of ESIPT is an obvious process in the S_1 state of curcumin in nonpolar aprotic solvent and this reaction is expected to be complete within a few hundred femtosecond.¹³⁸⁻¹⁴¹ Since the reaction is reversible because of low energy barrier between the reactant and the product, the excited state may be described as two rapidly interconverting structures III and IV. The very efficient nonradiative relaxation of the S_1 state of curcumin in nonpolar solvents is the obvious manifestation of the process of interconversion by the ESIHT reaction.

However, in protic solvents, the intramolecular hydrogen bond is perturbed or broken, but intermolecular hydrogen bond is formed during the process of hydrogen bond reorganization (also called the specific interaction via intermolecular hydrogen bonding). The hydrogen stretching vibration in this intermolecular hydrogen bond provides another efficient channel for nonradiative relaxation of the S_1 state.^{170,171} However, we have observed an ultrafast component with lifetime of about 0.3 ps in methanol and we have assigned this component to vibrational relaxation process keeping an analogy to a similar component observed in aprotic solvents (Table 3.2). We are not sure whether this component can be assigned to the excited state (intermolecular) hydrogen atom transfer or ESHT reaction, similar to that observed in the case of 3HF in alcohols. However, we have not been able to resolve this component in other alcohols.

3.4. Conclusion

Dynamics of the excited singlet (S_1) state of curcumin has been investigated in detail in various solvents using subpicosecond time-resolved fluorescence and absorption spectroscopic techniques. Since curcumin exists mainly as a cis-enol conformer in the ground state, the dynamics of the excited singlet (S_1) state of curcumin described above can be assigned to this form. This conformer is characterized by a strong intramolecular hydrogen-bonding, which induces a strong nonradiative deactivation mechanism leading to shorter lifetime of this form as compared to those of other conformers. Additionally, because of the planar structure of this conformer, the S_1 state possesses a strong intramolecular charge transfer character and the dynamics of this state is dominated by the solvation process, which is multimodal and follows nonexponential dynamics. A good correlation between the long component of solvation with the longitudinal relaxation time of the alcoholic solvents justifies its assignment to the hydrogen bond reorganization in the solvent hydrogen bond network structure and hence specific hydrogen bonding interaction between the S_1 state of curcumin and the solvent.

However, we also find a good correlation between the average solvation time determined in this work in all kinds of solvents and that determined using a coumarin probe, which has already been proved to be a good marker for the dielectric continuum model, suggests that dielectric relaxation of the pure solvent also have an important contribution in the solvation process. Although because of the presence of intramolecular hydrogen bond in the cis-enol conformer, the ESIHT is an obvious process in the excited state, two spectroscopic techniques applied here do not allow us to monitor it in real time. However, its signature is clearly evident in the shorter lifetime of the S_1 state in nonpolar aprotic solvents, in which the intramolecular hydrogen bond remains nearly unperturbed. In polar solvents the intramolecular hydrogen bond is disturbed leading to the reduced efficiency of the noradiative deactivation mechanism. However, in protic solvents, intermolecular hydrogen bonding interaction between curcumin and solvent provides another efficient channel for nonradiative deactivation mechanism of the S_1 state.

Chapter 4

Ultrafast Dynamics of Excited State Intramolecular Proton Coupled Charge Transfer Reaction

4.1 Introduction

Electron transfer and Proton transfer are the two most fundamental processes, ubiquitous in chemistry and biology. Photoinduced charge transfer and proton transfer processes in model molecular systems has been a major focus to understand the basic molecular mechanism of electron and proton transfer reactions.¹⁷³⁻¹⁷⁶ Excited state intramolecular proton transfer (ESIPT) studies in various model systems have revealed ultrafast timescale of the intramolecular proton transfer reactions.^{35,37,177-181} Large amplitude structural relaxation has been found to follow the proton transfer process of many model systems.¹⁸²⁻¹⁸⁵ Presence of strong charge transfer character in ESIPT molecules, charge transfer and proton transfer has appeared to be strongly coupled. Proton coupled electron transfer reactions have emerged as a concerted mechanism to govern the many biological and chemical reactions.^{4,186,187} Thus, the issue of coupled charge and proton transfer has been an intense research focus in recent years and a significant development has been achieved.^{39,188-193} In strong intramolecular charge transfer molecules, twisted intramolecular charge transfer (TICT) has been established^{58,71,73,75} to be general phenomena, in which donor and acceptor moieties relax to perpendicular geometry in the charge transfer excited state to facilitate complete charge separation via orbital decoupling of the donor and acceptor group. Thus, in strong donor-acceptor substituted ESIPT molecules, proton transfer, charge transfer and structural relaxation are expected to be strongly coupled and observed photodynamics will be controlled by all these processes. In present

chapter, we describe the ESIPT directed structural relaxation dynamics in an unsymmetrically substituted charge transfer 1,3-diketone molecule, namely N,N-dimethylanilino-1,3-diketone (DMADK, Figure 4.1). Because of *unsymmetrical* structure, the molecule can exist in two possible cis-enol forms (Figure 4.1) which may interconvert via intramolecular proton transfer reaction and may allow probing the ESIPT reaction. Unlike the conventional ESIPT molecules (where the proton transferred keto tautomeric form possess very high energy in ground state), the two possible cis-keto-enol forms of a 1, 3-diketone may coexist in the ground state.¹⁹⁴ Photophysical behavior of this system is expected to be governed by the relative energies of the two tautomers in the excited state. Consequently, the direction of the proton transfer process will be dictated by the energetic preference of one of the tautomer in the excited state. Moreover, due to strong charge transfer character of the molecule, solvent polarity may strongly influence the kinetics and thermodynamics of excited state processes. In this chapter, we present the effect of polarity of the solvents on the dynamics of the excited states of DMADK using steady state as well as sub-picosecond time-resolved absorption and fluorescence spectroscopic techniques. Quantum chemical calculations have been performed to determine the structure and energetic of these tautomers in the S_1 state. We show that the solvent polarity controlled energetic preference of the tautomeric forms dictate the direction of proton transfer and subsequent charge transfer dynamics in the charge transfer excited state.

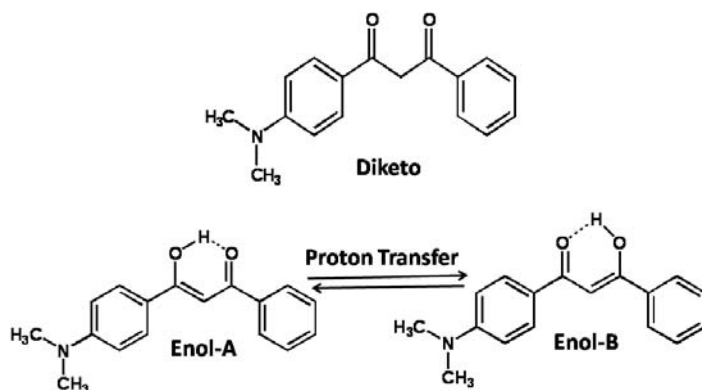


Figure 4.1. Structure of DMADK in diketo- and two cis-enol (Enol-A and Enol-B) tautomeric forms.

Condon excited state population of both the tautomeric forms. Thus, the photophysical properties and relaxation dynamics of the molecule will depend on the structure and energy of the two tautomers in their first electronic excited state. Steady state and time resolved spectroscopic experiments in conjunction with the TDDFT calculated structure and energy has been presented and discussed for the concise understanding of photodynamics of the DMADK molecule.

4.2.2. Steady state photophysical studies: Figure 4.3 (A and B) presents the steady state absorption and emission spectra of DMADK recorded in aprotic solvents of varying polarities at room temperature. The lowest energy absorption band in the 350-450 nm region has a large molar extinction coefficient ($\epsilon_{\text{max}} \sim 4.5 \times 10^4 \text{ dm}^3 \text{ mol}^{-1} \text{ cm}^{-1}$ in acetonitrile) and is assigned to the $\pi\pi^*$ transition. Fluorescence spectrum of DMADK recorded in each of these solvents at room temperature, except in cyclohexane, is broad and structureless. Both the absorption and fluorescence maxima undergo bathochromic shifts in solvents of larger polarities (Table 4.1).

In order to characterize the photophysical processes occurring in the excited state, we tried to correlate the energies corresponding to the absorption and fluorescence maxima as well as the Stokes shift with the solvent polarity parameter, $E_{\text{T}}(\text{N})$.¹⁴⁸ $E_{\text{T}}(\text{N})$ parameter is a measure of both the polarity as well as the hydrogen bonding ability of the solvent. We could find good linear correlations between these three photophysical parameters and $E_{\text{T}}(\text{N})$ values of the solvents (Insets of Figure 4.3). The strong polarity dependence of the absorption and fluorescence maxima of DMADK suggests the ICT character of the excited state and hence the large change in the dipole moment of the molecule following photoexcitation. The change in dipole moment, $\Delta\mu$ between the ground and the first excited singlet (S_1) states has been calculated using the Lippert-Mataga plot (i.e. the plot of Stokes shift ($\Delta\bar{\nu}$) vs ΔF) and has been determined to be ca 8.1 D (Figure 4.3C).

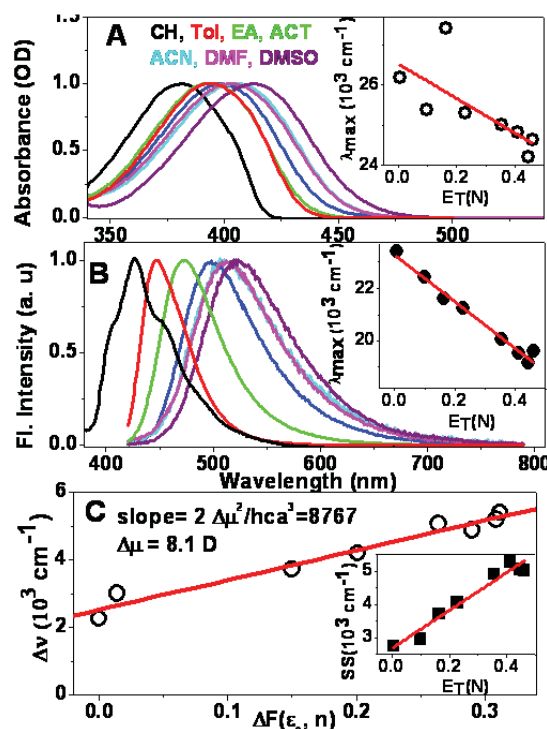


Figure 4.3. Normalized steady state absorption spectra (A), fluorescence spectra (B) and Lippert-Mataga Plot (C) in aprotic solvents. Insets shows the correlation of the absorption and fluorescence maxima and the Stokes shift (SS) with the solvent polarity parameter, $E_T(N)$.

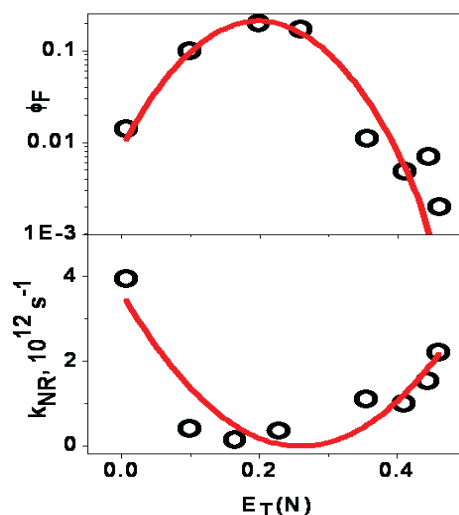


Figure 4.4. Solvent Polarity, $E_T(N)$, dependence of Φ_F and k_{NR} of DMADK. Solid lines (red colored) simply provide a guide to the eye and not any functional fit.

Fluorescence quantum yields (Φ_F) have been determined in a wide range of aprotic polar solvents. We also calculated the other photophysical parameters, namely the radiative and nonradiative rate constants (k_R and k_{NR} , respectively) (Table 4.1), using the values of the

Table 4.1. Solvent Dependence of the Photophysical Parameters of DMADK.

Solvents	$E_T(N)^a$, $\Delta F(\epsilon_0, n)^b$		Stokes shift, $\Delta\bar{\nu}$, cm^{-1}	Φ_F	τ_F , ps	k_R , 10^8 s^{-1}	k_{NR} , 10^{10} s^{-1}
Cyclohexane	0.006,	0.00	2759	0.014	25	5.6	3.9
Toluene	0.099,	0.02	2959	0.102	220	4.6	0.4
1,4-Dioxane	0.164,	0.03	3718	0.20	570	3.5	0.14
Ethylacetate	0.228,	0.40	4085	0.136	250	5.4	0.3
Acetone	0.355,	0.65	4920	0.011	90	1.2	1.1
Acetonitrile	0.46,	0.71	5023	0.002	45	4.4	2.2
Dimethylformamide	0.41,	0.67	5283	0.005	100	4.8	1.0
Dimethylsulfoxide	0.444,	0.66	5056	0.007	65	1.1	1.5
Methanol	0.762	0.71	5096	0.003	30	0.8	3.3
^a Ref. 40, ^b Ref. 195. $\Delta F(\epsilon_0, n) = [(\epsilon_0-1)/(\epsilon_0+2)] - [(n^2-1)/(n^2-2)]$.							

lifetimes of the S_1 state (τ_F) determined by the transient fluorescence and / or absorption experiments (vide infra). These parameters show very interesting solvent polarity dependence (Figure 4.4). In aprotic solvents of lower polarity region, Φ_F increases with increase in solvent polarity in the range of $E_T(N) = 0.0 - 0.2$, but the trend is reversed in the solvents of larger polarity and Φ_F reduces significantly in the polar aprotic solvents with $E_T(N)$ values larger than 0.2. The k_{NR} values show just a reverse trend as compared to that of Φ_F . Dramatic changes in the Φ_F and k_{NR} values clearly indicate some intricate changes in the structure and dynamics of the S_1 state with change in polarity.

4.3.3. Transient Absorption and Fluorescence Spectroscopic Studies:

4.3.3.1. Transient absorption studies in cyclohexane: Figure 4.5 presents the time-resolved differential transient absorption (TA) spectra of the excited states populated following photoexcitation of DMADK in cyclohexane solution at room temperature using 400 nm laser pulses of 50 fs duration. The TA spectrum recorded at 0.2 ps delay time consists of three ESA bands extending through the entire probe wavelength (470–1000 nm) region. In sub-0.5 ps

time domain, ESA bands in the 460-750 nm region decays but that in the 750- 950 nm region rises, leading to the appearance of a temporary isosbestic point at ca 750 nm. This suggests a precursor– successor relationship between two states. At longer time domain, all three ESA bands decay monotonously in the entire wavelength region.

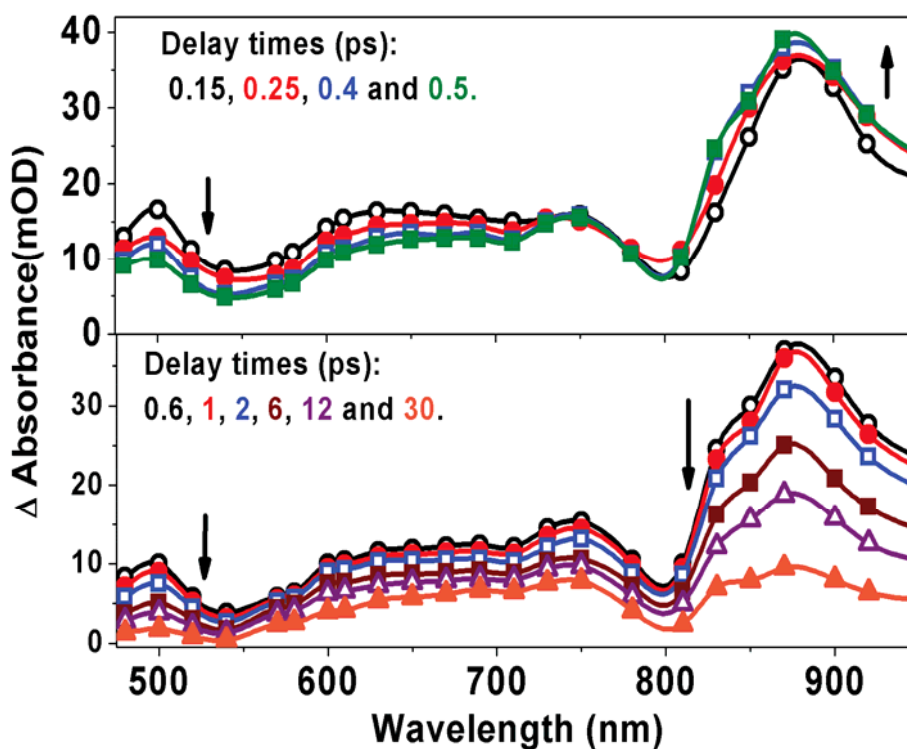


Figure 4.5. Time-resolved absorption spectra of the transient species formed following photoexcitation of DMADK in cyclohexane using 400 nm laser pulses. Delay times are given in the insets.

In Figure 4.6, we have presented the temporal profiles recorded at a few selective wavelengths following photoexcitation of DMADK in cyclohexane. Each of the temporal profiles recorded at different wavelengths in the entire wavelength region could be fitted using an exponential function consisting of three components, with the average lifetimes of about 0.18 ± 0.02 , 2.1 ± 0.4 and 22 ± 3 ps, along with another long-lived component, which appeared as residual absorption extending even beyond 100 ps delay time. The ultrafast component with the average lifetime of about 180 fs, is associated with the spectral evolution in the sub 0.5 ps time domain and we assign this component tentatively to the ‘excited state intramolecular proton transfer’

(ESIPT) process. On the other hand, the component with the average lifetime of about 22 ps can be assigned to the lowest excited singlet (S_1) state. The long lived residual absorption associated with each of the temporal profiles may be assigned to the T_1 state. The intermediate component of 2.1 ps may possibly be associated with the vibrational relaxation or some small amplitude intramolecular relaxation occurring in the S_1 state.

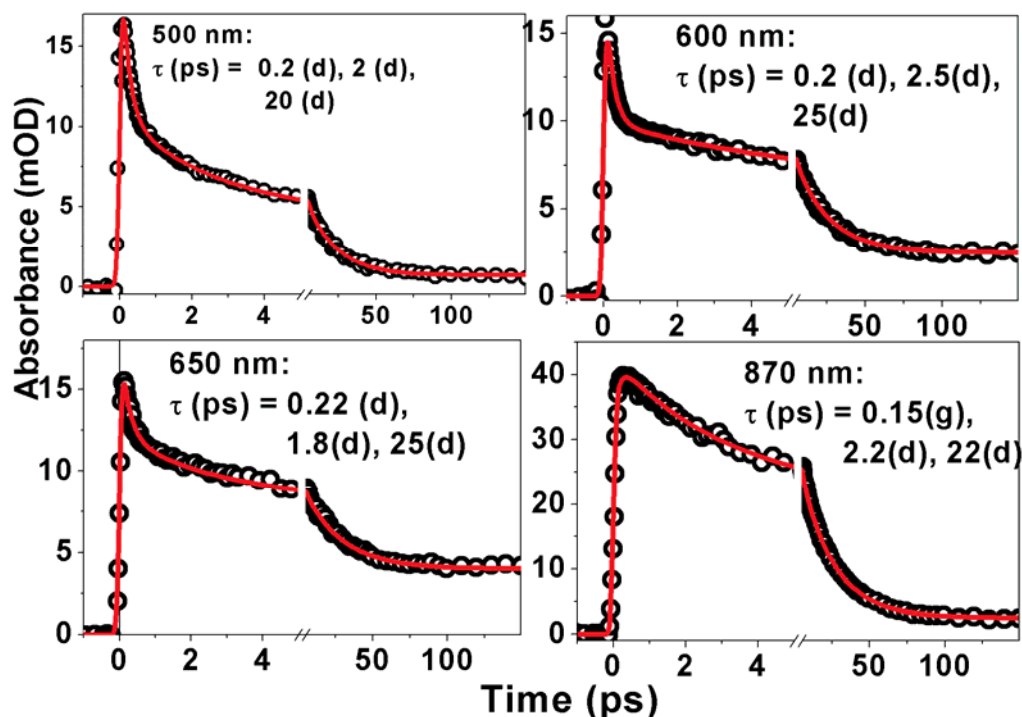


Figure 4.6. Temporal profiles (circles) recorded at a few selective wavelengths following photoexcitation of DMADK in cyclohexane using 400 nm light along with the best-fit multiexponential functions. Associated lifetimes are given in the insets. The temporal profiles recorded at 600 and 650 nm are also associated with a long-lived residual absorption, assigned to the T_1 state.

4.3.3.2 Transient fluorescence studies in cyclohexane: We also recorded the fluorescence decay profiles for DMADK in cyclohexane in the 430 – 580 nm region using fluorescence upconversion technique. In Figure 4.7, we have shown two typical fluorescence decay profiles recorded at 430 and 510 nm. Each of the fluorescence decay profiles is associated with an instrument response time limited rise (~ 160 fs) followed by a biexponential decay with the average lifetimes of about 3 and 25 ps. These values agree well with those measured using transient absorption spectroscopic technique.

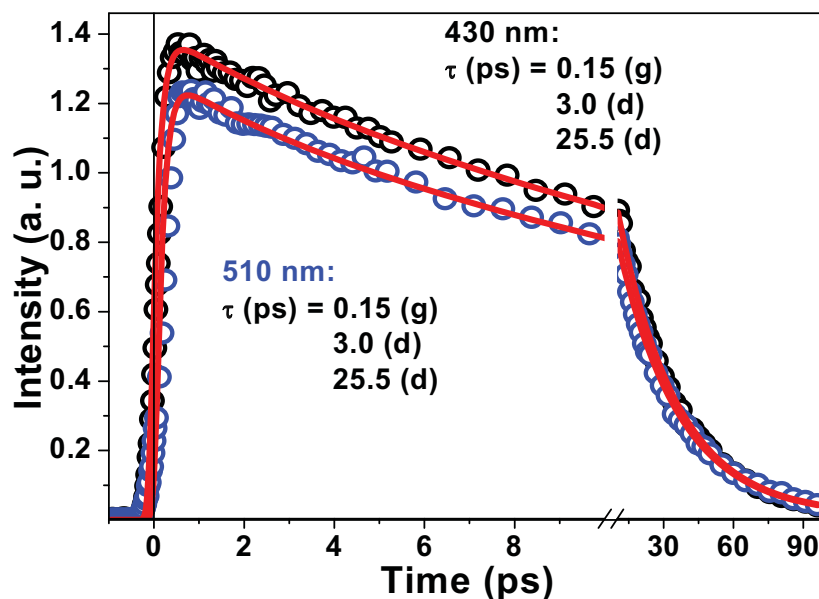


Figure 4.7. Fluorescence temporal profiles of DMADK in cyclohexane.

4.3.3.3 Transient absorption studies in toluene: Figure 4.8 shows the time-resolved TA spectra recorded in toluene. Important features of the time evolution of the TA spectra in the 0.6 ps time domain are the development of the SE band in the 480 - 550 nm region (SE band below 480 nm could not be recorded using our spectrometer) and the rise of the ESA bands in the 570 - 670 nm and 800 - 950 nm regions. We see the appearance of the temporary isosbestic point at ca 580 nm in sub-0.6 ps time domain. With further increase in delay time up to about 10 ps, only the SE band continues to grow, but all the ESA bands show little evolution. At longer delay time, both the SE and ESA bands decay monotonously.

In Figure 4.9, we have presented the temporal profiles recorded at three selective wavelengths, namely 480, 610 and 870 nm, to reveal the associated dynamics. Each of these temporal profiles could be fitted with a triexponential function and the lifetimes of the three rising and / or decay components thus obtained were seen nearly to be independent of wavelength. The average lifetimes could be determined as 0.4, 3.7 and 220 ps. In this case, the lifetime of the ultrafast component (~ 0.4 ps) is significantly longer than that of the ESIPT process determined in cyclohexane.

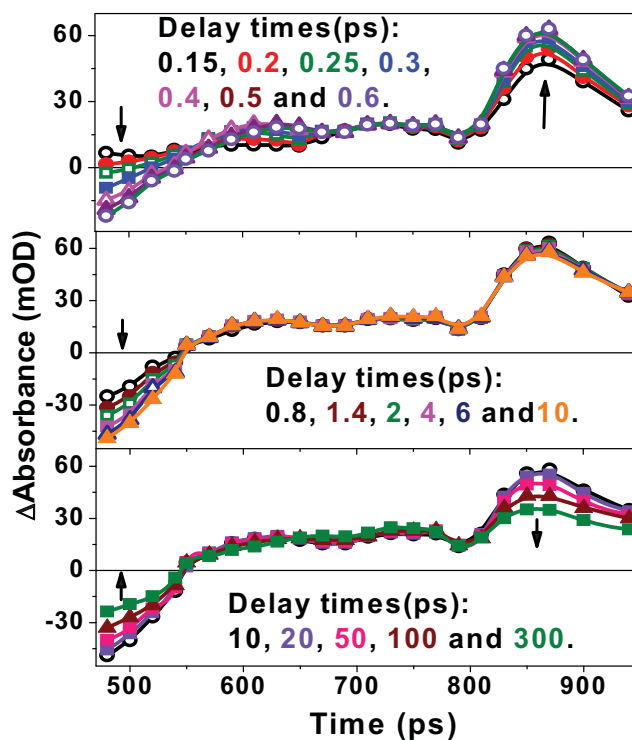
Reaction

Figure 4.8. Time-resolved TA spectra recorded in toluene following 400 nm photoexcitation.

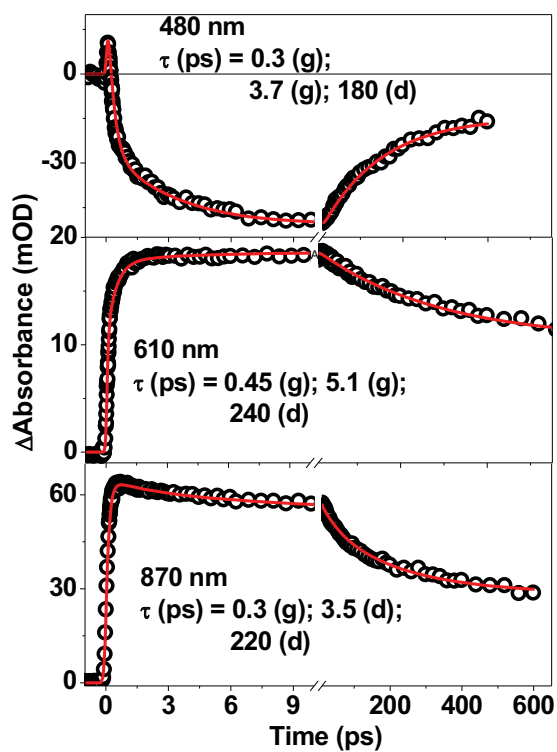


Figure 4.9. Temporal dynamics of transient absorption signal of DMADK in toluene recorded at a few selective wavelengths.

It is important to note that the following photoexcitation with 400 nm light, the the S_1 state is populated with an excess vibrational energy of about 1526 cm^{-1} . Therefore, both the vibrational as well as the ESIPT processes might have contributed to the time evolution of the transient spectra occurring in the early time domain (Figure 4.8) and the ultrafast component with the lifetime of 0.4 ps appears due to occurrence of both these process. In addition, the increase in intensity of the SE band up to about 10 ps with the lifetime of about 3.7 ps suggests the population of the structurally relaxed ICT state, which decays with the lifetime of about 220 ps.

4.3.3.4. Transient absorption studies in acetonitrile: Figure 4.10 presents the time-resolved differential TA spectra recorded following photoexcitation of DMADK in acetonitrile solution. The TA spectrum constructed for 0.15 ps delay-time shows the presence of a SE band in the 460 - 550 nm region with the maximum at ca. 510 nm and two excited-state absorption (ESA) bands in the 570 - 1000 nm region with the maxima at ca. 750 nm and at ca. 850 nm. With increase in delay time, the maximum of the SE band gradually shifts toward the lower energy region with a significant increase in intensity of the SE band. As a result of the time evolution of the TA spectra in sub-2 ps time domain, the SE band maxima shifts from 510 nm, observed at 0.15 ps, to ca. 590 nm at 2 ps delay time. Concurrent increase in intensity of the SE band as well as the dynamic red shift of the SE maximum suggest that the evolution of the initially populated local excited (LE) state is associated with not only the solvation process, but also some other relaxation processes occurring in the similar time domain. On further increase in delay time beyond 2 ps, the SE band as well as the ESA bands in the 750 - 900 nm region decays monotonously. Time dependence of the dynamic shift of the SE maximum has been shown in the inset of Figure 4.10.

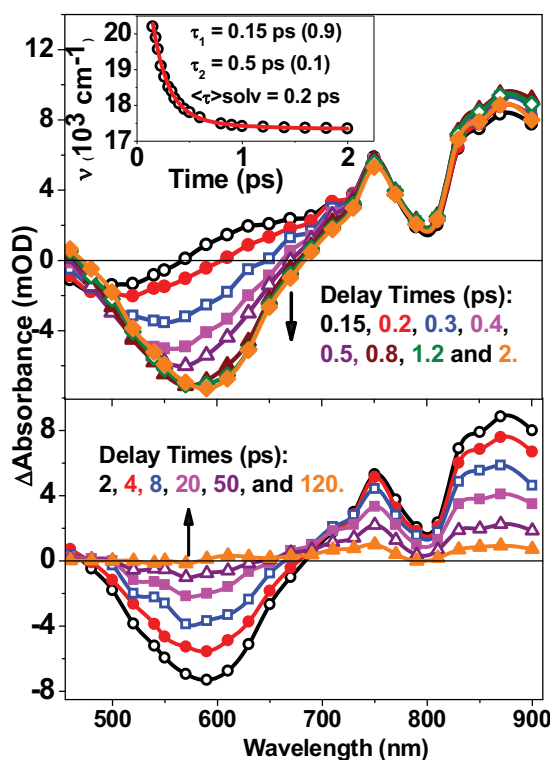
Reaction

Figure 4.10. Time-resolved TA spectra constructed following photo-excitation of DMADK in acetonitrile using 400 nm laser pulses. Inset shows the time-dependence of the dynamic red shift of stimulated emission maxima ($\bar{\nu}_p$) vs time.

Table 4.2. Time constants for the relaxation dynamics of DMADK measured in different solvents using transient absorption spectroscopic technique.

Solvents	Solvent parameter		Time constants			
	$\eta(\text{cP})^a$	$\langle\tau\rangle_{\text{solv}}^b, \text{ps}$	τ_1, ps	τ_2, ps	τ_3, ps	$\tau_4, \text{ps},$
cyclohexane	1.02	--	0.18		2.1	20
n-hexadecane	3.044	-	0.15		4.0	48
Toluene	0.59	2.5	0.4		3.7	220
1,4-dioxane	1.18	1.7	0.25		2.9	570
Ethyl acetate	0.43	2.0	0.2		2.4	250
Acetone	0.30	0.58	---	0.85	6.5	90
Acetonitrile	0.34	0.5	0.14	0.45	4.3	40
DMF	0.8	0.9	0.15	1.5	9	100
DMSO	1.99	1.8	0.19	1.9	13	65
PC	2.5	2.6	0.16	3.0	15	90

^aRef 40, ^bRef 46. τ_1 , τ_2 , τ_3 and τ_4 values are assigned to the lifetimes of the ESIPT, solvation, structural relaxation and the IC and / or ISC processes occurring in the S_1 state, respectively.

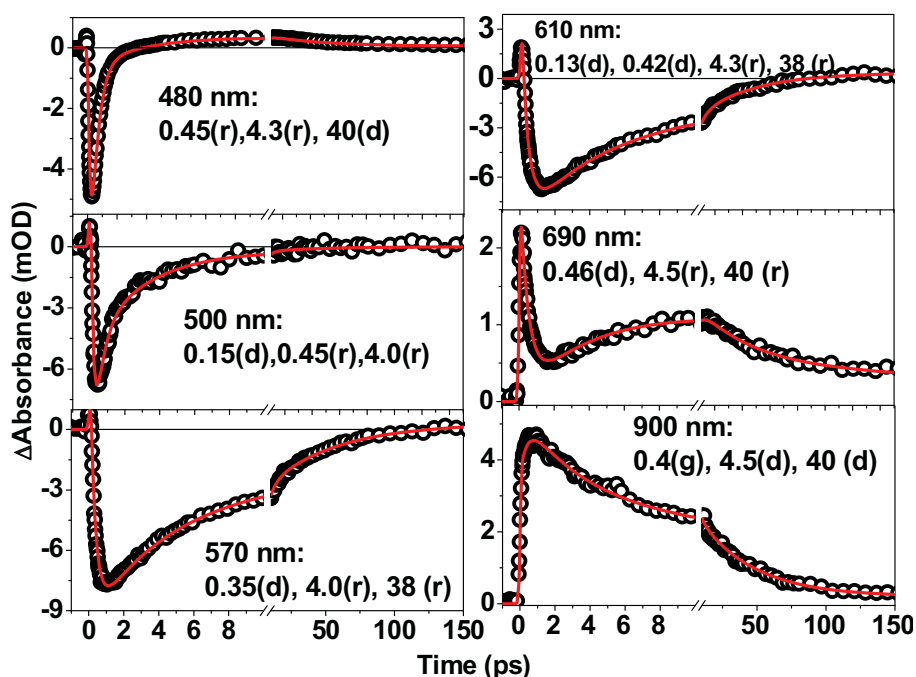


Figure 4.11. Temporal evolution of transient absorption monitored at different wavelengths following photo-excitation of DMADK in acetonitrile. Solid lines represent the best multi-exponential fit-functions. The lifetimes of the decay (d) and /or rising (r) components, thus determined, are given in the insets.

A few typical TA profiles, which have been recorded following photoexcitation of DMADK in acetonitrile, are shown in Figure 4.11 along with the best multi-exponential fit functions. Pattern of the wavelength dependence of the lifetimes associated with the time evolution of the SE band in the 460 – 650 nm region is the typical characteristics of the solvation process.²⁰⁶ Each of the temporal profiles recorded in the red edge region of the SE band (i.e. 610 – 650 nm region) is associated with a biexponential rise of SE with the lifetimes of about 0.15 and 0.42 ps. In addition, the time dependence of the dynamic shift of the SE maximum (Inset of Figure 4.10), could also be fitted with a biexponential function with the lifetimes of 0.15 ps (0.9) and 0.5ps (0.1) and the value of the average lifetime thus calculated is about 0.2 ps. This value is shorter than the average solvation time, $\langle\tau\rangle_{\text{solv}}$, determined earlier using other kinds of probes.²⁰⁶ These observations confirm the fact that in early timescale, TA spectral evolution (Figure 4.11) may be associated with ESIPT and / or vibrational relaxation, in addition to the

solvation process. The decay of the stimulated emission is biexponential with the average lifetime of about 4.3 and 40 ps. The ESA at 690 nm region also found to grow with 4.5 ps time constant followed by 40 ps decay lifetime. Similar ESA growth-decay behavior has also been observed at 480 nm. Thus, the 4.3 ps component can be tentatively assigned to an intermediate structural conformational relaxation followed by S_1 state decay with 40 ps lifetime. Structural relaxation to weakly emissive conformer may be responsible for the weak fluorescence yield, as observed in the steady state experiments in polar solvents.

To explore the effect of solvent polarity and viscosity, transient absorption studies have also been performed in several other polar aprotic solvents of varying viscosities. The time constants obtained from kinetic analysis are listed in the Table 4.2.

4.3.3.5 Transient fluorescence studies in acetonitrile: To gain better understanding about the excited state processes in polar solvents, we also performed the fluorescence upconversion experiments in acetonitrile. Temporal kinetics of the emission transients at different wavelengths are shown in Figure 4.12. Analysis of fluorescence transient kinetics revealed four component dynamics with time constants similar to that observed in transient absorption studies. Fluorescence upconversion signal at 460 nm reveals the instrument response time limited growth of emission, followed by triexponential decay. The ultrafast component with the lifetime of 0.17 ps is the major component and can be assigned to the ESIPT process. Tuning the monitoring wavelength towards the red region, the rise time of the fluorescence signal increases and the lifetimes of the components associated with the nonexponential decay of fluorescence also increases. These are the typical characteristics of solvation process in the blue edge (i.e. 460 – 520 nm) of the fluorescence spectra. However, the biexponential decay of the fluorescence signal at the red edge (i.e. 580 – 680 nm), following its rise with the lifetime of about 0.5 ps, suggest the consecutive population of two different kinds of excited states with the lifetimes of about 4.5 and 48 ps. This result agrees well with that obtained from the

transient absorption experiment. The component with the lifetime of 4.5 ps can be assigned to the structural relaxation to weakly emissive state following the ESIPT and solvation process. The nature of structural relaxation has been revealed from the quantum chemical calculation (See Section 4.3.4). Subsequently this relaxed state undergoes internal conversion (IC) to the S_0 state with 45 ps lifetime.

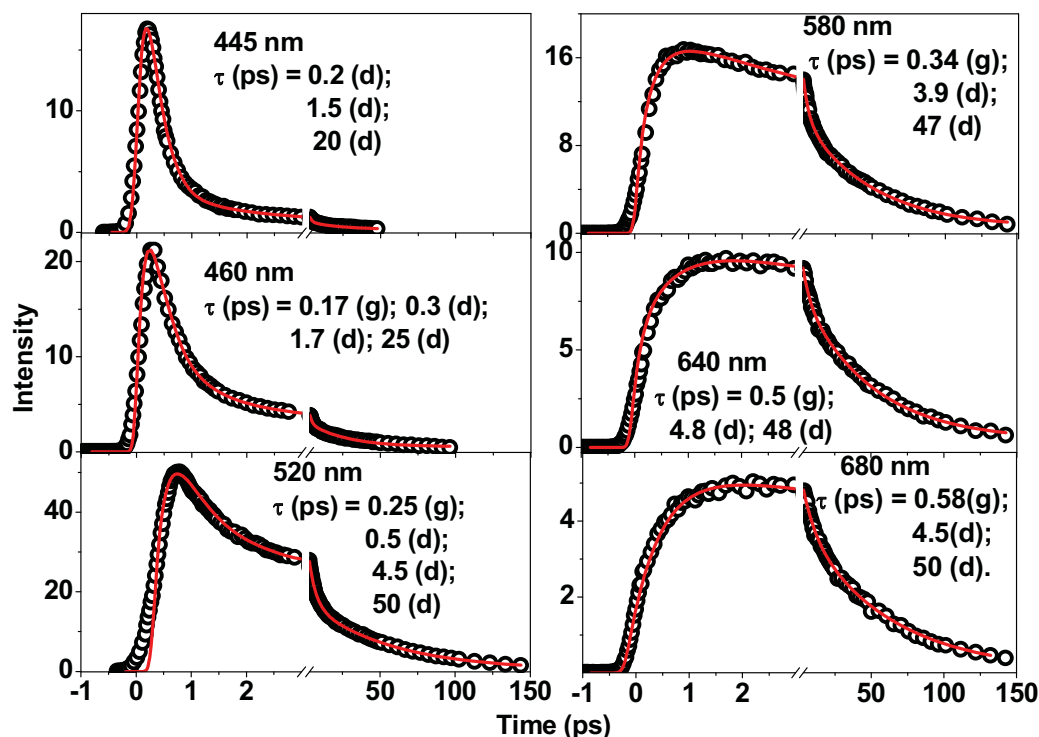


Figure 4.12. Fluorescence upconversion signals recorded at a few selective wavelengths along with the multi-exponential fit functions and the lifetimes associated with the different components given in the insets.

4.3.4 Excited State Calculations: In section 4.3.1, we have seen from DFT calculation that the DMADK molecule exist in both the tautomeric forms (Enol-A and Enol-B) with similar absorption characteristics, indicating simultaneous electronic excitation of both the structures. Here we describe the excited state geometry and energy calculations to understand the experimental results described in previous sections. To determine the relative energies of the two tautomeric species in the excited state, we first optimized their structures in the S_1 state using TDDFT method, which have been shown in Figure 4.13. S_1 state optimized

conformation of Enol-A differs little from the ground state conformation, whereas Enol-B takes perpendicular orientation of dimethylanilino group in S_1 state, characteristic of TICT state. We find that the energy level of the optimized structure or the relaxed S_1 state of Enol-A, which we designate here as $A^*(ICT)$, in the gas phase lies about $6.1 \text{ kcal mol}^{-1}$ lower as compared to that of Enol-B*, which is being designated here as $B^*(TICT)$ (Table 4.3). This implies that in non polar solvents the photophysics of DMADK will be governed by that of Enol-A*. Following photoexcitation of both the tautomers of DMADK in a nonpolar solvent, say cyclohexane, the $B^*(LE)$ state undergoes ESIPT reaction to populate $A^*(LE)$. Now we find that the calculated dipole moments of the energy optimized structure of Enol-A* or $A^*(ICT)$ state is larger than that of the $A^*(LE)$ state (Table 4.3) suggesting that the $A^*(LE)$ state undergoes the ICT process to attain the minimum energy configuration in the S_1 state. Table 4.3 reveals some differences in the geometrical parameters between the $A^*(LE)$ and the $A^*(ICT)$ state. For example, due to occurrence of this ICT process, the dihedral angle between the dimethylaniline group and the keto-enol chelate ring increases by about 10° and that between the phenyl ring and the keto-enol chelate ring decreases by about 10° . The phenyl group and the chelate ring get planarized in the $A^*(ICT)$ state and the twisting angle between the dimethylaniline group and the rest of the molecule is only about 20° . Therefore, it can be concluded that the $A^*(LE)$ state undergoes certain degrees of intramolecular structural relaxation to ICT state.

The effect of solvent polarity on the excited state energies of the two tautomers was calculated in DMSO using PCM solvation model (Table 4.3). It has been observed that the optimized structure of Enol-B* or $B^*(TICT)$ state is about $3.1 \text{ kcal mol}^{-1}$ more stable than the $A^*(ICT)$ state. This suggests that in polar solvents, the relative energies of the structurally relaxed two

tautomeric forms are reversed as compared to gas phase. Therefore, we predict that following photoexcitation of DMADK in a polar solution using 400 nm light, which populates the S_1 state of both the tautomers, $A^*(LE)$ state undergoes the ESIPT reaction in the S_1 state populating the $B^*(LE)$ state. Subsequently, the latter undergoes solvation and structural relaxation to populate the $B^*(TICT)$ state prior to deactivation to ground state. It is interesting to note that in $B^*(TICT)$ state, the dimethylaniline group is twisted by about 90° , with respect to the rest of the molecule. However, in the case of the $A^*(ICT)$ state, twisting angle is only about 20° . To understand this difference in structural relaxation characteristics, we calculated the potential energies of Enol-A and Enol-B at different twist angles of N, N-dimethylaniline group, which show that TICT is energetically favorable process in Enol-B but not in the case of Enol-A. This difference in the behavior of the excited states of two tautomers towards the structural relaxation possibly arises due to the different distances between the dimethylaniline group and the carbonyl group, which acts as the acceptor. In the case of Enol-B, the electronic coupling between the donor and the acceptor groups is strong enough to favor formation of the TICT state.

Table 4.3. Energies of the two enol tautomers in the ground (S_0) state and the first singlet excited (S_1) state in the gas phase and in polar solvent, DMSO. DFT/TDDFT calculations were performed using B3LYP functional and 6-31G (d,p) basis set. Calculations in DMSO were performed using polarizable continuum model (PCM).

Tautomeric Species	Gas phase			DMSO		
	S_0	$S_1(FC)$	$S_1(opt)$	S_0	$S_1(FC)$	$S_1(opt)$
Enol-A (Hartee)	-862.75381	-862.63040	-862.66171	-862.76520	-862.65085	-862.65805
Enol-B (Hartee)	-862.75367	-862.63001	-862.65185	-862.76492	-862.65184	-862.664132
$\Delta E(Enol-B - Enol-A)$ (kcal.mol ⁻¹)	0.08	0.01	6.1	0.007	-0.03	-3.8

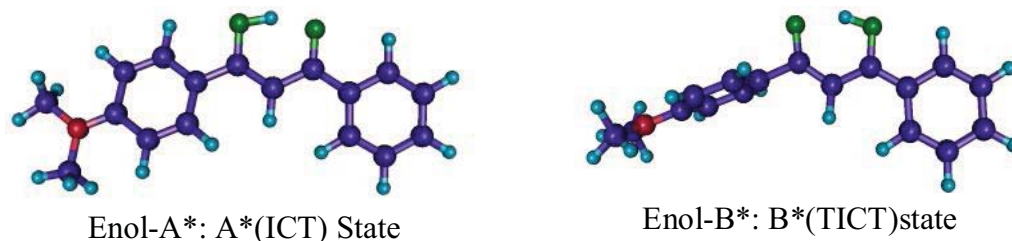


Figure 4.13. TDDFT optimized structures of Enol-A and Enol-B, in the S_1 states in the gas phase using B3LYP/6-31G(d,p) basis set.

4.3.5 Potential Energy Surface Diagram:

Solvent polarity dependent photophysical properties and excited state dynamics of the DMADK molecule described above can be explained by the simplified schematic potential energy surface (PES) diagram, as shown in Figure 4.14. DFT and TDDFT calculated geometry and corresponding energies in the ground state as well as S_1 excited state has been employed to construct the simplified PES diagram representing the excited state relaxation behavior of this molecule. As discussed in the earlier section that in the gas phase (or nonpolar solvents), the energy of the geometry optimized structure of the A*(ICT) state is the most stable one and its energy is lower by about 6 kcal.mole^{-1} as compared to that of the B*(ICT) state (Table 4.3). Thus the A*(ICT) state is responsible for the fluorescence emission in low polarity solvents. We predict that following photoexcitation to the S_1 state, the B*(LE) state undergoes ESIPT reaction to populate the A*(LE) state. Our transient absorption study in cyclohexane indeed revealed an ultrafast component of 100-200 fs, which could be attributed to the ESIPT process. Earlier studies on chemical systems having asymmetric intramolecular hydrogen bonded chelate centre and hence asymmetric potential energy surface (PES) for ESIPT reaction, have established the fact that the ESIPT process is ultrafast and occurs in the range of a hundred femtosecond.¹⁷⁷⁻¹⁸¹ Gil et. al. reported <100 fs timescale for the ESIPT process in a 1, 3-diketone compound, namely pyroxicam dye.¹⁹⁶

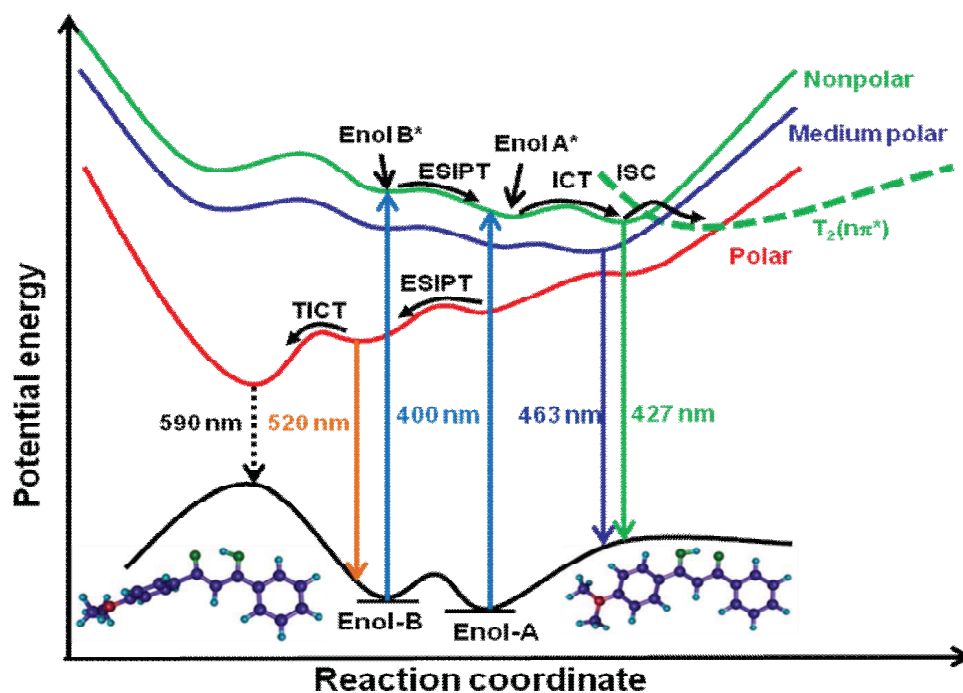


Figure 4.14. Oversimplified schematic potential energy surface (PES) diagram depicting the polarity tuning of the excited state dynamics of the S_1 state of DMADK.

Fluorescence quantum yield measurements have revealed that DMADK is weakly fluorescent in nonpolar solvent but increases significantly (by about 10 times) with increase in solvent polarity in the low polarity region (i.e. solvents with the $E_T(N)$ values in the range 0 – 0.2). Our TDDFT calculations reveal that in the gas phase (or nonpolar solvents) the $T_2(n\pi^*)$ state lies only about $0.6 \text{ kcal.mol}^{-1}$ above the $A^*(ICT)$ state and hence thermally accessible by the molecules populating the latter state. Therefore, the ISC process is expected to be quite efficient to drive the molecules to the triplet manifold and hence responsible for significantly low fluorescence quantum yield in nonpolar solvents. The large nonradiative rate ($k_{NR} \sim 3.9 \times 10^{10} \text{ s}^{-1}$) and observation of long lived residual absorption (or larger triplet yield) in transient absorption study in cyclohexane (Figure 4.3) support the prediction that ISC is important nonradiative deactivation pathway. With increase in solvent polarity in the low polarity region, the polar $A^*(ICT)$ state is preferentially stabilized over T_2 state, therefore ISC process becomes less important. This electronic effect causes the significant increase in the fluorescence

quantum yield as well as reduction in the k_{NR} values with increase in the solvent polarity in low polarity region. In highly polar solvents, the significant decrease in the fluorescence quantum yield and increase in k_{NR} has been explained by invoking nonradiative relaxation to a weakly emissive transient which is substantiated by both TDDFT calculation and transient absorption experiments. TDDFT calculations reveal that in highly polar solvents, the B*(TICT) state with the twisted dimethylaniline group is energetically more stable than the A*(ICT) state. This indicates that, in the solvents of larger polarity, the photophysical properties are governed by the properties of the excited state of Enol-B. The results of our transient absorption experiments reveal that occurrence of four different kinds of processes in large polarity solvents. The ultrafast component with the lifetime of <200 fs can be assigned to the ESIPT process corresponding to the conversion of the A*(LE) to the B*(LE) state. This means that the direction of the ESIPT reaction is reversed in polar solvents because of the reversal of the relative energies of the excited states of two tautomeric forms. However, the ultrafast time constant, τ_1 (Table 4.2), is likely to have contributions from the vibrational relaxation and / or inertial component of the solvation processes, which could not be resolved because of similar time scales of these processes. The lifetime of the second component (τ_2 in Table 4.2) is comparable to the average solvation time, $\langle\tau\rangle_{solv}$, in each of the solvents and hence is correlated with the solvation process. The latter has also been identified from the dynamic shift of the SE band maximum. Bimodal solvation behavior has been observed from the biexponential fit to the time-dependence curve of the dynamic shift of the SE maximum. It is interesting to note that the average solvation time determined from the bimodal solvent response is much shorter than the $\langle\tau\rangle_{solv}$ of the solvent.⁴⁶ This supports the prediction that the dynamic shift of the SE band in the ultrafast timescale has a contribution from the ESIPT process. The third dominant component (τ_3 in Table 4.2) has been assigned to the structural relaxation process via twisting of the dimethylaniline group. A linear correlation¹⁹⁷ has been

found between this rate constant and the viscosity of the polar solvents, confirming the occurrence of large amplitude conformational relaxation process to produce weakly emissive TICT state, followed by internal conversion to ground state in longer timescale (τ_4).

4.4 Conclusion

In this chapter, we have shown that the photophysical properties and the excited state relaxation behavior of DMADK are mainly governed by the relative energies of two cis-enol tautomers in the S_1 state. In low polarity solvents, the $A^*(ICT)$ state is thermodynamically more stable than that of $B^*(ICT)$ state and thus $A^*(ICT)$ state governs the properties of the S_1 state of DMADK. In nonpolar solvents, following photoexcitation of Enol-A and Enol-B to their first excited singlet state, Enol- $B^*(LE)$ state undergoes ultrafast ESIPT reaction to populate Enol- A^* state, followed by intramolecular relaxation to populate the $A^*(ICT)$ state prior to its decay via two parallel channels, namely IC to the S_0 state and ISC to the T_2 state. In solvents of medium polarity, stabilization of $A^*(ICT)$ state, compare to the T_2 state results in the decrease of intersystem crossing rate and thus fluorescence yield increases. On the other hand, in high polarity solvents, strongly polar Enol- $B^*(TICT)$ state is more stable than the $A^*(ICT)$ state in the S_1 state. Thus in polar solvents, excited state dynamics mainly governed by conformational relaxation towards weakly emissive $B^*(TICT)$ state which explains the strong quenching of fluorescence in polar solvent. The occurrence of twisting dynamics in polar solvents was confirmed by the viscosity dependence of the rate of the process assigned to the TICT process.

Chapter 5

Effect of Donor-Acceptor Conjugation on the Intramolecular Charge Transfer Relaxation Dynamics

5.1 Introduction

The photoinduced charge transfer or electron transfer process plays the fundamental role in light energy conversion e.g. photosynthesis in plants, artificial light harvesting systems and in numerous existing or conceived molecular photonic applications.¹⁹⁸⁻²⁰⁰ Donor acceptor substituted conjugated organic molecular systems undergo extensive charge transfer upon photoexcitation to the electronically excited state. The photoinduced charge transfer state may lead to quantitative charge separation by structural reorganization which is highly desirable for solar energy conversion. Thus, the fundamental understanding of the structure and dynamics of intramolecular charge transfer (ICT) process in the excited states has been of great interest and numerous donor acceptor substituted aromatic molecules (D-Ar-A) have been studied extensively.^{58,61-63,68-74} The concept of twisting relaxation in the excited state has mainly evolved from two different directions. The dual fluorescence of DMABN and related molecules led to the concept of twisted intramolecular charge transfer (TICT) where highly polar long wavelength emission is attributed to the dimethylamino (donor) twisted structure.⁵⁸ This twisted geometry allows maximum charge separation between the donor and acceptor

moiety due to the minimum orbital overlap.⁵⁸ On the other hand, the strong viscosity dependent fluorescence properties of several diphenyl and triphenylmethane dyes led to the concept of large amplitude structural relaxation to facilitate nonradiative deactivation of the excited state. Ultrafast spectroscopic measurements on these molecules revealed that twisting of dimethylanilino group generates nonemissive TICT excited state in picosecond timescale depending on the viscosity of the medium.^{61,68-72} Dimethylamino substituted aromatic ketone derivatives, such as 4-dimethylaminobenzophenone, michler's ketone also exhibit similar ultrafast twisting relaxation dynamics of dimethylanilino group.^{74,75,201} It is generally believed that large charge transfer upon photoexcitation drives the structural relaxation to TICT state in D-Ar-A molecules.⁵⁸ On the other hand, it has been established in many cases that high charge transfer state can be observed without TICT relaxation in D-Ar-A molecules.²⁰²⁻²⁰⁶ For example, 4, 4'-Dimethylaminocyanostilbene has been established to have planar ICT structure in excited state without any TICT relaxation.^{205,206} It is intuitive that the ICT dynamics via twisting relaxation will depend on relative energy of ICT and TICT states and intervening barrier height along the twisting coordinate. It is highly desirable to understand the structural effect on charge transfer dynamics facilitated by large amplitude twisting motion. In this chapter, we address this issue by comparing the spectroscopic properties and excited state dynamics of two isomeric 4-dimethylaminochalcones, DMAC-A and DMAC-B (Figure 5.1), where dimethylamino group and the carbonyl group act as donor and acceptor, respectively, but the two isomers differ in the relative positions of the carbonyl acceptor. This may have tremendous influence on the electronic properties due to alteration of conjugation between the donor and acceptor group. Photophysical properties of DMAC-B was reported earlier in connection with the lipid sensor activity due to prominent solvent polarity dependence of the fluorescence quantum yield.²⁰⁷⁻²¹¹ On the other hand, DMAC-A, which differs by the relative positioning of donor and acceptor group has not been studied so far. In this chapter, we show

that there is remarkable contrast in photophysical properties and excited state dynamics of these two isomeric dimethylaminochalcones. The comparison of the steady state and time resolved spectroscopic properties allow us to unravel the intricate role of donor-acceptor positioning on intramolecular charge transfer relaxation dynamics. Excited state structural optimization using time dependent density functional theory elucidates the geometrical consequence of the two isomers in the first excited singlet state to support the experimental observations.

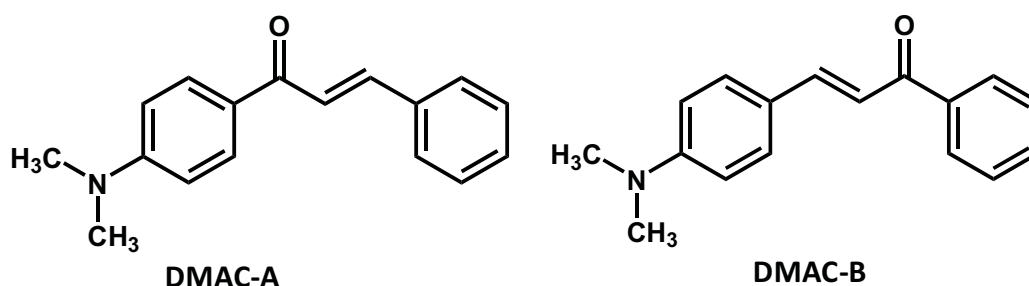


Figure 5.1. Structure of the two isomeric 4-dimethylaminochalcones.

5.2 Results and Discussion

5.2.1 Steady-state absorption and fluorescent studies: Steady state absorption and fluorescence spectra were recorded in different solvents of varying polarity. The absorption and fluorescence spectra of DMAC-A and DMAC-B in different solvents are shown in Figure 5.2 and Figure 5.3, respectively. The absorption spectra of DMAC-A show strong band in 350 -480 nm region and undergo significant bathochromic shift in polar solvents indicating charge transfer character of the Franck-Condon excited state. DMAC-B also shows similar solvent dependent shift of absorption spectra revealing the charge transfer nature of the excited state. It is important to point out that in any given solvent, DMAC-B shows red shifted absorption spectrum compare to that of DMAC-A. This suggests the extended donor-acceptor conjugation in the former case results to larger mesomeric stabilization to the charge transfer state.

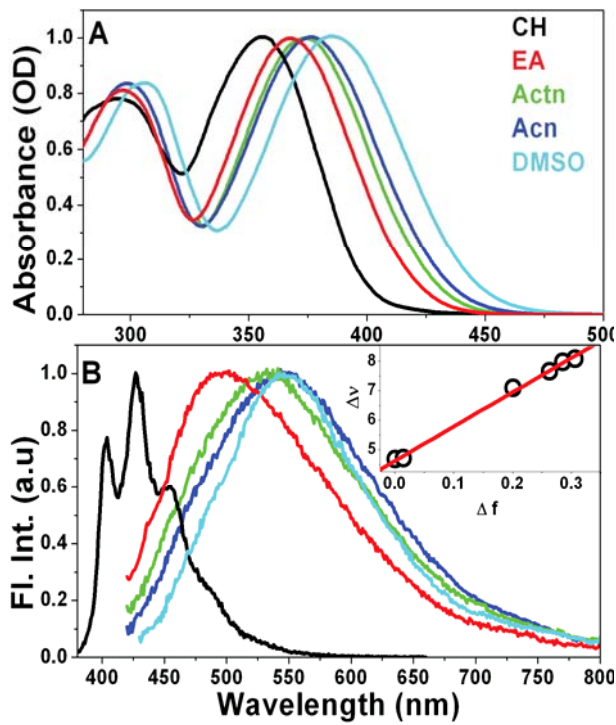


Figure 5.2. Steady-state absorption (A) and fluorescence (B) spectra of DMAC-A in different solvents. Inset shows Lippert-Mataga plot to calculate the change in dipole moment in the excited state.

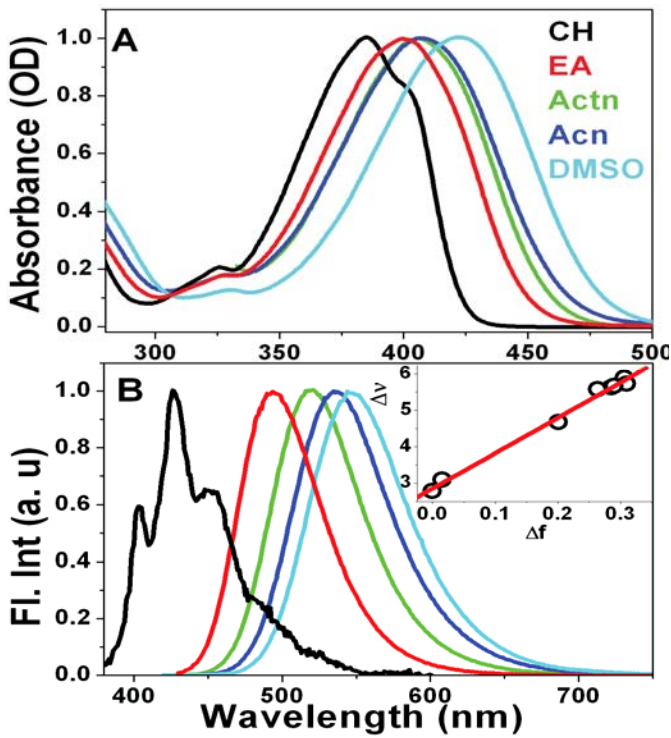


Figure 5.3. Steady-state absorption (A) and fluorescence (B) spectra of DMAC-B in different solvents. Inset shows Lippert-Mataga plot to determine the change in dipole moment in the excited state.

Steady state fluorescence spectra of both the compounds undergo large bathochromic shift (ca. 125 nm) on changing the solvent from nonpolar cyclohexane to polar DMSO. Systematic increase in fluorescence Stokes shift with solvent polarity clearly indicate strong charge transfer character of the excited states of both the compounds. Significant charge transfer upon photoexcitation is expected due to conjugated donor-acceptor structure of the molecules. Indeed, large increase in dipole moments ($\Delta \mu = 11.9$ D and 11 D for DMAC-A and DMAC-B, respectively) has been calculated from the Lippert-Mataga plots (insets of Figure 5.2B and 5.3B).¹¹ Thus, lowest singlet excited state is characterized by large intramolecular charge transfer (ICT). Quantitative measurement of fluorescence yield shows astonishing results. DMAC-A is weakly fluorescent in all solvents and the measured quantum yield decreases with polarity of the aprotic solvents. In high polarity solvents, fluorescence is extremely weak ($\Phi_f < 10^{-3}$, see Table 5.1). In contrast, DMAC-B fluorescence yield increases with polarity of the aprotic solvents and fluorescence yield is as high as 0.2 in high polarity solvents. Thus in polar aprotic solvents, emission yield of DMAC-A is more than two order of magnitude less than that of DMAC-B, even though, their emissive excited state is of similar intramolecular charge transfer character. Weak fluorescence of DMAC-A strongly suggests some unique ultrafast nonradiative relaxation towards a nonemissive state. Another intriguing observation is the difference in emission band widths of the two compounds (Table 5.1). In polar solvents, fluorescence spectra of DMAC-A is much broader (FWHM > 5000 cm⁻¹) compared to that of DMAC-B (FWHM ~ 2550 cm⁻¹). Such a low fluorescence yield and broad fluorescence spectra are characteristics of excited state reaction. On the other hand, narrow fluorescence spectrum of DMAC-B is a well characteristic of common structurally rigid solvatochromic fluorescence probes. These observations strongly suggest an excited state structural relaxation in DMAC-A which is absent in DMAC-B.

5.2.2 Time resolved fluorescence measurements: Fluorescence lifetime of DMAC-A was observed to be much shorter than instrumental resolution of TCSPC set up (<50 ps) and thus could not be measured by single photon counting. Fluorescence lifetimes of DMAC-B in polar solvents were longer and were measured by TCSPC technique (Figure 5.4B). On the other hand, short fluorescence lifetime of DMAC-A was measured by fluorescence upconversion technique (Figure 5.4A). The measured lifetimes are given in Table 5.1. It can be easily noted that in polar solvents, emissive excited state of DMAC-A is much shorter lived than DMAC-B. This is in accordance with the fluorescence quantum yield values of the two compounds. Using experimentally measured fluorescence lifetime and quantum yield, the radiative and nonradiative rate constants in different solvents were calculated which have been provided in Table 5.1. Radiative rate constants of the two compounds in different solvents have been found to be similar ($\sim 1.5 \times 10^8 \text{ s}^{-1}$), whereas the nonradiative rate constants differ more than two orders of magnitude. Large nonradiative decay rate ($> 10^{11} \text{ s}^{-1}$), low fluorescence yield and ultrashort fluorescence lifetime of DMAC-A is indicative of ultrafast nonradiative deactivation. To decipher the true character of excited state dynamics, femtosecond transient absorption spectroscopic measurements were performed as described in next section.

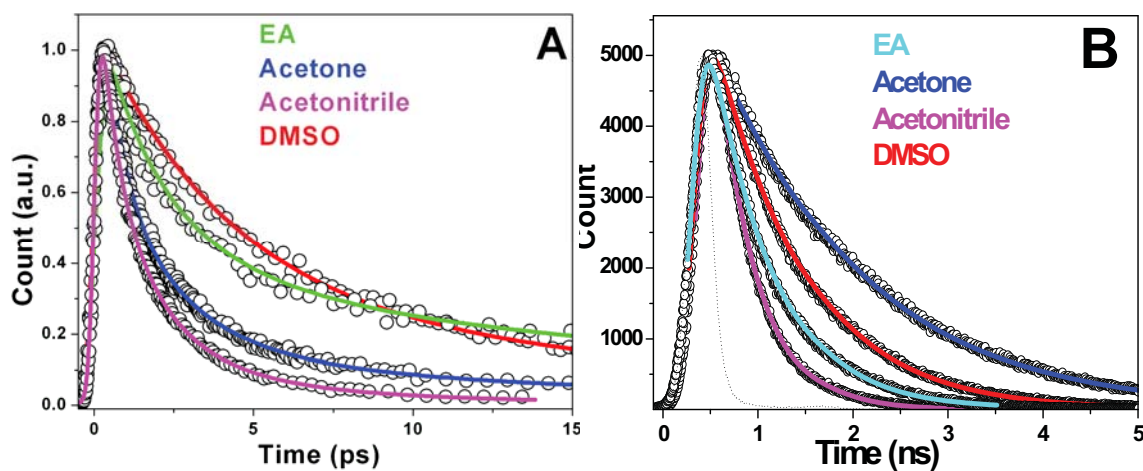


Figure 5.4. Fluorescence decays of DMAC-A measured by fluorescence upconversion (A) and of DMAC-B measured by TCSPC technique (B).

Table 5.1. Photophysical parameters of DMAC-A and DMAC-B in different aprotic solvents.

Solvents	DMAC-A					DMAC-B				
	Fl. band width FWHM cm ⁻¹	Quantum yield (Φ) (10 ⁻²)	Lifetime τ (ps)	k _r x10 ⁸ (s ⁻¹)	k _{nr} x10 ¹¹ (s ⁻¹)	Fl. band width FWHM Cm ⁻¹	Quantum yield (Φ) (10 ⁻²)	Lifetime τ (ps)	k _r x10 ⁸ (s ⁻¹)	k _{nr} x10 ⁹ (s ⁻¹)
Cyclohexane	3480	1.2	8.0	9	1.25	3400	0.22	5.2	4.2	192
Ethyl acetate	5789	0.16	3.1	5	3.2	2580	7.7	600	1.2	1.54
Acetone	5739	0.097	2.4	5	4.1	2560	19.6	1400	1.4	0.56
ACN	5780	0.046	1.4	3.5	7.1	2554	10	380	2.6	2.34
DMSO	5644	0.276	4.1	6.5	2.4	2544	13.9	880	1.6	0.97

5.3.3 Transient absorption studies of DMAC-A in polar solvents: Figure 5.5A shows the transient spectral evolution of DMAC-A in acetonitrile, following 400 nm photoexcitation. The main feature of spectral evolution is as follows: In first 0.5 ps timescale, the excited state

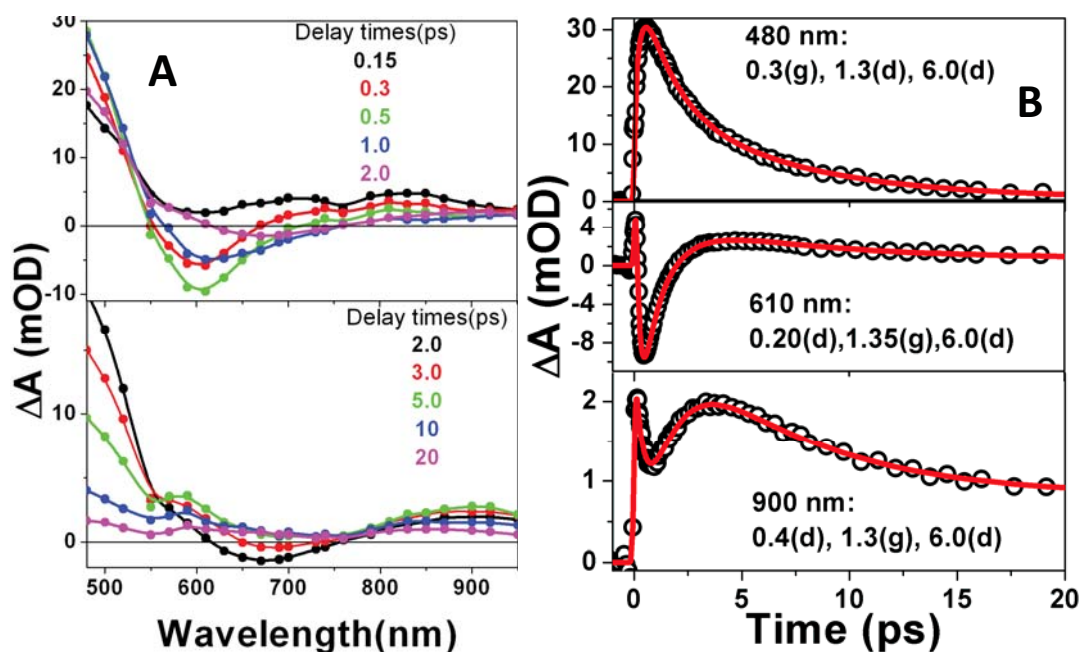


Figure 5.5. Femtosecond transient spectral evolution (A) and temporal decay behavior (B) at different probe wavelength of DMAC-A in acetonitrile. Lifetimes (in ps) from mutiexponential fitting are given in inset.

absorption band in 550-700 nm region decays and appears as stimulated emission band. During this time delay, strong ESA in 500 nm region grows in intensity whereas weak ESA decays in 800-900 nm region. On further increase in delay time, stimulated emission band decays up to 5 ps and appear as ESA band at 590 nm. ESA band in 800-900 nm region also grows marginally whereas 500 region band decays in this timescale. Upon further delay, ESA band in the entire spectral region decays up to 20 ps to produce long lived residual transients. Spectral evolution of the transient absorption spectra indicates the involvement of four different transients during the course of the excited state relaxation. Initial evolution of ESA spectra to form SE band indicates vibrational relaxation and solvation of the FC excited state to the ICT emissive state. Decay of this stimulated emission band within 5 ps timescale indicate that the

ICT state undergoes ultrafast nonradiative relaxation to a nonemissive excited state which deactivates to ground state in longer time scale. This ultrafast nonradiative relaxation may be ascribed to the twisting of dimethylanilino group leading to the formation of nonemissive TICT state. Such an ultrafast TICT relaxation is already established in dimethylaminobenzophenone derivatives. Kinetic analysis of the temporal profiles in selective wavelengths provides the timescale of the different processes described above (Figure 5.5B). Temporal profiles at different wavelengths were fitted with three decay or growth component with an additional long component corresponding to long lived residual absorption. The first component can be assigned to the solvation and vibrational relaxation to generate the planar ICT emissive state, which decays to the non emissive TICT state with a lifetime of 1.35 ps. This relaxed TICT state decays back to ground state with a lifetime of 6 ps in acetonitrile.

5.3.4 Effect of solvent viscosity on TICT dynamics of DMAC-A: One of the important characteristics of TICT relaxation is the strong viscosity dependence of the relaxation time due to the large amplitude twisting motion. A linear correlation of relaxation rate with solvent viscosity is considered as a direct probe for the large amplitude structural relaxation.⁷¹⁻⁷⁵ In addition, formation of TICT state is associated with the large charge transfer due to near quantitative charge separation at the twisted geometry. As a result, solvent polarity can also significantly influence the relaxation time. To study the effect of solvent polarity and viscosity, we measured the temporal dynamics of DMAC-A in different solvents and the time constants derived from multiexponential fit functions of temporal decays in various solvents are given in Table 5.2. Figure 5.6 shows the temporal dynamics in acetonitrile, DMF and acetonitrile-DMF (1:1 mixture) (isopolar solvents with different viscosity) at 590 nm. Comparison of twisting time in these solvents clearly shows that τ_2 linearly increase with the viscosity which confirms occurrence of large amplitude structural relaxation.

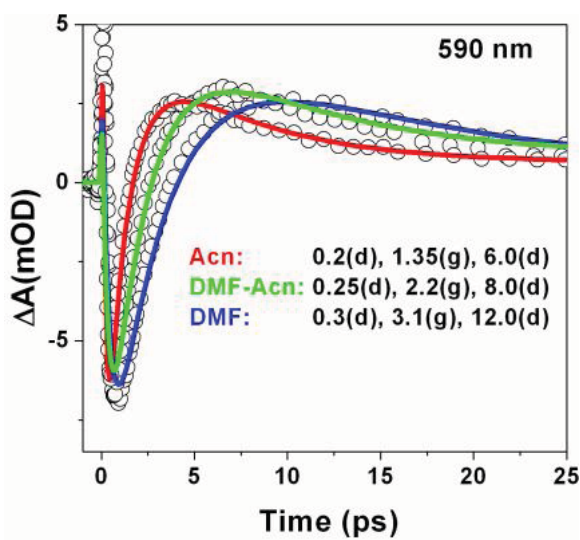


Figure 5.6. Effect of solvent viscosity on the twisting dynamics of DMAC-A. Lifetimes in respective solvents are given in the inset.

On the other hand, a clear dependence on solvent polarity is also apparent in isoviscous solvents of varying polarities, e.g ethylacetate, acetone and acetonitrile (Table 5.2). Increase in twisting rate with solvent polarity indicates polarity induced barrier reduction along the TICT coordinate. Because of larger polarity of the TICT state as compared to planar ICT state, barrier along the twisting coordinate is diminished on increase in solvent polarity. In case of higher viscosity solvent DMSO ($\eta= 1.99$), the twisting time is longer than acetonitrile or dimethylformamide, but viscosity effect is not much prominent due to larger polarity of DMSO. Thus time resolved transient absorption studies clearly establish TICT relaxation of DMAC-A in polar solvents.

Table 5.2. Average time constants of the relaxation dynamics of DMAC-A in different solvents of varying polarities and viscosities.

Solvent	ϵ_0 ,	$\eta(\text{cp})$	τ_1 (ps)	τ_2 (ps)	τ_3 (ps)
EA	6.0,	0.4	1.4	3.1	22
Acetone	20.0	0.35	0.7	2.4	9.5
Acn	35.5	0.44	0.4	1.35	6
Acn-dmf(1:1)	36.0	0.58	0.65	2.3	8.2
DMF	36.5	0.82	0.9	3.2	11
DMSO	46.5	1.99	1.9	4.2	12

τ_1 is solvation time. τ_2 represent the twisting time and τ_3 is the lifetime of the TICT state.

5.3.5 Transient absorption studies of DMAC-B in polar solvents: High fluorescence quantum yield and long fluorescence lifetime (measure by TCSPC) already indicated that nonradiative relaxation via large amplitude structural relaxation is possibly unimportant for the excited state dynamics of DMAC-B. To further investigate the early time dynamics of DMAC-B photoexcited state, transient absorption studies were performed in different aprotic solvents. Figure 5.5A shows the spectral evolution of DMAC-B in acetonitrile following 400 nm photoexcitation. TA spectra at 0.15 ps is characterized by weak SE band at 480-580 nm region and an ESA band in 600-750 nm region. With increase in delay time, the SE band grows in intensity up to 2 ps, along with significant red shift of the emission maxima. During this period, ESA band appears below 500 nm. At 2 ps, the TA spectrum is characterized by a strong stimulated emission band at 550 nm, corresponding to the steady state emission maxima. Thus, the spectral evolution in the first 2 ps component indicates formation of relaxed emissive excited state by vibrational relaxation and solvation process. Spectral evolution up to 30 ps show small growth of the SE band in 500-550 nm region and decay of SE band in the red.

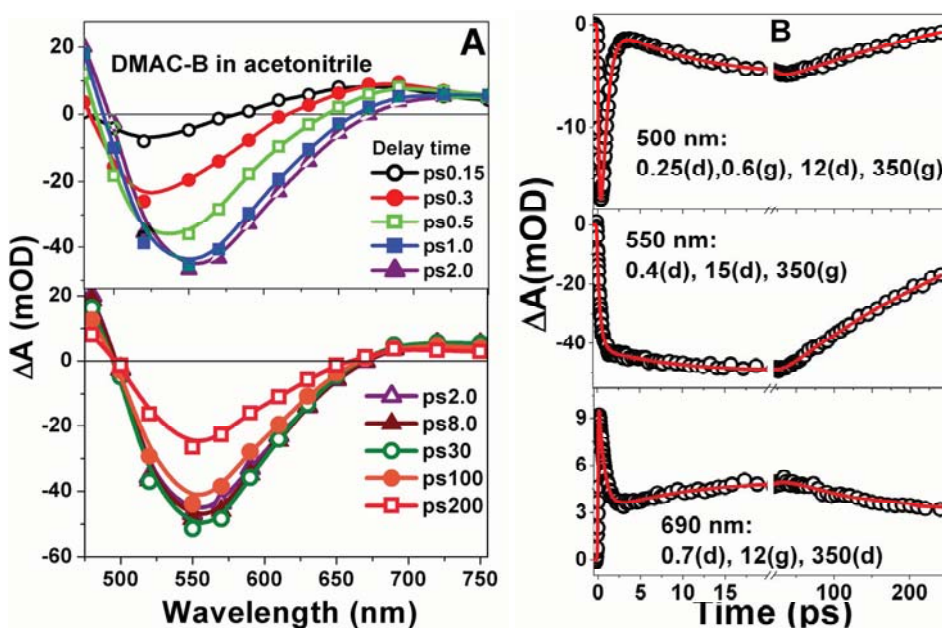


Figure 5.7. Femtosecond transient spectral evolution of DMAC-B in acetonitrile (A) and the temporal decay behavior at different probe wavelength (B). Lifetimes (in ps) are given in inset of Figure B.

During this delay period, significant growth of ESA band in 690-750 nm was also observed. Due to very small amplitude, these spectral evolutions were not very evident, but can easily be understood from the temporal profiles shown in Figure 5.5B. In longer timescale, the ESA and SE band in the entire spectral region decays towards zero indicating deactivation of S_1 state back to the ground state. Temporal analysis of the kinetic profiles presented in Figure 5.5B reveals mainly three component dynamics. An ultrafast component with a time constant of 0.4-0.7 ps (wavelength dependent) appears either as decay of SE in blue region or growth in the red region. Similar time constant appears in 690-730 nm region as decay of ESA. Spectral evolution of stimulated emission band and the time constant of the process essentially indicate solvation dynamics. An intermediate component of 13 ps appears in the entire spectral region followed by the decay of ESA or SE band with 350 ps lifetime. It can be noted that this long component (ca. 350 ps) nicely matches with the fluorescence lifetime of DMAC-B in acetonitrile measured by TCSPS technique and thus represent lifetime of the emissive singlet state. The intermediate component is possibly associated with some intramolecular relaxation to generate thermally relaxed S_1 (ICT) state.

We also studied the temporal kinetics of DMAC-B in other solvents such as ethyl acetate, acetone, DMF and DMSO and lifetime of different components are given in Table 5.3. The transient decay behavior is similar in all solvents but the time constants vary significantly. The first component corresponding to growth of stimulated emission is close to solvation time of the respective solvents. The intermediate component is associated to the relaxation of ICT state as emissive ICT state is long lived (>300 ps). Unlike in DMAC-A, the intermediate component in DMAC-B is almost independent of solvent viscosity. Absence of viscosity dependence of this component indicates that large amplitude twisting relaxation is not involved in the dynamics of DMAC-B excited state; rather some wagging motion including bond reorganization may be associated to produce relaxed ICT state. Absence of large amplitude

nonradiative relaxation to nonemissive state is in conformity with the long fluorescence lifetime and large emission quantum yield.

Table 5.3. Average time constants of the relaxation dynamics of DMAC-B in different solvents.

Solvent	ϵ_0 ,	$\eta(\text{cp})$	τ_1	τ_2	τ_3
EA	6.0,	0.4	2.0	12	600
Acetone	20.0	0.35	1.3	10	1400
Acetonitrile	35.5	0.44	0.6	13	350
DMF	36.5	0.82	1.5	13	900
DMSO	46.5	1.99	1.9	11	800
τ_1 correlates to solvation time. τ_2 represents relaxation of ICT state and τ_3 is the singlet lifetime.					

5.3.6 Transient absorption studies in cyclohexane: In earlier section, we have shown excited state dynamics of DMAC-A and DMAC-B is largely different, which is responsible for remarkable difference in fluorescence lifetime and quantum yield in polar solvents. However, in nonpolar cyclohexane both the compounds are weakly fluorescent which indicate strong nonradiative deactivation of emissive excited state of both the compounds in cyclohexane. To understand the deactivation mechanism, we have recorded the time resolved transient spectra of both the molecules in cyclohexane. TA spectra of both the molecules are characterized by the growth of long lived ESA. The TA spectral evolution of DMAC-B is shown in Figure 5.8 along with temporal kinetics in few selected wavelengths. TA spectral evolution shows that growth of long lived ESA in 500- 750 nm range is accompanied by the decay of ESA below 490 nm with a temporal isosbestic point at 490 nm. This clearly suggests ultrafast conversion of initial excited state to a long lived transient leading to the deactivation of singlet state within 25 ps. Long lived transient indicates the triplet character of the relaxed state. Thus, the deactivation mechanism of DMAC-B in cyclohexane can be assigned to the ultrafast intersystem crossing, which is responsible for weak fluorescence. Kinetic analyses of the temporal profiles yield 5 ps time constant of the ISC process. An additional short component

(0.25-0.4 ps) observed in 480-530 nm regions which can be tentatively ascribed to the vibrational relaxation in the singlet state prior to deactivation to triplet state.

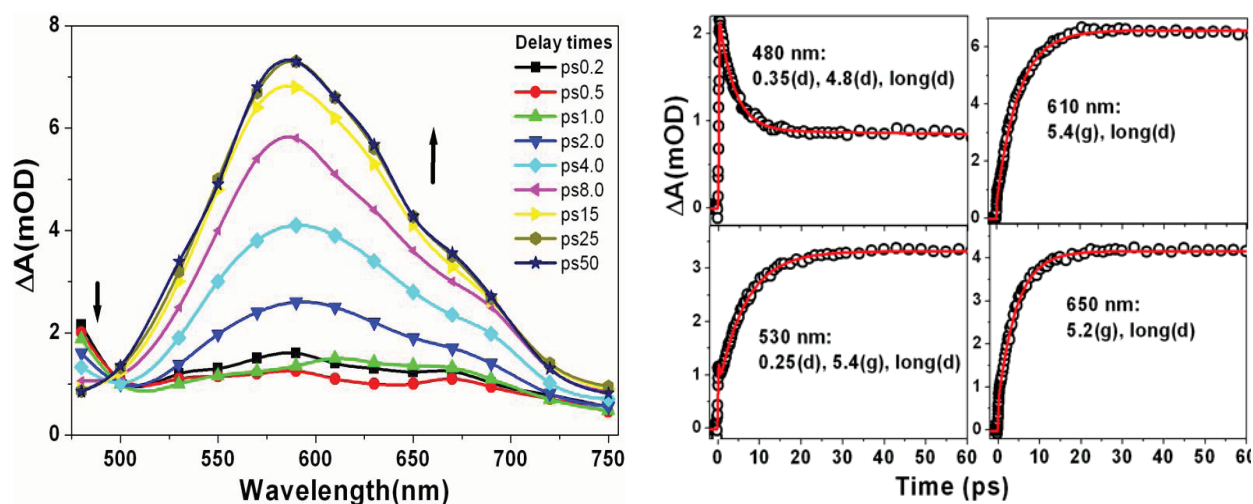


Figure 5.8. Femtosecond transient absorption spectra (left) and temporal decay kinetics (right) of DMAC-B in cyclohexane.

Transient spectral evolution of DMAC-A also indicates similar ISC relaxation mechanism (Figure 5.9). Spectral evolution from 4 ps to 30 ps clearly indicate growth of a long lived ESA in 620-750 nm region along with decay of ESA in 480-600 nm region with an isosbestic point at 610 nm. Short time evolution of ESA in 0.2-4 ps can be ascribed to the intramolecular relaxation within singlet state. Temporal analysis results 8 ps time constant for ISC process along with a shorter component having ca. 1.5 ps lifetime which can be ascribed to vibrational relaxation. It should be pointed out that the short component, which we tentatively assign as vibrational relaxation is significantly longer for DMAC-A than that in DMAC-B. This may be possibly due to some intramolecular structural change accompanied by vibrational relaxation. The main finding of the transient absorption studies is that ultrafast ISC is the main deactivation channel of the singlet state of both the DMAC-A ($\tau_{ISC} \sim 8$ ps) and DMAC-B ($\tau_{ISC} \sim 5$ ps) in nonpolar solvent.

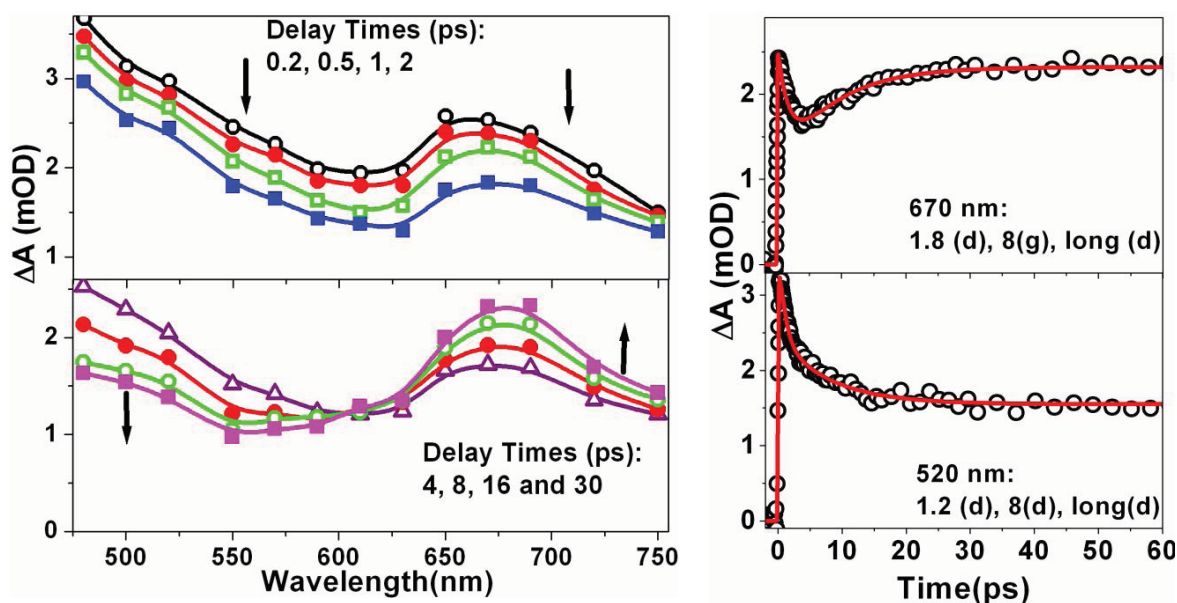


Figure 5.9. Femtosecond transient absorption spectra (left) and temporal decay kinetics (right) of DMAC-A in cyclohexane.

5.3.7. Quantum Chemical calculations: The steady state and time resolved experiments together suggest that DMAC-A undergoes large conformational relaxation to weakly emissive TICT state whereas DMAC-B is significantly emissive indicating large amplitude relaxation to a weakly emissive state does not participate in the excited state dynamics. To corroborate the experimental observation, we performed DFT/TDDFT calculation to determine the structures of the molecules in the ground state as well as in the first singlet excited state. DFT/TDDFT optimized geometries of the two isomers in S_0 and S_1 state have been shown in Figure 5.6. DFT optimized structures show that both the molecules are planar in ground state.²¹⁰ Starting with the ground state optimized structure (i.e. Franck Condon geometry) as the initial guess, geometry optimization in the first singlet excited state produces dimethylanilino twisted geometry of the DMAC-A as the minimum energy structure. This clearly establishes the large amplitude structural relaxation as the nonradiative deactivation pathway for DMAC-A photodynamics. On the other hand, the conformation of the S_1 optimized state of DMAC-B is similar to that in the ground state (i.e. only differs in the bond lengths and bond angles without large amplitude conformational change). Occurrence of planar optimized geometry indicates

significantly large barrier along the dimethylanilino twisting of DMAC-B. Thus, TDDFT calculations support the observation of TICT relaxation to form dimethylanilino twisted state of DMAC-A whereas the excited state of DMAC-B does not undergo large amplitude conformational relaxation.

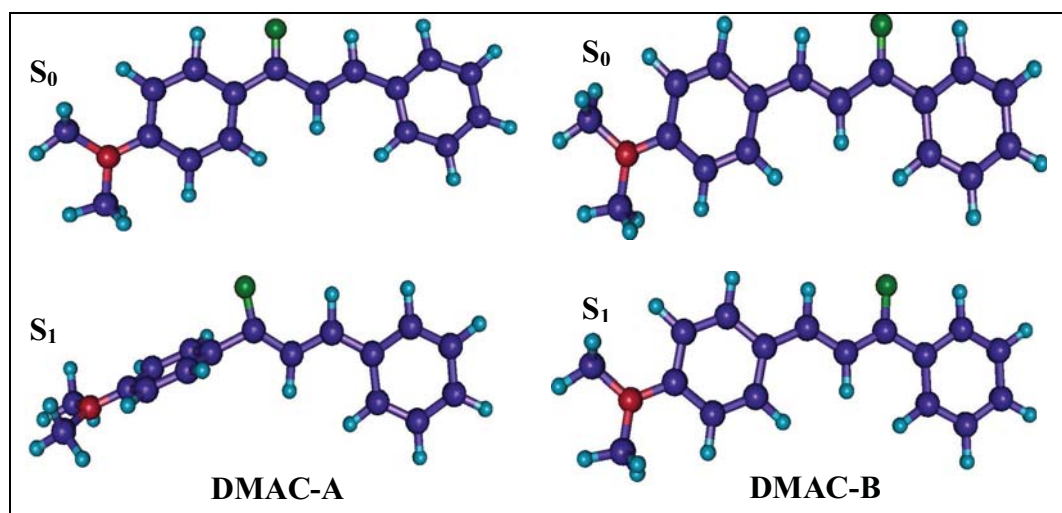


Figure 5.10. Gas phase optimized structure of DMAC-A and DMAC-B in the S_0 and S_1 state .

5.4 Discussion

Main findings of the experimental results and theoretical calculations described above can be summarized as follows: Both the isomers are strongly charge transfer in excited state owing to donor-acceptor substitution. In polar solvents, fluorescence yield of the two compounds are remarkably different. Weak emission and short fluorescence lifetime of DMAC-A in polar solvents indicate efficient and very fast nonradiative relaxation of emissive ICT state. Sub-picosecond transient absorption studies further revealed ultrafast structural to nonemissive TICT state in few picosecond timescale. Dependence of relaxation rate on solvent polarity and viscosity accords TICT dynamics. Excited state structure optimization clearly shows that dimethylanilino twisted structure is the minimum energy geometry. Thus the TICT relaxation occurs along the dimethylanilino twisting coordinate in picoseconds timescale as observed from femtosecond TA experiments in different polar solvents. On the other hand, strong

fluorescence ($\Phi_f = 0.1-0.2$) and long lifetime (300-1400 ps) of DMAC-B in polar solvents suggest strongly emissive planar ICT state without nonradiative structural relaxation. Excited state optimization indeed revealed planar ICT geometry for DMAC-B. TA experiment shows in addition to solvation, some intermediate relaxation ($\tau \sim 10$ ps) is involved in the ICT state which does not correlate to the viscosity of the solvents indicating absence of large amplitude structural relaxation. This intermediate relaxation may be associated with some low amplitude change in bond angles and dihedral angles required to form thermally relaxed ICT state from the Franck-Condon excited geometry.

The difference in the excited state properties of the two molecules is remarkably different though both of them possess strong charge transfer character. This strongly indicate large intramolecular charge transfer upon photoexcitation is not the sole criteria for TICT relaxation rather structure of the molecule has important influence to define excited state potential energy surface and consequent excited state reaction dynamics. The experimental results clearly suggest that, in case of DMAC-A the potential energy surface is quasi-barrierless (in polar solvents) along the dimethylanilino twisting coordinate which allow the excited state population relax to weakly emissive TICT state in ultrafast timescale whereas for DMAC-B, the TICT state is possibly separated by significantly large barrier from the planar ICT geometry and thus relaxation to twisted state is kinetically unfavorable. The nature of charge transfer excited singlet state potential energy surfaces of the two systems have been shown schematically in Figure 5.11.

We propose that the relative positioning of the donor and acceptor group plays important role on the energetic and barrier of ICT-TICT reaction. In comparison to DMAC-A, dimethylanilino group of DMAC-B is in extra conjugation with the carbonyl group by an additional olefinic bond. Because of the near planar geometry, this extra conjugation provides significant mesomeric stabilization to the planar ICT state of DMAC-B. This has been evident in

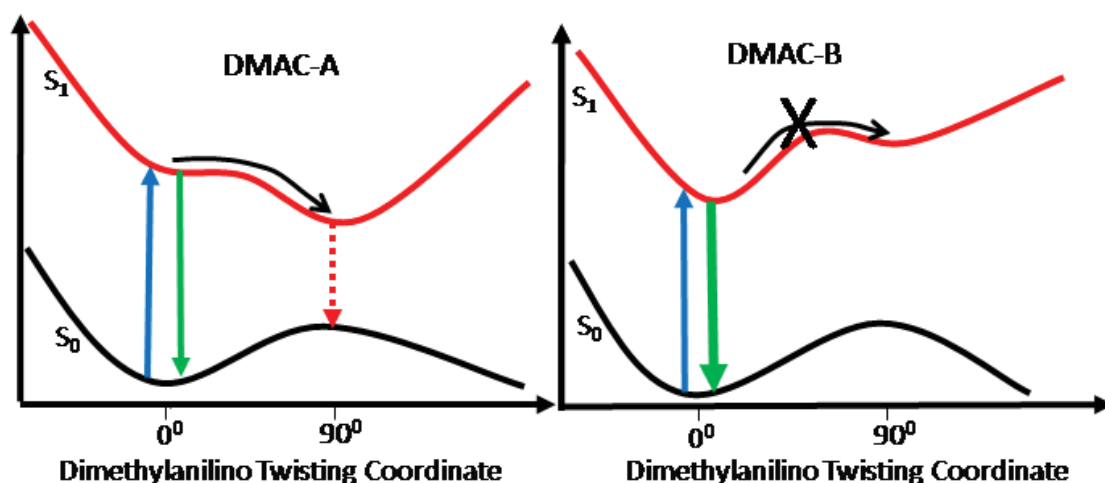


Figure 5.11. Schematic potential energy surface (PES) diagrams illustrating the difference between the photophysical processes occurring in the excited states of DMAC-A and DMAC-B in polar solvents.

absorption spectra, where DMAC-B absorption maxima was observed to be significantly lower in energy compare to DMAC-A in all solvents. In case of DMAC-A, the ICT state is not extensively conjugated rather coupling between donor and acceptor is very strong which leads to very low barrier along the twisting coordinate facilitating the ultrafast formation of weakly emissive TICT state. In case of DMAC-B the coupling between donor and acceptor is expected to be weaker as the donor and acceptor group are further apart. We demonstrate that the relative positioning of the donor and acceptor group strongly modulate the energetics and barrier of ICT to TICT along the reaction coordinate to manifest remarkably different excited state properties.

5.5 Conclusion

In this chapter, we demonstrate that the donor acceptor conjugation length is crucial in determining the excited state structural relaxation behavior in the ICT state. Comparison of fluorescence spectral characteristics, fluorescence quantum yield and excited state lifetime of two isomeric DMAC in different solvents led us to infer that strong interaction between donor and acceptor moieties is essential for TICT relaxation. Strong coupling between donor and

acceptor groups facilitating ultrafast twisting of DMAC-A along the twisting coordinate resulting to the formation of weakly emissive TICT state whereas for DMAC-B, emissive ICT state does not undergo large amplitude structural relaxation due larger barrier of twisting. We propose that the relative positioning of the donor and acceptor group strongly influence the relative energy of ICT and TICT state, as well as barrier along twisting coordinate.

Chapter 6

Ultrafast Dynamics of the Excited States of 1-(p-Nitrophenyl)-2-hydroxymethylpyrrolidine

6.1. Introduction

Understanding the structure and dynamics of the excited states of numerous donor (D) - acceptor (A) substituted aromatic molecules, D-Ar-A (Ar is the aromatic spacer moiety connecting D and A) or simply D/A, has been the subject of extensive theoretical and experimental investigations.^{57,58} The simplest and the most well studied molecule of this type is dimethylaminobenzonitrile (DMABN), which shows dual fluorescence because of the emissive properties of both the local excited (LE) and intramolecular charge transfer (ICT) states. Since the first report of this phenomenon in 1961,²¹¹ dual fluorescence has been observed with a large number of D/A molecules in solutions, in crystals as well as in the gas phase.^{58, 212-229} It is now well-established that this process is an intramolecular phenomenon and that the LE and ICT states are structural conformers. ICT state is characterized by twisted intramolecular charge transfer (TICT) state in which dimethylamino group is considered to be twisted to a configuration perpendicular to the plane of the phenyl ring. Variation of donor and acceptor strength in D-Ar-A molecules results to extend of charge transfer properties and dynamics of the excited states. Among a large number of disubstituted benzenes as the donor - acceptor molecules, *p*-nitroaniline (PNA) has served as the simplest but the most important model molecule for both theoretical as well as experimental investigations of the ICT reactions

and a variety of photophysical properties associated with it.^{230–241} Due to very strong electron accepting character of the nitro group, the derivatives of PNA show strong solvatochromic behavior and non-linear optical properties.^{242–247} Twisting of the nitro group in the excited state of PNA was first considered by Sinha and Yates, who showed that the dipole moment of the excited state, in which the nitro group is twisted, is larger than that having the coplanar conformation.^{233, 234} Thomsen et. al. undertook the sub-picosecond transient absorption study of PNA for the first time in water and 1,4-dioxane.²³⁵ They found that the excited state relaxation is extremely fast (<0.5 ps), and dominated by the intersystem crossing (ISC) in dioxane but by the internal conversion (IC) in water. The intersystem crossing quantum yields were determined to be 0.4 and 0.03 in dioxane and water, respectively. The order of magnitude decrease in the intersystem crossing yield, while going from dioxane to water, was ascribed to the lowering of the coupling between the S_1 and T_1 states with increasing solvent polarity.

Considering the fact that the estimate of the lifetimes were obtained by Thomsen et. al at the limit of the experimental time-resolution (0.3 ps), Ernsting and coworkers reinvestigated the relaxation dynamics of the S_1 state of PNA with better time resolution in order to expose the earliest evolution.^{236,237} Their results of investigations using ultrafast transient absorption spectroscopic technique having time resolution of about 40 fs, as well as semiempirical theoretical calculations for the optimized geometries of both the ground and the excited states, suggested that nitro twisting is an important coordinate to induce efficient IC process. Following photoexcitation, the excited state evolves along this coordinate to encounter with an isoenergetic point with the ground state, where vibronic coupling facilitates very rapid IC to the ground state. Ultrafast relaxation of the S_1 state of PNA taking place in sub-1 ps time domain has been described by the occurrence of several consecutive processes, such as vibrational relaxation, solvation, nitro twisting and internal conversion. Structure of the excited

state of PNA with the twisted nitro group has also been established using time dependent density functional theory (TDDFT) with solvation model.²⁴⁰ In addition, the fact that twisting of the nitro group, and not that of the donor group, is the only conformational relaxation process taking place in the excited states of nitroaromatics has been established in the cases of *p*-nitro-dimethylaniline.²⁴⁰

Understanding the dynamics of the electronically excited states of nitrated polycyclic aromatic hydrocarbons (NPAHs) has been of great importance since photochemical reactions determine the atmospheric stability of these toxic pollutants, which are released to the environment directly from a variety of incomplete combustion processes and also formed in situ by atmospheric reactions of PAHs.²⁴⁸⁻²⁵⁷ Among these NAPHs, 1-nitronaphthalene is the simplest one and its photophysical properties have been studied by several groups in different kinds of solvents.²⁵²⁻²⁵⁴ These studies have proposed that the lowest excited singlet $S_1(\pi\pi^*)$ state bifurcates into two essentially barrierless nonradiative decay channels with sub-200 fs lifetimes. The first main decay channel connects the S_1 state with a receiver T_n state that has considerable $n\pi^*$ character. Single exponential fluorescence decay with sub-100 fs lifetime is explained by the ultrafast intersystem crossing from the S_1 to the T_3 state with relatively large yield, which is a consequence of the small energy gap and strong vibronic coupling between these two states.^{254,258} The receiver T_3 state undergoes internal conversion to populate the vibrationally excited $T_1(\pi\pi^*)$ state in 2–4 ps. It has also been shown that vibrational cooling dynamics in the T_1 state takes place with the average lifetimes in the range from 6 to 12 ps depending on the solvent used. Furthermore, solvation dynamics competes effectively with vibrational cooling in the triplet manifold in primary alcohols. The relaxed T_1 state undergoes intersystem crossing back to the ground state within a few microseconds in all kinds of

solvents. The second minor channel involves conformational relaxation of the $S_1(\pi\pi^*)$ state via twisting of the NO_2 -group to populate a dissociative singlet state.

Similar kind of relaxation mechanism is operative in a few other derivatives of 1-nitronaphthalene.²⁵² In contrast, for the amino-substituted 1-nitronaphthalene, the excited-state evolution shows a strong solvent dependence. In nonpolar solvents, the same type of intersystem crossing through an upper receiver triplet state dictates the photochemistry. However, in polar solvents, where the first singlet excited state shows an important solvent-induced stabilization, the prevailing relaxation process proceeds through repopulation of the electronic ground state in the time scale of less than 1 ps followed by vibrational cooling. Peon and his coworkers also studied the photochemistry of 9-nitroanthracene, 1-nitropyrene, 6-nitrochrysene, and 3-nitrofluoranthene in solution samples.²⁵¹ In contrast to the fact that the fluorescence decay of 1-nitronaphthalene is single exponential, the emission of all these molecules follow double-exponential decay. Conformational relaxation of the nitro group has been proposed as a major nuclear relaxation coordinate in the S_1 state, which occurs with a lifetime of <100 fs.²⁵¹ However, in a recent publication, Nath and his coworkers suggested that the observed ultrafast decay for 1-nitropyrene is due to an efficient intersystem crossing rather than to the torsional motion of the nitro group.²⁵⁷ The longer component of the fluorescence decay has been assigned to the conformationally relaxed S_1 state. In the case of 1-nitroperylene, ISC was only observed in nonpolar solvents. Instead, the main deactivation pathway of the excited singlet state of nitroperylene is IC, with a mechanism and dynamics that depend strongly on the solvent.²⁵⁶

Above discussion reveals that addition of a nitro group to an aromatic hydrocarbon considerably affects its photophysical and photochemical properties. Two phenomena, namely, the intersystem crossing (ISC) and internal conversion (IC), which are sensitive to molecular

structure as well as the nature of the solvent, control the dynamics of the excited state of a nitroaromatic compound. The presence of an electron donating group in a nitroaromatic compound makes the photophysical properties of the excited states solvent sensitive, since these two mechanisms become operative in different polarities.

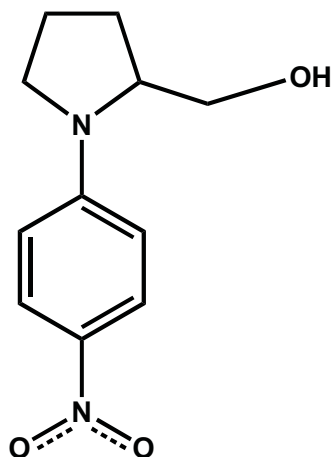


Figure 6.1. Chemical structure of 1-(p-nitrophenyl)-2-hydroxymethyl-pyrrolidine (*p*-NPP).

Although several reports have been published in recent times to establish the occurrence of the nitro twisting process in PNA, not many reports have been published exploring the role of the differently substituted donor groups in the conformational relaxation process, except the one published recently by Rafiq et. al.,²⁶⁰ who investigated the photophysics of 1-(p-nitrophenyl)-2-hydroxymethyl-pyrrolidine (*p*-NPP) (Figure 6.1) in different kinds of solvents using fluorescence upconversion method. Although *p*-NPP is very weakly fluorescent, this technique could reveal the two-state relaxation process in the singlet excited (S_1) state, but because of inherent limitations of this technique, the lifetimes of several other processes, such as intersystem crossing (ISC), twisting of the nitro group as well as vibrational cooling or reverse nitro twisting processes, could not be determined. In this chapter, we provide a detailed picture of the dynamics of the excited states of *p*-NPP by determining the rates of these processes. We describe the results of our investigations on the dynamics of the excited state of *p*-NPP in solvents of varying polarities and viscosities employing transient

absorption spectroscopic technique and quantum chemical calculations using time dependent density functional theory (TD-DFT) to reveal the strong solvent dependence of the photophysical processes occurring in the excited state of p-NPP.

6.2. Results

6.2.1 Steady-State Absorption and Fluorescence Studies: Figure 6.2 shows the steady state absorption and fluorescence spectra of *p*-NPP in 1, 4-dioxane, ethanol, dimethyl sulfoxide (DMSO) and water at room temperature. Each of the absorption spectra presented in this Figure shows an intense absorption band in the 300 – 500 nm wavelength regions. In agreement with the observation of Rafiq et. al., we find that the absorption spectra exhibit a significant solvent polarity effect.²⁶⁰ The absorption maximum shows a regular shift towards longer wavelength with increase in polarity of the aprotic solvents as well as in water. Increase in the width of the absorption band and the large bathochromic shift of the absorption maximum with increase in solvent polarity indicate the charge transfer character and hence the large dipole moment of the ground state. But in ethanol, a protic solvent, the absorption maximum lies midway between those found in DMSO and dioxane. This is possibly a consequence of hydrogen bonding interaction between *p*-NPP and alcohol molecules.^{253, 261}

In all kinds of solvents at room temperature, the fluorescence is very weak and the quantum yield determined in acetonitrile has been reported to be in the order of 10^{-4} .²⁶⁰ Fluorescence spectrum recorded in each of these solvents used here shows a single fluorescence band and the fluorescence maximum too is sensitive to solvent polarity and shifts from 447 nm recorded in dioxane to 492 nm in DMSO and 517 nm in water. But again, the fluorescence maximum in ethanol appears at 492 nm, which nearly coincides with that observed in dioxane, a solvent of lower polarity. The Stokes shifts, however, show a regular increase with increase in polarity of the solvents, e.g. the Stokes shift values are 3401 cm^{-1} in

dioxane, 3532 cm^{-1} in ethanol, 3946 cm^{-1} in DMSO and 4300 cm^{-1} in water. Rafiq et. al determined the dipole moments of the ground and the excited states of *p*-NPP using the solvatochromic data to fit the Kawasaki's equation as 7.4 and 14.9 D, respectively.²⁶⁰

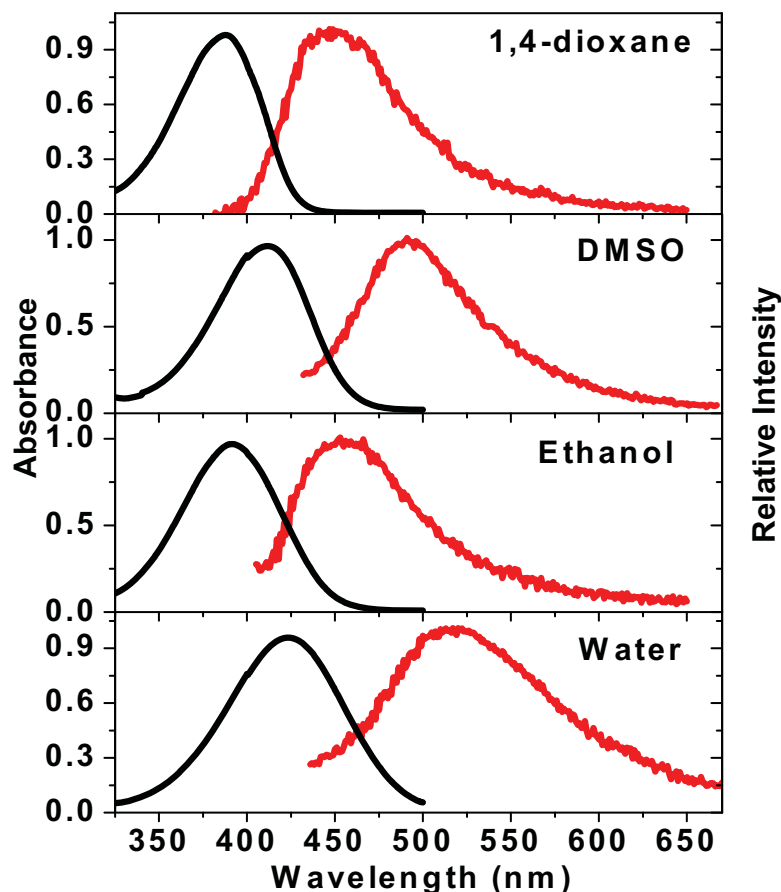


Figure 6.2. Steady state absorption and fluorescence spectra of *p*-NPP in 1,4-dioxane, ethanol, DMSO and water.

6.2.2 Transient Absorption Spectroscopic Study:

6.2.2.1 In Nonpolar Aprotic Solvent: Figure 6.3 presents the time-resolved differential transient absorption (TA) spectra of *p*-NPP in dioxane, following photoexcitation using 400 nm light. The TA spectrum constructed for 0.2 ps delay time shows the presence of a stimulated emission (SE) band in the 460 - 550 nm region and three excited state absorption (ESA) bands

in the 550 – 1000 nm region. Because of limitation of our spectrometer, spectrum of the SE band could not be recorded below 460 nm. In sub-0.5 ps time-domain, the SE band as well as

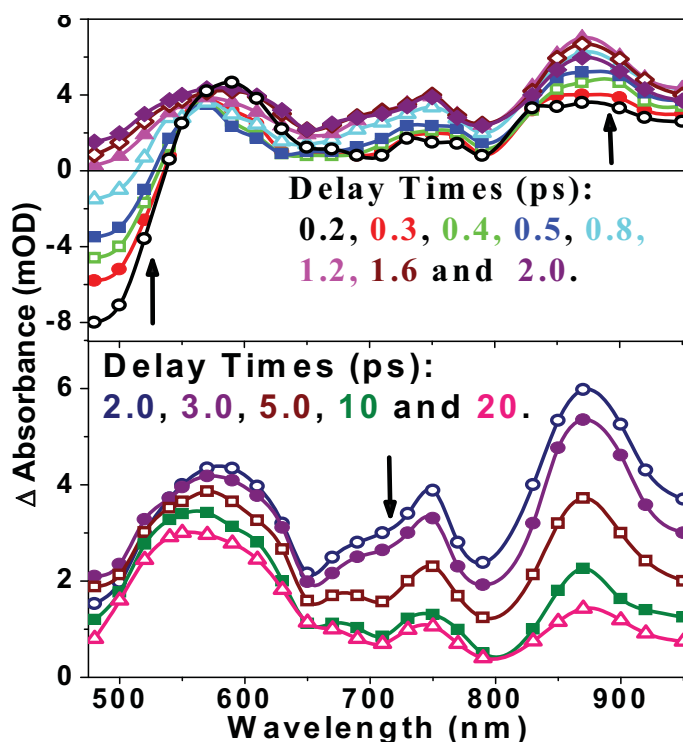


Figure 6.3. Time-resolved TA spectra constructed for different delay times following photo-excitation of *p*-NPP in 1,4-dioxane using 400 nm laser pulses of 50 fs duration.

the ESA band in the 560 - 650 nm region decay, but the other ESA bands in the 650 - 950 nm region show a rise. With further increase in delay time up to about 2 ps, decay of the SE band continues leading to the development of an ESA band in the 480 – 550 nm region, and all other three ESA bands also continue to rise. The transient spectrum recorded at 2 ps delay time is characterized by three ESA bands with the maxima at ca 580, 750 and 860 nm. All these bands decay at longer delay times but leading to offsets (residual absorption) having different amplitudes at different wavelengths. As a result, the TA spectrum recorded at 20 ps delay time has the main absorption band with the maximum at 550 nm and two weaker ESA bands with the maxima at ca 750 and 860 nm. We observe a small dynamic blue shift of the absorption maximum of the ESA band in the 480 – 650 nm region. The long-lived transient species

characterized by the spectrum with the absorption maximum at ca 550 nm can be assigned to the lowest energy triplet (T_1) state because of its similarity with that reported for p-nitroaniline.²³⁵

Figure 6.4 presents the temporal profiles recorded at a few selective wavelengths. Each of the temporal profiles recorded at different wavelengths in the 480 – 1000 nm region could be fitted using two or three exponential function consisting of rise and/or decay components along with a longer lived ESA component as the offset. Instrument response time limited rise of the SE band monitored at 480 nm suggests that the TA spectrum recorded at 0.2 ps delay time (Figure 6.3) can be assigned to the vibrationally relaxed local excited singlet or S_1 (LE) state, which is formed following photoexcitation using 400 nm light. SE intensity decays biexponentially with the lifetimes of about 0.13 and 0.9 ps, leading to the development of an ESA. At longer delay times, this ESA decays with the lifetime of about 3 ps leading to a longer-lived residual absorption. On the other hand, the temporal profiles recorded at 590 and 670 nm show an instrument response time limited rise of ESA, which decay with the lifetime of 0.16 ps, but is followed by another rise with the lifetime of about 0.9 ps. Subsequently, ESA decays with the lifetime of 2.9 ps, but leading to a residual absorption of larger amplitude as compared to that observed at 480 nm. Each of the temporal profiles recorded in the 750 – 950 nm region could be fitted with a rising component and a subsequent decay component along with an offset of ESA. The average lifetimes of the rising and decay components are 0.8 and 2.5 ps, respectively.

Comparison of the temporal profiles recorded at 480 and 590 nm clearly suggests that the biexponential decay of SE monitored at 480 nm does not represent two parallel processes but the involvement of two consecutive processes occurring in the S_1 state. We assign the ultrafast component with the lifetime of about 0.15 ps to the lifetime of the S_1 (LE) state, which

undergoes ICT process accompanied by the conformational relaxation via twisting of the nitro group. Previous experiments and calculations have suggested that twisting of the nitro group is one of the main nuclear relaxation coordinates in the excited state of NAPHs.^{235, 236, 250-254} Thus the nitroaromatic torsion angle has been considered here as the most probable conformational relaxation process in the $S_1(\text{LE})$ state to form the $S_1(\text{ICT})$ state.

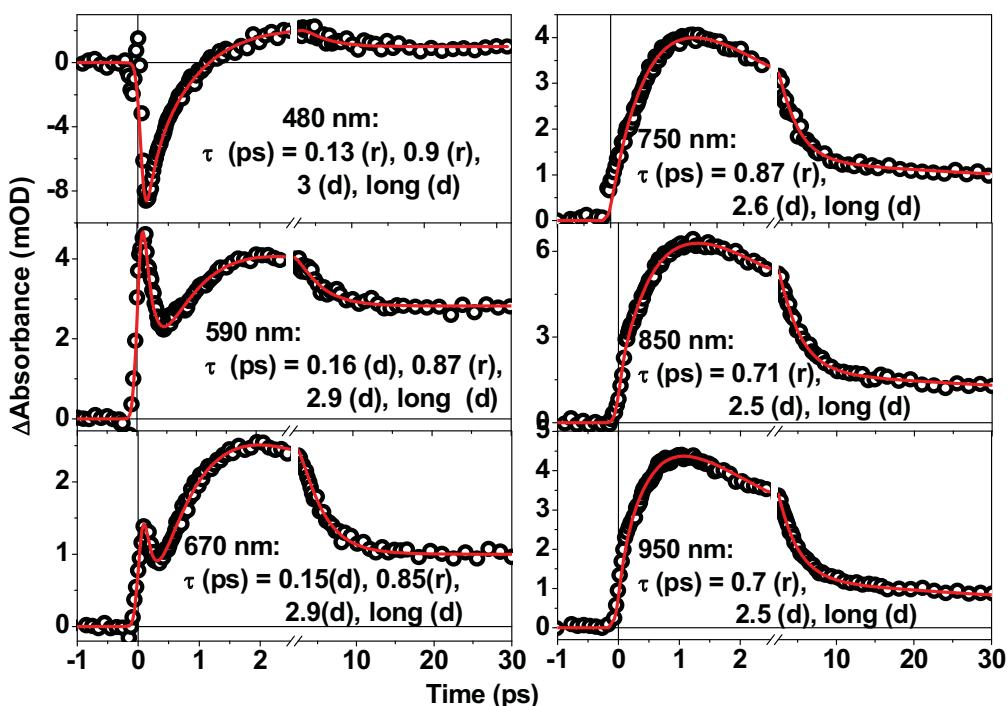


Figure 6.4. Temporal evolution of TA monitored at a few selective wavelengths following photo-excitation of *p*-NPP in dioxane. Solid lines represent the best-fit multi-exponential functions along with an offset for a longer lived component of ESA. The lifetimes associated with the fit functions are given in the insets.

Vertical transition energies of the fully optimized structure of *p*-NPP in vacuum as well as in the presence of various solvent media of different polarities have been calculated by Rafiq et. al.²⁶⁰ This has revealed that, like in the case of several other NPAHs, in the case of *p*-NPP too, the T_3 state is isoenergetic or degenerate with the S_1 state, while the energies of both the T_2 and T_1 states are lower than that of the S_1 state in vacuum or nonpolar solvents. Therefore, the component with the average lifetime of about 0.8 ps, which has been determined from the rise time of transient absorption in the 750 – 950 nm region, can be assigned to ISC

from the S_1 state to the T_n state. The average rise time of transient absorption (~ 0.8 ps) determined in the 500 – 670 nm also agrees well with that determined in the red region of the spectrum. Therefore, the TA spectrum recorded at about 2 ps delay time consisting of three ESA bands with the maxima at 580, 750 and 860 nm and is assigned to the T_n states.^{253, 254} The average decay time of the T_n state has been determined to be about 2.5 ps from the decay of transient absorption in the 750 – 950 nm region. However, we observe a dynamic blue shift of the absorption maximum from 580 nm to 550 nm as well as the decay time of the T_n state increases marginally upto about 3 ps as the monitoring wavelength is tuned towards the blue region up to 480 nm. These characteristics of time evolution of the TA spectrum in this time domain suggests the possibility of occurrences of any one or more than one of the three processes, namely, IC process in the triplet manifold from the T_n state to T_1 state, vibrational cooling in the T_1 state and solvation of the T_1 state (solvation time of dioxane is about 1.7 ps).²⁶²

6.2.2.2 In Polar Aprotic Solvents: In order to obtain information regarding the solvent dependence of these processes, excited state dynamics of *p*-NPP were studied in solvents of larger polarities, both aprotic and protic. Figure 6.5 presents the time-resolved differential TA spectra recorded following photoexcitation of *p*-NPP in DMSO solution, a polar aprotic solvent. The TA spectrum recorded at 0.15 ps delay time consists of an intense SE band in the 460 – 600 nm region with the maximum at *ca* 490 nm and two weak ESA bands in the 630 - 950 nm region. In sub-0.5 ps time domain, the SE band in the 460 - 540 nm region decay but accompanied by an increase in intensity of SE in the 540 - 700 nm region leading to the appearance of a temporary isoemissive point at 550 nm, which is possibly fortuitous. We also observe a marginal rise of the ESA band in the 750 – 950 nm region (Inset I of Figure 6.5). The dynamic red shift of the SE maximum accompanied by its fast decay with the increase in

delay time suggests the evolution of the excited state along a potential energy surface representing a conformational relaxation process. Solvation of the excited state may also contribute to the time evolution of the TA spectra in this time domain. Increasing the delay time up to about 1 ps, the entire SE band in the 460 – 700 nm continues to decay accompanied by further rise of the ESA bands in the 700 – 950 nm region (Inset II of Figure 6.5). However, further increase in delay time up to about 3 ps, these ESA bands decay accompanied by the development of a new ESA band with the maximum at 480 nm.

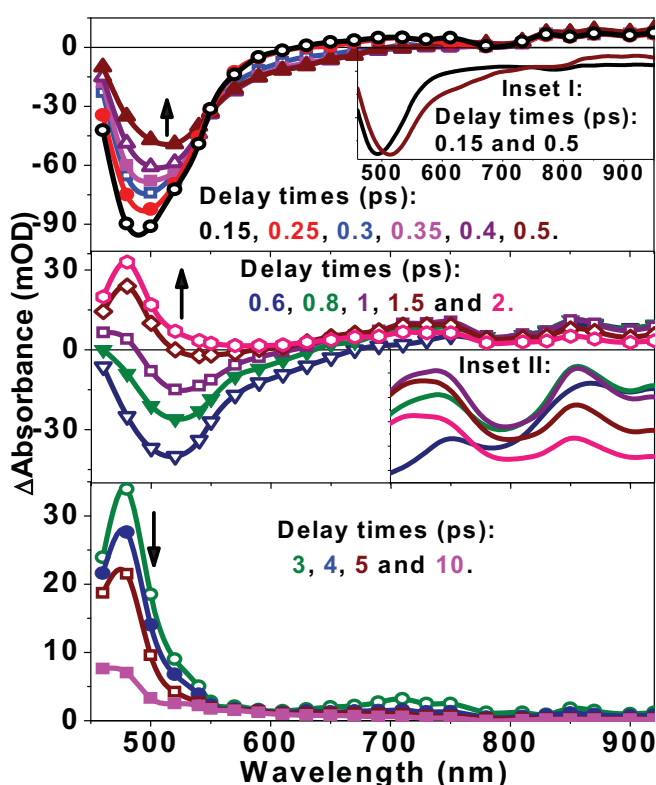


Figure 6.5. Time-resolved TA spectra constructed for different delay times following photo-excitation of *p*-NPP in DMSO. Inset provides the normalized TA spectra recorded at 0.15 and 0.5 ps delay times.

Comparing the spectral characteristics of the TA spectra in DMSO with those observed in dioxane (Figures 6.5 and 6.3, respectively), in the former solvent, we observe two very low intensity ESA bands with the maxima at 730 and 850 nm, which are the characteristics of the T_n state. However, we do not observe an ESA band with the maximum at 570 nm, possibly because of its overlapping with a much stronger SE band. Further, unlike in the case of

dioxane, these three ESA bands observed in DMSO are much shorter lived and decay within 10 ps time domain. All these characteristics of the TA spectra suggest that the yield of the triplet or the ISC process is negligibly small in DMSO and internal conversion in the singlet manifold is the major relaxation pathway for the excited state of p-NPP in this solvent.

In Figure 6.6, we have presented the temporal profiles recorded at a few selective wavelengths following photoexcitation of *p*-NPP in DMSO along with the best-fit functions and the lifetimes associated with the different components are given in the insets. Wavelength dependence of the lifetimes of different components is shown in Table 6.1. Each of the temporal profiles recorded in the 460 – 500 nm is associated with the rise of SE intensity with the instrument response time. SE intensity decays biexponentially leading to the rise of ESA, which decays within 15 ps delay time. In each case, the offset or residual absorption is nearly negligible. The average lifetime of the first component of SE decay is about 0.15 ± 0.03 ps. Following the same arguments as presented in the case of dioxane, this component is assigned to the lifetime of the $S_1(\text{LE})$ state, which undergoes a conformational relaxation via twisting of the nitro group. However, the lifetime of the second decay component of SE (τ_2 in Table 6.1) increases marginally from 0.7 ps to 1.0 ps as the wavelength is tuned from 550 to 460 nm and so also the decay time of ESA (τ_3 in Table 6.1), which increases from 1.5 ps to 4.9 ps.

Each of the temporal profiles recorded in the 590 – 700 nm region could be fitted with a four exponential function with the average lifetimes of 0.18 ps (decay component), 0.4 ps (rising component), 0.8 ps (decay component) and a very small offset or residual absorption. The latter suggests the very low yield of the T_1 state. On the other hand, the temporal profiles recorded in the 750 – 950 nm region is free from overlapping with the SE band. Like in the case of dioxane, the rise time of ESA can be assigned to the ISC or the decay of the nitro-twisted $S_1(\text{ICT})$ state with the average lifetime of about 0.4 ps. The decay time of SE measured

at 590 nm also supports this assignment. The average decay time of ESA monitored in the 700 – 950 nm regions is about 0.9 ps (Table 6.1).

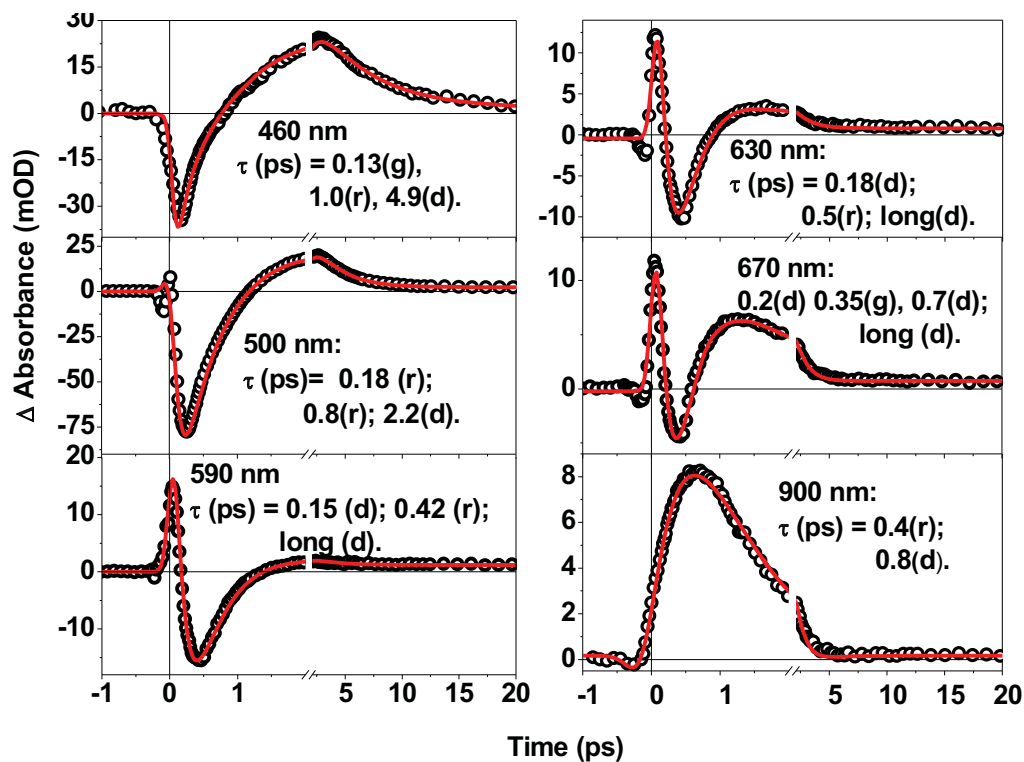


Figure 6.6. Temporal evolution of transient absorption of *p*-NPP in DMSO along with the best fit multi-exponential functions. Lifetimes of different components are given in the inset.

Table 6.1: Wavelength dependence of the lifetimes of the three processes in DMSO.

Wavelength (nm)	τ_1 (ps)	τ_2 (ps)	τ_3 (ps)
460	0.13 (r)	1.0 (r)	4.9 (d)
480	0.15 (r)	0.9 (r)	2.7 (d)
500	0.17 (r)	0.8 (r)	2.2 (d)
520	0.4 (r)	0.9 (r)	1.8 (d)
550	-	0.7 (r)	1.5 (d)
590	0.15 (d)	0.4 (r)	- ^a
630	0.18 (d)	0.5 (r)	0.8(d) ^a
670	0.2 (d)	0.35 (r)	0.7 (d) ^a
710	0.17 (d)	0.4 (r)	1.0 (d)
750	-	0.5 (r)	1.0 (d)
900	-	0.4 (r)	0.8 (d)

^aTemporal profile is associated with a long decay of very low amplitude.

Table 6.2. Lifetimes of the processes associated with the relaxation dynamics of the excited states of p-NPP in different kinds of solvents, determined using the transient absorption spectroscopic technique.

Solvents	Solvent parameters					Lifetimes			
	π^* ^a	η (cP) ^b	$\langle\tau\rangle_{\text{solv}}$ (ps) ^c	μ (D) ^b	TC (W/m.°C) ^d	$\tau_{\text{LE}}/\tau_{\text{NT}}$ (ps) ^e	$\tau_{\text{isc}}/\tau(\text{S}_1)$ (ps) ^f	$\tau_{\text{R}}(\text{T})$ (ps) ^g	$\tau_{\text{vib}}(\text{S}_0)$ (ps) ^h
Dioxane	0.49	1.4	1.7	0.5	-	0.15	0.7	2.5	-
Triacetin	-	20	49		-	0.15	0.6	2.2	6.0
1-Butanol	0.47	2.3	63	1.8	0.167	0.2	0.37	2.0	2.6
1-Propanol	0.52	1.9	26	1.7	0.161	0.2	0.34	1.7	3.0
Ethanol	0.54	1.1	16	1.7	0.171	0.15	0.3	1.5	2.4
Acetonitrile	0.66	0.34	0.26	3.5	0.208	0.12	0.25	0.45	2.3
EG	0.92	18	15.3	2.3	0.258	0.2	0.45	0.7	2.6
DMSO	1.0	2.0	1.8	4.1	0.2	0.15	0.4	0.8	4.9
Water	1.09	0.9	<0.05 ^d	1.84	0.609	<0.1	0.4	-	1.35

^aTaken from ref. (263); ^bTaken from ref. (264), Viscosity values are for 25 °C; ^cTaken from refs. (262) and (265); ^dThermal conductivity, values taken from ref (266); ^eDetermined from the ultrafast decay component of SE at 460 or 470 nm. ^fThe lifetime of the $\text{S}_1(\text{ICT})$ state, determined from the rise time of ESA measured in the 750 – 950 nm region. ^g τ_{R} is the lifetime of relaxation in the triplet manifold, determined from the decay time of ESA measured in the 750 – 950 nm region. ^hThe vibrational cooling time in the S_0 state, which is the decay time of ESA monitored in the 460 – 480 nm region.

IC process produces the molecules in the Franck-Condon (FC) region of the ground electronic state (S_0) and these molecules are vibrationally hot and have the structure with the twisted nitro group. The wavelength dependence of the rise or decay time of ESA measured in the 460 – 550 nm regions suggests that the vibrationally hot molecules undergo relaxation on the same potential energy surface (PES) by dissipation of excess vibrational energy to the solvent. More precisely, the TA signal recorded with the probe of higher energy reflects changes to the ground-state absorption spectrum caused by excess vibrational energy in the FC active vibrational modes. Vibrational cooling generally requires no more than a few tens of picoseconds in solution and it has been observable in this case because the internal conversion process takes place more rapidly than the vibrational cooling process.²⁶⁷⁻²⁷² In this case, the

vibrational cooling process is accompanied by the reverse twisting of the nitro group. The decay time of ESA (4.9 ps) measured at 460 nm, which falls at the red edge of the absorption spectrum of *p*-NPP in DMSO can be assigned to the lifetime of vibrational cooling process.²⁶⁷ These observations revealed the fact that twisting, solvation and internal conversion are the three major processes associated with the relaxation of the excited state of *p*-NPP in a polar solvent.²³⁵⁻²³⁷ Temporal dynamics of the excited state in two other polar aprotic solvents, namely acetonitrile and triacetin, as well as in ethylene glycol, for which the solvation times and viscosities are widely different (Table 6.2). The trend of wavelength dependence of the lifetimes of the three components in these three solvents is very similar to that observed in DMSO, suggesting that similar relaxation mechanisms are operative in all these solvents. Following the same arguments as put in the case of DMSO, we have assigned the lifetimes of different components associated with the best fit functions to the $S_1(\text{LE})$ state, which decays to the $S_1(\text{ICT})$ state via nitro twisting, internal conversion and the vibrational cooling processes and these values have been given in Table 6.2.

6.2.2.3 In Water: Figure 6.7 presents the time-resolved differential TA spectra of *p*-NPP in water. The TA spectrum recorded at 0.15 ps delay time shows a broad SE band with the maximum at *ca* 520 nm and a shoulder at *ca* 600 nm region. In sub-0.3 ps time domain, the intensity of the SE band in the 460 – 550 nm region decays, whereas that in the 550 – 950 nm region rises leading to a new SE band with the maximum at 600 nm. Appearance of the temporary isoemissive point at 540 nm suggests the conversion of the $S_1(\text{LE})$ state with the emission maximum at 515 nm to the nitro twisted $S_1(\text{ICT})$ state with the emission maximum at 600 nm. However, as explained earlier in the case of DMSO, observation of the temporary isoemissive point is fortuitous. Although in sub-0.3 ps time-domain the time-evolution of the transient spectra in polar solvents is associated with the nitro-twisting process, and an

isoemissive point is expected because of precursor - successor relationship between the $S_1(\text{LE})$ and $S_1(\text{ICT})$ states (Figures 6.5 and 6.7). The SE band recorded at 0.3 ps delay time is exceptionally broad and extends from 480 to 950 nm. With further increase in delay time up to 1 ps, the entire SE band in the 500 – 900 nm region decays with the similar time constant. This possibly suggests the population of the excited molecules having wide distribution of nitro-twisting angles. The decay of this SE band leads to a new ESA band with the maximum at 500 nm, which subsequently decays within 5 ps time domain.

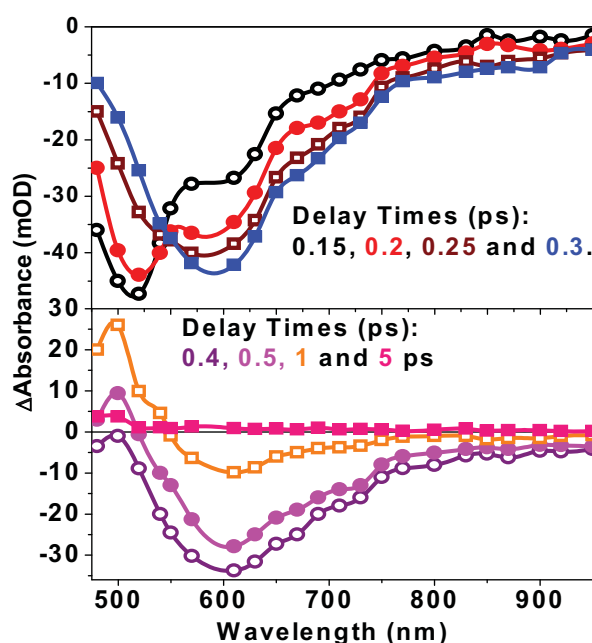


Figure 6.7. Time-resolved TA spectra constructed at different delay times following photo-excitation of *p*-NPP in water.

Temporal evolution of transient absorption monitored at a few selective wavelengths following photo-excitation of *p*-NPP in water is shown in Figure 6.8. If we follow the same arguments, which have been used to determine the lifetimes of the processes occurring in the excited state in DMSO, the lifetime of the $S_1(\text{LE})$ state or the nitro twisting process is ultrafast ($\text{ca} \leq 0.1$ ps) and it has not been possible to determine its value here with reasonable accuracy because of limitation of the time resolution of the spectrometer. However, the decay time of the $S_1(\text{ICT})$ state, having the structure with the twisted nitro group, and the lifetime of the vibrational

cooling process have been determined as 0.45 and 1.35 ps, respectively. In this solvent, the triplet yield is negligibly small and the yield of the IC process is near unity.

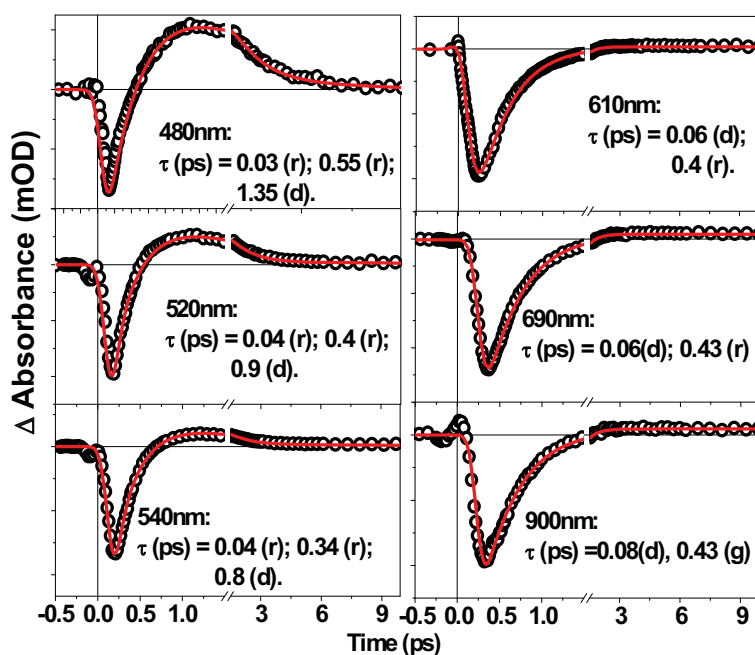


Figure 6.8. Temporal evolution of transient absorption monitored at different wavelengths following photo-excitation of *p*-NPP in water. The lifetimes (in ps) associated with the multiexponential fit functions are given in the insets.

6.2.2.4 Dynamics in alcoholic solvents: Excited state dynamics of *p*-NPP has also been investigated in a few alcoholic solvents in order to explore the effect of hydrogen bonding on the dynamics of the relaxation processes of the excited state. We have indicated earlier that the alcohols form intermolecular hydrogen bonds with the nitro group of *p*-NPP in the ground state. Figure 6.9 presents the time evolution of the differential TA spectra recorded following photoexcitation of *p*-NPP in ethanol. Let us compare the characteristics of the time resolved TA spectra in this solvent with those observed in DMSO and dioxane. In sub-1 ps time domain, the time-evolution of the SE spectra in the 500 – 700 nm region is very similar to those observed in DMSO, but we observe the development of an ESA band in the 500 – 650 nm region. In addition, in the 700 – 1000 nm region, we also observe the development of two broad ESA bands with the maxima at ca 750 and 860 nm, which are more intense as compared

to those observed in the TA spectra recorded in DMSO. Let us compare the features of the TA spectra recorded in ethanol at 1.5 ps delay time with those recorded in dioxane and DMSO at the same delay time. The ESA bands with the maxima at 550, 750 and 860 nm are the characteristics of the T_n state (Figure 6.2). This suggests that the triplet yield is larger in alcohols as compared to that in polar aprotic solvents. The time evolution of the T_n spectra in the 1.5 – 20 ps time domain represents the relaxation in the triplet manifold.

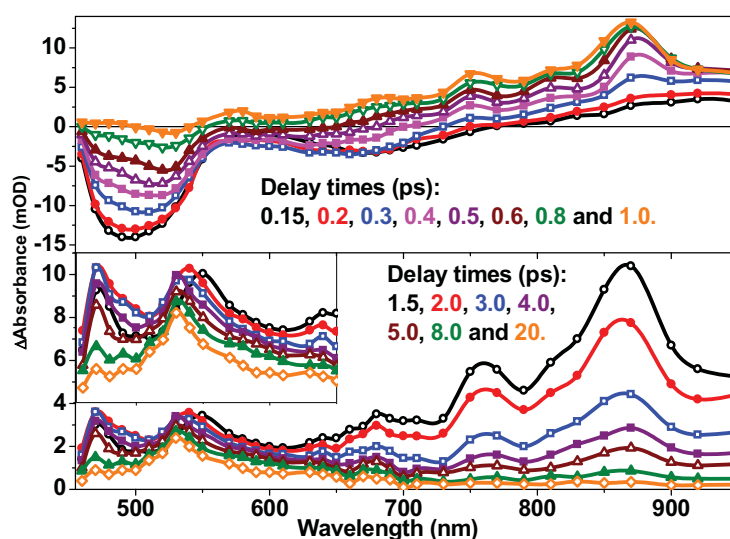


Figure 6.9. Time-resolved TA spectra constructed at different delay times following photo-excitation of *p*-NPP in ethanol. Inset shows the blown up of the spectral region 460 – 600 nm.

We also observe the occurrence of the ESA band with the maximum at ca 470 nm, which is the feature of the vibrationally hot S_0 state, and is formed via the IC proces from the S_1 (ICT) to the S_0 state. The band narrowing during its decay suggests the vibrational cooling process accompanied by the reverse nitro-twisting.²⁶⁷ These observations establish the fact that the excited state relaxation process in ethanol proceeds through two parrallel channels, namely the IC and ISC processes.

In Figure 6.10, we have presented the temporal profiles recorded at a few selective wavelengths. Following the similar explanation, which has been put forth in the case of other solvents, ultrafast rise time of SE with the lifetime of about 0.15 ps determined in the 470–

500 nm region can be assigned to the lifetime of the $S_1(\text{LE})$ state or the nitro twisting process. On the other hand, the rise of ESA in the 750 – 950 nm region with the average lifetime of about 0.3 ps can be assigned to the lifetime of the $S_1(\text{ICT})$ state, which decays through IC and ISC channels. The average decay time of 1.5 ps of ESA measured in this region is assigned to the relaxation in the triplet manifold leading to the vibrationally relaxed and solvated T_1 state. Wavelength dependence of the lifetime of the second component of SE decay or ESA rise as well as the ESA decay observed in the 470 – 530 nm suggests the evolution of the transient state along the potential energy surface (PES) of the S_0 state via vibrational cooling and reverse nitro twisting. The cooling time of the vibrationally hot S_0 state has been determined by analysing the temporal profile recorded at 470 nm to be about 2.4 ps. Long-lived residual absorption associated with the temporal profiles recorded in the 520 – 600 nm region is assigned to the long-lived T_1 state.

We have also investigated the temporal dynamics of the excited state of *p*-NPP in 1-propanol and 1-butanol, which are more viscous than ethanol. The lifetimes of the different processes involved in the relaxation of the excited states of *p*-NPP in these solvents are given in Table 6.1. It has been interesting to note that, in spite of an increase of viscosity of the solvents from ethanol to 1-butanol by about 2.5 times, the lifetimes associated with the $S_1(\text{LE})$ state or the nitro-twisting process are very similar (about 0.2 ps) and the lifetime of the $S_1(\text{ICT})$ state increases only marginally from 0.3 to 0.37 ps, so also the relaxation time occurring in the triplet manifold, which increases from 1.6 ps to 2.0 ps. The lifetime of the vibrational cooling process taking place in the ground electronic state does not show any regular trend and these values also do not show large variation.

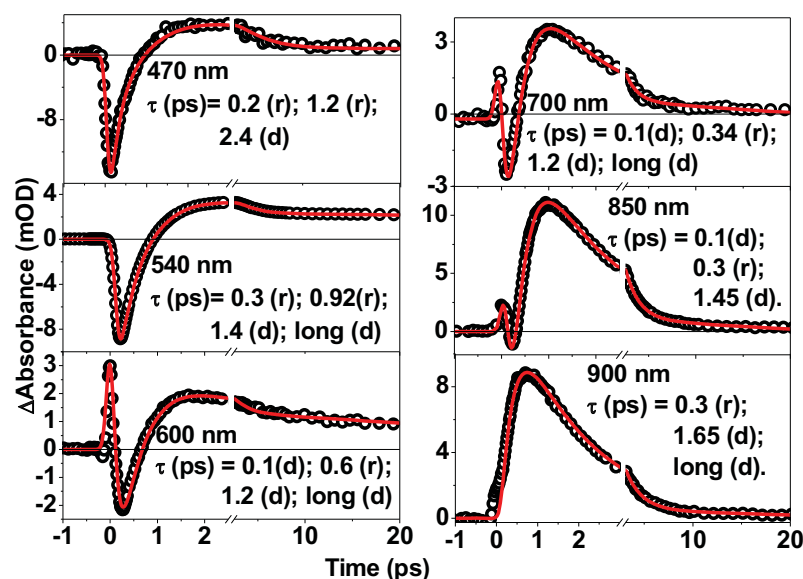


Figure 6.10. Temporal profiles recorded at a few selective wavelengths following photo-excitation of *p*-NPP in ethanol. Each of the temporal profiles is associated with a long-lived residual absorption.

6.3 Discussion

Our detailed investigation on the excited state dynamics of *p*-NPP in different kinds of solvents have revealed that the excited states of *p*-NPP undergo several ultrafast relaxation processes depending on the polarity of the solvent. The lifetimes of these processes are given in Table 6.2. The vibrationally relaxed S_1 (LE) state, which is formed within less than 100 fs following photoexcitation of *p*-NPP using 400 nm light, undergoes an ultrafast relaxation process, the lifetime of which is ≤ 200 fs, and is nearly independent of the polarity and viscosity of the solvents. In correlation with the earlier studies on the photophysics of similar kind of nitroaromatic compounds, we have assigned this lifetime to the conformational relaxation via twisting of the nitro group. However, consideration of the chemical structure of *p*-NPP molecule clearly suggests the only conformational relaxation process observed in this study may involve the twisting of either the 2-hydroxymethyl-pyrrolidine group or the nitro group. Our experimental results do not distinguish between these two kinds of processes. Similar arguments can also be put forth in the case of the earlier work published by Rafiq et. al.²⁶⁰ To resolve this issue, we have carried out quantum chemical calculations using time-dependent

density functional theory (TDDFT) to examine the possibility of either of these two intramolecular motions. Geometry optimized structures of the molecule, both in the ground and the S_1 states, are shown in Figure 6.11. In the ground state, all the three chromophoric groups, namely, 2-hydroxymethyl-pyrrolidine, the phenyl and the nitro groups, in the molecule reside on the same plane. In the optimized structure of the S_1 state, the nitro group is twisted at a plane perpendicular to that on which the other two groups reside. The TDDFT calculations show that the excitation to the S_1 state is strongly allowed (oscillator strength ~ 0.44) with the main contribution from the transition from the HOMO to the LUMO in the gas phase as well as in the polar solvents. HOMO is largely localized on the pyrrolidine and the phenyl rings whereas the LUMO is largely localized at the nitro group. This suggests that the S_1 state has a strong ICT character and explains the strong solvent polarity dependence of the absorption and fluorescence spectra.

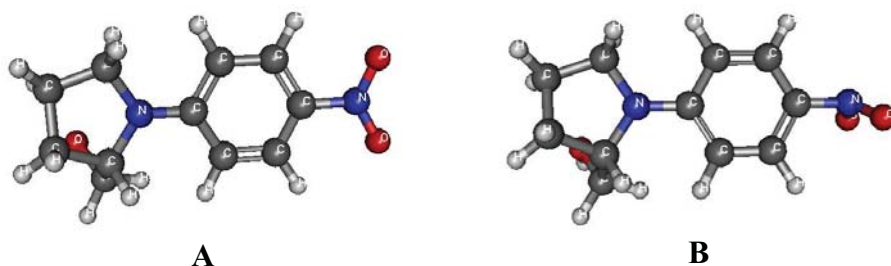


Figure 6.11. Gas phase optimized structure of *p*-NPP in the ground electronic state (A) and the first excited singlet state (B).

However, considering the possibility that structural relaxation in the S_1 state may occur via twisting of either the 2-hydroxymethyl-pyrrolidine group or the nitro group, we have calculated the potential energy surfaces for both the ground (S_0) and the S_1 states as a function of both the twisting coordinates. Figures 6.12A and 6.12B show the variations of the potential energies of both the S_0 and S_1 states as a function of the twisting angle of the nitro group and the 2-hydroxymethyl-pyrrolidine group, respectively. Excited state potential energy surface indicates that twisting of the 2-hydroxymethyl-pyrrolidine group leads to the minimum

energy at 90° but only after passing through a large barrier (~ 0.14 eV) existing at the twisting angle of 40° . On the other hand, the potential energy of the excited state decreases gradually as the nitro group is twisted and reaches to a minimum at its perpendicular configuration with respect to the rest of the molecule. These results suggest that twisting of the nitro group in the S_1 state is a barrierless process. In addition, we have seen earlier that geometry optimization of the S_1 state leads to a structure in which the nitro group resides on a plane perpendicular to that of the rest of the molecule. The structure of the S_1 state of PNA with the twisted nitro group was reported earlier from the TDDFT calculation.^{241,260} Therefore, the bulky and stronger donor group has not much effect on the conformational relaxation of the excited state of *p*-NPP. The excited state optimized geometrical parameters reveal one interesting feature that, in the S_1 state, the nitro group becomes pyramidal and the N-O bond lengths increase from 1.23 Å to 1.305 Å. This originates from the strong accepting nature of the nitro group, which induces large charge localization at the nitro moiety and thus increases the sp^3 character of the nitrogen atom of the NO_2 group. Pyramidalization of the nitrogen atom of the electron acceptor group following ICT process was earlier predicted by Sobolewski and Domcke.²³² This is also apparent from the HOMO – LUMO electron distribution in the ground and the excited state geometries. In the excited state geometry, the LUMO electron density is largely localized at the nitro group as compared to that in the FC state. Solvent independence of the lifetime of the ultrafast component (τ_{LE}/τ_{NT} in Table 6.2), which is associated with the nitro-twisting process, suggests that pyramidalization of the nitrogen atom is also associated along with twisting process due to rehybridization of the nitrogen. Therefore, this observation leads us to support the RICT concept of Sobolewski and Domcke, i.e. twisting of the nitro group via rehybridization of the nitrogen atom.²³²

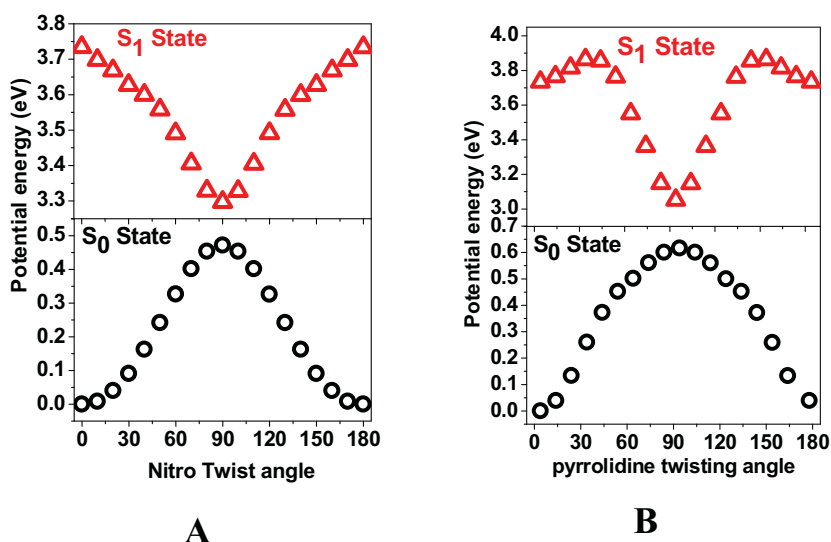


Figure 6.12. Potential energy surfaces in the S_0 and S_1 states of *p*-NPP with respect to the twisting angle of the Nitro group (A) and the 2-hydroxymethyl-pyrrolidine group (B).

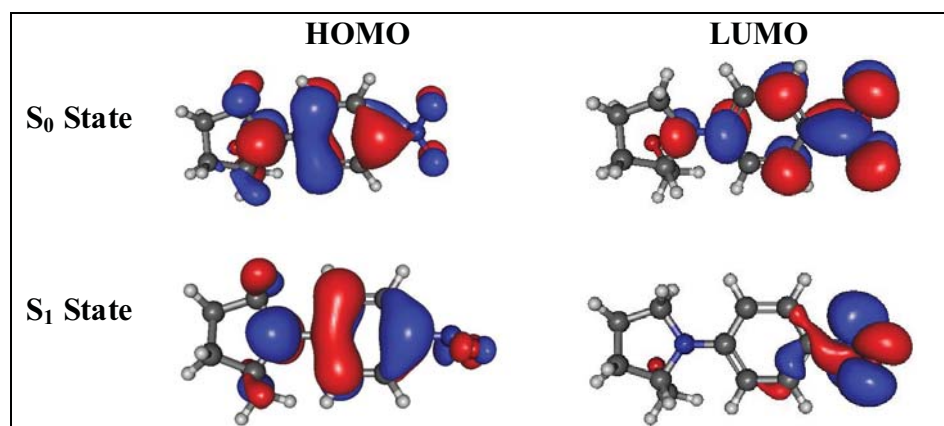


Figure 6.13. HOMO - LUMO pictures of the optimized ground and the first excited singlet states of *p*-NPP.

Our experimental results also have established the fact that ultrafast ISC and / or IC processes are responsible for the short lifetime of the S_1 state. Therefore, the other important aspect associated with the photophysics of *p*-NPP (as well as other nitroaniline derivatives) needs to be addressed is the predominance of either the IC or the ISC channels of the S_1 decay. Ultrafast ISC and IC processes are feasible only in the cases of isoenergicity and conical intersection (CI) or crossing between the potential energy surfaces (PES) of the S_1 state and the S_0 or T_n states, respectively. These issues as well as the solvent dependence of other relaxation processes can be explained by the schematic potential energy surface (PES) diagrams presented in Figure 6.14. Figure 6.14A represents the case for a solvent of lower polarity, e.g.

dioxane. Although the gas phase equilibrium geometry of nitroaromatics is predicted to be planar, DFT calculations indicate that the nitro group makes a twist angle of $\pm 27^\circ$ relative to the aromatic plane.^{236,256,273} As a consequence, a distribution of ground-state geometries with different twist angles can be expected at room temperature. Moreover, the S_0 - S_1 transition energy depends on the nitro twist angle and the light at a short wavelength predominantly interacts with the molecules having a large twist angle, while longer wavelength excitation photo-selects planar molecules.²⁶⁶ Although, the situation in solution might differ substantially from that calculated in the vacuum or gas phase, these calculations offer a good basis for a qualitative discussion of the excited-state dynamics of the nitroaniline derivatives. In solution, the range of oscillation of the nitro twisting angle in the S_0 state expected to be reduced significantly. However, it can be predicted that photoexcitation of *p*-NPP using 400 nm light, which falls in the red edge of the absorption spectrum of *p*-NPP in dioxane, leads to the S_1 (FC) state having a near planar geometry.

Rafiq et. al. calculated the PESs of the S_0 and S_1 states as well as the T_1 , T_2 and T_3 states as a function of the twisting angle of the nitro group in the gas phase. However, the relative energies of these excited states, which play important roles in the photophysics of *p*-NPP, are sensitive to the solvent polarity.²⁶⁰ The reason is that while the S_1 and T_1 have nearly 100% $\pi\pi^*$ character, T_3 has mainly $n\pi^*$ character and the T_2 state has mixed ($n\pi^*$ with some percentage of $\pi\pi^*$) character. In addition, the percentage of $\pi\pi^*$ and $n\pi^*$ character of the vertical excited states also varies with a change in the nitro twisting angles.^{251, 252} In vacuum or in the gas phase, the $S_1(\pi\pi^*)$ and $T_3(n\pi^*)$ states are nearly isoenergetic and the potential energy curves for the S_1 and T_3 states cross with each other.²³⁸ We can assume that ordering of these states in solvents of lower polarity does not change significantly from that in the gas phase. Therefore, in the case of low polarity solvents, deactivation of the S_1 (ICT) state takes

place exclusively by ISC to the $T_3(n\pi^*)$ state, which is an allowed process (El-Sayed rule).²⁷⁴ The ISC process is followed by IC and solvation processes occurring in the triplet manifold. This explains why the triplet yield is large in the case of p-NPP and other nitro aromatics in nonpolar solvents.

With increase in solvent polarity, the energy levels of the $S_1(\pi\pi^*)$ and $T_1(\pi\pi^*)$ states decrease and those of $T_3(n\pi^*)$ and $T_2(n\pi^*/\pi\pi^*)$ remains unchanged or increase marginally. Therefore, in highly polar solvents, e.g. acetonitrile, DMSO and water, the energy gap between the PESs of the S_1 and S_0 states reduces significantly and this ensures an ultrafast IC process from the S_1 to the S_0 state. In these solvents, the PESs of both the T_3 and T_2 states lie at higher energies than that of the S_1 state, eliminating the possibility of the ISC process. Figure 6.14C represents the PES diagram for the relaxation processes of the excited state of p-NPP in polar solvents. Although the PES of the $T_1(\pi\pi^*)$ remains below the $S_1(\pi\pi^*)$ state, the ISC from the latter state to the former is not an allowed process by El-Sayed rule.²⁷⁴ In this case, the IC process leads the molecule onto a FC region of the S_0 state of the molecule with the twisted nitro group and a large vibrational energy content. Therefore, the molecules need to relax in the S_0 state by reverse nitro twisting, which also should be associated with the dissipation of excess vibrational energy to the solvent molecules. The case of the solvents of medium polarity e.g. triacetin and alcohols, can be explained by the PES diagram given in Figure 6.14.B. In this case, possibly the S_1 state becomes isoenergetic with the T_2 state, which is not a pure $n\pi^*$ state but possess significant $\pi\pi^*$ character. Therefore, during the motion on the PES along the nitro twisting coordinate, the IC and ISC processes compete with each other leading to parallel transitions taking place from the S_1 state to the S_0 state as well as to the T_2 state. This diagram also explains the possibility of nitro twisting as well as vibrational relaxation processes both in the triplet and singlet manifolds.

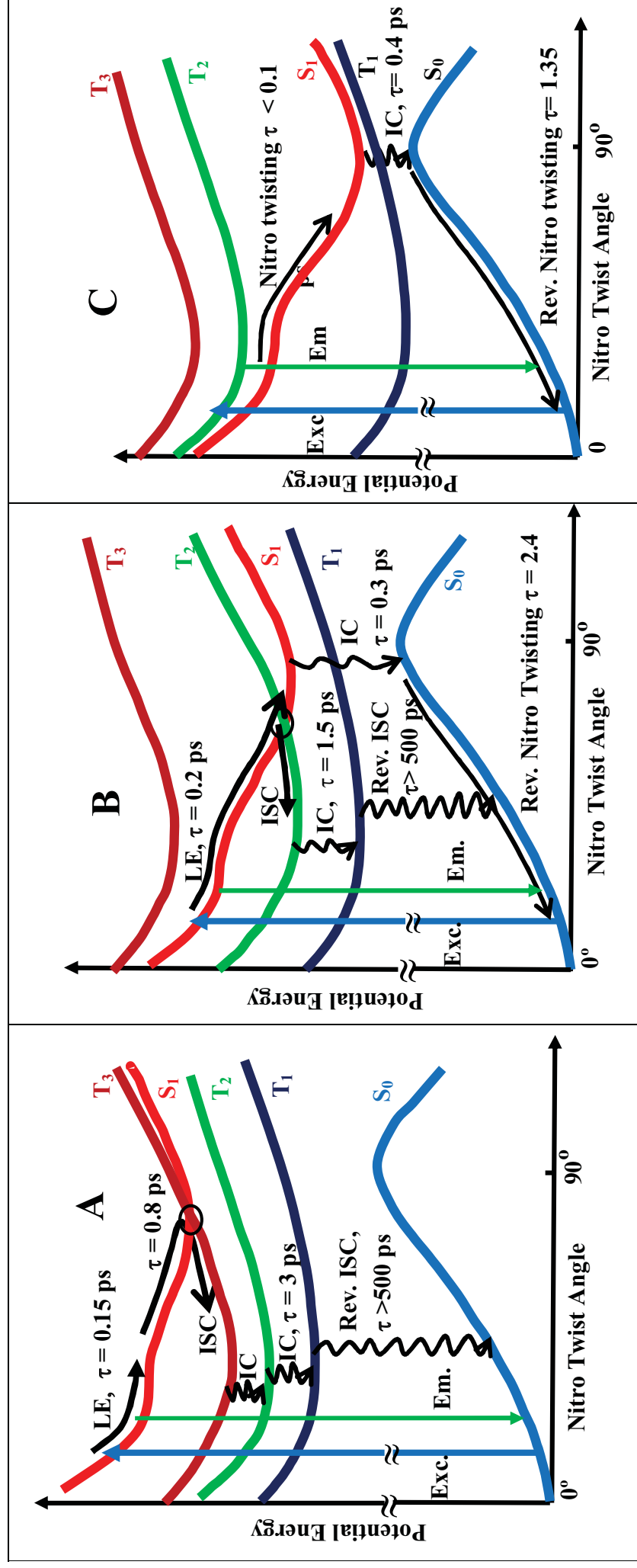


Figure 6.14. Schematic potential energy surface (PES) diagrams illustrating the different photophysical processes occurring in the excited states of p-NPP in solvents of low polarity (A), medium polarity (B) and large polarity (C).

6.4. Conclusion

In this chapter, detail dynamics of the excited states of 1-(p-Nitrophenyl)-2-hydroxymethylpyrrolidine (p-NPP) has been investigated using sub-picosecond transient absorption spectroscopic technique in different kinds of solvents. Following photoexcitation using 400 nm light, the molecule undergoes ultrafast vibrational relaxation in a time scale faster than the instrument response time. Subsequently, three major relaxation processes, namely, conformational relaxation via twisting of the nitro group, internal conversion (IC) and the intersystem crossing (ISC) have been established to be responsible for the ultrafast deactivation of the singlet excited (S_1) state. While the nitro twisting process has been observed in all kinds of solvents, relative probability of occurrence of the other two processes have been shown to be extremely sensitivity to solvent polarity, because of alteration of the relative energies of the excited states in the singlet and triplet manifolds. In the solvents of lower polarity, the ISC is predominant over the IC, because of near isoenergeticity of the $S_1(\pi\pi^*)$ and $T_3(n\pi^*)$ levels and the crossing of the potential energy surfaces (PESs) of these two states. In the solvents of larger polarity, the $S_1(\pi\pi^*)$ state becomes lower than both the $T_3(n\pi^*)$ and $T_2(n\pi^*/\pi\pi^*)$ states, but the $T_1(\pi\pi^*)$ state and the nitro twisting and the IC are predominant over the ISC, and hence the triplet yield is nearly negligible. In solvents of medium polarity, the PESs of the S_1 and T_2 states intersect and the excited state deactivation process is directed to both the IC and ISC channels.

Chapter 7

Charge Localization Dynamics in Heteroleptic Ruthenium Complex

7.1 Introduction

The charge transfer process is a pivotal step in the conversion of photochemical and photoelectrical energy in dye-sensitized solar cells, photoinduced water oxidation catalysis and artificial photosynthesis. Photoinduced charge-transfer processes in ruthenium(II) polypyridyl compounds have long been exploited for solar-energy harvesting due to strong metal to ligand charge transfer (MLCT) absorption in the visible region and relatively large stability in oxidized and reduced forms.²⁷⁵⁻²⁸⁰ Moreover, the spectral and photophysical properties can easily be tuned by introducing appropriate ligands. A great deal of efforts is spent to synthesize various ruthenium complexes containing different ligands in order to improve light absorption characteristics in the solar spectral region as well as to improve the charge transfer characteristics. Mixed ligand (heteroleptic) complexes found special importance for application in photovoltaic systems due to broadened MLCT absorption envelope with increased absorption cross section and thus a more efficient use of the solar spectrum for photoenergy conversion. In any of such molecular system, effective use of the photoexcitation energy is possible only if efficient charge separation is achieved in the excited state. Thus, detail understanding of metal to ligand charge transfer (MLCT) processes and excited-state relaxation dynamics of ruthenium polypyridyl complexes are of great importance, for both fundamental reason and potential applications in solar energy conversion. A great deal of research endeavor has been devoted towards molecular level understanding of the real time excited state dynamics of the ruthenium polypyridyl complexes.²⁸¹⁻²⁸⁹ Extensive studies on prototype $[\text{Ru}(\text{bpy})_3]^{2+}$ complex using time resolved spectroscopic techniques revealed ultrafast ISC (< 50 fs) process followed by vibrational relaxation to produce relaxed $^3\text{MLCT}$

within a picosecond timescale.²⁸¹⁻²⁸⁵ Another fundamental property is the localized nature of the electronic charge in the relaxed MLCT excited state. In the homoleptic D_3 symmetric complexes like $[\text{Ru}(\text{bpy})_3]^{2+}$, the excited state is expected to be symmetric and the charge transfer induced excited electron should be evenly shared between the three ligands. However, contrary to this expectation, it has been well established that the relaxed excited state is best described as one formally reduced bpy and two neutral ones (i.e. $[\text{Ru}^{\text{(III)}}(\text{bpy})^-(\text{bpy})_2]^{2+}$) and thus charge is localized in one ligand and the charge localization occurs in femtosecond timescale.²⁸⁶⁻²⁹⁵ Symmetry breaking via vibrational trapping or the solvent fluctuation has been proposed as the possible mechanism for charge localization.²⁹⁶ Though ultrafast dynamics of prototype $[\text{Ru}(\text{bpy})_3]^{2+}$ has been extensively studied to discern ISC, vibrational relaxation and charge localization process, real time dynamics of mixed ligand (heteroleptic) complexes have not been extensively undertaken and studies on such complexes has gained impetus in recent years.²⁹⁷⁻³⁰² As mentioned earlier, heteroleptic ruthenium complexes have gained a lot of interest in photovoltaic systems due to broadened MLCT absorption envelope covering solar spectrum due to multiple MLCT bands corresponding to different ligands. Effective use of the photoexcitation energy depends on the temporal kinetics of charge distribution around different ligands. The ultrafast spectroscopy of low-symmetry complexes is therefore of special interest not only for addressing fundamental questions regarding excited-state relaxation mechanisms but also for ultimate manipulation of excited state processes in molecular assemblies employing these types of complexes as photosensitizers. Time resolved vibrational studies in nanosecond timescale on many mixed ligand complexes strongly suggest that the photoexcited electron in the relaxed MLCT state is localized on the lowest energy ligand, at least on long timescale. Thus excitation to higher energy MLCT excited state will undergo interligand electron transfer (ILET) to generate the charge localized lowest energy MLCT state. However, the real time dynamics of the charge localization processes with subpicosecond time resolution

is still scarce and only a few studies are reported in literature.^{292, 300-302}

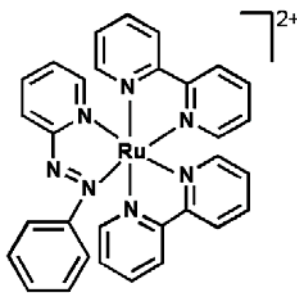


Figure 7.1. Structure of $[\text{Ru}(\text{bpy})_2(\text{pap})]^{2+}$

To explore the real time dynamics of charge transfer and vibrational relaxation of heteroleptic complex, the subpicosecond transient absorption spectroscopy of $[\text{Ru}(\text{bpy})_2(\text{pap})]^{2+}$, (where *bpy*= 2, 2'-bipyridine and *pap*= 2-(phenylazo)pyridine) (Figure 7.1) has been studied and detailed in this chapter. This complex allowed us to monitor the localization of charge from the *bpy* to *pap* ligand because of the stronger π -acidity of *pap* ligand in comparison to the *bpy* ligand and thus lowest MLCT state (either in the singlet or in triplet manifold) will be centered on the *pap* ligand whereas, *bpy* localized MLCT states will lie in next higher energy state. Optical excitation to the *bpy* centered $^1\text{MLCT}$ state will ultimately leads to the formation of lowest energy $^3\text{MLCT}$ state during the course of the excited state relaxation process which has been monitored by femtosecond transient absorption spectroscopy. Nanosecond laser flash photolysis and pulse radiolysis experiments confirmed the formation of charge localized state. This chapter describes the ultrafast charge localization and vibrational relaxation dynamics in this heteroleptic complex in few organic solvents as well as in aqueous solution.

7.2 Result and discussion

7.2.1 Steady-state absorption spectra: The steady state absorption spectra of $[\text{Ru}(\text{bpy})_2(\text{pap})]^{2+}$ in acetonitrile and water are shown in Figure 7.2. The similarity of the absorption spectra in the two solvents suggests that the electronic character and energies of the Franck-Condon singlet

excited MLCT states are not significantly solvent dependent. The absorption spectra in both the solvents mainly consist of two absorption bands above 300 nm, one is in 440-580 nm region having maxima at 490 nm and another one in 330-440 nm region having maxima at 370 nm. The important point to be noted is that the lowest energy absorption band is strongly red shifted in comparison to that of $[\text{Ru}(\text{bpy})_3]^{2+}$, in which lowest energy absorption maxima appears at 450 nm. The largely red shifted absorption band in $[\text{Ru}(\text{bpy})_2(\text{pap})]^{2+}$ can be ascribed to the metal to ligand charge transfer transition (MLCT) from Ru ($d\pi$) to *pap* (π^*) due to lower energy π^* state of strongly π -acidic *pap* ligand.³⁰³

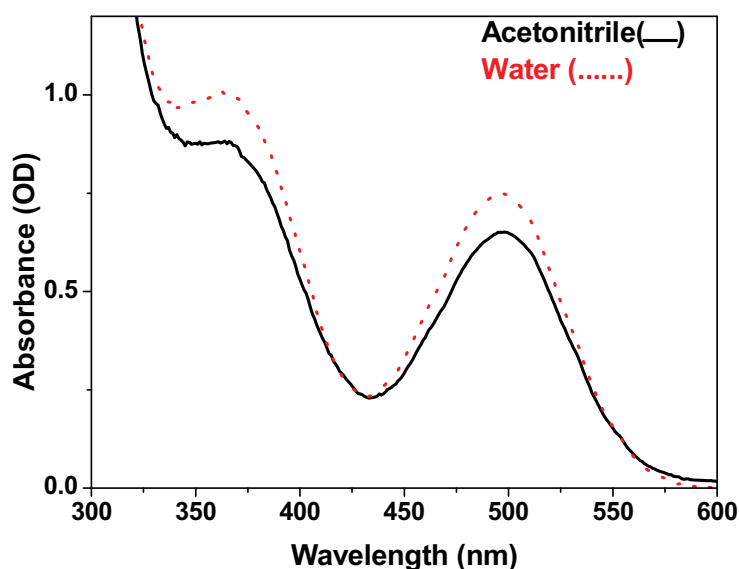


Figure 7.2. Steady state absorption spectra of $[\text{Ru}(\text{bpy})_2(\text{pap})]^{2+}$ in acetonitrile and water.

The higher energy absorption band in the visible region arises due to the MLCT transition from Ru ($d\pi$) to *bpy* (π^*) ligand. This transition appears at higher energy as compared to that of $[\text{Ru}(\text{bpy})_3]^{2+}$ complex due to the stronger π accepting character of the *pap* ligand which stabilizes the ruthenium $d\pi$ orbital leading to increase in the $\pi^*(\text{bpy}) \leftarrow \text{Ru}(d\pi)$ transition energy. This has been schematically illustrated in Figure 7.3. Systematic studies on the series of homoleptic and heteroleptic complexes have already established the general trend of absorption spectral shift by the variation of π accepting character of the ligands.³⁰⁰ The

absorption feature in UV region originates from the ligand centered transition as well as the higher energy MLCT transitions. However, the assignment of these higher energy transitions is not important for the present study.

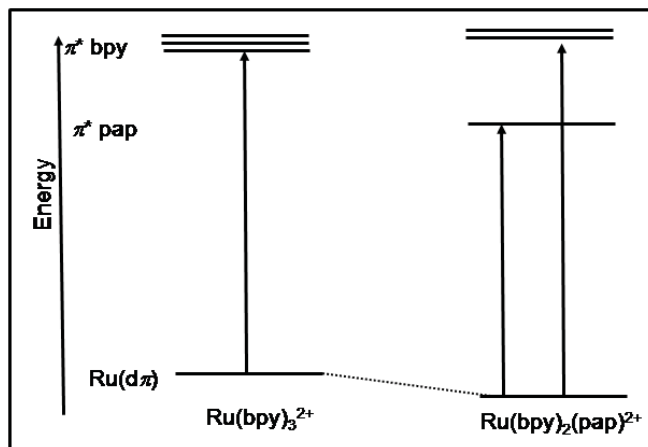


Figure 7.3. Simplified energy level diagram to compare the MLCT transition of $[\text{Ru}(\text{bpy})_2(\text{pap})]^{2+}$ and $[\text{Ru}(\text{bpy})_3]^{2+}$.

7.2.2. TDDFT calculation: The assignment of the absorption characteristics in the visible region has been supported from the TDDFT calculations. The TDDFT calculated transition energies, oscillator strengths and orbital contributions corresponding to different electronic excited state have been presented in Table 7.1 and the different molecular orbitals involved in the transition have been shown in Figure 7.4. It can be easily noted from the Figure 7.4 that the different occupied molecular orbitals (i.e. HOMO, HOMO-1 or HOMO-2) are mainly consist of ruthenium $d\pi$ orbital, whereas the lowest unoccupied orbital (LUMO) located mainly at *pap* ligand and the next two higher unoccupied orbitals (LUMO+1 and LUMO+2) located either of the two *bpy* ligands. It can be seen that the three lowest electronic excitations are associated with the charge transfer from the metal to *pap* ligand, among which $S_1 \rightarrow S_3$ transition (ca. 460nm) has appreciable oscillator strength. Considering the error involved in the TDDFT calculated energies, we can attribute the lowest energy absorption band observed at 440-550 nm to the MLCT transition to *pap* ligand. On the other hand, the higher energy electronic transitions are mainly associated with the metal to *bpy* ligand which appears below 430 nm.

Significant differences in the energy levels between *pap* and *bpy* ligands creates distinct MLCT energy manifold corresponding to the excitation of different ligand localized MLCT states. Thus, it can be concluded that 400 nm excitation preferentially (though not exclusively) produce *bpy* centered ¹MLCT excited state with significant vibrational energy.

Table 7.1. TDDFT (B3LYP/6-31++G, ECP (Ru)) calculated electronic excitation energies of [Ru(bpy)₂(pap)]²⁺ complex.

Electronic transition	Transition energy eV (nm)	Oscillator strength	Dominant orbital contribution
S ₀ →S ₁	1.93 (640)	0.001	HOMO→LUMO
S ₀ →S ₂	2.17 (570)	0.000	HOMO-1→LUMO
S ₀ →S ₃	2.7 (460)	0.080	HOMO-2→LUMO
S ₀ →S ₄	2.82 (438)	0.040	HOMO→LUMO+1
S ₀ →S ₅	2.84 (435)	0.01	HOMO→LUMO+2
S ₀ →S ₆	3.02 (412)	0.015	HOMO-4→LUMO
S ₀ →S ₇	3.07	0.025	HOMO-1→LUMO+1
S ₀ →S ₈	3.15	0.06	HOMO-1→LUMO+2

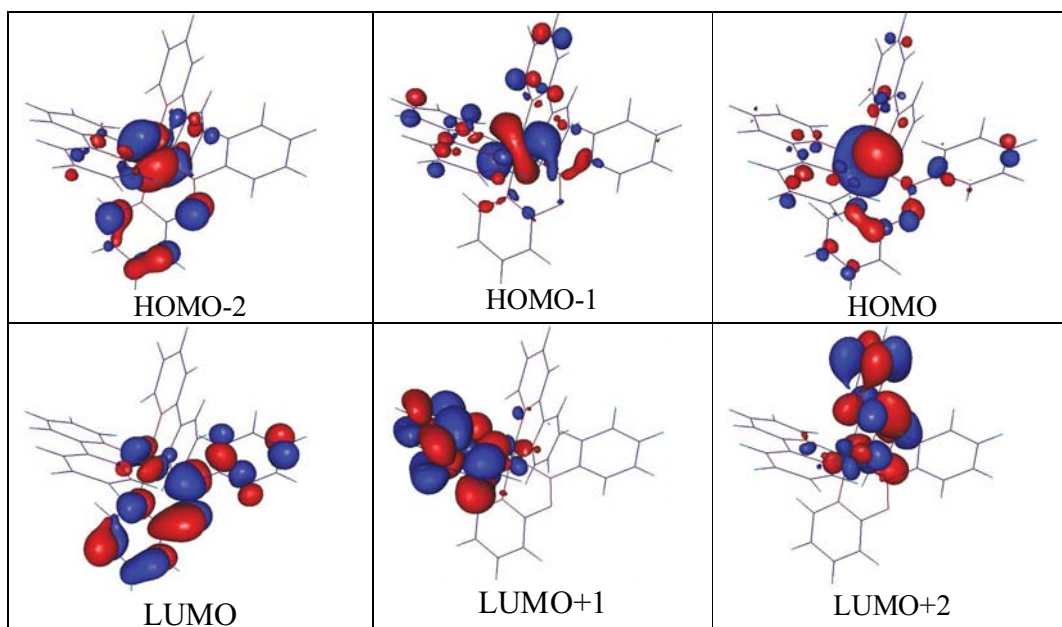


Figure 7.4. DFT calculated molecular orbitals associated with the different electronic transitions.

7.2.3. Nanosecond flash photolysis study: To determine the excited state properties of the complex, nanosecond flash photolysis experiments were performed. Figure 7.5 shows the TA

spectra of the complex in acetonitrile following 532 nm laser excitation. The TA spectral feature mainly shows bleach at 500 nm corresponding to the ground state absorption maxima. The excited state absorption has prominent features at 560 nm and 430 nm region. The apparently observed two ESA band may be due to the strong bleach band at 500 nm region which distorts the broad ESA band extended from 400 to 650 nm region. True ESA spectrum of the complex was extracted by subtracting the ground state absorption contribution in the excited state. A well defined ESA peak at 550 nm has been clear in the bleach corrected TA spectra. In the earlier section, we have shown that the lowest excited state is characterized by the Ru(d π) to *pap* (π^*) MLCT transition, thus the TA spectra is expected to have characteristic of the *pap* anion radical spectra. To understand the characteristics of the excited electronic state, ESA feature in visible region was compared with the *pap* radical anion spectra recorded using pulse radiolysis of *pap* in acetonitrile in deaerated condition (Figure 7.6). It can easily be noted that the *pap* anion radical spectra in the 400-650 nm region with maxima at 540 nm which resembles with the bleach corrected TA spectra measured in flash photolysis experiments. This clearly indicates that the lowest energy excited state of the complex is characterized by *pap* centered charge localized 3 MLCT state.

Analysis of the temporal kinetics of nanosecond flash photolysis at 500 and 570 nm shows that excited state decays single exponentially with 4.7 ns lifetime of the excited state. It can be noted that the lifetime of the complex is measured to be much shorter than prototype Ru(bpy) $_3^{2+}$ complex (~ 1 μ s in acetonitrile).²⁷⁷ This can partly be attributed to the lower energy of 3 MLCT state of the complex compare to the homoleptic Ru(bpy) $_3^{2+}$ complex and shorter lifetime is expected from the energy gap law. It is necessary to emphasize that the lower energy gap alone cannot account for the remarkable shortening of excited state lifetime of the complex. Strong nuclear displacement in the lowest energy triplet excited state impart stronger vibronic coupling with the ground state leading to faster excited state deactivation. This has

indeed been observed in several ruthenium or other metal complexes.³⁰⁴ The effect of lower energy gap and large nuclear displacement in the lowest energy triplet state has also been justified from the nonemissive nature of the complex.

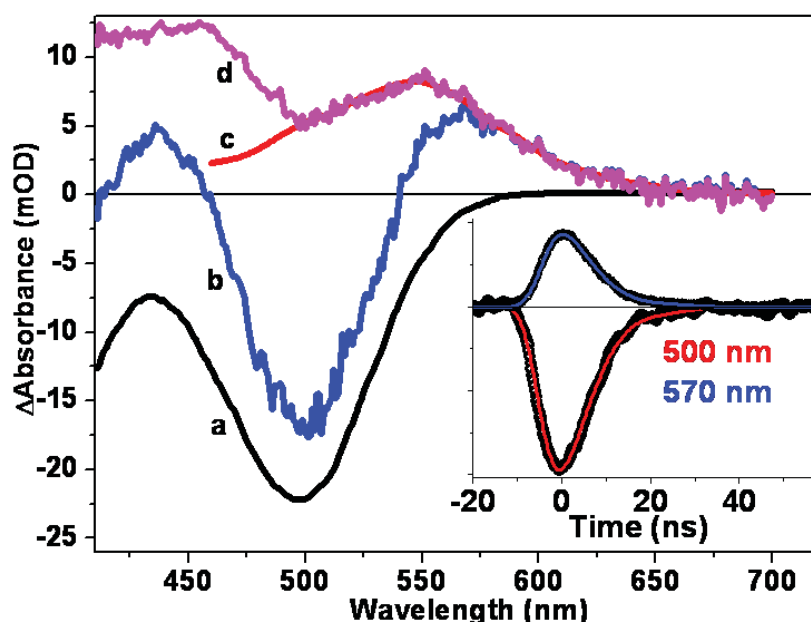


Figure 7.5. (a) Steady state absorption spectrum in acetonitrile (inverted); (b) Differential TA spectrum recorded immediately after photoexcitation of $[\text{Ru}(\text{bpy})_2(\text{pap})]^{2+}$ complex using nanosecond laser pulses; (c) TA spectrum of the anion radical of *pap* ligand using pulse radiolysis technique; (d) True TA spectrum of the $^3\text{MLCT}$ state of the $[\text{Ru}(\text{bpy})_2(\text{pap})]^{2+}$ complex. Insets: Temporal profiles recorded at 570 nm and 500 nm with the single exponential fit function (solid line) deconvoluted with the laser pulse width (6 ns).

7.2.4. Femtosecond transient absorption studies: To probe the relaxation dynamics in the excited state of the complex, femtosecond transient absorption studies in the visible region have been performed following photoexcitation to the bipyridine localized singlet MLCT states of $[\text{Ru}(\text{bpy})_2(\text{pap})]^{2+}$ complex. Figure 7.6 represents the time-resolved differential absorption spectra due to photoexcitation of $[\text{Ru}(\text{bpy})_2(\text{pap})]^{2+}$ in acetonitrile solution at room temperature using 400 nm laser pulses of 50 fs duration. 400 nm laser excitation dominantly excite *bpy* localized MLCT state. Transient absorption spectra at 0.2 ps timescale show a negative band below 530 nm corresponding to ground state bleaching and an excited state absorption band in 530-720 nm region.

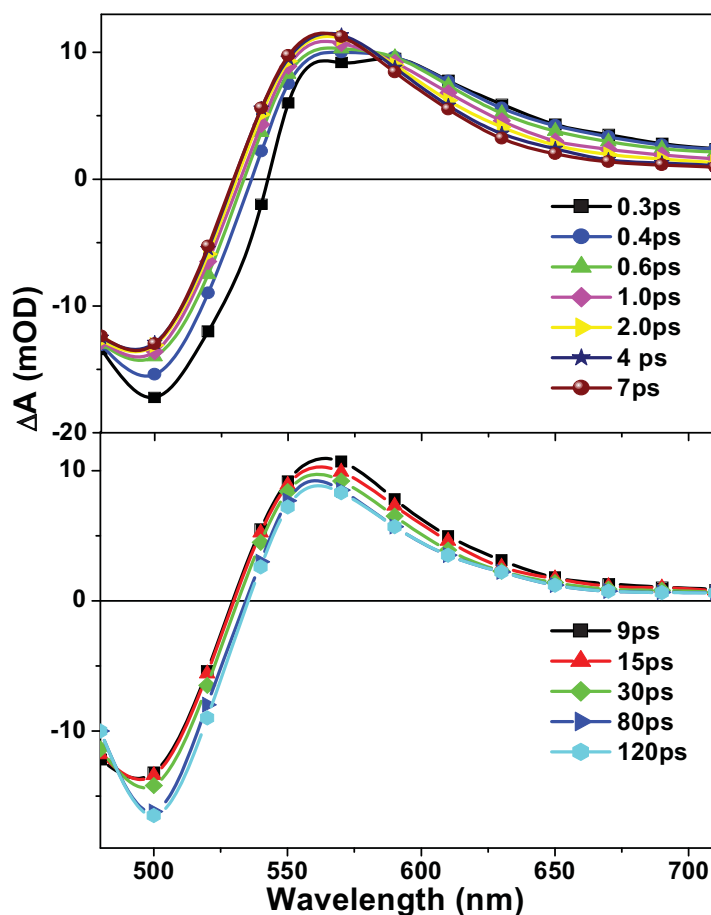


Figure 7.6. Transient absorption spectral evolution of $[\text{Ru}(\text{bpy})_2(\text{pap})]^{2+}$ in acetonitrile following 400 nm excitation.

In first 8 ps timescale, ESA band grows in 530-570 nm region and decay in 600-700 nm region showing an apparent isobestic point at 590 nm region. In this timescale, bleach band also apparently recovers partially due to the overlap with the excited state absorption in this region. With further time delay up to 100 ps, ESA band maxima slightly blue shifted and bleach band gains appreciable intensity. The temporal evolution of bleach band actually reflects the ESA band which is strongly overlapped with the bleach band in this spectral region. After 100 ps, the transient absorption spectrum does not evolve up to nanosecond timescale indicating long lifetime of the relaxed excited state. The TA spectra at >100 ps timescale nicely matches with the nanosecond TA spectra recorded in laser flash photolysis experiments. This clearly suggests that the completely thermalized lowest $^3\text{MLCT}$ excited state is produced in 100 ps

timescale which decays with 4.5 ns lifetime. As described in the earlier section, the thermalized lowest energy $^3\text{MLCT}$ state is characterized by *pap* localized state. Temporal isobestic point at early timescale of femtosecond TA experiment clearly indicates conversion between two distinct electronic states. Since the initial photoexcitation at 400 nm produces *bpy* localized MLCT states, the spectral growth observed in the 540-570 nm region is due to the charge localization to the *pap* ligand in the MLCT excited manifolds. The characteristic spectrum of the *pap* anion radical appears in 430-600 nm region with a maximum at 530 nm which has good resemblance with the ESA band of the TA spectra in longer time scale. Thus the growth of ESA band in the 550 nm region of TA spectra can be ascribed to the formation of *pap* localized $^3\text{MLCT}$ state which occurs in 8 ps timescale. Further evolution of the transient absorption spectra upto 100 ps possibly reflects the vibrational relaxation in the *pap* localized $^3\text{MLCT}$ potential energy surface. Temporal kinetics in a few selective wavelengths have been shown in Figure 7.7 along with the best multiexponential fit functions. Temporal analysis of the decay traces shows three component dynamics having time constants of 0.2-0.5 ps, 2.5 ± 0.1 ps and 16-35 ps along with a long lived (>1 ns) component corresponding to lifetime of the relaxed excited state. It is well established that in ruthenium polypyridyl complexes, intersystem crossing occurs in < 100 fs timescale and thus expected to be completed within the time resolution of the instrument. Thus, the three component dynamics observed in the present transient absorption study mainly reveal the kinetic feature of the relaxation dynamics occur in the $^3\text{MLCT}$ manifold following the ultrafast ISC process from the initially produced singlet MLCT state centered on bipyridine ligand. The first time constant (0.2-0.4 ps) can be tentatively assigned as the intramolecular vibrational redistribution after the ultrafast ISC process as observed for many other ruthenium complexes.²⁸¹⁻²⁸³ The second component with time constant of 2.5 ± 0.1 ps is attributed to the charge localization at the *pap* ligand which has been evident from the comparison of spectral characteristics of TA spectra with *pap* anion

radical spectra (vide supra). Thus, present result shows the ultrafast nature of the charge localization dynamics to the lowest energy $^3\text{MLCT}$ state in heteroleptic ruthenium complex. Earlier work of Papanikolas and coworkers on osmium polypyridyl complexes revealed ultrafast interligand electron transfer.²⁹² A recent study on ruthenium terpyridyl complex revealed 2.5 ps timescale for the interligand electron transfer dynamics.³⁰² Ultrafast localization of electronic charge in the excited state has also been observed for a DNA light switch complex, but occurs in relatively longer timescale.²⁹⁹

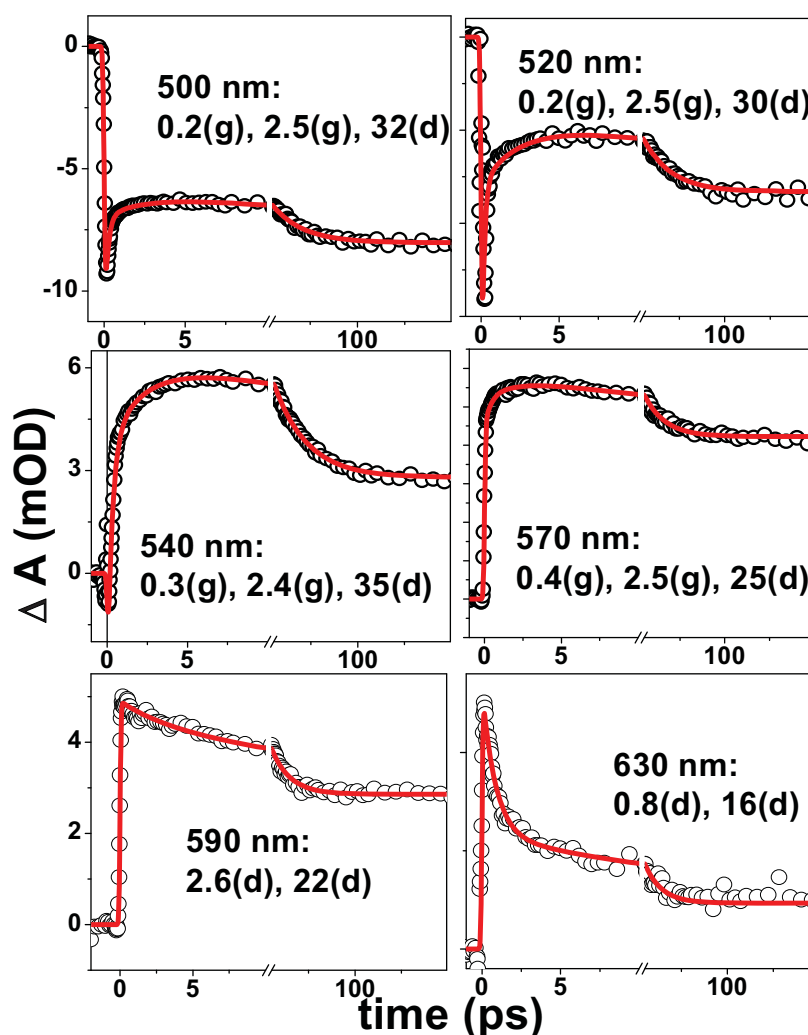


Figure 7.7. Temporal dynamics of $[\text{Ru}(\text{bpy})_2(\text{pap})]^{2+}$ in acetonitrile at different wavelengths along with triexponential fit function.

Third component possibly represents the thermalization of the *pap* localized $^3\text{MLCT}$ state via vibrational cooling process. The assignment of this component to vibrational

relaxation is justified from the significant wavelength dependence. The time constant of this component increases from 15 ps in 650 nm to 35 ps 540 nm.

We have also studied the temporal dynamics in few selective wavelengths in methanol, and in aqueous solution (Figure 7.8). Three component relaxation dynamics observed in these solvents are similar to that in acetonitrile. Time constants obtained from the multi-exponential fitting (given in inset of Figure 7.8) is also in similar range to that observed in acetonitrile. Thus, the observed dynamics are more or less independent of the solvent characteristics, although the studied solvents are of different polarity and solvation time. For example, the charge localization time in acetonitrile and methanol was found to be similar (2.5 ps and 2.7 ps, respectively) whereas solvation time differs significantly ($\langle\tau\rangle_{\text{sol}}$ is 0.5 ps and 5 ps). Absence of solvent polarity and solvation time effect on charge localization process can be explained by considering the fact that both the initial (*bpy* localized $^3\text{MLCT}$) and final (*pap* localized $^3\text{MLCT}$) state are almost equally polar and solvent polarity stabilizes both the state equally. In acetonitrile and water, time constant for the charge localization process is significantly longer than solvation time. This indicates intramolecular reorganization energy govern the kinetics of the process. It is known that charge accumulation at *pap* ligand results to significant bond length alteration at azo bond which contributes to large intramolecular reorganization.³⁰⁵ The ultrafast nature of charge localization process or interligand electron transfer process is possibly facilitated by the sufficiently strong coupling between the two diabatic electronic states, namely $^3\text{MLCT}$ (*bpy* localized) and $^3\text{MLCT}$ (*pap* localized). We could not monitor the dynamics in low polarity solvents due to insufficient solubility to acquire data with good signal to noise ratio. The detail mechanistic aspects of the charge localization dynamics can be enumerated by tuning the energy levels of the two MLCT states by introducing different donor and/or acceptor substituent either at *bpy* and *pap* ligand and this can be an important aspect of further studies.

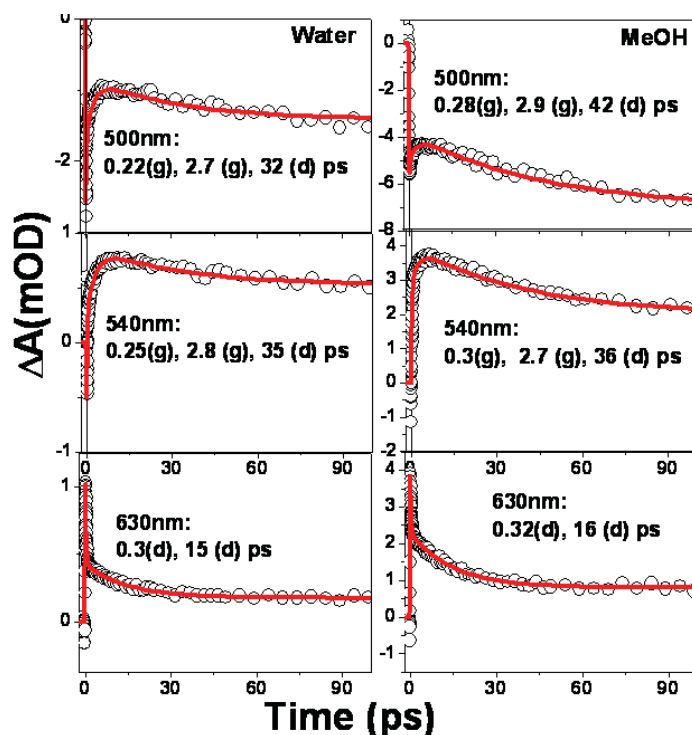


Figure 7.8. Temporal dynamics of $[\text{Ru}(\text{bpy})_2(\text{pap})]^{2+}$ in methanol and water at few selective wavelengths.

Another important aspect of the present study is the long timescale for vibrational relaxation process ($\sim 30\text{--}40$ ps). This deserves attention, as most of the earlier transient absorption studies of $\text{Ru}(\text{bpy})_3^{2+}$ proposed that the relaxed $^3\text{MLCT}$ state forms within a picoseconds timescale following the photoexcitation.^{281, 282} Similar time scale was also proposed from the results of fluorescence upconversion experiments.²⁸³ Despite such consensus in earlier studies, the issue of vibrational relaxation in ruthenium polypyridyl complex remains a subject of debate because recent time resolved infrared and Raman studies demonstrated that the formation of thermally relaxed $^3\text{MLCT}$ does not complete within 1 ps timescale rather takes 20 ps timescale for complete relaxation.²⁹⁷ Hammarstrom et al. also observed a 10 ps process, in their ultrafast transient absorption measurements at 360 nm probe wavelength which reveals an apparent discrepancy with the earlier reports of McCusker and coworkers.²⁹⁸ The difference in the results obtained was attributed to the difference in the probe wavelengths employed. In the earlier study of McCusker et al., the TA kinetics of $\text{Ru}(\text{bpy})_3^{2+}$ were probed in the 400–500 nm

region, where ground-state depletion is the dominant process.²⁸² In contrast, the 360 nm probe falls within the absorption band of the *bpy* anion radical (*bpy*^{•-}) species and, thus, the absorption of the thermally relaxed ³MLCT state, where most of the solvation and vibrational relaxation processes are expected to be observed. Based on similar argument, we can expect prominent dynamical feature for vibrational relaxation in the absorption region of *pap* anion radical (in 460-600 nm region). Our present transient absorption study monitors the dynamics in 480-600 nm region where 25-40 ps component has dominantly been observed. Thus, present TA study supports the conclusion drawn from the earlier time resolved vibrational studies as well as recent transient absorption results probed in the UV region.

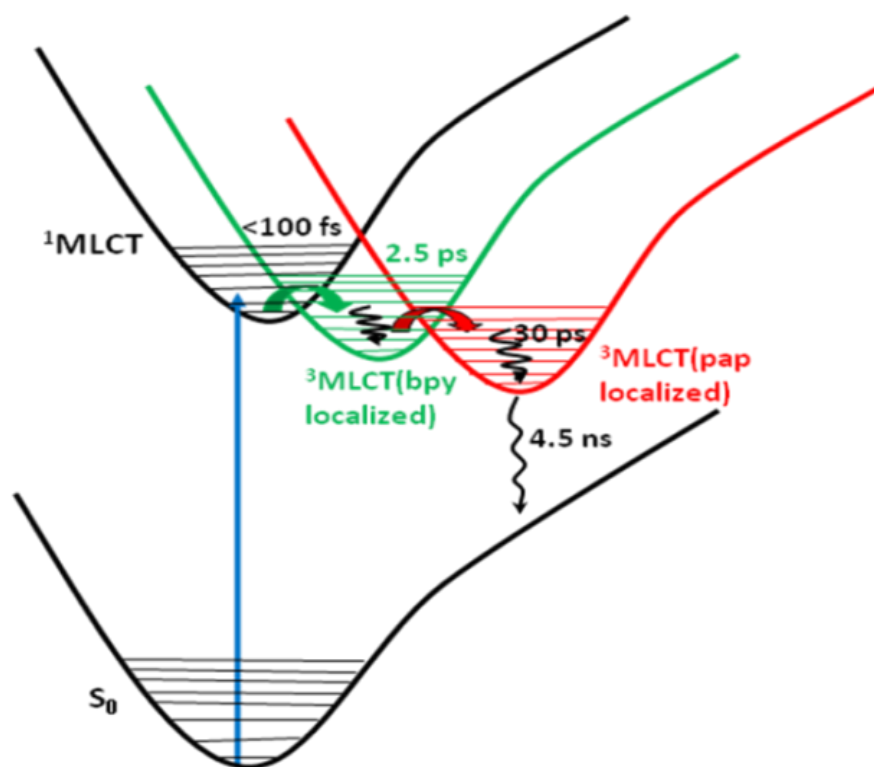


Figure 7.9. Simplified Schematic potential energy diagram showing excited state processes of $[\text{Ru}(\text{bpy})_2(\text{pap})]^{2+}$ in acetonitrile.

The overall dynamics of the studied complex can be described by the intramolecular vibrational redistribution, followed by charge localization to the phenylazopyridyl ligand and vibrational relaxation in the triplet manifold of the excited states of $[\text{Ru}(\text{bpy})_2(\text{pap})]^{2+}$ complex

which have been shown in Figure 7.9 using a simplified schematic potential energy diagram of the complex. Because of insufficient time resolution (~140 fs), the intersystem crossing process from $^1\text{MLCT}$ to $^3\text{MLCT}$ state could not be monitored which accomplished in <50 fs timescale.

7.3. Conclusion

In conclusion, we have probed the nanosecond and sub-picosecond dynamics of $[\text{Ru}(\text{bpy})_2(\text{pap})]^{2+}$ complex using transient absorption spectroscopic technique. Nanosecond TA spectra shows that lowest energy $^3\text{MLCT}$ state is localized on phenylazopyridine ligand which decays with 4.7 ns lifetime. Time-resolved absorption spectroscopy on the femtosecond time scale reveal that charge localization to the *pap* ligand take place in picosecond timescale. Though the current data cannot give detail mechanistic understanding of the electron transfer processes but it clearly reveals that the two diabatic $^3\text{MLCT}$ states are strongly coupled to induce ultrafast charge localization processes. The present experimental outcome also support the recent literature report which claims that vibrational cooling in the $^3\text{MLCT}$ manifold does not complete within a picosecond rather takes at least tens of picoseconds. The observations reported here may have important consequences for the design of supramolecular systems based on heteroleptic complexes for light harvesting system, as the charge localized state will determine the charge separation kinetics in covalently linked donor-acceptor system or interfacial electron injection efficiency in dye sensitized solar cell.

Chapter 8

Ultrafast Dynamics of the Excited States of the Uranyl Ion in Solutions

8.1 Introduction

Detailed investigation of the photochemistry of uranium(VI) received significant importance in the beginning of the nineteenth century from the discovery that uranyl oxalate provides a suitable actinometer and much later from the Manhattan project in relation to isotopic enrichment.^{306,307} Photochemistry of uranium compounds attracted wide interest from chemists and spectroscopists and the mechanism of photochemical reactions have been studied in detail.³⁰⁷⁻³²¹ Uranyl nitrates play an important role in the nuclear fuel cycle. Information on the electronic structure of various kinds of uranyl nitrate complexes in solution is very important to understand their stability and to design useful ligands. A typical form of uranyl nitrate in nitric acid solution is $\text{UO}_2(\text{NO}_3)_2 \cdot 2\text{H}_2\text{O}$, where the UO_2 species is surrounded by four oxygen atoms of the two bidentate nitrate groups and two oxygen atoms of the two equivalent water molecules.^{307,309,319} In the dihydrated crystals of uranyl nitrate, the uranyl group has the same ligands as in solution and the structure is considered to be similar to that in nitric acid solution. The electronic absorption and luminescence spectra of the uranyl ion (UO_2^{2+}) are probably the most extensively studied topics in the field of molecular spectroscopy of inorganic complexes. However, understanding yet remains far from complete. A comparison of a large set of different uranyl complexes has revealed that their electronic spectra exhibit remarkable similarities, even though they show extreme sensitivity to the environment and temperature.³¹¹⁻
³¹³ The steady-state absorption and emission spectra of the uranyl ion are spread in the 350-500

and 470-650 nm regions, respectively, with the well-defined vibrational structures in each spectrum (Figure 8.1). The absorption spectrum in the 350-500 nm region consists, almost invariably, of two or three low intensity band systems, but assignment of the electronic states involved in this spectrum is, however, rather controversial. McGlynn and Smith suggested that these absorption bands result from the transitions $^3\Pi_u \leftarrow ^1\Sigma_{g+}$ or $^3\Delta_u \leftarrow ^1\Sigma_{g+}$, with a preference to the former.³¹⁴ Because of the presence of significant spin-orbit coupling, this transition becomes reasonably intense ($\epsilon_{\text{max}} \sim 101 \text{ mol}^{-1} \text{ cm}^{-1}$), even though spin forbidden. They argued that these bands could be divided into three groups with origins at 22050 cm^{-1} (453 nm), 24215 cm^{-1} (415 nm), and 27000 cm^{-1} (370 nm), representing the three components of the triplet state, which is split by the local field. Further, vibronic fine structures are superimposed on these absorptions. Although Burrows and co-workers supported these arguments, Sidall and Prohaska questioned the assignment of these low energy bands to a triplet \leftarrow singlet transition.^{309,322} On the other hand, Görller-Walrand and Vanquickenborne, on the basis of their analyses by means of group theory and qualitative molecular orbital theory, showed that the band system situated at 20000 (500 nm) - 22000 cm^{-1} (450 nm) is due to a $^1\Phi_g \leftarrow ^1\Sigma_{g+}$ transition, while the band system at 22500 (440 nm) - 27000 cm^{-1} (370 nm) is due to $^1\Delta_g \leftarrow ^1\Sigma_{g+}$ transition.^{323,324} Volod'ko and co-workers also assigned the four series of lines in the 330-500 nm region to four separate singlet levels.³²⁵ Detailed spectroscopic studies have been reported by Denning on crystalline $\text{Cs}_2\text{UO}_2\text{Cl}_4$ and $\text{CsUO}_2(\text{NO}_3)_3$.³²⁶ Excitation energies for all states corresponding to the first seven excited states of $[\text{UO}_2]^{2+}$ are reported and are quite similar for the two different crystals. Spectroscopic measurements on uranyl nitrate complexes in aqueous solution also point to a limited effect of the $[[\text{UO}_2]^{2+}]/[(\text{NO}_3^-)]$ ratio on the excitation energies.³²⁷ The feature article by Denning presents the most current state of knowledge, both experimental and theoretical, about the electronic structure and bonding in uranyl ions and other related actinyl species.³²⁸ Many of the theoretical works reported recently also agree with the assignments made by him that the lower excited states located within the

20000-27000 cm^{-1} energy range correspond to excitations from the HOMO σ_u to the nonbonding f_δ and f_ϕ orbitals.³²⁹⁻³³⁴ These yield states that are labeled $^3,^1\Delta$ and $^3,^1\Phi$ states in the spin-orbit free picture. However, this assignment differs from that proposed by McGlynn and Smith who referred to π_u states arising from excitations out of π_g orbitals, which really appear at much higher in energy. Additionally, since the spin-orbit coupling mixes the singlet and triplet states, justification of using the triplet and singlet labels are questionable. The first detailed ab initio calculations were performed by Pitzer and his co-workers using a combined configuration interaction (CI) and spin-orbit coupling method, denoted as SOC-CI.^{329,330} A comparison of the calculated spectra of free, uncomplexed uranyl ion, $[\text{UO}_2]^{2+}$, with that of the complex $[\text{UO}_2\text{Cl}_4]^{2-}$ showed only a small shift of the excitation energy (at most 2000 cm^{-1}), and no change in the character of the low lying excited states.^{329,330} These observations all seem to indicate that the position of the low-lying excited states in uranyl ion complex is relatively independent of the nature or even of the mere presence of any weakly bound equatorial ligands. However, calculations performed by Pierloot and Beisen on the basis of multi-configurational perturbation theory, which is a second order perturbation theory based on a complete-active-space reference wave function (CASSCF/CASPT2), combined with a method to treat spin-orbit coupling on $[\text{UO}_2]^{2+}$ and $[\text{UO}_2\text{Cl}_4]^{2-}$, have indicated a considerable blue- shift (by 1500-4300 cm^{-1}) of the energies by the presence of the chloride ligands.³³¹ Rather a change in the character of the luminescent state from Δ_g in the case of $[\text{UO}_2]^{2+}$ to Π_g in the case of $[\text{UO}_2\text{Cl}_4]^{2-}$ has been found. More recently, Pierloot and van Besien have analyzed the lower part of the electronic spectra of $[\text{UO}_2]^{2+}$ and $[\text{UO}_2\text{Cl}_4]^{2-}$ by means of the relativistic time dependent density functional theory (TDDFT) formalism including the effects of spin-orbit coupling.³³² Results of these calculations were very much in conformity with the experimental data for $[\text{UO}_2\text{Cl}_4]^{2-}$. Comparison of the results for $[\text{UO}_2]^{2+}$ and $[\text{UO}_2\text{Cl}_4]^{2-}$ indicated that the energy levels of the excited states are not significantly dependent on the type of equatorial ligand supporting the conclusions of Pitzer and co-workers.^{329,330} All the lower

energy excited states arising from the excitation out of the σ_u highest occupied orbital to the nonbonding f_δ and f_ϕ orbitals are symmetric. R  al et al. optimized the geometries with D_{2h} symmetry constraints (which the uranyl nitrate belongs to), both at the all-electron and at the relativistic effective core potential (RECP) levels, adopting several different kinds of computational methods.³³⁴ Both these levels of calculations provided very similar geometries. However, the vertical and excitation energies determined using different methods at the spin-orbit free level were seen to vary widely. The potential energy curves along the symmetric vibrational mode relative to the ground state geometry were also calculated by different methods and compared to those determined by Pierloot and van Besien at the CASSCF/CASPT2 level.³³¹ Potential energy curves of the uranyl(VI) ion along the symmetric stretching mode computed with TD-DFT (B3LYP) and DFT/MRCI (BHLYP) methods indicated that the energy minima for the lower excited electronic energy levels arising from $\delta_u \rightarrow f_\delta$ (Δ_g) states and $\delta_u \rightarrow f_\phi$ (Φ_g) states are in the order ${}^3\Phi_g < {}^3\Delta_g < {}^1\Phi_g$ (i.e., ${}^3\Phi_g$ state is the lowest excited triplet state), whereas the same obtained using LR-CCSD method is ${}^3\Delta_g < {}^3\Phi_g < {}^1\Phi_g$ (i.e., ${}^3\Delta_g$ state is the lowest excited triplet state in this case). Calculation of Pierloot and van Beisen for $[\text{UO}_2]^{2+}$ also agreed with the later sequence of energy levels.³³¹ As we mentioned earlier, the striking features of all these methods of calculations are the wide variation of the positions of minimum energy as well as intersection of the individual potential energy curves. However, in spite of the fact that it is really difficult to determine the exact vertical excitation energies of these three lower energy excited states for the uranyl complex formed with various ligands, all these theoretical calculations indicate that the lowest and the next higher energy excited states of the uranyl compound are triplets, either ${}^3\Delta_g$ or ${}^3\Phi_g$ and the next higher energy level is the singlet state, ${}^1\Phi_g$. However, observing a good agreement between the energy of the lowest excited triplet level, as predicted by the TD-DFT and DFT/MRCI methods and that determined from the steady-state phosphorescence spectrum, we intend to accept that the lowest excited energy level of $[\text{UO}_2]^{2+}$ species is $T_1({}^3\Phi_g)$ and the next

two higher excited states are $T_2(^3\Delta_g)$ and $S_1(^1\Phi_g)$, respectively. Results of calculations by Görller-Walrand and Vanquickenborne also supports this assignment of two lower excited triplet states.^{323,324} Photoexcitation using 400 nm light possibly leads the molecule to the $S_1(^1\Phi_g)$ state. Uranyl salts in aqueous solution exhibit a highly structured luminescence spectrum in the 470-650 nm wavelength region both in the solid state and in solution.^{309,315,313,335-342} The lifetime of the luminescence decay of the excited state of uranyl perchlorate ion has been determined using single photon counting technique in D_2O and H_2O , and these values are 2.6 and 3.0 μs , respectively.^{315,335} Considering the very long lifetime of the excited state of a molecular species consisting of a heavy metal atom like uranium, which can induce a strong spin-orbit coupling mechanism in the excited states leading to very efficient intersystem crossing process, it becomes obvious that the luminescence takes place from the lowest excited triplet state.³⁴³⁻³⁴⁶ Therefore, the luminescence of uranyl compounds is strictly an example of phosphorescence,^{309,315,317,335-340} although a few groups of workers adhere to its description as fluorescence.^{341,342} Recently, Bernhard determined the lifetimes of the luminescence of the calcium salts of uranyl carbonates, both in aqueous solutions and in solid samples, using gated intensified array detector following excitation using 266 nm laser pulses.³⁴² The luminescence lifetimes measured in solutions have been shown to be much shorter (about 40 ns) as compared to those measured in solid samples (about 300 μs). Because of the short luminescence lifetime of the excited state in solution, the authors assigned it to fluorescence emission. However, similarities of the features of luminescence spectra of the uranyl carbonate salts to those reported for other uranyl salts clearly suggest that luminescence of the uranyl carbonate salts should also be assigned to phosphorescence.^{337-340,342} Nanosecond laser flash photolysis of uranyl compounds in aqueous solution yields a transient, which has been characterized as the triplet state. The absorption spectrum of the triplet state has λ_{max} at ca. 570 nm and the decay lifetime of this transient has been determined to be about 1.25

μs .^{309,315,347-349} This value is nearly in agreement with that of the luminescence lifetime of uranyl perchlorate or nitrate salts in aqueous solution. These facts confirm the assignment of the luminescence of uranyl salts to phosphorescence. While a number of reports have been published characterizing the photophysical and photochemical properties of the triplet states of the uranyl salts, initial events following photoexcitation is not yet known, which can provide information regarding the different lower energy electronic excited state pertinent to photophysical and photochemical properties of uranyl ion. In this chapter, we describe the relaxation dynamics of the higher excited singlet and triplet states of uranyl nitrate in aqueous and methanolic solutions using transient absorption spectroscopic technique having about 100 fs time resolution. Spectral and temporal evolution revealed that the relaxation of the higher excited states leads to the formation of the lowest excited triplet state, $T_1(^3\Phi_g)$, within a few picosecond following photoexcitation.

8.2. Results and discussion

8.2.1 Steady State Absorption and Fluorescence Studies: Figure 8.1 shows the normalized absorption and luminescence spectra of uranyl nitrate salt dissolved in aqueous solution of 1N nitric acid and in methanol. In aqueous solution, the vibronic bands of the absorption spectrum are not as well resolved as those in the luminescence spectrum. In methanol, the vibronic bands in both the absorption and luminescence spectra are poorly resolved and broad. It is also important to note that although the positions of the maxima of the luminescence bands nearly coincide with those observed in aqueous solution, the absorption maximum in methanol shows a significant shift (by about 18 nm) to lower energy with respect to that observed in aqueous solution. In aqueous nitric acid solutions, formation of three different complexes of uranyl nitrate, namely $[\text{UO}_2(\text{NO}_3)]^+$, $[\text{UO}_2(\text{NO}_3)_2]$, and $[\text{UO}_2(\text{NO}_3)_3]^-$ have been proposed by Houwer and Görller- Walrand, and they also illustrated the distribution of these three species, which exist in equilibrium in solution as a function of the concentration of nitrate ion.^{8,22,8.45} This work reveals that in a solution of 1N nitric acid, all these forms, including free $[\text{UO}_2]^{2+}$, are

likely to coexist. They have also determined the absorption spectroscopic properties of the free form as well as the mono-, di-, and trinitrato complexes (single component spectra) by deconvolution of the mixed species spectra.³²⁷ The most important results revealed by these analyses are that, by successive addition of the bidentate nitrate ion ligand to the uranyl ion, the vibronic structures become more well resolved with an overall shift of the band position toward the lower energy region.³²⁷ The different electronic transitions and the typical vibronic progressions in $[\text{UO}_2]^{2+}$ and $[\text{UO}_2(\text{NO}_3)]^+$ are not distinctly distinguishable because of lower symmetry, while those for $[\text{UO}_2(\text{NO}_3)_3]^-$ are well structured.

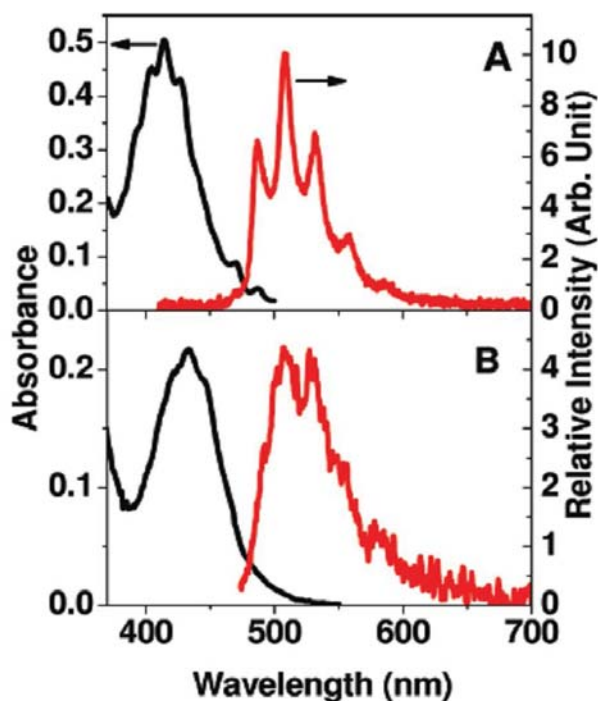


Figure 8.1. Normalized absorption and luminescence spectra of uranyl nitrate in aqueous solution of 1N nitric acid (A) and methanol (B).

Recently Ikeda-Ohno et al. used multiple spectroscopic techniques, such as UV-visible-NIR absorption and EXAFS, as well as DFT calculations to reveal the speciation and structures of the aquo-nitrate species of U(VI) in aqueous HNO_3 solutions.³⁵¹ Their results suggest that the U(VI)NO_3 complexation system in HNO_3 undergoes formation of a 5-fold bidentate coordinate mononitrato complex, $[\text{UO}_2(\text{NO}_3)(\text{H}_2\text{O})_3]^+$, and a 6-fold bidentate coordinate dinitrato complex, $[\text{UO}_2(\text{NO}_3)_2(\text{H}_2\text{O})_2]$, with increasing concentration of HNO_3 , terminating with the

formation of a bidentate coordinate trinitrato complex, $[\text{UO}_2(\text{NO}_3)_3]^-$. They have also concluded that the presence of unidentate coordinate complexes or a tetranitrato U(VI) complex is less probable in the aquo- HNO_3 system. Ikeda et al. have also investigated the speciation of U(VI) nitrate species in acetonitrile and identified the complex structures of the individual species in the system. With increasing nitrate concentrations up to 0.15 M, the spectra were gradually changed with better resolved and more intense vibronic absorption bands but no significant change in the spectral position.³⁵² The well resolved vibronic structures are the characteristic features of the trinitrato uranyl complex, $[\text{UO}_2(\text{NO}_3)_3]^-$, having higher symmetry.^{327,351} There was no further change of the spectrum by increasing nitrate concentration over 0.15 M. Hence, it was concluded that the trinitrato complex becomes the dominant species in higher nitrate concentration. Lahr and Knoch found evidence for the formation of $\text{UO}_2(\text{NO}_3)_2(\text{aq})$ in solutions of HNO_3 with concentration varying in the range 0-8 M HNO_3 .³⁵³ The same has been supported by the spectrophotometric study of Klygin et al., who found no evidence for HUO_2NO_3 but found evidence instead for $\text{HUO}_2(\text{NO}_3)_3(\text{aq})$ too.³⁵⁴ Lahr and Knoch also found evidence for the formation of $\text{HUO}_2(\text{NO}_3)_3$.⁴⁸ However, there is no reliable quantitative information on the enthalpy of formation of these different kinds of dioxouranium(VI) nitrate complexes.³⁵⁵ Figure 8.1 reveals that, in aqueous solution, the vibronic structures of the absorption spectra are not as well resolved as those predicted from the calculated single component spectrum of $[\text{UO}_2(\text{NO}_3)_3]^-$ and also not as blurred as predicted for $[\text{UO}_2(\text{NO}_3)]^+$.³²⁷ Hence, the reported results on spectral analyses and speciation of uranyl nitrate species led us to assume that our solution of uranyl nitrate in 1 N solution may contain all three complexes, namely, $[\text{UO}_2(\text{NO}_3)(\text{H}_2\text{O})_3]^+$, $[\text{UO}_2(\text{NO}_3)_2(\text{H}_2\text{O})_2]$, and $[\text{UO}_2(\text{NO}_3)_3]^-$ and we do not have precise knowledge about their relative compositions. However, both the theoretical and experimental results, as discussed above, lead us to predict no significant dependence of the nature of the lowest excited state energy levels on the kind of ligands but only a little variation in the vertical excitation energies. Hence, we may assume, as well, that

there will be no significant dependence of the spectroscopic and dynamic properties of the lower excited states of the uranyl ion on the composition of the solution containing different kinds of dioxouranium(VI) nitrate complexes. The species existing in methanol solution has earlier been identified as $\text{UO}_2(\text{NO}_3)_2 \cdot 2\text{CH}_3\text{OH}$.³⁵⁶ However, recent DFT calculations performed by Tsushima suggest that in the ground state geometry, in all cases, there is only a weak hydrogen bond between the solvent molecules and the axial oxygen and the structure of the complex should be represented by $\text{UO}_2(\text{NO}_3)_2(\text{H}_2\text{O})_2 \cdot \text{CH}_3\text{OH}$.³¹⁶ The shift of absorption maximum primarily reflects the change in $\text{U}-\text{O}_{\text{ax}}$ bond, because this absorption band originates from the electronic transition from HOMOs to LUMOs both of which are located on $[\text{UO}_2]^{2+}$ moiety.³¹⁶ However, the DFT calculation revealed that the $\text{O}_{\text{ax}} \cdots \text{H}$ distances between axial oxygen and alcohol is overall long, indicating only a weak interaction between the uranyl oxygen and alcohol. It has also been found that the $\text{O}_{\text{ax}} \cdots \text{H}$ distance is much longer when the axial linkage is formed via the methyl group than via the OH group. However, the Gibbs energy for the formation of the axial linkage via the methyl hydrogen is slightly lower than that via the hydroxyl oxygen. Hence, it has not been possible to conclude which linkage is energetically more preferred at the ground state. However, a large red shift (by about 18 nm) of the absorption maximum in methanol as compared to that in aqueous solution also possibly indicates the existence of much stronger interaction between the uranyl nitrate complex and methanol molecule via formation of an apical $\text{O}_{\text{ax}} \cdots \text{H}$ linkages between the excited state of UO_2^{2+} ion, $(\text{UO}_2^{2+})^*$, and alcohol molecules. Assuming that the lowest energy transition related to the absorption spectra of uranyl complex in solutions is assigned to $\text{T}_1(^3\Phi_g) \leftarrow \text{S}_0(^1\Sigma_g)$, the energy corresponding to the wavelength of crossing of the normalized absorption and phosphorescence spectra can be correlated with that of the phosphorescent state or the lowest excited triplet state, $\text{T}_1(^3\Phi_g)$. These values have been determined to be about 21008 and 20833 cm^{-1} (corresponding to the wavelengths of 476 and 480 nm) in aqueous and methanol solutions, respectively. This value agrees reasonably well with that of the lowest excited triplet

state ($^3\Phi_g$) obtained from the theoretical calculations using different methods varying in the range 20000-22000 cm^{-1} .³²⁸⁻³³⁴

8.2.2 Femtosecond Transient Absorption Spectroscopic Studies:

8.2.2.1 In Aqueous Solution. Figure 8.2 shows the time-resolved absorption spectra of the transient species created following photoexcitation of uranyl nitrate in aqueous solution of 1N nitric acid using 400 nm light. The transient spectrum constructed at 0.2 ps delay time shows a broad excited state absorption (ESA) band in the 500-800 nm region with a maximum at 630 nm and shoulders at ca. 570 and 720 nm. With increase in delay time up to about 1 ps, we observe a significant decrease of absorbance in the 700-800 nm region but a marginal growth of absorption at 630 nm. However, with a further increase in delay time up to about 10 ps, we observe a decrease in absorbance at 630 nm and the development of a new absorption maximum at ca. 570 nm. We observe the appearance of a temporary isosbestic point at ca. 610 nm during the evolution of the transient spectra in the 1-10 ps time domain. The spectrum recorded at 10 ps delay time can be assigned to the triplet state because of its similarity to that reported earlier.^{309,315,317,344} A numerous number of earlier studies showed that flash excitation of different kinds of uranyl salts in different kinds of media, including aqueous acid solutions, viscous media, doped glasses and others, yielded a broad intense absorption spectrum, which was seen to shift only slightly with change of medium with an absorption maximum at ca. 570 nm.³¹⁵ Figure 8.3 shows the temporal profiles, along with their bestfit functions, recorded at a few selective wavelengths. Because of overlapping of the absorption spectra of more than one excited states involved in the evolution of the time-resolved spectra shown in Figure 8.2, the dynamics of transient absorption is wavelength dependent. In the 690-800 nm region, where the absorption coefficient of the lowest excited triplet (T_1) state is negligibly small,^{315,347} transient absorption initially grows with the instrument response time, followed by a two exponential decay. Between these two decay components, the first one is ultrafast and its

lifetime is dependent on the monitoring wavelength and varies from 0.4 ps measured at 790 nm to 1 ps at 690 nm. This kind of wavelength dependent dynamics leads to band narrowing in the

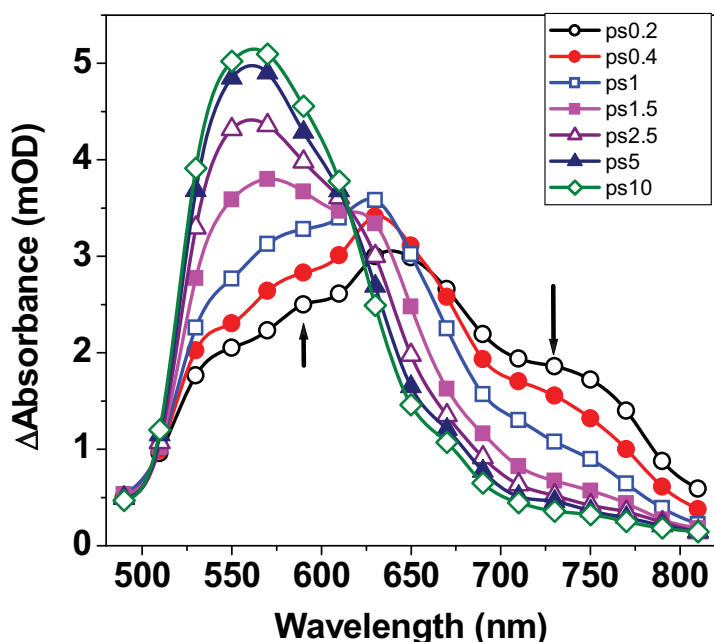


Figure 8.2. Time-resolved absorption spectra of the transient species created following photoexcitation of uranyl nitrate in aqueous solution of 1 N nitric acid using 400 nm light.

lower energy region of the spectrum and suggests the intramolecular vibrational relaxation of the excited state created with an excess vibrational energy. Following this decay, transient absorption reaches a residual value, which is also dependent on the wavelength, and the lifetime of this residual component is much longer than a few hundred picoseconds. On the other hand, each of the temporal profiles monitored in the 610-670 nm region shows another component with growing absorption, in addition to that growing with the instrument response time, and the former is followed by an exponential decay to reach the long-lived residual value. The lifetime of the slower growing component increases from 0.16 ps measured at 670 nm to 0.85 ps at 610 nm. The lifetime of the decay component ($\sim 0.95 \pm 0.1$ ps), however, does not show wavelength dependence in this wavelength region. The residual value of the longer-lived absorption increases gradually by changing the wavelength from 670 to 610 nm, at which the decay component is absent and transient absorption shows only the growth component of absorption followed by the component growing with the instrument response time. Further, the

temporal profiles monitored in the 530-590 nm region show twocomponent growth of transient absorption. The growth lifetimes of these components are 0.85 ± 0.1 and 1.6 ± 0.1 ps and the lifetimes are nearly independent of the monitoring wavelength in this region. The time-resolved spectra and the temporal dynamics as presented in Figures 8.2 and 8.3, in combination with the fact of appearance of a temporary isosbestic point at 610 nm in the time-resolved spectra, clearly suggest the involvement of at least three excited states or photophysical processes taking place in sub-10 ps time domain. Considering the fact that we have used laser light of 400 nm wavelength (energy $25\,000\text{ cm}^{-1}$) for excitation of the uranyl compound, we will consider only the lower excited states located within the $20000\text{--}25000\text{ cm}^{-1}$ energy range correspond to excitations from the HOMO σ_u to the nonbonding f_δ and f_ϕ orbitals.³²⁸⁻³³⁴

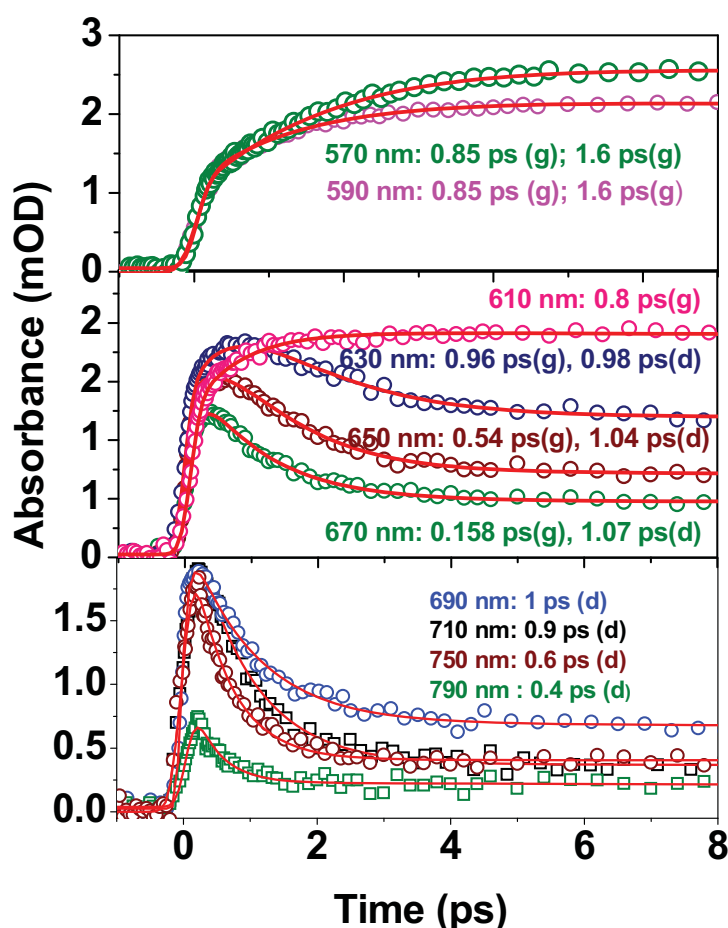


Figure 8.3. Temporal profiles recorded at a few selective wavelengths following photoexcitation of uranyl nitrate in 1M nitric acid solution. The solid lines represent the best fit multiexponential function associated with the temporal profile. The lifetimes of the ultrafast components are given in inset.

Following the detailed discussion presented in the Introduction of this chapter regarding identification of three lower energy excited states, we propose that three states, namely $^3\Phi_g$, $^3\Delta_g$, and $^1\Phi_g$ (in the order of increasing energy), are responsible for the photophysical processes observed following photoexcitation of uranyl nitrate in aqueous solution using 400 nm light. Following the potential energy schemes described by several authors earlier, the excited state relaxation processes taking place following photoexcitation of the uranyl nitrate ion in aqueous solution using 400 nm light can be described by the schematic potential energy surface diagram shown in Figure 8.4.³²⁸⁻³³⁴

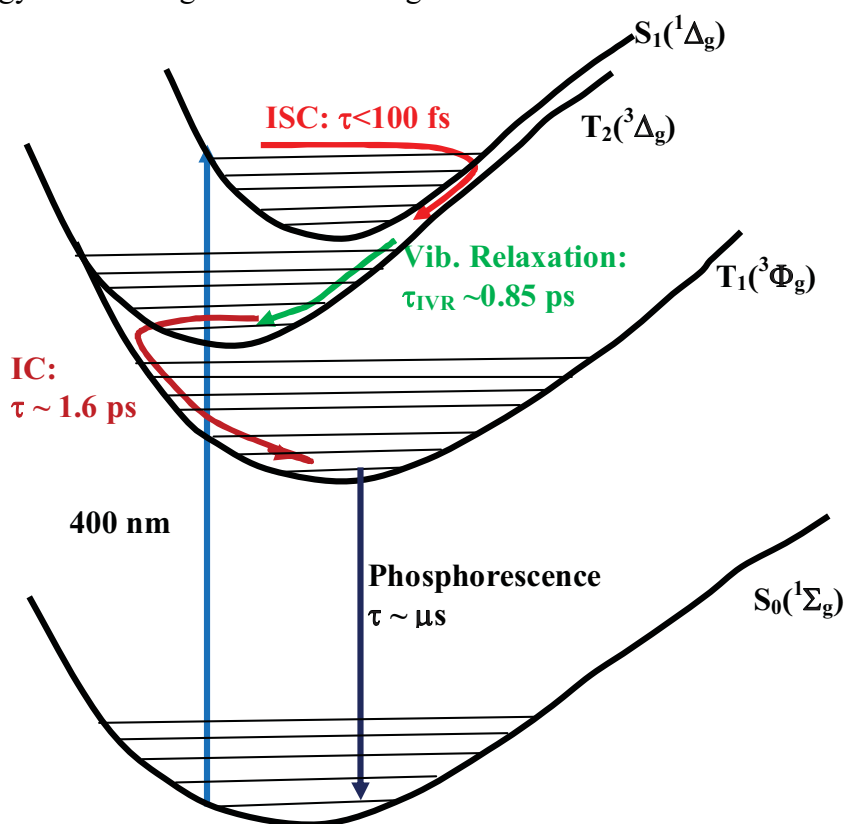


Figure 8.4. Schematic potential energy surface diagram depicting the excited state relaxation processes taking place following photoexcitation of the uranyl nitrate ion in aqueous solution using 400 nm light.

Uranyl nitrate ion is excited to the $S_1(^1\Phi_g)$ state with some amount of excess vibrational energy, the amount of which is not predictable, since the energy levels of these three states are not precisely known from spectroscopic measurements and those obtained from theoretical calculations vary significantly depending on the method of calculation as well as the structure of the complex. Because of the presence of the heavy atom in uranyl ion as well as the open

shells in the triplet states, the spin orbit coupling between the singlet and the triplet excited states is very strong.³⁴³⁻³⁴⁶ Therefore, the intersystem crossing process is expected to be extraordinarily fast and taking place in the sub- 100 fs time scale to cross over from the higher energy vibrational manifold of the $S_1(^1\Phi_g)$ state to the higher vibrational level of the $T_2(^3\Delta_g)$ state.³⁴⁴⁻³⁴⁶ Therefore, the lifetime of about 0.85 ps measured for this state in aqueous solution, can be assigned to the ultrafast intramolecular vibrational relaxation (IVR) process taking place in the $T_2(^3\Delta_g)$ state following the ultrafast ISC process.³⁴³⁻³⁴⁶ The latter is faster than the time-resolution of our spectrometer (~ 100 fs) and could not be resolved using our spectrometer. The spectral evolution observed within 1 and 5 ps time domain is associated with the decay of absorbance in the red region and growth in the blue region, resulting the occurrence of an isosbestic point at ca. 610 nm. This suggests the 1:1 conversion between two states, namely the conversion of the $T_2(^3\Delta_g)$ state to the lowest excited triplet, $T_1(^3\Phi_g)$ state via the internal conversion (IC) process. This process has the lifetime of about 1.6 ps in aqueous solution. The subsequent process is the radiative (phosphorescence) decay from the $T_1(^3\Phi_g)$ state to the $S_0(^1\Sigma_g)$ state.

8.2.2.2 In Methanol Solution. Figure 8.5 shows the time resolved absorption spectra of the transient species created following photoexcitation of uranyl nitrate dissolved in methanol using 400 nm laser pulses. We observed degradation of the sample following photoexcitation because of reaction between the triplet excited state of UO_2^{2+} ion via abstraction of a hydrogen atom from the solvent molecule.^{315,354-360} Hence special care has been taken for replacement of the sample during acquisition of the spectra. However, it is important to remember that we are concerned here with the dynamics of the shorter lived excited states prior to the formation of the longer lived lowest excited triplet state, which undergoes the photochemical reduction reaction.³¹⁵

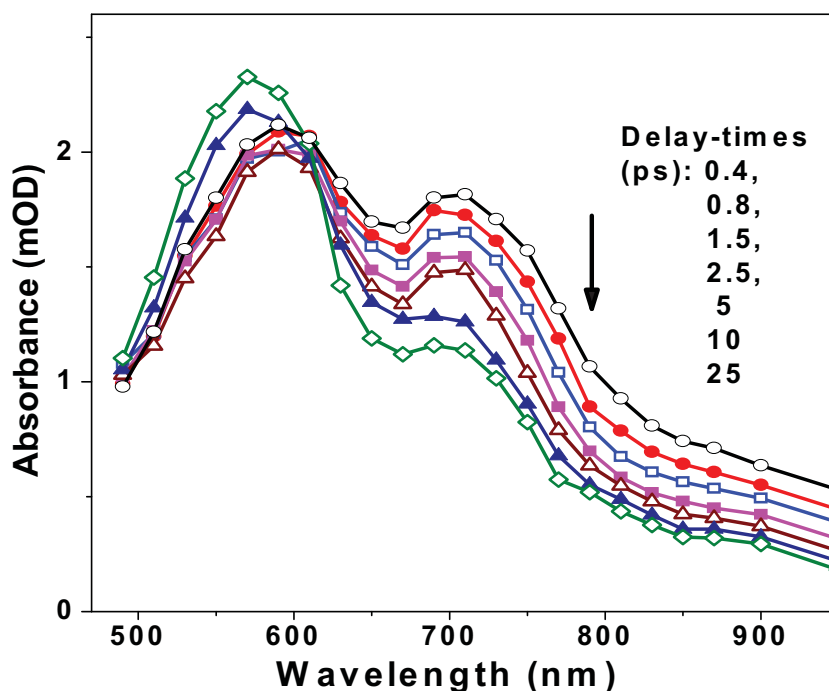


Figure 8.5. Time-resolved absorption spectra of the transients created following photoexcitation of uranyl nitrate in methanol using 400 nm light.

This reaction is not expected to alter the dynamics of the higher excited states being investigated here significantly. The transient spectrum recorded at 0.4 ps delay time consists of two distinct absorption bands with maxima at ca. 570 and 690 nm as well as a shoulder at ca. 800 nm. With an increase in delay time up to about 2.5 ps, all three absorption bands in the 470-950 nm region decay with very little change in the shape of the spectrum. However, with a further increase in delay time up to about 25 ps, absorption in the 650-800 nm region continues to decay, but that in the 530-600 nm region increases marginally. This indicates the involvement of two photophysical processes in the evolution of the time-resolved spectra presented in Figure 8.5. As a result of this evolution, the transient spectrum recorded at 25 ps delay time has the main absorption band with a maximum at 570 nm and another band appearing as a shoulder at ca. 690 nm. The characteristics of evolution of the time-resolved spectra in methanol are apparently not very similar to those observed in the case of aqueous solution. However, the temporal evolution of transient absorption in methanol reveals the similar kinds of processes as in the case of aqueous solution. The temporal profiles, which

reveal the nature of evolution of the transient absorption, recorded at a few selective wavelengths following photoexcitation of uranyl nitrate in methanol solution, along with the best fit functions and the associated lifetimes have been presented in Figure 8.6. The temporal profile recorded at 900 nm could be fitted with a biexponential decay function consisting of an ultrafast component with lifetime of about 0.4 ps and another long-lived component with lifetime longer than 500 ps, which can be assigned to the long-lived lowest excited triplet state.³¹⁵ However, each of the transient absorption decay profiles in the 650-850 nm region could be well-fitted with a triexponential decay function. While the lifetime of the third component is longer than 500 ps measured at all the wavelengths in this region, the decay of the other two components are ultrafast. The lifetime of the shortest component is wavelength dependent and the lifetime increases from 0.6 ps measured at 870 nm to 0.9 ps at 690 nm. This suggests the occurrence of IVR process, which is similar to that observed in aqueous solution. Assuming that the uranyl nitrate ion is excited to the $S_1(^1\Phi_g)$ state using 400 nm light, the ultrafast intersystem crossing process leads the excited uranyl ion to the higher vibrational levels of the $T_2(^3\Delta_g)$ state, which relaxes to the zero vibrational level with the lifetime of about 0.9 ps. The lifetime of the other component, shows a marginal increase as the wavelength is tuned from 850 to 690 nm. However, the average lifetime of this component is about 4.2 ± 0.3 ps and this can be assigned to the conversion of the $T_2(^3\Delta_g)$ state to the lowest excited triplet, $T_1(^3\Phi_g)$ state via the internal conversion (IC) process. Further, the nature of the temporal profiles recorded within the absorption band in the 520-600 nm region is wavelength dependent. Two such typical profiles recorded at 540 and 570 nm have been shown in Figure 8.6. Multiexponential fittings of these temporal profiles also revealed the occurrence of three photophysical processes with the lifetimes of about 0.9 ± 0.2 , 4.5 ± 0.3 , and >500 ps. These lifetimes agree well with those determined from the analyses of the temporal profiles recorded in the 690-900 nm wavelength region and can be assigned to the same processes. These results

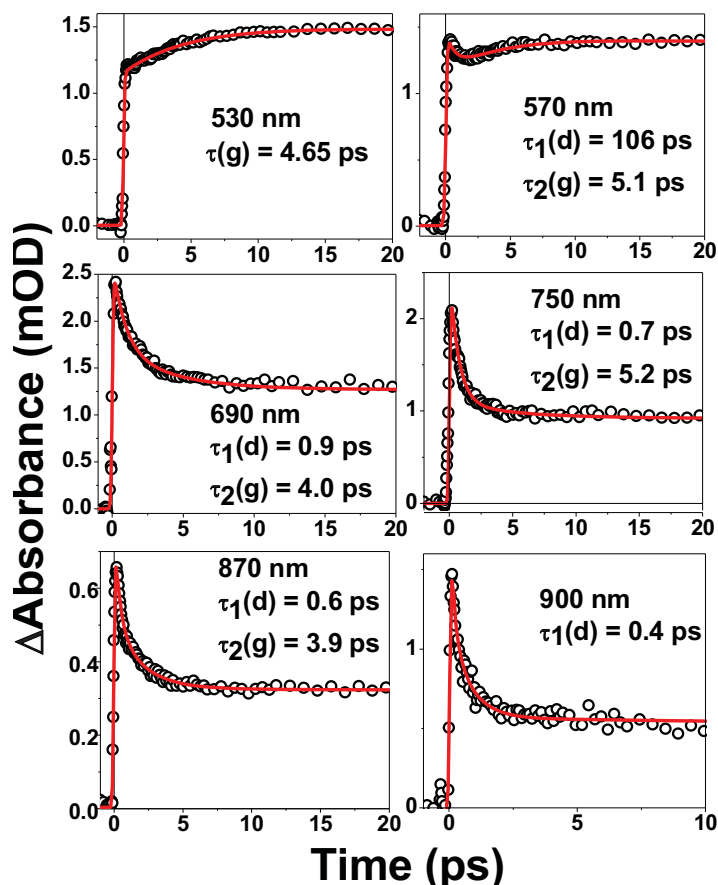


Figure 8.6. Temporal profiles recorded at a few selective wavelengths along with the best-fit functions, depicting the temporal evolution of the transient species created following photoexcitation of uranyl nitrate in methanol. The lifetimes of the ultrafast components associated with the best-fit functions are also given in the insets.

lead us to conclude that, like in the case of aqueous solution, vibrational relaxation followed by a process of interconversion between two transient states is responsible for the evolution of the time-resolved spectra presented in Figure 8.5. We observe that while the lifetimes of the vibrational relaxation process are comparable in aqueous and methanol solutions, the lifetimes of the IC process determined in methanol solution ($\tau_{ic} \sim 4.5$ ps) is much longer than that in aqueous solution ($\tau_{ic} \sim 1.6$ ps). This may indicate a larger energy gap between the $T_2(^3\Delta_g)$ and the $T_1(^3\Phi_g)$ states. We observe that although the analyses of the temporal profiles recorded over the entire 500-900 nm wavelength region in methanol solution, establish the prevalence of two photophysical processes (namely, vibrational relaxation, and internal conversion), which are similar to those occurring in aqueous solution, large dissimilarities in the characteristics of

the transient spectra in these two solvents (Figures 8.2 and 8.5) raise the question regarding the identities of the excited states in methanol solution, as shown in Figure 8.4. It is well-known that the UO_2^{2+} ion in aqueous alcoholic solutions or in neat alcohols can be photochemically reduced to UO_2^+ ion (and eventually to U^{4+} ion through disproportionation).^{307,309,357-360} Hill et al. investigated the spectra, kinetics, and reactivity of $(\text{UO}_2^{2+})^*$ by means of laser flash absorption spectroscopy (which enabled to identify the excited state absorption spectrum of $(\text{UO}_2^{2+})^*$), single photon counting (to enable to measure very short lifetime of UO_2^{2+*} in emission), and conventional or steady-state fluorescence measurements (enabling to determine the quenching mechanism, whether dynamic or static, by comparing the rate of quenching determined by other two methods).³¹⁵ They observed that both the 570 nm absorption (which is the characteristic of the triplet state) and the emission as determined by both single photon counting and steady-state fluorometry, were quenched on addition of various alcohols and the Stern-Volmer quenching constants were closely correlated with the absolute quenching constants for the transient determined by laser flash photolysis. Hence they concluded that the same electronic state of UO_2^{2+} is responsible for (i) emission to the ground state, (ii) the absorption at 570 nm to a higher excited state, and (iii) the photooxidation of aliphatic alcohols. Further, a close agreement between the quenching constants determined by the steady-state and time-resolved emission experiments throughout the range of alcohol concentration used (up to about 2 mol dm^{-3}) suggests that the dynamic nature of the quenching mechanism and not via formation of UO_2^{2+} -alcohol complex. In addition, detection of the $\text{R}_2\text{C}^*\text{OH}$ kind of radical in photolysis of glassy alcoholic solutions of UO_2^{2+} by ESR spectroscopic technique led them to suggest a mechanism of attack on alcohols via the type of reaction given in eq. 1.^{340,361} However, Ledwith et al. have succeeded in spin trapping the $\text{CH}_3\text{O}^\bullet$ radical in photolysis of UO_2^{2+} in neat methanol solution, but not in other neat alcohols.³⁶² This suggests the possibility of extraction of hydroxylic hydrogen too in neat methanol.



Tsushima studied the photochemical process of reduction of UO_2^{2+} to UO_2^+ in alcohols using DFT calculations.³¹⁶ As mentioned earlier (section 8.2.1), his calculation has revealed very weak interaction between UO_2^{2+} and methanol in the ground state via formation of a weak apical $\text{O}_{\text{ax}} \cdots \text{H}$ linkage. Again, at the ground state geometry of the UO_2^{2+} - H_2O complex too, the hydrogen bond between the water molecules and the axial oxygen is weak, but the apical $\text{O}_{\text{ax}} \cdots \text{H}$ distance is shorter than that in the UO_2^{2+} -methanol complex. However, in the excited triplet state, the situation becomes different. In the case of the UO_2^{2+} -methanol complex the $(\text{UO}_2^{2+})^*$ -to-alcohol apical $\text{O}_{\text{ax}} \cdots \text{H}$ linkage is significantly shortened and there is a partial electron outflow from the apical solvent to the uranyl ion. Consequently, $\text{U}^{\text{VI}}\text{O}_2^{2+}$ reduces to $\text{U}^{\text{V}}\text{O}(\text{OH})^{2+}$ via a hydrogen abstraction reaction from alcohol. On the other hand, in the case of the UO_2^{2+} - H_2O complex, the lowest excited triplet state is mostly metal-centered charge transfer (MCCT) or metal to ligand charge transfer (MLCT) states, although some contribution from uranyl to solvent charge transfer has also been found. Hence, the charge remains localized mainly within the UO_2^{2+} unit and hence the interaction between the $(\text{UO}_2^{2+})^*$ and apical H_2O molecule remains weak in the excited state. This is also revealed by the similar apical $\text{O}_{\text{ax}} \cdots \text{H}$ distances in the ground and excited states of the UO_2^{2+} - H_2O complex. In the light of the above discussion, it becomes obvious that the mechanism of photooxidation of alcohols by the excited state of the uranyl ion, $(\text{UO}_2^{2+})^*$ may follow different mechanisms in aqueous-alcoholic solutions (in which the alcohol concentration used is about 2 mol dm^{-3}) and in neat methanol. In the former case, $(\text{UO}_2^{2+})^*$ may retain its structure as that has been predicted in aqueous solution, and hence the energy level diagram and the relaxation dynamics should be very similar to that observed in aqueous solution (Figure 8.4). However, in neat methanol, because of stronger interaction via solvent to uranyl charge transfer in the excited state, possibly the lowest excited triplet state, $\text{T}_1(^3\Phi_g)$, gains solvent-uranyl charge transfer character, leading to partial reduction of U(VI) to U(V) in neat methanol solution to form a

transient species having the structure $[\text{UO}(\text{OH})^{2+}]^*$.³¹⁶ Hence the structure of the lowest excited triplet state in methanol is different than that in aqueous solution. The energy level of the latter species is possibly lower than that of $(\text{UO}_2^{2+})^*$ and hence increasing the energy gap between the T_2 and T_1 states. These arguments possibly explain the different spectral characteristics of the transient species produced in neat methanol and aqueous solutions as well as the longer lifetime of the IC process in methanol solution, which have been observed in the present work. To the best of our knowledge, this is the first report on the relaxation dynamics of the excited state of uranyl ion to establish different kinds of interactions between $(\text{UO}_2^{2+})^*$ and the solvent in aqueous and methanolic solutions, as theoretically predicted by Tsushima.³¹⁶

8.3 Conclusion

In conclusion, ultrafast events on visible excitation of uranyl ion in aqueous and methanolic solution have been deciphered using femtosecond time resolved transient absorption spectroscopy. Following 400 nm laser excitation, The $S_1(^1\Phi_g)$ state undergoes ultrafast intersystem crossing ($\tau_{\text{ISC}} < 100$ fs) to the higher vibrational levels of the $T_2(^3\Delta_g)$ state, followed by the intramolecular vibrational relaxation (IVR) process in the later electronic state ($\tau_{\text{IVR}} \sim 0.85$ and 1 ps in aqueous and methanolic solutions, respectively). Subsequently, the $T_2(^3\Delta_g)$ state undergoes an internal conversion (IC) process ($\tau_{\text{IC}} \sim 1.6$ and 4.5 ps in aqueous and methanol solutions, respectively) to the long-lived $T_1(^3\Phi_g)$ state, which is responsible for the luminescent properties of the uranyl ion. In neat methanol, because of stronger interaction between the excited triplet, $T_1(^3\Phi_g)$, state and the solvent via solvent to uranyl charge transfer, the U(VI) ion undergoes partial reduction to U(V) and the energy level of this state possibly lies lower than that of $(\text{UO}_2^{2+})^*$, which is the transient species existing in aqueous solution, and hence increasing the energy gap between the T_2 and T_1 states in methanol solution. These facts possibly explain different spectral characteristics of the transient species produced in methanol and aqueous solutions as well as the longer lifetime of the IC process in methanol solution.

Summary and Outlook

In this thesis, we have made an effort to understand structure-dynamics relation in photoinduced electronic excited states of various model molecular systems. The main emphasis has been elucidation of intramolecular charge transfer and proton transfer reactions and associated large amplitude structural relaxation dynamics to discern the role of electronic and geometric factors responsible for the dynamical evolution of the excited electronic states. Effects of solvent polarity, proticity and viscosity have been extensively studied to understand charge transfer excited state and their relaxation dynamics in real time. In inorganic systems, intersystem crossing is known to be a general phenomenon which occurs in ultrafast timescale. The rate of ISC and subsequent charge transfer dynamics in triplet manifolds plays crucial role in many applications such as solar energy harvesting. As these processes occur in ultrafast timescale, femtosecond time resolved transient absorption and fluorescence spectroscopy are proved to be efficient techniques to disentangle the complex relaxation dynamics of several competing pathways. Here we summarize the observations made from femtosecond studies of different chemical systems.

In chapter 3, we have described the excited state relaxation and deactivation processes of curcumin in various solvents. In polar solvents, solvation was revealed to be the main relaxation process. Because of six membered intramolecular hydrogen bonded structure with flexible geometry, excited state intramolecular proton transfer and isomerization reaction can be important excited state events in curcumin. In nonpolar solvents, ESIPT was proposed to reduce excited state lifetime, though ESIPT process could not be monitored due to the symmetrical structure around the keto-enol moiety. To monitor ESIPT dynamics, an unsymmetrically substituted 1, 3-diketone (DMADK) with high degree of charge transfer was synthesized and ultrafast relaxation studies were performed as described in chapter 4. An

ultrafast ESIPT reaction was observed in all solvents but direction of proton transfer was found to be strongly solvent dependent. In high polarity solvents, large amplitude twisting motion of dimethylanilino group was observed to follow ESIPT process. ESIPT, charge transfer, solvation and large amplitude structural relaxation in femtosecond to picoseconds time domain was revealed to participate in excited state relaxation of charge transfer keto-enol molecule.

The dynamics of twisted intramolecular charge transfer (TICT) reaction has long been of interest in the field of photochemistry. The necessity of twisting for attainment of high degree of charge transfer has been intensely debated for over a few decades. On one side, compelling evidences for TICT in dimethylaminobenzonitrile family have been put forward, highly intramolecular charge transfer state without twisting has also been observed in many molecular systems. From the comparative studies on two isomeric dimethylaminochalcones (DMAC-A and DMAC-B), we have shown in chapter 5 that degree of conjugation between the donor and acceptor group plays important roles to govern twisting relaxation in the excited state. When conjugation length is large (DMAC-B), large charge transfer is attained in polar solvents without TICT relaxation. Whereas, in short conjugated system ultrafast relaxation to TICT state is the dominant reaction. On the other hand in nonpolar solvents, ICT-TICT relaxation is inhibited for both the molecules and ISC becomes the common relaxation mechanism. We have further shown in chapter 6 that in case of extremely high charge transfer systems due to large donor/acceptor strength of the D-A molecules, twisting relaxation may be operative even in nonpolar media followed by other relaxation events depending upon solvent polarity. This has been extensively illustrated in the excited state dynamics of p-NPP molecule, where nitro group imparts very large charge transfer due to strong electron accepting ability of nitro group. A generalized picture of proton and charge transfer reactions may be obtained from the studies of various molecular systems with fine tuned electronic structure. Future exploration in this direction is warranted for better understanding of elusive factors behind molecular level control of excited state reaction dynamics.

Summary and Outlook

Emission property of uranium is known from over a century. Emission lifetime of different uranyl complexes have been used for speciation studies. Long lifetime of uranyl ion emission has been understood to be the phosphorescence phenomenon which originates from the lowest energy excited triplet state. But, the initial events following photo excitation were not well studied. As described in chapter 7, our study revealed that ultrafast ISC process followed by vibrational relaxation and internal conversion take place in a few picoseconds timescale to form the long lived excited triplet state responsible for phosphorescence emission. We believe this study on uranyl ion would be an important step towards revelation of excited state dynamical aspects of various lanthanide and actinide complexes. The detailed dynamical information of excited state relaxation may open up potential utilization of heavy metal complexes in optoelectronic devices.

In chapter 8, dynamics of a heteroleptic ruthenium complex has revealed an ultrafast charge localization process to the lower energy π accepting ligand. The localized nature of electronic charge in the lowest energy $^3\text{MLCT}$ state and its formation in ultrafast timescale may have huge impact on subsequent electron transfer dynamics in multi-chromophoric assembly which can significantly affect the solar energy harvesting efficiency. A generalized picture of charge localized state and corresponding timescale can be achieved by employing varieties of ligand substituted complexes which can be an important research direction in future.

The investigations presented in the thesis provide some interesting and important insights into the electronic and structural dynamics of intramolecular charge transfer excited states. The events described in different chapters are specific to the structure of the molecules, though systematic variations observed in the excited state dynamics is possible to correlate with the structures and functional groups present in the molecular system. A deeper understanding and attaining a generalized picture of excited state reaction dynamics need elaborate investigation with larger number of molecular systems. Moreover, different newer

Summary and Outlook

techniques which appeared in near past such as femtosecond X-ray or electron diffraction can directly monitor the atomic motion in real time scale.^{363, 364} These techniques are capable to directly mapping the atomic coordinates during the structural evolution in ultrafast timescale. Though these techniques presently offer studies on transient structure of simpler molecules with a few numbers of atoms, the scope of research with these techniques will certainly improve in near future to resolve time evolution of complex molecular systems. Improvement in time resolution such as attosecond laser pulses is emerging to directly observe electronic motion around the nucleus.³⁶⁵ Myriad research avenues are present, which need to be explored to understand matter and dynamics with improved atomic and temporal resolution.

References

1. Clayton, R. K. Photosynthesis: physical mechanisms and chemical patterns", Cambridge University Press, Cambridge (1980).
2. Balzani, V (Ed). *Electron Transfer in Chemistry*, Wiley-VCH Publishers Inc., New York, Volumes I to V, 2001.
3. Jortner J.; Bixon, M. eds. *Electron Transfer: from isolated molecules to biomolecules*, Adv. Chem. Phys. vol. 106, 107, J. Wiley, New York (1999)
4. Cukier, R. I.; Nocera, D. G.; *Annu. Rev. Phys. Chem.* **1998**, 49, 337.
5. Gust, D.; Moore, T. A.; Moore, A.L.; *Acc. Chem. Res.* **2009**, 42, 1890.
6. Wasielewski, M. R. *Chem. Rev.*, **1992**, 92, 435.
7. Bredas, J. L. Durrant, J. R. *Acc. Chem. Res.*, **2009**, 42 1689.
8. Balzani, V., Credi, A., Venturi, M. *Chem. Soc. Rev.* **2009**, 38, 1542.
9. Baranoff E, Barigelletti F, Bonnet S, Collin J-P, Flamigni L, *Struct. Bond.* **2007**, 123, 41–78.
10. Sundstrom, V, *Annu. Rev. Phys. Chem.* **2008**, 59, 53.
11. Rohatgi-Mukherjee, K. K. "*Fundamentals of Photochemistry*", Wiley EsternLtd.India, **1986**.
12. Birks, J. B. "*Photophysics of Aromatic Molecules*", Wiley, New York, **1970**.
13. Turro, N. J. "*Modern Molecular Photochemistry*", Benjamin, Menlo Park, CA, **1978**.
14. Norrish, R. G. W., Porter, G., *Nature* **1949**, 164, 658.
15. Fleming, G. R., *Chemical Applications of Ultrafast Spectroscopy*, Oxford University Press, NewYork, **1986**, p.186.
16. Khundkar, L. R, Zewail A. H. *Annu. Rev. Phys. Chem.* **1990**, 41, 15.
17. Zewail, A. H. *J. Phys. Chem. A* **2000**, 104, 5660.
18. Hubert, R. Moser, J.-E., Grätzel, M., Wachtveitl, J., *J. Phys. Chem. B*, **2002**, 106, 6494.
19. (a) Franck, J. *Transactions of the Faraday Society*, **1926**, 21, 536. (b) Condon, E. *Physical Review*, **1928**, 32, 858.
20. Owrutsky, J. C.; Hochstrasser, R. M. *Annu. Rev. Phys. Chem.* **1994**, 45, 519.
21. Liu, J. Y.; Fan, W. H.; Han, K. L.; Deng, W. Q.; Xu, D. L.; Lou, N. Q. *J. Phys. Chem. A* **2003**, 107, 10857.
22. Lim, S. H.; Bjorklund, T. G.; Bardeen, C. J. *Chem. Phys. Lett.* **2001**, 342, 555.
23. Mokhtari, A.; Chesnoy, J. *Chem. Phys. Lett.* **1989**, 155, 593.
24. Kasha, M. *Discussions of the Faraday Society*, **1950**, 9, 14.

References

25. (a)Robinson, G. W.; Frosch, R. P. *J. Chem. Phys.* **1963**, 38, 1187. (b)Siebrand, W. *J. Chem. Phys.* **1967**, 47, 2411.
26. Fidler, H., Rini, M., Nibbering, E. T. J., *J. Am. Chem. Soc.*, **2004**, 126, 3789.
27. Carlos E. Crespo-Hernández, C. E., Cohen, B., Hare, P. M., Kohler, B. *Chem. Rev.*, **2004**, 104, 1977.
28. Hydrogen Bonding and Transfer in the Excited State, Ke-Li Han, Guang-Jiu Zhao Eds., Wiley Interscience, **2010**.
29. Morales-Cueto, R.; Esquivelzeta-Rabell, M.; Saucedo-Zugazagoitia, J.; Peon, J. *J. Phys. Chem. A* **2007**, 111, 552.
30. Electron and proton transfer in chemistry and biology, Eds: Müller, A.;Ratajczak, H.;Junge, W.;Diemann, E., Elsevier Science Ltd, **1992**.
31. Weller A. *Naturwiss* **1955**, 42, 175.
32. Kasha, M. In *Molecular Electronic Devices*; (Eds.: F. L. Carter, R. E. Siatkowski,H. Wohltjen) Elsevier Science Publishers: New York,**1988**, p 107-121.
33. Zhao, J., Ji, S., Chen, Y., Guo, H., Yang, P. *Phys. Chem. Chem. Phys.*, **2012**, 14, 8803.
34. Zhong, D. P., Douhal, A., Zewail, A. H. *Proc. Natl. Acad. Sci. U.S.A.* **2000**, 97, 14056.
35. Douhal, A., Lahmani, F. Zewail, A. H. *Chem. Phys.* **1996**, 207,477.
36. Strandjord, A. J. G., Courtney, S.H., Friedrich, D. M., Barbara, P. F. *J. Phys. Chem.* **1983**, 87, 1125.
37. Barbara, P. F.; Walsh, P. K.; Brus, L. E. *J. Phys. Chem.* **1989**, 93, 29.
38. Nosenko, Y. Wiosna-Sałyga, G. Kunitski, M. Petkova, I. Singh, A. Buma, W. J. Thummel, R. P. Brutschy, B. Waluk, J. *Angew. Chem., Int. Ed.* **2008**, 47, 6037.
39. Hsieh, C.; Jiang, C. C.; Chou, P. T. *Acc. Chem. Res.*, **2010**, 43, 1364.
40. Reichardt, C. ‘*Solvents and Solvent Effects in Organic Chemistry*’, VCH Verlagsgesellschaft mbH, D-6940 Weinheim, FRG, **1988**.
41. Barbara, P. F.; Jarzeba, W. *Adv. Photochem.* **1990**, 15, 1.
42. Maroncelli, M.; MacInnis, J.; Fleming, G. R. *Science*, **1989**, 243, 1674.
43. McHale, J. L.; *Acc. Chem. Res.* **2001**, 34, 265.
44. Sumi, H.; Marcus, R. A. *J. Chem. Phys.* **1986**, 84, 4894.
45. Walker, G. C.; Åkesson, E.; Johnson, A. E.; Levinger, N. E.; Barbara, P. F. *J. Phys. Chem.* **1992**, 96, 3728.
46. Horng, M. L.; Gardecki, J. A.; Papazyan, A.; Maroncelli, M. *J. Phys. Chem.* **1995**, 99, 17311.

References

47. Reynolds, L.; Gardecki, J. A.; Frankland, S. J. V.; Horng, M. L.; Maroncelli, M. *J. Phys. Chem.* **1996**, *100*, 10337.
48. Rosenthal, S. J., Xie, X.; Du, M.; Fleming, G. R. *J. Chem. Phys.* **1991**, *95*, 4715.
49. Maroncelli, M.; *J. Mol. Liq.* **1993**, *57*, 1.
50. Maroncelli, M.; *J. Chem. Phys.* **1991**, *94*, 2084.
51. Kosower, E. M.; Huppert, D. *Ann. Rev. Phys. Chem.* **1986**, *37*, 127.
52. Loring, R. F.; Mukamel, S.; *J. Chem. Phys.* **1987**, *87*, 1272.
53. Castner, E. W. Maroncelli, M. Fleming, G. R. *J. Chem. Phys.* **1987**, *86*, 1090.
54. Rotkiewicz, K.; Grellmann, K. H.; Grabowski, Z. *Chem. Phys. Lett.* **1973**, *19*, 315
55. Rotkiewicz, K.; Grabowski, Z.; Krowczynski, A. *J. Lumin.* **1976**, 877.
56. Grabowski, Z.; Dobkowski, J. *Pure Appl. Chem.* **1983**, 245.
57. Rettig, W. *Angew. Chem., Int. Ed. Engl.* **1986**, *25*, 971.
58. Grabowski, Z. R.; Rotkiewicz, K.; Rettig, W. *Chem. Rev.* **2003**, *103*, 3899
59. Tominaga, K.; Walker, G. C.; Jarzeüba, W.; Barbara, P. F. *J. Phys. Chem.* **1991**, *95*, 10475.
60. Kwok, W. M., Ma, C.; Matousek, P.; Parker, A. W.; Phillips, D.; Toner, W. T.; Towrie, M.; Umapathy, S.; *J. Phys. Chem. A* **2001**, *105*, 984
61. Oster, G.; Nishijima, Y. *J. Am. Chem. Soc.* **1956**, *78*, 1581.
62. Forster, T.; Hoffman, G. Z. *Phys. Chem. N. F.* **1971**, *75*, 63.
63. Bagchi, B.; Fleming, G. R.; Oxotoby, D. W. *J. Chem. Phys.* **1983**, *78*, 7375.
64. Bagchi, B.; Fleming, G. R. *J. Phys. Chem.* **1990**, *94*, 9.
65. Ben-Amotz, D.; Jeanloz, R.; Harris, C. B. *J. Chem. Phys.* **1987**, *86*, 6119.
66. Ben-Amotz, D.; Harris, C. B. *Chem. Phys. Lett.* **1985**, *119*, 305; **1987**, *86*, 4856.
67. Martin, M. M.; Plaza, P.; Changenet, P.; Meyer, Y. H. *J. Photochem. Photobiol. A. Chem.* **1997**, *105*, 197.
68. Martin, M. M.; Plaza, P.; Meyer, Y. H. *J. Phys. Chem.* **1991**, *95*, 9310.
69. Jurczok, M.; Plaza, P.; Martin, M. M.; Rettig, W. *J. Phys. Chem. A* **1999**, *103*, 3372.
70. Changenet, P.; Zhang, H.; van der Meer, M. J.; Glassbeek, M.; Plaza, P.; Martin, M. M. *J. Phys. Chem. A* **1998**, *102*, 6716.
71. Singh, C.; Modak, B.; Mondal, J. A.; Palit D. K. *J. Phys. Chem. A*, **2011**, *115*, 8183.
72. Van der Meer, M. J.; Zhang, H.; Glasbeek, M. J. *Chem. Phys.* **2000**, *112*, 2878.
73. Glasbeek, M.; Zhang, H. *Chem. Rev.* **2004**, *104*, 1929.
74. Singh, A. K.; Ramakrishna, G.; Ghosh, H. N.; Palit, D. K. *J. Phys. Chem. A* **2004**, *108*, 2583.

References

75. Mondal, J. A.; Ghosh, H. N.; Mukherjee, T.; Palit, D. K. *J. Phys. Chem. A* **2006**, *110*, 3432.
76. (a) Sinha, H. K.; Yates, K. *J. Chem. Phys.* **1990**, *93*, 7085. (b) Sinha, H. K.; Yates, K. *Can. J. Chem.* **1991**, *89*, 550.
77. Thomsen, C. L.; Thogersen, J.; Keiding, S. R.; *J. Phys. Chem. A* **1998**, *102*, 1062.
78. Balzani, V.; Juris, A.; Venturi, M.; Campagna, S.; Serroni, S. *Acc. Chem. Res.* **1998**, *31*, 26.
79. Kalyanasundaram, K.; Gratzel, M. *Coord. Chem. Rev.* **1998**, *177*, 347.
80. Forster, L. S. *Coord. Chem. Rev.* **2006**, *250*, 2023.
81. McCusker, J. K. *Acc. Chem. Res.* **2003**, *36*, 876.
82. Lackowicz, J. R. *Principles of fluorescence spectroscopy*, 3rd ed.; Springer: New York, **2006**.
83. O'Connor, D.V.; and Phillips, D.; *Time Correlated Single Photon Counting*, Academic Press, New York, **1984**. (these 4 are for TCSPC)
84. Demas, J. N.; *Excited State Life Time Measurements* Academic Press, New York, **1983**.
85. Ware, W.R.; *Creation and Detection of the Excited State* Eds. Lamola, A.A.; Marcel Dekker, New York, **1971**, vol-1, Part A, Chap.5.
86. Bevington, P.R.; *Date Reduction and Error Analysis for the Physical Sciences*, McGraw Hill, New York, **1969**.
87. D. W. Marquardt, *Journal of the Society for Industrial and Applied Mathematics*, **1963**, *11*, 431.
88. Duguay, M. A. *Progress in Optics* Amsterdam, Netherlands, **1976**; Vol. XIV.
89. Duguay, M. A.; Hansen, J. M. *Opt. Commun* **1969**, *1*, 254.
90. Kahlow, M. A.; Jarzeba, W.; DuBruil, T. P.; Barbara, P. F. *Rev. Sci. Instrum.* **1988**, *59*, 1098.
91. Mahr, H.; Hirsch, M. D. *Opt. Commun.* **1975**, *13*, 96.
92. Shah, J. *IEEE J. Quant. Elect.* **1988**, *24*, 276.
93. Fleming, G. R., “*Chemical Applications of Ultrafast Spectroscopy*”, Oxford University Press, N.Y.
94. Reid, G. D.; Wynne, K.; *Ultrafast laser technology and spectroscopy*, Encyclopedia of analytical chemistry, Eds: R. A. Meyers, John Wiley & Sons Ltd. **2000**.
95. Rulliere, C. *Femtosecond Laser Pulses; Principles and Experiments*, Springer, **1998**.
96. Franken, P.; Hill, A.; Peters, C.; Weinreich, G. (1961). "Generation of Optical Harmonics". *Physical Review Letters* 1961, *7*, 118.

References

97. Manz J.; Wöste, L. Eds. *Femtosecond Chemistry*, Vols. I and II, VCH, New York, **1994**.
98. Alfano R. R. and Shapiro, S. L. *Observation of self-phase modulation and small-scale filaments in crystals and glasses*, *Phys. Rev. Lett.* **1970**, *24*, 592.
99. Alfano, R. R. Ed., *The Supercontinuum Laser Source*, Springer-Verlag, New York, **1989**.
100. Schmidt, M. W.; Baldrige, K. K.; Boatz, J. A.; Elbert, S. T.; Gordon, M. S.; Jensen, J. H.; Koseki, S.; Matsunaga, N.; Nguyen, K. A.; Su, S. J.; Windus, T. L.; Dupuis, M.; Montgomery, J. A. *J. Comput. Chem.* **1993**, *14*, 1347.
101. Becke, A. D. *J. Chem. Phys.* **1993**, *98*, 5648.
102. Lee, C.; Yang, W.; Parr, R. G. *Phys. Rev. B* **1998**, *37*, 785.
103. (a) Miertus, S.; Scrocco, E.; Tomasi, J. *Chem. Phys.* **1981**, *55*, 117. (b) Tomasi, J.; Persico, M. *Chem. Rev.* **1994**, *94*, 2027.
104. Aggarwal, B. B.; Sundaram, C.; Malini, N.; Ichikawa, H. in *Molecular Targets and Therapeutic uses of curcumin in health and disease*, Aggarwal, B. B.; Surth, Y. J. (Eds.) **2007**, Springer, New York, USA.
105. Srimal, R. C.; Dhawan, B. N. *Journal of Pharma. Pharmac.*, **1973**, *25*, 447.
106. Sharma, O. P. *Biochem. Pharmacol.* **1976**, *25*, 1811.
107. Singh, S.; Aggarwal, B. B. *J. Biol. Chem.* **1995**, *270*, 24995.
108. Goel, A.; Kannumakkara, A. B.; Aggarwal, B. B. *Biochem. Pharmacol.* **2008**, *75*, 787.
109. Lantz, R. C.; Chen, G. J.; Solyom, A. M.; Jolad, S. D.; Timmerman, B. M. *Phytomedicine*, **2005**, *12*, 445.
110. Aggarwal, B. B.; Kumar, A.; Bharti, A. C. *Anticancer Res.* **2003**, *23*, 363.
111. Anand, P.; Thomas, S. G.; Kunnumakkara, A. B.; Sundaram, C.; Kuzhuvelil, B. H.; Sung, B.; Tharakan, S. T.; Aggarwal, B. B. *Biochem. Pharmacology*, **2008**, *76*, 1590.
112. Yang, F.; Lim, G. P.; Begum, A. N.; Ubeda, O. J.; Simmons, M. R.; Ambegaonkar, S. S.; Chen, P. P.; Kaye, R.; Glabe, C. G.; Frautschy, S. A.; Cole, G. M. *J. Biol. Chem.* **2005**, *280*, 5892.
113. Masuda, M.; Suzuki, N.; Taniguchi, S.; Oikawa, T.; Nonaka, T.; Iwatsubo, T.; Hisanga, S.; Goedert, M.; Hasegawa, M. *Biochemistry* **2006**, *45*, 6085.
114. Gorman, A. A.; Hamblett, I.; Srinivasan, V. S.; Wood, P. D. *Photochem. Photobiol.* **1994**, *59*, 389.
115. Khopde, S. M.; Priyadarsini, K. I.; Palit, D. K.; Mukherjee, T. *Photochem. Photobiol.* **2000**, *72*, 625.

References

116. (a) Priyadarsini, K. I. *Free. Rad. Chem. Biol.* **1997**, 23, 838. (b) Barik, A.; Priyadarsini, K. I.; Mohan, H. *Orient. J. Chem.* **2002**, 18, 427. (c) Priyadarsini, K. I.; Maity, D. K.; Naik, G. H.; Kumar, M. S.; Unnikrishnan, M. K.; Satav, J. G.; Mohan, H. *Free. Rad. Chem. Biol.* **2003**, 35, 475. (d) Priyadarsini, K. I. *J. Photochem. Photobiol. C.* **2009**, 10, 81.
117. (a) Nardo, L.; Paderno, R.; Andreoni, A.; Masson, M.; Haukvik, T.; Tonnesen, H. H. *Spectroscopy* **2008**, 22, 187. (b) Nardo, L.; Andreoni, A.; Bondani, M.; Masson, M.; Tonnesen, H. H. *J. Photochem. Photobiol. B. Biol.* **2009**, 97, 77.
118. Caselli, M.; Ferrari, E.; Imbriano, C.; Pignedoli, F.; Saladini, M.; Ponterini, G. *J. Photochem. Photobiol. A: Chem.* **2010**, 210, 115.
119. Adhikary, R.; Mukherjee, P.; Kee, T. W.; Petrich, J. W. *J. Phys. Chem. B.* 2009, 113, 5255.
120. Adhikary, R.; Carlson, P. J.; Kee, T. W.; Petrich, J. W. *J. Phys. Chem. B*, **2010**, 114, 2997.
121. Dahl, T. A.; Bilski, P.; Reszka, K. J.; Chignell, C. F. *Photochem. Photobiol.* **1994**, 59, 290.
122. Chignell, C. F.; Bilski, P.; Reszka, K. J.; Motten, A. G.; Sik, R. H.; Dahl, T. A. *Photochem. Photobiol.* **1994**, 59, 295.
123. Sun, Y. M.; Wang, R. X.; Yuan, S. L.; Lin, X. J.; Liu, C. B. *Chinese J. Chem.* **2004**, 22, 827.
124. Balasubramanian, K. *J. Agric. Food Chem.*, **2006**, 54, 3512.
125. Barclay, L. R.; Vinqvist, M. R.; Mukai, K.; Goto, H.; Hashimoto, Y.; Tokunaga, A.; Uno, H. *Org. Lett.* **2000**, 2, 2841.
126. Payton, F.; Sandusky, P.; Alworth, W. L. *J. Nat. products*, **2007**, 143.
127. Roughley, P. J.; Whiting, D. A. *J. Chem. Soc. Perkin Trans. I*, 1973, 20, 2379.
128. Matthes, H. W. D.; Luu, B.; Ourisson, G. *Photochemistry* **1980**, 170, 425.
129. Pedersen, U.; Rasmussen, P. B.; Lawesson, S. -O. *Liebigs Ann. Chem.* **1985**, 8, 1557.
130. Bong, P. -H. *Bull. Korean Chem. Soc.* **2000**, 21, 81.
131. Shen, L.; Ji, H. -F. *Spectrochim. Acta.- Part A* **2007**, 67, 619.
132. Shen, L.; Zhang, H. Y.; Ji, H. -F. *Organic Letters*, **2005**, 7, 243.
133. Kong, L.; Priyadarsini, K. I.; Zhang, H. Y. *J. Molec. Struct. Theochem*, **2004**, 688, 111.
134. Sun, Y. M.; Zhang, H. Y.; Chen, D. Z.; Liu, C. B. *Organic Letters*, **2002**, 4, 2909.
135. Wright, J. S. *J. Mol. Struct. Theochem*, **2002**, 591, 207.

References

136. Maroncelli, M.; Fleming, G. R. *J. Chem. Phys.* **1987**, *86*, 6221.
137. Cross, A. J.; Fleming, G. R. *Biophys. J.* **1984**, *46*, 45.
138. (a) Elsaesser, T. In *Femtosecond Chemistry*; Manz, J., Wöste, L., Eds.; VCH-Verlag: Weinheim, Germany, **1995**; Vol. 2, pp 563-579. (b) Elsaesser, T.; Kaiser, W. *Chem. Phys. Lett.* **1986**, *128*, 231. (c) Laermer, F.; Elsaesser, T.; Kaiser, W. *Chem. Phys. Lett.* **1988**, *148*, 119. (d) Frey, W.; Laermer, F.; Elsaesser, T. *J. Phys. Chem.* **1991**, *95*, 10391.
139. (a) Lochbrunner, S.; Wurzer, A. J.; Riedle, E. *J. Phys. Chem. A*, **2003**, *107*, 10580. (b) Lochbrunner, S.; Schultz, T.; Schmitt, M.; Shaffer, J. P.; Zgierski, M. Z.; Stolow, A. *J. Chem. Phys.* **2001**, *114*, 2519. (c) Lochbrunner, S.; Szeghalmi, A.; Stock, K.; Schmitt, M. *J. Chem. Phys.* **2005**, *122*, 244315. (d) Lochbrunner, S.; Wurzer, A. J.; Riedle, E. *J. Phys. Chem.* **2003**, *107*, 10580. (e) de Vivie-Riedle, R.; De Waele, V.; Kurtz, L.; Riedle, E. *J. Phys. Chem.* **2003**, *107*, 10591. (f) Stock, K.; Bizjak, T.; Lochbrunner, S. *Chem. Phys. Lett.* **2002**, *354*, 409. (g) Lochbrunner, S.; Schultz, T.; Schmitt, M.; Shaffer, M.; Zgierski, M. Z.; Stolow, A. *J. Chem. Phys.* **2001**, *114*, 2519. (h) Lochbrunner, S.; Wurzer, A. J.; Riedle, E. *J. Chem. Phys.* **2000**, *112*, 10699.
140. Abou-Zeid, O. K.; Jimnez, R.; Thompson, E. H. Z.; Millar, D. P.; Romesberg, F. E. *J. Phys. Chem. A* **2002**, *106*, 3665.
141. Schwartz, B. J.; Peteanu, L. A.; Harris, C. B. *J. Phys. Chem.* **1992**, *96*, 3591.
142. Ormoson, S. M.; LeGourrierec, D.; Brown, R. G.; Foggi, P. *J. Chem. Soc. Chem. Comm.* **1995**, 2133.
143. Douhal, A.; Lahmani, F.; Zewail, A. H. *Chem. Phys.* **1996**, *207*, 477.
144. Huston, A. L.; Scott, G. W.; Gupta, A. *J. Chem. Phys.* **1982**, *76*, 4978.
145. Arthen-Engeland, Th.; Bultmann, T.; Ernsting, N. P.; Rodriguez, M. A.; Thiel, W. *Chem. Phys.* **1992**, *163*, 43.
146. Takeuchi, S.; Tahara, T. *Proc. Natl. Acad. Sci.* **2007**, *104*, 5285.
147. Share, P.; Pereira, M.; Sarisky, M.; Repinec, S.; Hochstrasser, R. M. *J. Lumn.* **1991**, *48* & *49*, 204.
148. Horng, M. L.; Gardeki, J. A.; Papazyan, A.; Maroncelli, M. *J. Phys. Chem.* **1995**, *99*, 17311.
149. Jarzeba, W.; Walker, G. C.; Johnson, A. E.; Barbara, P. F. *Chem. Phys.* **1991**, *152*, 57.
150. Nibbering, E. T. J.; Fidler, H.; Pines, E. *Annu. Rev. Phys. Chem.* **2005**, *56*, 337.
151. Nibbering, E. T. J.; Elsaesser, T. *Chem. Rev.* **2004**, *104*, 1887.
152. Martini, I.; Hartland, G. V. *J. Phys. Chem.* **1996**, *100*, 19764.

References

153. Harju, T. O.; Huizer, A. H.; Varma, C. A. G. O. *Chem. Phys.* **1995**, *200*, 215.
154. Horng, M. L.; Dahl, K.; Jones II, G.; Maroncelli, M. *Chem. Phys. Lett.* **1999**, *315*, 363.
155. Yu, J.; Berg, M. *Chem. Phys. Lett.* **1993**, *208*, 315.
156. Benigno, A. J.; Ahmed, E.; Berg, M. *J. Chem. Phys.* **1996**, *104*, 7382.
157. (a) Samant, V.; Singh, A. K.; Ramakrishna, G.; Ghosh, H. N.; Ghanty, T.; Palit, D. K. *J. Phys. Chem. A* **2005**, *109*, 8693. (b) Varne, M.; Samant, V.; Mondal, J.; Nayak, S. K.; Ghosh, H. N.; Palit, D. K. *Chem. Phys. Chem.* **2009**, *10*, 2979. (c) Mondal, J. A.; Samant, V.; Varne, M.; Singh, A. K.; Ghanty, T. K.; Ghosh, H. N.; Palit, D. K. *Chem. Phys. Chem.* **2009**, *10*, 2995.
158. Garg, S. K.; Smyth, C. P. *J. Phys. Chem.* **1965**, *69*, 129
159. Bertolini, D.; Cassattari, M.; Salvetti, G. *J. Chem. Phys.* **1982**, *76*, 325.
160. Matsumoto, M.; Gubbins, K. *J. Chem. Phys.* **1990**, *93*, 1981.
161. Kovalenko, S. A.; Ernsting, N. P.; Ruthmann, J. *J. Chem. Phys.* **1997**, *106*, 3504.
162. Nagarajan, V.; Bearley, A. M.; Kang, T. J.; Barbara, P. F.; *J. Chem. Phys.* **1987**, *86*, 3183.
163. Kang, T. J.; Kahlow, M. A.; Giser, D.; Swallen, S.; Nagarajan, V.; Jarzeba, W.; Barbara, P. F. *J. Phys. Chem.* **1988**, *92*, 6800.
164. Kang, T. J.; Jarzeba, J.; Barbara, P. F.; Fonseca, T. *Chem. Phys.* **1990**, *149*, 81.
165. Kivelsion, D.; Madden, P. A.; *Annu. Rev. Phys. Chem.* **1980**, *31*, 583.
166. Frohlich, H. *Theory of Dielectrics*; Oxford University Press, Oxford, 1949.
167. Simon, J. D. *Acc. Chem. Res.* **1988**, *21*, 128.
168. Maroncelli, M. *Chem. Phys.* **1997**, *106*, 1545; *J. Mol. Liq.* **1993**, *57*, 1.
169. Rossetti, R.; Haddon, R. C.; Brus, L. E. *J. Am. Chem. Soc.* **1980**, *102*, 6913.
170. Palit, D. K.; Pal, H.; Mukherjee, T.; Mittal, J. P. *J. Chem. Soc. Faraday Trans.* **1990**, *86*, 3861.
171. Folm, S. R.; Barbara, P. F. *J. Phys. Chem.* **1985**, *89*, 4489.
172. (a) Zhao, G.; Han, K. *J. Phys. Chem. A*, **2007**, *111*, 2469. (b) Zhao, G., J., Han, K. *J. Phys. Chem. A*, **2007**, *111*, 9218. (c) Zhao, G., Kan, K. *Chem. Phys. Chem.* **2008**, *9*, 1842. (d) Zhao, G., Kan, K. *J. Comput. Chem.* **2008**, *29*, 2010.
173. Marcus, R. A. ; Sutin, N. *Biochimica et Biophysica Acta*, **1985**, **811**, 265
174. Müller, A. *Electron and proton transfer in chemistry and biology*, Elsevier, 1992
175. Elsaesser, T.; Bakker, H. J.; *Ultrafast Hydrogen Bonding Dynamics and Proton Transfer Processes in the Condensed Phase*, Kluwer Academic Publishers, 2002.

References

176. *Hydrogen-Transfer Reactions* (Eds.: Hynes, J. T.; Klinman, J. P.; Limbach, H. H.; Schowen, R. L.), Wiley-VCH, Weinheim, 2007.
177. Douhal, A.; Kim, S. K.; Zewail, A. H.; *Nature* 1995, **378**, 260.
178. Laermer, F.; Elsaesser, T.; Kaiser, W. *Chem. Phys. Lett.* 1988, **148**, 119.
179. Schwartz, B. J.; Peteanu, L. A.; Harris, C. B. *J. Phys. Chem.* 1992, **96**, 3591.
180. Arthen-Engeland, Th.; Bultmann, T.; Ernsting, N. P. *Chem. Phys.* 1992, **163**, 43.
181. Abou-Zeid, O. K.; Jimnez, R.; Thompson, E. H. Z.; Millar, D. P.; Romesberg, F. E. *J. Phys. Chem. A* **2002**, *106*, 3665.
182. Nosenko, Y.; Wiosna-Sałyga, G.; Kunitski, M.; Petkova, I.; Singh, A.; Buma, W. J.; Thummel, R. P.; Brutschy, B.; Waluk, J. *Angew. Chem., Int. Ed.*, 2008, **47**, 6037.
183. Kim, S.; Seo, J.; Park, S. Y. *J. Photochem. Photobiol. A: Chemistry*, 2007, **191**, 19
184. Sobolewski A. L.; Domcke, W. *Phys. Chem. Chem. Phys.* 2006, **8**, 3410.
185. Minoura, Y.; Nagashima, N.; Kudoh, S.; Nakata, M. *J. Phys. Chem. A*, 2004, **108**, 2353.
186. Huynh, M. H. V.; Meyer, T. J. *Chem. Rev.* 2007, **107**, 5004.
187. Hammes-Schiffer, S.; Stuchebrukhov, A. A. *Chem. Rev.*, 2010, **110**, 6939.
188. Chou, P. T.; Martinez, M. L.; Clements, J. H. *J. Phys. Chem.* 1993, **97**, 2618.
189. Cheng, Y. M.; Pu, S. C.; Hsu, C. J.; Lai, C. H.; Chou, P. T.; *ChemPhysChem*, 2006, **7**, 1372.
190. Chou, P. T.; Huang, C. H.; Pu, S. C.; Cheng, Y. M.; Liu, Y. H.; Wang, Y.; Chen, C. T. *J. Phys. Chem. A*, 2004, **108**, 6452.
191. Seo, J.; Kim, S.; Park, S. Y. *J. Am. Chem. Soc.* 2004, **126**, 11154.
192. Kim, C. H.; Park, J.; Seo, J.; Park, S. Y.; Joo, T. *J. Phys. Chem. A*, 2010, **114**, 5618
193. Zgierski, M. Z.; Fuziwara, T.; Lim, E. C. *J. Phys. Chem. A*, 2011, **115**, 10009.
194. Nie, D.; Bian, Z.; Yu, A.; Chen, Z.; Liu, Z.; Huang, C. *Chemical Physics* 2008, **348**, 181.
195. Riddick, J. A.; Bunger, W. B. *Organic Solvents*, 3rd ed. Wiley: New York, 1970.
196. Gil, M.; Douhal, A. *J. Phys. Chem. A* 2008, **112**, 8231.
197. (a) Kramers, H. A. *Physica*, 1940, **7**, 284; (b) “*New Trends in Kramers Reaction Rate Theory*” Talkier, P.; Hanggi, P. Eds. Kluwer Academic, London, 1995.
198. *Molecular Electronics: Science and Technology*; Aviram, A., Ratner, M. M., Eds.; New York Academy of Sciences, New York, 1998; Vol. 852.
199. *Electron Transfer in Chemistry*; Balzani, V., Ed.; Wiley V. C. H.: Weinheim, 2001; Vol. 5.

References

200. Skourties, S. S.; Beratan, D. N. Theories of Structure-Function Relationships for Bridge-Mediated Electron-Transfer Reactions. In *Electron Transfer - From Isolated Molecules to Biomolecules*; Jortner, J., Boxon, M., Eds.; Advances in Chemical Physics, John Wiley: New York, 1999; Vol. 106, Part 1, p 377.
201. von Veldhoven, E.; Zhang, H.; Rettig, W.; Brown, R. G.; Hepworth, J. D.; Glasbeek, M. *Chem. Phys. Lett.* **2002**, *363*, 189
202. Techert, S.; Zachariasse, K. A. *J. Am. Chem. Soc.* **2004**, *126*, 5593.
203. Zachariasse, K. A.; Druzhinin, S. I.; Bosch, W.; Machinek, R. *J. Am. Chem. Soc.* **2004**, *126*, 1705.
204. 204 Yoshihara, T; Sergey I.; Druzhinin, S. I.; Zachariasse K. A. *J. Am. Chem. Soc.* **2004**, *126*, 8535-8539
205. Arzhantsev, S.; Zachariasse, K. A.; Maroncelli, M; *J. Phys. Chem. A* **2006**, *110*, 3454-3470.
206. Kovalenko, S. A.; Schanz, R. T.; Senyushkina, A; Ernsting, N. P.; *Phys. Chem. Chem. Phys.* **2002**, *4*, 703–707
207. Svetlichny, V. Y.; Merola, F.; Dobretsov, G. E.; Gularyan, S. K.; Syrejschchikova, T. I. *Chem. Phys. Lipids*, **2007**, *145*, 13.
208. Dobretsov, G. E.; Petrov, V. A.; Mishijev, V. E.; Klebanov, G. I.; Vladimirov, Y. A. *Stud. Biophys.*, **1977**, *65*, 91.
209. Gularyan, S. K.; Dobretsov, G. E.; Sarkisov, O. M.; Gostev, F. E.; Svetlichnyi, V. Y. *Biophysics*, **2005**, *50*, 685.
210. Romanov, A. N.; Gularyan, S. K.; Polyak, B. M.; Sakovich, R. A.; Dobretsovc, G. E.; Sarkisovb, O. M. *Phys. Chem. Chem. Phys.*, **2011**, *13*, 9518.
211. Lippert, E.; Lüder, W.; Moll, F.; Nägele, W.; Boos, H.; Prigge, H.; Seibold-Blankenstein, I. *Angew. Chem.* **1961**, *73*, 695.
212. 212 Rettig, W.; Marschner, F. *New J. Chem.* **1990**, *14*, 819.
213. 213 Cornelissen-Gude C.; Rettig, W. *J. Phys. Chem. A* **1998**, *102*, 7754.
214. Yoshihara, T.; Galievsky, V. A.; Druzhinin, S. I.; Saha, S.; Zachariasse, K. A. *Photochem. Photobiol. Sci.* **2003**, *2*, 342.
215. Schuddeboom, W.; Jonker, S. A.; Warman, J. M.; Leinhos, U.; Kuñhnle, W.; Zachariasse, K. A. *J. Phys. Chem* **1992**, *96*, 10809.
216. Baumann, W.; Bischof, H.; Froñhling, J.-C.; Brittinger, C.; Rettig, W.; Rotkiewicz, K. *J. Photochem. Photobiol., A* **1992**, *64*, 49.
217. Druzhinin, S. I.; Demeter, A.; Zachariasse, K. A. *Chem. Phys. Lett.* **2001**, *347*, 421.

References

218. Daum, R.; Druzhinin, S. I.; Ernst, D.; Rupp, L.; Schroeder, J.; Zachariasse, K. A. *Chem. Phys. Lett.* **2001**, *341*, 272.
219. Rettig, W.; Bliss, B.; Dirnberger, K. *Chem. Phys. Lett.* **1999**, *305*, 8.
220. Zachariasse, K. A. *Chem. Phys. Lett.* **2000**, *320*, 8.
221. Il'ichev, Yu. V.; Ku'hnle, W.; Zachariasse, K. A. *J. Phys. Chem. A* **1998**, *102*, 5670.
222. Yoshihara, T.; Druzhinin, S. I.; Zachariasse, K. A. *J. Am. Chem. Soc.* **2004**, *126*, 8535.
223. Zachariasse, K. A.; Druzhinin, S. I.; Bosch, W.; Machinick, R. *J. Am. Chem. Soc.* **2004**, *126*, 1705.
224. Galievsky, V. A.; Druzhinin, S. I.; Demeter, A.; Kovalenko, S. A.; Senyuskina, T. A.; Meyer, P.; Zachariasse, K. A. *J. Phys. Chem. A* **2011**, *115*, 10823.
225. Demeter, A.; Druzhinin, S. I.; Kovalenko, S. A.; Senyuskina, T. A.; Zachariasse, K. A. *J. Phys. Chem. A*, **2011**, *115*, 1521.
226. Zachariasse, K. A.; Druzhinin, S. I.; Galievsky, V. A.; Demeter, A.; Allones, X.; Kovalenko, S. A.; Senyuskina, T. A.; *J. Phys. Chem. A*, **2010**, *114*, 13031.
227. Galievsky, V. A.; Druzhinin, S. I.; Demeter, A.; Meyer, P.; Kovalenko, S. A.; Senyuskina, T. A.; Zachariasse, K. A. *J. Phys. Chem. A*, **2010**, *114*, 12622.
228. Tretchert, S.; Zachariasse, K. A. *J. Am. Chem. Soc.* **2004**, *126*, 5593.
229. Druzhinin, S. I.; Meyer, P.; Stalke, D.; Noltemeyer, M.; Zachariasse, K. A. *J. Am. Chem. Soc.* **2010**, *132*, 7730.
230. Lewis, F. D.; Holman, B. III. *J. Phys. Chem.* **1980**, *84*, 2328.
231. Hamaguchi, H.; Hashimoto, M. *J. Phys. Chem.* **1995**, *99*, 7875.
232. Sobolewski, A. L.; Domcke, W. *Chem. Phys. Lett.* **1996**, *250*, 428; **1996**, *259*, 119.
233. Sinha, H. K.; Yates, K. *J. Chem. Phys.* **1990**, *93*, 7085.
234. Sinha, H. K.; Yates, K. *Can. J. Chem.* **1991**, *89*, 550.
235. Thomsen, C. L.; Thogersen, J.; Keiding, S. R.; *J. Phys. Chem. A* **1998**, *102*, 1062.
236. Farztdinov, V. M.; Schanz, R.; Kovalenko, S. A.; Ernsting, N. P. *J. Phys. Chem.* **2000**, *104*, 11486.
237. Kovalenko, S. A.; Schanz, R.; Farztsinov, V. M.; Hening, H.; Ernsting, N. P. *Chem. Phys. Lett.* **2000**, *323*, 312.
238. Sugita, A.; Yanagi, K.; Kuroyanagi, K.; Takahashi, H.; Aoshima, S.; Tsuchiya, Y.; Tasaka, S.; Hashimoto, H. *Chem. Phys. Lett.* **2003**, *382*, 613.
239. Shigeto, S.; Hiramatsu, H.; Hamaguchi, H. *J. Phys. Chem. A*, **2006**, *110*, 3738
240. Dobkowski, J.; Herbich, J.; Waluk, J.; Koput, J.; Kuhnle, W. *J. Lum.* **1989**, *44*, 149.

References

241. Scalmani, G; Frisch, M. J; Mennucci, B; Tomasi, J; Cammi, R; Barone, V. *J. Chem. Phys.* **2006**, *124*, 094107.
242. Khalil, O. S.; Seliskar, C. J.; McGlynn, S. P. *J. Chem. Phys.* **1973**, *58*, 1607.
243. Carsey, T. P.; Findley, G. L.; McGlynn, S. P. *J. Am. Chem. Soc.* **1979**, *101*, 4502.
244. Bredas, J. L.; Meyers, F. *Nonlinear Opt.* **1996**, *1*, 57.
245. Woodford, J. N.; Pauley, M. A.; Wang, C. H. *J. Phys. Chem. A* **1997**, *101*, 1989.
246. Champgne, B. *Chem. Phys. Lett.* **1996**, *261*, 57.
247. Karna, S. P.; Prasad, P. N.; Dupuis, M. *J. Chem. Phys.* **1991**, *94*, 1171.
248. Anderson, R. W., Jr.; Hochstrasser, R. M.; Lutz, H.; Scott, G. W. *Chem. Phys. Lett.* **1980**, 407.
249. Hamanoue, K.; Hirayama, S.; Nakayama, T.; Teranishi, H. *J. Phys. Chem.* **1980**, *84*, 2074.
250. Heinz, B.; Schmierer, T.; Laimgruber, S.; Gilch, P. *J. Photochem. Photobiol., A* **2008**, *199*, 274.
251. Morales-Cueto, R.; Esquivelzeta-Rabell, M.; Saucedo-Zugazagoitia, J.; Peon, J. *J. Phys. Chem. A* **2007**, *111*, 552.
252. Collado-Fregoso, E.; Zugazagoitia, J. S.; Plaza-Medina, E. F.; Peon, J. *J. Phys. Chem. A* **2009**, *113*, 13498.
253. Reichardt, C.; Vogt, R. A.; Crespo-Hernandez, C. E. *J. Chem. Phys.* **2009**, *131*, 224518.
254. Zugazagoitia, J. S.; Almora-Diaz, C. X.; Peon, J. *J. Phys. Chem. A* **2008**, *112*, 358.
255. Crespo-Hernández, C. E.; Burdzinski, G.; Arce, R. J. *J. Phys. Chem. A* **2008**, *112*, 6313.
256. Mohammad, O. F.; Vauthey, E. *J. Phys. Chem. A* **2008**, *112*, 3823.
257. Mondal, J. A.; Sarkar, M.; Samanta, A.; Ghosh, H. N.; Palit, D. K. *J. Phys. Chem. A* **2007**, *111*, 6122.
258. Hurley, R.; Testa, A. C. *J. Am. Chem. Soc.* **1968**, *90*, 1949.
259. Murudkar, S.; Mora, A. K. Singh, P. K.; Nath, S. J. *Phys. Chem. A* **2011**, *115*, 10762.
260. Rafiq, S.; Yadav, R.; Sen, P. *J. Phys. Chem. A* **2011**, *115*, 8335
261. Ellena, J.; Goeta, A. E.; Howard, J. A. K.; Punte, G. *J. Phys. Chem. A* **2001**, *105*, 8696.
262. Horng, M. L.; gardecki, J. A.; Papazyan, A.; Maroncelli, M. *J. Phys. Chem.* **1995**, *99*, 17311.
263. Reichardt, C. ‘*Solvents and Solvent Effects in Organic Chemistry*’, VCH Verlagsgesellschaft mbH, D-6940 Weinheim, FRG, 1988.

References

264. Riddick, J. A.; Bunger W. B. *Organic Solvents*, 3rd ed. Wiley: New York, 1970.
265. Jimenez, R.; Fleming, G. R.; Kumar, P. V.; Maroncelli, M. *Nature* **1994**, 369, 471
266. Bridgman, P. *Proc. Natl. Acad. Sci. USA*. **1923**, 9, 341.
267. Middleton, C. T.; Cohen, B.; Kohler, B. *J. Phys. Chem. A* **2007**, 111, 10460.
268. Kovalenko, S. A.; Schanz, R.; Hennig, H.; Ernsting, N. P. *J. Chem. Phys.* **2001**, 115, 3526.
269. Martini, I.; Hartland, G. V. *J. Phys. Chem.* **1996**, 100, 19764.
270. Miller, R. J. D. *Ann. Rev. Phys. Chem.* **1993**, 42, 581.
271. Owrutsky, J. C.; Raftery, D.; Hochstrasser, R. M. *Ann. Rev. Phys. Chem.* **1994**, 45, 519.
272. Pigliucci, A.; Vauthey, E. *Chimica* **2003**, 57, 200.
273. Takezaki, M.; Hirota, N.; Terazima, M.; Sato, H.; Nakajima, T.; Kato, S. *J. Phys. Chem. A* **1997**, 101, 5190.
274. El-Sayed, M. A. *Acc. Chem. Res.* **1968**, 1, 8.
275. Balzani, V.; Juris, A.; Venturi, M.; Campagna, S.; Serroni, S. *Acc. Chem. Res.* **1998**, 31, 26.
276. Balzani, V.; Juris, A.; Venturi, M.; Campagna, S.; Serroni, S. *Chem. Rev.* **1996**, 96, 759.
277. Kalyanasundaram, K.; Gratzel, M. *Coord. Chem. Rev.* **1998**, 177, 347.
278. Wenger, O. S.; *Chem. Rev.* **2009**, 253, 1439.
279. Hagfeldt, A.; Boschloo, G.; Sun, L.; Kloo, L.; Pettersson, H.; *Chem. Rev.* **2010**, 110, 6595.
280. O'Regan, B.; Gratzel, M. *Nature* **1991**, 353, 737.
281. Damrauer, N. H.; Cerullo, G.; Yeh, A.; Boussie, T.; Shank, C. V.; McCusker, J. K. *Science* **1997**, 275, 54.
282. McCusker, J. K. *Acc. Chem. Res.* **2003**, 36, 876.
283. Bhasikuttan, A. C.; Suzuki, M.; Nakashima, S.; Okada, T. *J. Am. Chem. Soc.* **2002**, 124, 8398.
284. Cannizzo, A.; van Mourik, F.; Gawelda, W.; Zgrablic, G.; Bressler, C.; Chergui, M. *Angew. Chem., Int. Ed.* **2006**, 45, 3174.
285. Cannizzo, A.; Milne, C. J.; Consani, C.; Gawelda, W.; Bressler, C.; van Mourik, F.; Chergui, M. *Coord. Chem. Rev.* **2010**, 254, 2677.
286. Dallinger, R. F.; Woodruff, W. H. *J. Am. Chem. Soc.* **1979**, 101, 4391.
287. Bradley, P. G.; Kress, N.; Hornberger, B. A.; Dallinger, R. F.; Woodruff, W. H. *J. Am. Chem. Soc.* **1981**, 103, 7441.

References

288. Oh, D. H.; Boxer, S. G. *J. Am. Chem. Soc.* **1989**, *111*, 1130.
289. Kober, E. M.; Sullivan, B. P.; Meyer, T. J. *Inorg. Chem.* **1984**, *23*, 2098.
290. McClanahan, S. F.; Dallinger, R. F.; Holler, F. J.; *J. Am. Chem. Soc.* **1985**, *107*, 4853.
291. Yeh, A. T.; Shank, C. V.; McCusker, J. K. *Science*. **2000**, *289*, 935.
292. Shaw, G. B.; Styers-Barnett, D. J.; Gannon, E. Z.; Granger, J. C.; Papanikolas, J. M. *J. Phys. Chem. A* **2004**, *108*, 4998.
293. Omberg, K. M.; Smith, G. D.; Kavaliunas D. A.; Chen, P.; Treadway, J. A.; Schoonover, J. R.; Palmer, R. A.; Mayer, T. J. *Inorg. Chem.* **1999**, *38*, 951.
294. Omberg, K. M.; Schoonover, J. R.; Treadway, J. A.; Leasure, R. M.; Dyer, R. B.; Meyer, T. J. *J. Am. Chem. Soc.* **1997**, *119*, 7013.
295. Schoonover, J. R.; Strouse, G. F.; *Chem. Rev.* **1998**, *98*, 1335.
296. Moret, M.; Tavernelli, I.; Chergui, M.; Rothlisberger, U.; *Chem. Euro. J.* **2010**, *16*, 5889-5894.
297. Henry, W.; Coates, C. G.; Brady, C.; Ronayne, K. L.; Matousek, P.; Towrie, M.; Botchway, S. W.; Parker, A. W.; Vos, J. G.; Browne W. R.; McGarvey, J. J. *J. Phys. Chem. A* **2008**, *112*, 4537.
298. Wallin, S.; Davidsson, J.; Modin, J.; Hammarstrom, L.; *J. Phys. Chem. A* **2005**, *109*, 4697.
299. Sun, Y., Liu, Y., and Turro, C.; *J. Am. Chem. Soc.*, **2010**, *132*, 5594.
300. Curtright, A. E.; McCusker, J. K.; *J. Phys. Chem. A* **1999**, *103*, 7032.
301. McCusker, C. E.; McCusker, J. K.; *Inorg. Chem.* **2011**, *50*, 1656.
302. Hewitt, J. T.; Vallett, P. J.; Damrauer, N. H. *J. Phys. Chem. A* **2012**, *116*, 11536.
303. Goswami, S.; Mukherjee, R.; and Chakravorty, A. *Inorg. Chem.* **1983**, *22*, 2825.
304. Damrauer, N. H., Boussie, T. R.; Devenney, M.; McCusker, J. K. *J. Am. Chem. Soc.* **1997**, *119*, 8253.
305. Wolfgang, S., Streckas, T. C., Gafney H. D., Kraus, R. A., Kraus, K. *Inorg. Chem.* **1984**, *23*, 2650.
306. Bucholtz, A. *Ann. Chim. Phys.* **1805**, *56*, 142.
307. Rabinowitch, E.; Belford, R. L. *Spectroscopy and Photochemistry of Uranyl Compounds*; Pergamon Press: London, 1964.
308. Balzani, V.; Carasitti, V. *Photochemistry of Coordination Compounds*; Academic Press: New York, 1970.
309. Burrows, H. D.; Kemp, T. J. *Chem. Soc. ReV.* **1974**, *3*, 139.

References

310. Denning, R. G. In *Gmelin Handbook of Inorganic Chemistry*; Buschbeck, K.-C.; Keller, C., Eds.; Springer-Verlag: Heidelberg, Germany, 1983; Vol. A6, p 31-79.
311. Dieke, G. H.; Duncan, A. B. F. *Spectroscopic Properties of Uranium Compounds*; McGraw-Hill: New York, 1949.
312. Jezowska-Trzebiatowska, B.; Bertecki, A. *Spectrochim. Acta* **1962**, *18*, 799.
313. Bell, J. T.; Biggers, R. E. *J. Mol. Spectrosc.* **1965**, *18*, 247.
314. McGlynn, S. P.; Smith, J. K. *J. Mol. Spectrosc.* **1961**, *6*, 164.
315. Hill, R. J.; Kemp, T. J.; Allen, D. M.; Cox, A. *J. Chem. Soc., Faraday Trans I* **1974**, *70*, 847.
316. Tsushima, S. *Inorg. Chem.* **2009**, *48*, 4856.
317. Azehna, M. E. D. G.; Burrows, H. D.; Formosinho, S. J.; Miguel, M. G. M.; Daramanyan, A. P.; Khydyakov, I. V. *J. Lumin.* **1991**, *48 & 49*, 522.
318. Azehna, M. E. D. G.; Burrows, H. D.; Formosinho, S. J.; Miguel, M. G. M. *J. Chem. Soc., Faraday Trans I* **1989**, *85*, 2625.
319. Ryzkhov, M. V.; Gubanov, V. A. *J. Radioanal. Nucl. Chem.* **1990**, *143*, 85.
320. Formosinho, S. J.; Burrows, H. D.; Miguel, M. G. M.; Azehna, M. E. D. G.; Saraiva, I. M.; Ribeiro, C. D. N.; Khydyakov, I. V.; Gasanov, R. G.; Bolte, M.; Sarakha, M. *Photochem. Photobiol. Sci.* **2003**, *2*, 569.
321. Morrison, I. D.; Denning, R. G. *Chem. Phys. Lett.* **1988**, *143*, 409.
322. Sidall, T. H.; Prohaska, C. A. *Nature* **1963**, *202*, 1088.
323. Görrler-Walrand, C.; Vanquickenborne, L. G. *J. Chem. Phys.* **1971**, *54*, 4178.
324. Görrler-Walrand, C.; Vanquickenborne, L. G. *J. Chem. Phys.* **1972**, *57*, 1436.
325. Volod'ko, L. V.; Komayak, A. I.; Sleptsov, L. E. *Opt. Spectrosc.* **1967**, *23*, 397.
326. Denning, R. G. *Struct. Bonding (Berlin)* **1992**, *79*, 215.
327. De Houwer, S.; Görrler-Walrand, C. *J. Alloys Compd.* **2001**, *323-324*, 683.
328. Denning, R. G. *J. Phys. Chem. A* **2007**, *111*, 4125.
329. Zhang, Z.; Pitzer, R. M. *J. Phys. Chem. A* **1999**, *103*, 6880.
330. Matsika, S.; Pitzer, R. M. *J. Phys. Chem. A* **2001**, *105*, 637.
331. Pierloot, K.; van Besien, E. *J. Chem. Phys.* **2005**, *123*, 204309.
332. van Besien, E.; Pierloot, K.; Görrler-Warland, C. *Phys. Chem. Chem. Phys.* **2006**, *8*, 4311.
333. Pierloot, K.; van Besien, E.; van Lenthe, E.; Baerends, E. J. *J. Chem. Phys.* **2007**, *126*, 194311.
334. Řeal, F.; Vallet, V.; Marian, C.; Wahlgren, U. *J. Chem. Phys.* **2007**, *127*, 214302.

References

335. Kropp, J. L. *J. Chem. Phys.* **1967**, *46*, 843.
336. Bell, J. T. *J. Mol. Spectrosc.* **1972**, *41*, 409.
337. Glinka, Y. D.; Krak, T. B. *Phys. Rev. B* **1995**, *52*, 14985.
338. Allen, D. M.; Burrows, H. D.; Cox, A.; Hilla, R. J.; Kemp, T. J.; Stone, T. J. *J. Chem. Soc., Chem. Comm.* **1973**, 59.
339. Okuyama, K.; Ishikawa, Y.; Kato, Y.; Fuku-Tomi, H. *Bull. Res. Lab. Nucl. React. Jpn.* **1978**, *3*, 39.
340. Formosinho, S. J.; Burrows, H. D.; Miguel, M. d.-G.; Emilla, M.; Azenha, D. G.; Saraiva, I. M.; Ribeiro, A. D. N.; Khudyakov, I. V.; Gasanov, R. G.; Bolte, M.; Sarakha, M. *Photochem. Photobiol. Sci.* **2003**, *2*, 569.
341. Billard, I.; Rustenholtz, Z. A.; Semon, L.; Lu'tezenkirchen, K. *Chem. Phys.* **2001**, *270*, 345.
342. Bernhard, G.; Geipel, G.; Reich, T.; Brendler, B.; Amayari, S.; Nitsche, H. *Radiochim. Acta* **2001**, *89*, 511.
343. Cannizzo, A.; van Mourik, F.; Gawelda, W.; Zgrablic, G.; Bressler, C.; Chergui, M. *Angew. Chem., Int. Ed.* **2006**, *45*, 3174.
344. Hedley, G. J.; Ruseckas, A.; Samuel, I. D. W. *J. Phys. Chem. A* **2009**, *113*, 2.
345. Benko, G.; Kallioinen, J.; Korpi-Tommola, J. E. I.; Yartsev, A. P.; Sundstro'm, V. *J. Am. Chem. Soc.* **2002**, *124*, 489.
346. Hedley, G. J.; Ruseckas, A.; Liu, Z. H.; Lo, S. C.; Burn, P. L.; Samuel, I. D. W. *J. Am. Chem. Soc.* **2008**, *130*, 11842.
347. Burrows, H. D. *Inorg. Chem.* **1990**, *29*, 1549.
348. Burrows, H. D.; Formosinho, S. J.; Miguel, M. G. M.; Coelho, F. P. *J. Chem. Soc., Faraday Trans.* **1976**, *72*, 163.
349. Marcantonatos, M. D. *J. Chem. Soc., Faraday Trans.* **1980**, *76*, 2625.
350. Görrler-Walrand, C.; De Jaegere, S. *J. Chim. Phys.* **1972**, *4*, 726.
351. Ikeda-Ohno, A.; Hennig, C.; Tsushima, S.; Scheinost, A. C.; Bernhard, G.; Yaita, T. *Inorg. Chem.* **2009**, *48*, 7201.
352. Ikeda, A.; Hennig, C.; Rossberg, A.; Tsushima, S.; Scheinost, A. C.; Bernhard, G. *Anal. Chem.* **2008**, *80*, 1102.
353. Lahr, H.; Knoch, W. *Radiochim. Acta* **1970**, *13*, 1. (a) Comyns, A. E. *Chem. Rev.* **1960**, *60*, 115.
354. Klygin, A. E.; Kolyada, N. S.; Smirnova, I. D. *Russ. J. Inorg. Chem.* **1970**, *15*, 1719.
(a) Emilla, M.; Azenha, F. G.; Burrows, H. D.; Formosinho, S. J.; Miguel, M. G. M. *J.*

References

- Chem. Soc., Trans. I* **1989**, 85, 2625.
355. Grenthe, I.; Fuger, J.; Konings, R. J. M.; Lemire, R. J.; Muller, A. B.; Nguyen-Trung, C.; Wanner, H. In *Chemical Thermodynamics of Uranium*; Wanner, H., Forest, I., Eds.; OECD Nuclear Energy Agency, Data Bank: Issy-les-Moulineaux, France, 1991. (a) Bell, J. T.; Buxton, S. R. *J. Inorg. Nucl. Chem.* **1974**, 36, 1575.
356. Nagaishi, R.; Katsumura, Y. K.; Ishigure, K.; Aoyagi, H.; Yoshida, Z.; Kimura, T.; Kato, Y. *J. Photochem. Photobiol. A: Chem.* **1996**, 96, 45.
357. Sakuraba, S.; Matsushima, R. *Bull. Chem. Soc. Jpn.* **1970**, 43, 2359.
358. (a) Sakuraba, S.; Matsushima, R. *J. Am. Chem. Soc.* **1972**, 94, 6010. (b) Matsushima, R.; Sakuraba, R. *J. Am. Chem. Soc.* **1971**, 93, 5421.
359. Matsushima, R. *J. Am. Chem. Soc.* **1976**, 94, 6010.
360. Kannan, S.; Vaughn, A. E.; Weiss, E. M.; Barnes, C. L.; Duval, P. B. *J. Am. Chem. Soc.* **2006**, 128, 14024.
361. Greatorex, D.; Hill, R. J.; Kemp, T. J.; Stone, T. J. *J. Chem. Soc., Faraday I* **1972**, 68, 2059.
362. Ledwith, A.; Russel, P. J.; Sutcliffe, L. H. *Proc. R. Soc. A* **1973**, 332, 151.
363. Zewail, A. H. *Annu. Rev. Phys. Chem.* **2006**, 57, 65.
364. Hada M.; Pichugin, K.; Sciaini, G. *Eur. Phys. J. Special Topic* **2013**, 222, 1093.
365. Kling, M. F.; Vrakking, M. J. J. *Annu. Rev. Phys. Chem.* **2008**, 59, 463.

